UNIVERSIDAD DE CHILE
FACULTAD DE CIENCIAS FÍSICAS Y MATEMÁTICAS
DEPARTAMENTO DE FÍSICA

LABYRINTHINE PATTERNS IN OUT-OF-EQUILIBRIUM SYSTEMS

TESIS PARA OPTAR AL GRADO DE DOCTOR EN CIENCIAS, MENCIÓN FÍSICA

SEBASTIÁN IGNACIO ECHEVERRÍA ALAR

PROFESOR GUÍA:
MARCEL CLERC GAVILÁN

MIEMBROS DE LA COMISIÓN:
IGNACIO BORDEU WELDT
PAULINA HIDALGO CÓRDOVA
ALEJANDRO LEÓN VEGA
MUSTAPHA TLIDI
JUÁN VALDIVIA HEPP

SANTIAGO DE CHILE
2023

PATRONES LABERÍNTICOS EN SISTEMAS FUERA DEL EQUILIBRIO

Esta tesis está dedicada a la descripción e implementación de técnicas teóricas y computacionales para comprender la emergencia de patrones laberínticos en sistemas fuera del equilibrio. En particular, este trabajo se enfoca en dos contextos físicos en los cuáles se han observado patrones laberínticos: ecosistemas bajo estrés hídrico y experimentos de cristales líquidos nemático-quirales sometidos a frustración geométrica.

En el Capítulo 1, se da una breve introducción a los sistemas fuera del equilibrio y a la formación de patrones para motivar la investigación de los patrones laberínticos. Además, se definen los objetivos general y específicos de la tesis. El Capítulo 2 consiste en un compendio de conceptos y técnicas, los cuáles sirven de base para abordar los objetivos de esta investigación.

El Capítulo 3 introduce una definición precisa de patrones laberínticos, basada en la estructura global y local de estos equilibrios. Además, se proponen parámetros de orden adecuados, como la densidad de defectos, longitud de correlación y factor de estructura, para revelar transiciones entre distintos tipos de laberintos observados en un modelo prototipo de formación de patrones. En el Capítulo 4, se describe la existencia de patrones laberínticos localizados en dos y tres dimensiones, y se proponen los ingredientes mínimos para observar estas estructuras en diferentes sistemas físicos. En particular, el Capítulo 5 aborda este asunto en el contexto de la auto organización de la vegetación en regiones áridas y semiáridas.

Los Capítulos 6 y 7 están destinados a explorar el efecto de las heterogeneidades espaciales en la formación de estructuras de vegetación. Por una parte, el Capítulo 6 propone una forma simple de incorporar inhomogeneidades en modelos ecológicamente relevantes, y discute la formación de estructuras desde la perspectiva de separación de fases. Por otra parte, en el Capítulo 7 se discute cómo la adición de heterogeneidades puede explicar la formación de patrones laberínticos imperfectos.

En los Capítulos 8, 9 y 10 se investiga la formación de patrones laberínticos en celdas de cristal líquido nemático quiral. Primero, en el Capítulo 8, se describe la observación de laberintos colestéricos y burbujas quirales en experimentos forzados con temperatura. En base a estas observaciones, se propone un modelo minimal tipo Ginzburg-Landau que da cuenta de la anisotropía y quiralidad de la mezcla de cristal líquido utilizada. Empleando experimentos, integraciones numéricas del modelo y una ecuación de interfaz, se revela el mecanismo de aparición/desaparición de vórtices localizados. Luego, en el Capítulo 9 se estudia detalladamente la emergencia de laberintos colestéricos ramificados, en donde se expone cómo la manifestación mesoscópica de la quiralidad es responsable de la creación de patrones desordenados. Finalmente, en el Capítulo 10 se explora la estabilización de otro tipo de laberintos colestéricos, los cuáles son generados por una inestabilidad de invaginación. El capítulo 11 resume las principales conclusiones de este trabajo.

LABYRINTHINE PATTERNS IN OUT-OF-EQUILIBRIUM SYSTEMS

This dissertation is devoted to describing and implementing theoretical and computational techniques to understand the emergence of labyrinthine patterns in out-of-equilibrium systems. In particular, this work focuses on two physical contexts in which labyrinthine patterns have been observed: ecosystems under hydric stress and chiral nematic liquid crystal experiments subjected to geometric frustration.

In Chapter 1, a brief introduction to out-of-equilibrium systems and pattern formation is given to encourage the investigation of labyrinths. Additionally, the general and specific objectives of the dissertation are defined. Chapter 2 consists of a compendium of concepts and techniques, which are the essential tools to address the objectives of this research.

Chapter 3 introduces a precise definition of labyrinthine patterns based on the global and local structure of these equilibria. Additionally, proper order parameters, such as defect density, correlation length, and structure factor, are proposed to reveal transitions between different types of labyrinths observed in a pattern-forming prototype model. Chapter 4 describes the existence of localized labyrinthine patterns in two and three dimensions, and it proposes the minimum ingredients to observe these structures in different physical systems. In particular, Chapter 5 addresses this issue in the context of the self-organization of vegetation in arid and semi-arid regions.

Chapters 6 and 7 are devoted to exploring the effect of spatial heterogeneities on the formation of vegetation structures. On the one hand, Chapter 6 proposes a simple way to incorporate inhomogeneities into ecologically relevant models and discusses structure formation from the perspective of phase separation. On the other hand, Chapter 7 outlines how adding heterogeneities can explain the formation of imperfect labyrinthine patterns.

In Chapters 8, 9, and 10, the formation of labyrinthine patterns in chiral nematic liquid crystal cells is investigated. First, Chapter 8 describes the observation of cholesteric labyrinths and chiral bubbles in temperature-forced experiments. Based on these observations, a Ginzburg-Landau type of model is proposed, which accounts for the anisotropy and chirality of the liquid crystal mixture used. By using experiments, numerical integrations of the model, and an interface equation, the appearance/disappearance mechanism of localized vortices is revealed. Then, in Chapter 9, the emergence of branching cholesteric labyrinths is studied in detail, exposing how the mesoscopic manifestation of chirality is responsible for creating disordered patterns. Finally, in Chapter 10, the stabilization of another type of cholesteric labyrinths is explored, in which an invagination instability governs the dynamics. Chapter 11 summarizes the main conclusions of this work.

Y yo canto para usted
El que atrasa los relojes
El que ya jamás podrá cambiar
Y no se dio cuenta nunca
Que su casa se derrumba
Sui Generis, Para Quien Canto Yo Entonces

Acknowledgements

Quisiera agradecer a Jaqueline y Alfredo por haberme entregado el cariño y comodidad suficientes para tratar de darle sentido al día a día. Agradezco también a Nicolás; verte avanzar mientras vas cuestionando las cosas me transmite paz.

Agradezco a Magdalena por su amor, comprensión, compañía y ayuda durante este largo proceso.

Agradezco a Benjamín, Camila, Felipe, Julio, Sebastián, Sergio, Clemente y Juan Pablo por su amistad, que ha trascendido tiempo y distancia. También agradezco a David y Gregorio por su camaradería y amistad.

Quiero agradecer a mis compañeras y compañeros del LAFER por el tiempo compartido.

Estoy agradecido de Tatiana Toro por sus enseñanzas que se transformaron en la motivación inicial.

Agradezco a Francisco Suárez y Cristián Escauriaza por motivarme a ir más allá.

Agradezco a Ignacio Bordeu por su afectuoso recibimiento en Inglaterra.

Me gustaría agradecer a Paulina Hidalgo y Jorge Vergara por su recibimiento en Concepción y por la sintetización del cristal líquido colestérico utilizado en parte de esta tesis.

Agradezco a Mustapha Tlidi por su gentil recibimiento en Bélgica y por sus consejos científicos.

Finalmente, quiero agradecer a Marcel Clerc, por su guía, preocupación, rigurosidad y pasión. Me siento muy afortunado de haber sido parte de la institución que has creado.

Table of Content

List of Figures

Chapter 1

Introduction

Patterns are dissipative structures appearing in systems out-of-equilibrium [1, 2, 3, 4]. Product of a balance between energy injection and dissipation mechanisms, these systems exhibit a collective behavior in which their constituents self-organize, giving rise to extended patterns in space [5, 6]. This type of collective behavior, which can not be understood by looking at the isolated constituents, is an emerging phenomenon [7]. Some of the forms observed in nature are dunes, ripples in the sand near the beach, vegetation structures in semi-arid and arid climates, animal fur, skin shapes in fish and butterflies, papillary ridges, honeycombs, dendrites, river networks, and branches in trees, to name a few [8, 9, 10, 11, 12, 13]. The presence of patterns in various systems means that the phenomenon is robust; it does not depend on the underlying physics nor the scales. The characteristic length of the spatial textures can be determined by extrinsic factors, such as the geometry containing convective rolls in the Bénard-Rayleigh experiment [14, 15, 16], or by intrinsic factors, such as diffusion constants of chemical reactants regulating morphogenesis as shown by the pioneer work of Alan Turing [17]. From a theoretical point of view, the emergence of patterns can be seen as a spatial symmetry breaking instability experienced by a uniform (spatially and temporally invariant) equilibrium. During the last century, this phenomenon has been described through weakly nonlinear analysis methods based on amplitude or envelope equations [4, 5, 6, 18, 19, 20]. These methods are inspired by linear analysis and nonlinear saturation; that is, systems at the onset of a spatial instability are described by the unstable critical modes and their nonlinear saturation. This balance gives birth to stripe, hexagonal, square, superlattice, and/or quasi-crystal patterns near the spatial instability [4, 5, 6, 18, 19, 20]. The stripe patterns are understood as the stable equilibrium of a single mode [4, 5, 6, 18, 19, 20]. Likewise, the square, hexagonal, and superlattice patterns are understood as coupled equilibria between two, three, and several resonant modes, respectively [4, 5, 6, 18, 19, 20, 21]. Quasicrystals result from higher co-dimensional instabilities including modes of different wavelengths [4, 5, 6, 18, 19, 20, 22].

In isotropic two-dimensional systems, and far from the onset of spatial instabilities, complicated patterns govern the dynamics of out-of-equilibrium systems. These dissipative structures have been coined as labyrinthine patterns [23, 24], and they consist in several domains of stripes in different orientations connected by localized and extended defects [25]. They have been observed in various physical systems, such as Bénard-Rayleigh convection [26, 27], ferrofluids [28, 29], chemical reactions [30, 31], vegetation in semi-arid areas [32, 33, 34, 35], liquid crystals [36, 37, 38], mollusk populations [39], block polymers [40], metal nanosurfaces [41], and ferroelectric thin films [42]. Although complicated striped patterns have been

termed labyrinths in numerous works, a precise quantitative definition that makes it possible to understand, characterize, and differentiate labyrinthine patterns is lacking. The first part of this dissertation is dedicated to defining and describing extended and localized labyrinthine patterns based on numerical observations of these equilibria in a prototype pattern-forming model called the Swift-Hohenberg (SH) equation [16, 43]. Then, this work aims to investigate the emergence of labyrinthine patterns in two physical contexts: vegetation self-organization in arid environments and confined chiral nematic liquid crystals (CNLCs).

Macroscopic self-organized structures arise in plant ecology, where stressed vegetation biomass can self-organize when resources, such as water or nutrients, are limited [8, 44, 45, 46, 47, 48, 49, 33]. Under these arid conditions, the plant community displays coherent distributions, which are maintained by facilitative and competitive processes involving plants and the environment [44]. These distributions, whose wavelengths range from centimeter to kilometer scales, are vegetation patterns. From an ecological modeling perspective, a generic sequence of patterns, depending on climate stress, has been established. Starting from a uniform cover, as the aridity level (resource availability) is increased (decreased), the first pattern that appears consists of a periodic spatial distribution of gaps followed by labyrinths and then spots. The first paper to discuss the sequence was [45] in 1999. Later on, the sequence was analyzed from reaction-diffusion models approach in 2001 [46] and 2002 [47]. Besides periodic, other aperiodic and localized vegetation patterns have been reported [50, 51, 52, 53, 54, 55, 56, 57, 58, 59, 60, 61, 62]. The second part of this dissertation is focused on the investigation of localized and extended labyrinthine vegetation patterns in real ecosystems, and the effect of heterogeneities in the latter.

CNLCs can be created by doping a nematic liquid crystal, characterized by a long-range orientational order, but not a positional one, with chiral molecules [63, 64, 65]. In this dissertation, we have used a mixture composed of a commercial nematic liquid crystal E7 (Merck) and chiral molecules EOS12 [66]. The addition of chiral dopants can induce a spontaneous twist deformation in the nematic phase creating a helical structure [63, 67, 64]. When subjected to homeotropic anchoring in a cell, the helical phase gets frustrated, so that given a critical degree of frustration, the system unwinds. This state is purely geometric and is sustained by the competition between the cholesteric pitch, geometric effects introduced by the cell thickness, and elasticity [68, 69, 64]. The twisted or winded structure can be recovered by applying a voltage, a temperature difference, or changing the thickness to the cell in the unwound state [64]. In general, the reappearance of the twisted phase is in the form of a translationally invariant configuration (TIC) or in the form of cholesteric fingers of type 1 (CF1) [70, 71, 36, 72]. Besides, localized structures, known as elementary torons or chiral bubbles, can also be exhibited by cholesteric phases [64, 73, 74]. The last part of this dissertation dedicates to understanding temperature-triggered transitions in CNLCs from the point of view of Ginzburg-Landau (GL) equations. The emphasis is given to the stabilization of localized vortices and the emergence of labyrinthine patterns.

1.1.   Contents

This dissertation is a compendium of manuscripts consisting of 7 peer-reviewed published papers and one conference paper. Each manuscript has an associated Chapter, including a small introduction focused on the motivation of the particular paper and some perspectives at the end. The first chapter of this dissertation is the present Introduction, which is followed by Chapter 2 where the essential concepts and techniques needed to tackle this research are

introduced. Chapter 3 introduces a precise definition of labyrinthine patterns based on the global and local structure of these equilibria in Fourier space. Additionally, proper order parameters, such as defect density, correlation length, and structure factor, are proposed to reveal transitions between different types of labyrinths–fingerprint, glassy, and scurfy– observed in a pattern-forming prototype model, the Swift-Hohenberg (SH) equation. Chapter 4 describes the existence of localized labyrinthine patterns in two and three dimensions in the SH equation, and the minimum ingredients to observe these structures in different physical systems (ecology, optics and chemistry) are proposed. In particular, Chapter 5 addresses this issue in the context of the self-organization of vegetation in arid and semi-arid regions, where localized disordered bands of vegetation in Africa motivates the employment of pattern-forming ecological models.

Chapters 6 and 7 are devoted to exploring the effect of spatial heterogeneities on the formation of vegetation structures. Chapter 6 proposes a simple way to incorporate inhomogeneities into ecologically relevant models motivated by the topographic variations in arid landscapes. The heterogeneities are included by promoting an aridity parameter to be space dependent by using correlated and non-correlated distributions. Moreover, the formation of vegetated structures is discussed from the perspective of phase separation. Chapter 7 addresses the addition of heterogeneities to perfect labyrinthine patterns obtained in ecological models, in order to explain the formation of imperfect labyrinthine patterns or disordered self-organizations, which are in a closer qualitative agreement with the satellite images of arid and semi-arid landscapes.

In Chapters 8, 9, and 10, the formation of labyrinthine patterns in chiral nematic liquid crystal cells is investigated. First, Chapter 8 describes the observation of cholesteric labyrinths and localized vortices in temperature-forced experiments. Based on these observations, a Ginzburg-Landau type of model is proposed, which accounts for the anisotropy and chirality of the liquid crystal mixture used. By using experiments, numerical integrations of the model, and an interface equation, the appearance/disappearance mechanism of localized vortices is revealed, which turns out to be a saddle-node bifurcation. Then, in Chapter 9, the emergence of branching cholesteric labyrinths is studied from the point of view of instabilities of the rounded tips of cholesteric fingers of type I (CF1), exposing how the mesoscopic manifestation of chirality is responsible for creating disordered patterns. Finally, in Chapter 10, the stabilization of another type of cholesteric labyrinths is explored, in which an invagination instability governs the dynamics. This instability occurs spontaneously due to energy minimization processes. Chapter 11 summarizes the main conclusions of this work.

1.2. General objective

The main objective of this dissertation is to study and characterize creation, stabilization and disappearance of labyrinthine-like patterns in out-of-equilibrium systems from theoretical and numerical perspectives.

1.3. Specific objectives

The specific objectives of this doctoral dissertation are:

- Define the labyrinthine pattern from the physical and mathematical points of view.

- Understand the emergence and disappearance of the labyrinthine pattern, defining ap-

propriate order parameters.

- Study the coexistence of labyrinths with uniform states and explore the localization of non-trivial symmetry patterns in different physical systems.

- Use and extend the concepts of labyrinthine structures to understand the irregular labyrinthine-like patterns observed in vegetation ecosystems.

- Characterize the appearance and stabilization of labyrinthine patterns in confined chiral nematic liquid crystals (CNLCs).

- Study the formation of localized vortices, fingers, and labyrinths in CNLCs using the amplitude equation approach.

1.4.   Common abbreviations

- **SH**: Swift-Hohenberg equation.

- **gSH**: Generalized Swift-Hohenberg equation.

- **GL**: Ginzburg-Landau equation with real coefficients.

- **CAGL**: Chiral-anisotropic Ginzburg-Landau equation.

- **CNLCs**: Chiral nematic liquid crystals.

- **CF1**: Cholesteric fingers of type 1.

- **POM**: Polarized optical microscopy.

- **CMOS**: Complementary metal oxide semiconductor (camera).

1.5.   Contribution statement

1.5.1.   Labyrinthine pattern transitions (Physical Review Research 2, 042036)

Sebastián Echeverría-Alar performed research (implementation of computational algorithms, numerical integration of SH equation, and analysis of numerical data). Marcel G. Clerc designed the research and wrote the manuscript.

1.5.2.   Localized states with nontrivial symmetries: Localized labyrinthine patterns (Physical Review E 105, L012202)

Marcel G. Clerc designed the research. **Sebastián Echeverría-Alar** performed research (numerical integrations and analysis of numerical data). **Sebastián Echeverría-Alar** and Mustapha Tlidi wrote the manuscript.

1.5.3. Localised labyrinthine patterns in ecosystems (Scientific reports 11, 18331)

Marcel G. Clerc and Mustapha Tlidi designed the research. **Sebastián Echeverría-Alar** performed research (numerical integrations and analysis of numerical and satellite data). **Sebastián Echeverría-Alar** and Mustapha Tlidi wrote the manuscript.

1.5.4. Vegetation covers phase separation in inhomogeneous environments (Chaos, Solitons & Fractals 163, 112518)

David Pinto-Ramos performed research (implementation of computational algorithms, numerical integrations, analytical calculations, analysis of numerical data). **Sebastián Echeverría-Alar** performed research (numerical integrations and analysis of numerical and satellite data). David Pinto-Ramos, **Sebastián Echeverría-Alar**, and Mustapha Tlidi wrote the manuscript. Marcel G. Clerc and Mustapha Tlidi designed the research.

1.5.5. Effect of heterogeneous environmental conditions on labyrinthine vegetation patterns (Physical Review E 107, 054219)

Sebastián Echeverría-Alar performed research (implementation of computational algorithms, numerical integrations and analysis of numerical and satellite data). **Sebastián Echeverría-Alar**, David Pinto-Ramos, and Mustapha Tlidi wrote the manuscript. Marcel G. Clerc and Mustapha Tlidi designed the research.

1.5.6. Localized dissipative vortices in chiral nematic liquid crystal cells (Physical Review Research 4, L022021)

Marcel G. Clerc designed the research. Gregorio González-Cortés performed research (experiments). **Sebastián Echeverría-Alar** performed research (numerical integrations, analysis of experimental and numerical data, and analytical calculations) and wrote the manuscript.

1.5.7. Emergence of disordered branching patterns in confined chiral nematic liquid crystals (Proceedings of the National Academy of Sciences 120, e2221000120)

Sebastián Echeverría-Alar performed research (realization of experiments, implementation of computational algorithms, numerical integrations, analysis of experimental and numerical data; and analytical calculations) and wrote the manuscript. Marcel G. Clerc designed research. Ignacio Bordeu performed research (numerical simulations and analysis of experimental and numerical data) and wrote the manuscript.

1.5.8. Morphological transition of labyrinthine patterns in frustrated chiral nematic liquid crystals (Liquid Crystals XXVI 12207, 75-81)

Sebastián Echeverría-Alar designed and performed research (realization of experiments, implementation of isotropic algorithms, and numerical integrations), and wrote the manuscript.

Chapter 2

Theoretical framework

2.1. Dissipative Dynamical Systems

An observer experiences the dynamic world around us through their senses. They smell the vegetables on the fridge when they are past their due date, hear the boiling of water in the kitchen, see their beloved ones get older every day, taste chocolate while it is melting in their mouths, and feel pain because of a wound in their skin. All of the listed experiences have a particular initial condition (good vegetables, cold water, young people, solid chocolate, healthy skin, respectively), which are manifested in a macroscopic world, where inevitably, an arrow of time will lead the initial states into the future [75, 76].

From a modeler perspective, the situations described above are defined as dynamical systems and can be generally formulated as

$$\partial_t \mathbf{u} = \mathbf{f}(\mathbf{u}, \lambda), \tag{2.1}$$

where $\partial_t \mathbf{u}$ accounts for the temporal evolution of a state variable $\mathbf{u}$ describing the system, and $\vec{f}$ is a function governing the dynamics of the system. The set of parameters λ regulates the evolution of the variable $\mathbf{u}$.

In this dissertation, and in general, when dealing with real physical systems, the function $\mathbf{f}$ is nonlinear in $\mathbf{u}$. This key ingredient, nonlinearity, is responsible for the rich phenomenology exhibited by systems modeled with Eq. (2.1). In particular, the functional form of the nonlinear function $\mathbf{f}$ will dictate the type and stability of the equilibria ($\mathbf{f} = 0$) exhibited by Eq. (2.1). The stability of the solutions can be tested by a local linear analysis around them. In the present work, we will deal with systems out of thermodynamic equilibrium; thus, the concept *equilibria* should not be confused with thermodynamic equilibria [3, 19].

The set of control parameters λ is the connection between reality and models. A good model Eq. (2.1) should be able to receive data from real experiments and then use this information as realistic parameters to qualitatively or quantitatively describe natural phenomena. In experiments and models, the parameters can be controlled; they can be decreased or increased, obtaining changes between the equilibria of a dynamical system. These non-thermodynamic transitions are known as bifurcations [77, 78].

2.2. Bifurcations

Bifurcations account for qualitative changes in the dynamics of a system [79]. In this section, we briefly introduce some of the minimal functional forms associated to bifurcations between equilibria in zero-dimensional dynamical systems. These minimal or *normal* forms are valid near the transition or critical points.

2.2.1. Saddle-Node bifurcation

The normal form related to a saddle-node bifurcation is

$$\partial_t u = \epsilon - u^2, \tag{2.2}$$

where ϵ is the parameter controlling the bifurcation (bifurcation parameter) and u is a real variable of a relevant physical system. The equilibria of equation (2.2) are $u_{eq} = \pm\sqrt{\epsilon}$ with the positive root $\sqrt{\epsilon}$ being the stable solution. In particular, equation (2.2) illustrates the appearance (disappearance) of the equilibria u_{eq} when increasing (decreasing) the control parameter ϵ. Figure 2.1 shows the bifurcation diagram of Eq. (2.2) where at the critical (or saddle) point $\epsilon^* = 0$ the equilibria emerge $\epsilon \geq \epsilon^*$ or disappear $\epsilon < \epsilon^*$.
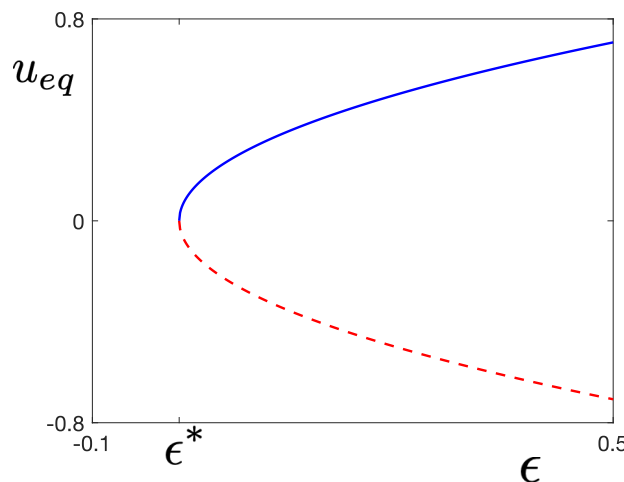
Figure 2.1: Saddle-node bifurcation diagram. The solid blue line accounts for the stable solution $\sqrt{\epsilon}$ and the dashed red line is the unstable solution $-\sqrt{\epsilon}$. The critical point is $\epsilon^* = 0$.

The behavior of the bifurcations can be represented in the phase space $\{u, \partial_t u\}$ of the dynamical systems. In the case of the saddle-node transition, which will be relevant in Chapter 8, a peculiarity is that the disappearance of the equilibria occurs through their collision at the critical point $\epsilon = \epsilon^*$ (see Fig. 2.2).
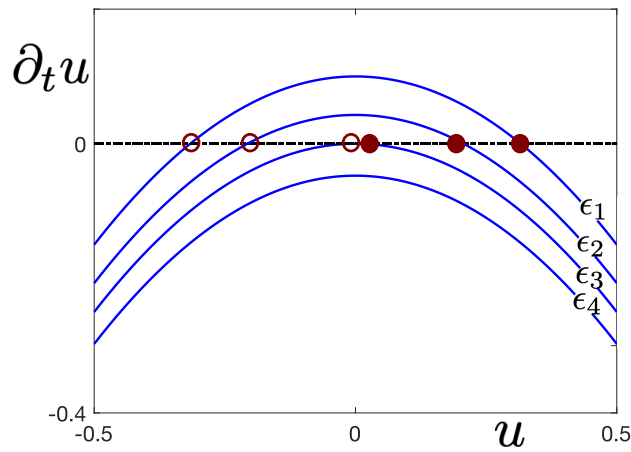
Figure 2.2: Saddle-node bifurcation in the phase space $\{u, \partial_t u\}$. The solid blue lines illustrates the functional form of Eq. (2.2) for different values of ϵ, where $\epsilon_1 > \epsilon_2 > \epsilon_3 > \epsilon^* > \epsilon_4$. The solid red dots indicate the stable equilibria while the hollow red dots the unstable equilibria.

2.2.2.   Transcritical bifurcation

The normal form associated to a transcritical bifurcation is

$$\partial_t u = \eta u - u^2, \tag{2.3}$$

where η is the parameter controlling the bifurcation and u is a real variable of a relevant physical system. The equilibria u_{eq} of equation (2.3) are $u_1 = 0$ and $u_2 = \eta$. The peculiarity of the normal form (2.3) is that at the critical point $\eta^* = 0$ an interchange of stability occurs between u_1 and u_2 as shown in Fig. 2.3.
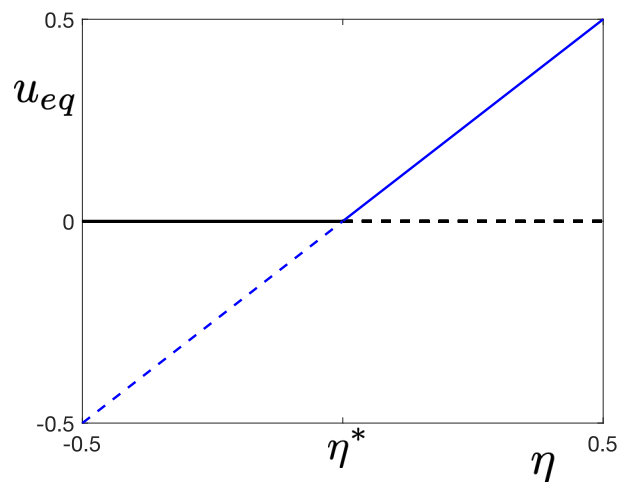
Figure 2.3: Transcritical bifurcation diagram. The solid (dashed) black line indicates the stable (unstable) $u_{eq} = u_1$ equilibrium. The solid (dashed) blue line indicates the stable (unstable) $u_{eq} = u_2$ equilibrium. The critical point is $\eta^* = 0$.

8

2.2.3.   Supercritical Pitchfork bifurcation

The normal form of a supercritical pitchfork bifurcation is

$$\partial_t u = \epsilon u - u^3, \tag{2.4}$$

where ϵ is the parameter controlling the bifurcation and u is a real variable of a relevant physical system. The equilibria u_{eq} of equation (2.4) are $u_o = 0$ and $u_\pm = \pm\sqrt{\epsilon}$. Figure 2.4 shows the bifurcation diagram of the dynamical system (2.4). Below the critical point $\epsilon^* = 0$, only the equilibrium u_o exists and it is stable. Above the bifurcation point, the two stable solutions $u_\pm$ emerge and the u_o state becomes unstable.
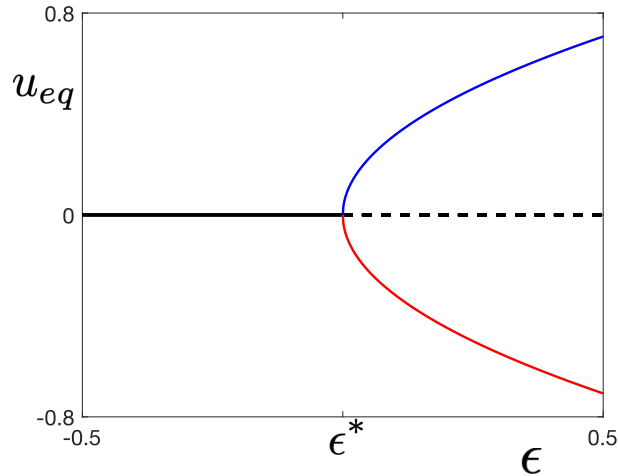
Figure 2.4: Supercritical bifurcation diagram. The solid (dashed) black line indicates the stable (unstable) $u_{eq} = 0$ equilibrium. The solid blue line shows the stable solution u_+, while the solid red line is the stable equilibrium u_-. The critical point is $\epsilon^* = 0$.

2.2.4.   Subcritical bifurcation with reflection symmetry

The subcritical bifurcation can be described by the fifth-order normal form

$$\partial_t u = \mu u + \beta u^3 - u^5, \tag{2.5}$$

where μ is the parameter controlling the bifurcation and u is a real variable of a relevant physical system. The parameter β controls the type of the bifurcation, which is subcritical when $\beta > 0$. In particular, we can set $\beta = 1$ for the present discussion. The five equilibria of the dynamical system (2.5) are $u_o = 0$ and $u_{\pm\pm} = \pm(1/2 \pm \sqrt{1/4 + \mu})^{1/2}$. The subcritical transition is manifested when the system is prepared with the initial condition $u = u_o$ at $\mu < \mu_{ub}^* = 0$ and then increasing μ until the critical point μ_{ub}^*. There the zero solution loses stability, and the system transitions abruptly to either u_{++} or u_{+-} (see Fig. 2.5).
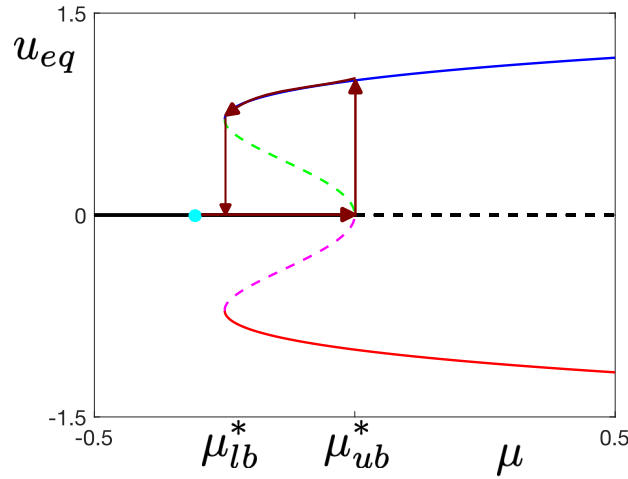
Figure 2.5: Subcritical bifurcation diagram. The solid (dashed) black line indicates the stable (unstable) $u_{eq} = 0$ equilibrium. The solid blue curve shows the stable solution $u_{++} = (1/2 + \sqrt{1/4 + \mu})^{1/2}$. The solid red curve shows the stable solution $u_{+-} = (1/2 - \sqrt{1/4 + \mu})^{1/2}$. The dashed green line indicates the unstable equilibria $u_{-+} = -(1/2 + \sqrt{1/4 + \mu})^{1/2}$. The dashed magenta line indicates the unstable equilibria $u_{--} = -(1/2 - \sqrt{1/4 + \mu})^{1/2}$. The critical point are $\epsilon_{lb}^* = -1/4$ and $\epsilon_{ub}^* = 0$. The red arrows illustrates the subcritical transition and hysteresis effect starting from the solution u_o at the sky blue dot.

The subcritical bifurcation has a lower codimension normal form, which has a pitchfork form ($\partial_t u = \epsilon u + u^3$). However, we have intentionally introduced the normal form (2.5) to address an interesting nonlinear phenomenon, hysteresis. This nonlinear effect is observed when decreasing the parameter μ starting from the stable branch u_{++} (it could be the symmetric one u_{-+}) at $\mu > \mu_{ub}^*$. Now, when going through the critical point μ_{ub}^* the system does not jump back to u_o because the branch u_{++} is stable until $\mu_{lb}^* = -1/4$. At μ_{lb}^*, the stable solution u_{++} collides with u_{-+} disappearing in a saddle-node bifurcation, and the system finally goes back to u_o. In summary, the hysteresis phenomenon is the access to different equilibria depending on the *history* of the system, and is expressed as a *loop*–multistability region–in the bifurcation diagram (see Fig. 2.5).

2.3.   Extended Systems

In the previous chapter, we introduced the notion of simple zero-dimensional dynamical systems, where the single state variable u only depends on time (for example, the position of a particle). However, throughout this dissertation, we will work with spatially extended systems where the variable u will be an extended field $u(\vec{x}, t)$ depending not only on time but also on space $\vec{x}$. This spatial dependence is possible by including spatial couplings in the right-hand side of Eq. (2.1), transforming ordinary differential equations into partial differential equations or even into integrodifferential forms. The couplings can be implemented through local terms (e.g., diffusion, hyperdiffusion, advection) [17, 80, 81, 82, 83, 84, 56, 43, 85] or nonlocal terms [86, 44]. Perhaps, the simple form of spatial coupling is the laplacian $\nabla^2 = \partial_{xx} + \partial_{yy}$, which accompanies prototype two-dimensional reaction-diffusion models; $\partial_t u(\vec{x}, t) = f(u(\vec{x}, t)) + \nabla^2 u(\vec{x}, t)$. The rich phenomenology introduced by spatially extended

systems is beyond words, and in this dissertation, we mainly address interface and pattern phenomena.

2.3.1. Interfaces

The notion of having two or more different states in a spatially extended dynamical system motivates the questioning of how they connect and if this connection is static or dynamic. In words of Pierre-Gilles de Gennes [87]:

"The borders between great empires are often populated by the most interesting ethnic groups. Similarly, the interfaces between two forms of bulk matter are responsible for some of the most unexpected actions. Of course, the border is sometimes frozen (the great Chinese wall). But in many areas, the overlap region is mobile, diffuse, and active (...)".

Let us give a more mathematical framework by considering the dynamical system (2.5) with $\beta = 1$, but including the one-dimensional spatial coupling ∂_{xx}, that is

$$\partial_t u = \mu u + u^3 - u^5 + \partial_{xx} u. \tag{2.6}$$

Now, we can use a computer and numerically integrate the above equation by discretizing the continuous operator ∂_{xx} using a second-order finite difference scheme with null-flux boundary conditions, and temporally evolve the system with a Runge-Kutta 4 algorithm. Figure 2.6 shows three different equilibria with their respective temporal evolution, starting from an initial condition meticulously prepared within the multistability region $[\mu_{lb}^*, \mu_{ub}^*]$. This initial condition is an interface connecting the equilibria u_o and u_{++}, exhibiting its major spatial variation at its core at $x = 0$. Figure 2.6(a) shows that the interface is static (an equilibria) at $\mu = -3/16$, while the interface moves in Figs. 2.6(b) and 2.6(c), establishing as equilibria u_o when $\mu < -3/16$ or u_{++} when $\mu > -3/16$, respectively.

The movement of the interface is related to a minimization principle underlying the dynamics of Eq. (2.6), that is the interface will move until the system reach a global minimum of a Lyapunov Functional $\mathcal{F}$ [88, 89, 90] obeying $\partial_t u = -\delta \mathcal{F}[u, \partial_x u]/\delta u$, where

$$\mathcal{F}[u, \partial_x u] = \int dx \left\{ -\mu \frac{u^2}{2} - \frac{u^4}{4} + \frac{u^6}{6} + \frac{(\partial_x u)^2}{2} \right\}. \tag{2.7}$$

An interesting feature to highlight is that in Fig. 2.6(a) the interface is motionless because both states u_o and u_{++} have the same Lyapunov Functional value (or free energy); $\mathcal{F}[u_o] = \mathcal{F}[u_{++}]$, at $\mu = -3/16$. This peculiar value of the bifurcation parameter is called the Maxwell point [91, 92]. Moreover, it can be proved that the speed of the interface c in Fig. 2.6(a) is proportional to the energy difference between the homogeneous states $\mathcal{F}[u_{++}] - \mathcal{F}[u_o]$ [19].

The above picture changes dramatically in two dimensions due to curvature effects. For example, if one thinks in a simple circular interface, the laplacian can be written in polar coordinates with azimuthal symmetry $\nabla^2 = \partial_{rr} + \partial_r/r$. Furthermore, if we assume that the circular interface is characterized by a big radius R, the curvature of the front can be introduced as $\kappa = 1/R$, and then $\nabla^2 = \partial_{rr} + \kappa \partial_r$. The geometrical correction incorporated through κ directly affects the speed of the interface, which at first order is $c = (\mathcal{F}[u_{++}] - \mathcal{F}[u_o]) - a\kappa$, where a is a constant. The interface will be in constant motion due to curvature effects as the system tries to minimize energy by reducing its curvature. Higher order velocity-curvature relations can arise in systems with more complicated interface shapes [93].
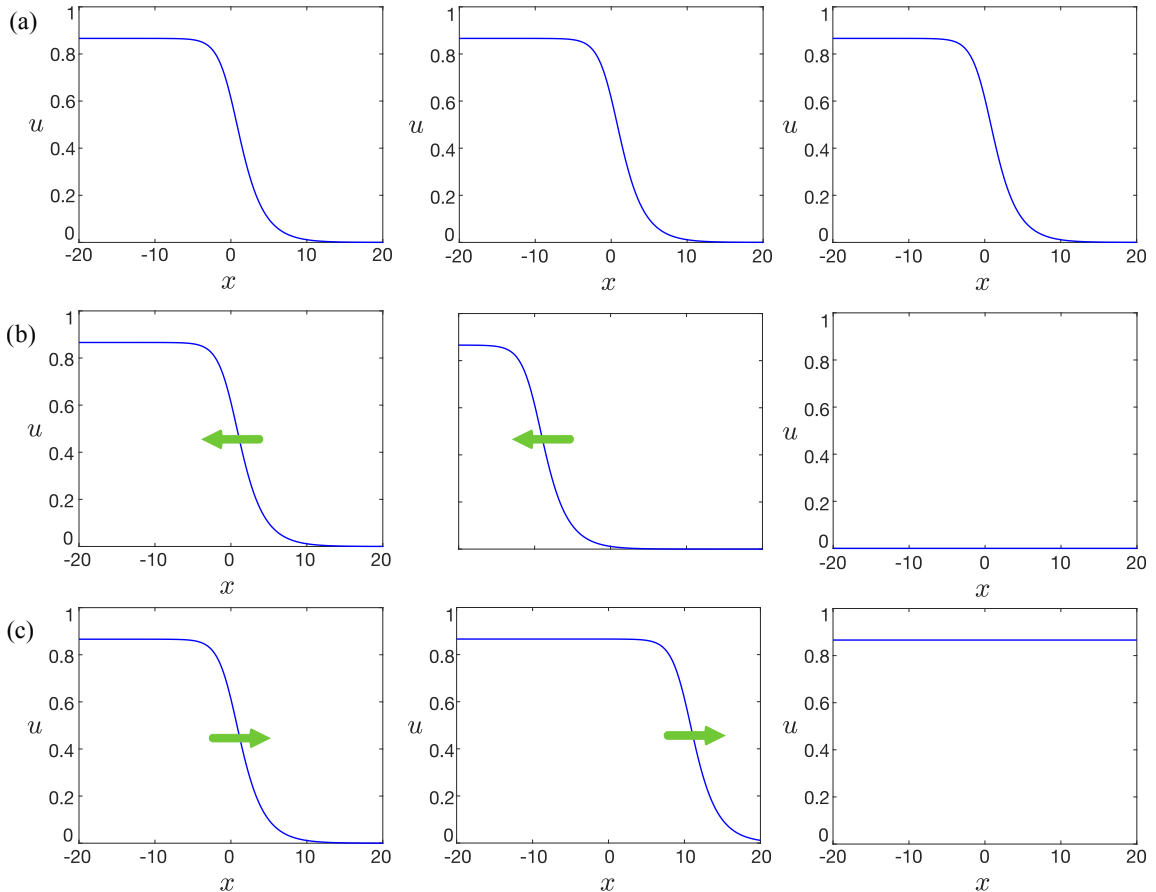
Figure 2.6: Dynamics of the one-dimensional interface connecting the equilibria u_o and u_{++} of Eq. (2.6). The initial condition, an interface of the form $u_f(x) = [3/4(1 + e^{\sqrt{3/4}x})]^{1/2}$ [94], is shown in the left panels and it evolves towards the right panels for different μ values. (a) $\mu = -3/16$, (b) $\mu < -3/16$, and (c) $\mu > -3/16$. The spatial length is in arbitrary units. The green arrows represent the propagation of the interface.

The role of curvature in driving dynamics (of minimization or not) has attracted scientists from different areas [95, 96, 97, 23, 19, 98, 99]. Part of this dissertation (Chapters 8, 9, and 10) is devoted to understand the curvature effects introduced by a nonlinear coupling.

2.3.2.   Pattern Formation

In Chapter 1, we have established that the main focus of this dissertation are labyrinthine patterns emerging in out-of-equilibrium systems and gave a proper introduction to the concept of patterns. In this Chapter, we discuss prototype spatially extended two-dimensional dynamical systems to establish some minimal ingredients needed to observe patterns, such as stripes, labyrinths and hexagons, in mathematical models. Let us introduce the Swift-Hohenberg equation (SH)

$$\partial_t u(x, y, t) = \epsilon u(x, y, t) - u(x, y, t)^3 - \nu \nabla^2 u(x, y, t) - \nabla^4 u(x, y, t), \tag{2.8}$$

where $u(x, y, t)$ is a real scalar variable, $x - y$ are spatial coordinates of a bidimensional plane, and t is time. The first two terms in the right hand side of Eq. (2.8) accounts for a supercritical

pitchfork bifurcation, between the homogeneous states $u = 0$ and $u = \pm\sqrt{\epsilon}$, controlled by the ϵ parameter. The last two terms, an antidiffusion ($\nu > 0$) and a hyperdiffusion, are the spatial mechanisms responsible for the formation of patterns; they establish a wavelength in the system, breaking the translational symmetry of the homogeneous states. This spatial instability can be captured by a linear analysis around the uniform solution $u = 0$, obtaining a dispersion relationship of the form $\sigma = \epsilon + \nu k^2 - k^4$, where σ is the growth rate of an arbitrary inhomogeneous perturbation around the uniform solution $u = 0$, and $k = |\vec{k}|$ is the arbitrary wave vector modulus of the perturbation. The patterns will emerge in the system when $\sigma > 0$, then, the critical condition is $\epsilon_c = -\nu^2/4$. At this critical point, or Turing point, patterns with a critical wavelength $2\pi/k_c = 2\sqrt{2}\pi/\sqrt{\nu}$ will dominate the system (see Fig. 2.7(a)). For bigger values of ϵ, not only the unstable mode k_c arise, but an unstable band of modes Δk is also lifted as depicted in Fig. 2.7(a). Figure 2.7(b) illustrates the dispersion relationship in the full wave vector space $\{k_x, k_y\}$. After the emergence of the pattern, nonlinear mechanisms will play their role and saturate the growth of the unstable mode and its accompanying band. For example, in the simple case when a single mode is selected near ϵ_c, i.e., $u = Ae^{ik_c x} + A^* e^{-ik_c x}$, its slowly varying amplitude $A(X, Y, T)$ obeys the Newell-Whitehead-Segel nonlinear equation [100, 101, 19]

$$\partial_T A = \Delta\epsilon A - |A|^2 A + \left(\partial_X - \frac{i}{\sqrt{2\nu}}\partial_{YY}\right)^2 A, \tag{2.9}$$

where $\Delta\epsilon$ measures the departure from the bifurcation point ϵ_c. The slow variables $\{X, Y, T\}$ are a renormalization of the temporal and spatial scales as a consequence of the proximity to ϵ_c. The reduction of the dynamics near the critical point unveils dynamical behaviors that were inaccessible in the starting equation (2.8). This amplitude equation formalism will be employed in Chapters 8, 9 and 10 to reveal some of the dynamics exhibited by confined chiral nematic liquid crystals.
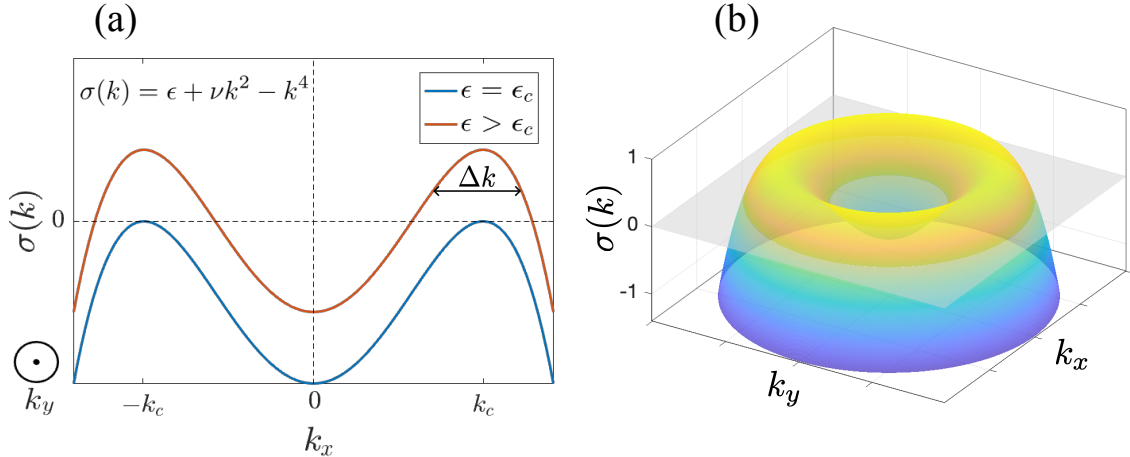
Figure 2.7: Linear spatial instability analysis around $u = 0$ in Eq. (2.8). (a) Arbitrary one-dimensional cut in the wave vector space showing the destabilization of one mode ($k_c = \sqrt{\nu/2}$) at $\epsilon = \epsilon_c = -\nu^2/4$, and a band of modes Δk at $\epsilon > \epsilon_c$. (b) The full two dimensional view of the desestabilization of a ring of modes at $\epsilon > \epsilon_c$.

The prototype pattern forming model (2.8) is variational, that is, $\partial_t u = -\delta\mathcal{F}[u, \nabla u, \nabla^2 u]/\delta u$, where

$$\mathcal{F} = \int\int\left(-\epsilon\frac{u^2}{2} + \frac{u^4}{4} - \nu\frac{(\nabla u)^2}{2} + \frac{(\nabla^2 u)^2}{2}\right)dxdy, \qquad (2.10)$$

is the Lyapunov functional of the SH model. The variational dynamics in pattern forming systems is not necessarily the rule. In out-of-equilibriums systems near the nascent of bistability and a symmetry breaking instability, i.e., Lifshitz point, a generalized model of the Swift-Hohenberg type (gSH) can be derived [83, 84]

$$\partial_t u = \eta + \epsilon u - u^3 - (\nu - bu)\nabla^2 u - c(\nabla u)^2 - \nabla^4 u, \qquad (2.11)$$

where the additional terms with respect to Eq. (2.8) are a constant term η, a nonlinear diffusion process controlled by a parameter b, and a nonlinear advection term tuned by a parameter c. Notice that the additional terms break the parity symmetry $u \to -u$ allowing the system to establish hexagonal patterns as equilibria [102, 103]. Additionally, the nonlinear spatial terms $\{u\nabla^2 u, (\nabla u)^2\}$ rule out the existence of a Lyapunov Functional in Eq. (2.11) (except in the particular case $c = b/2$), allowing the system to access spatiotemporal dynamics [104, 105, 106].

In practice, to study patterns in two dimensions an essential tool are computers, which allows the numerical integration of SH and gSH models starting from different initial conditions [107]. For example, purposedly prepared initial conditions can be implemented to obtain perfect stripes (see Fig. 2.8(a)), perfect hexagonal patterns (see Fig. 2.8(b)), axisymmetrical localized structures, which are a possible equilibria when the bistability and pattern formation ingredients are present (cf. Figs. 2.8(c) and 2.8(d))[108, 109, 110, 111]. Additionally, it is possible to start numerical integrations with a small amount of white noise allowing a system, such as Eq. (2.8), to access different local minima of Eq. (2.10) instead of only the global minimum. This freedom results in the emergence of defects in stripe patterns, breaking the local symmetry of a perfect stripe and costing energy (cf. a pair of dislocations in Fig. 2.8(e)). When the simulation box is sufficiently large, a lot of defects will take over the dynamics creating extended labyrinthine patterns as shown in Figs. 2.8(f) and 2.8(g). These equilibria are metastable states of model Eq. (2.8), while the perfect stripe pattern is the stable solution (see Fig. 2.9 for a schematical energy landscape). In the regime where the uniform solutions of Eq. (2.8) have a similar energy to the pattern solutions [112, 113], complicated localized states can emerge, such as, localized labyrinthine patterns (see Figs. 2.8(g)). Chapters 3 and 4 will focus on studying and extending the ideas of labyrinthine patterns in the SH model.
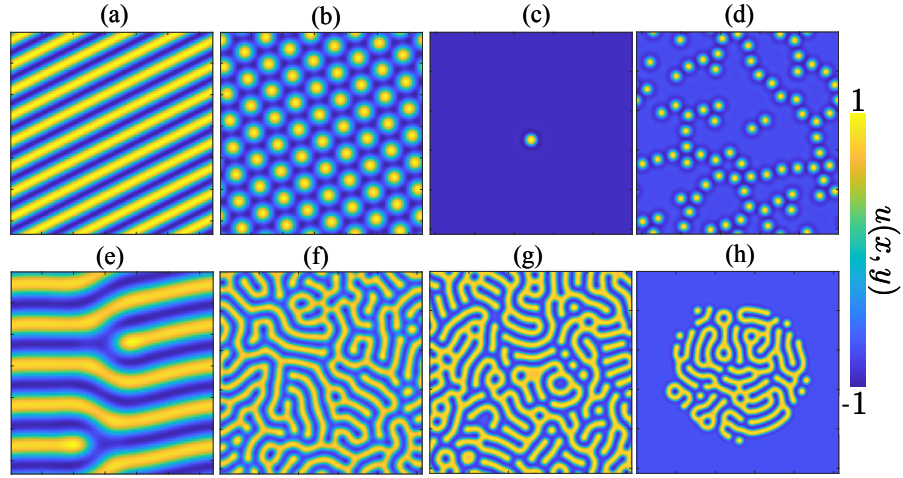
Figure 2.8: Various patterns in Eqs. (2.8) and (2.11) with $\nu = 1$ and $b = c = 0$. (a) Stripe pattern at $\epsilon = 0$ and $\eta = 0$. (b) Hexagonal pattern at $\epsilon = 0.1$ and $\eta = -0.03$. (c) Localized structure at $\mu = 1$ and $\eta = 0$. (d) Chains of localized structures at $\mu = 0.2$ and $\eta = -0.08$. (e) Dislocations at $\epsilon = 0$ and $\eta = 0$. (f) Labyrinthine pattern at $\epsilon = 0.2$ and $\eta = 0$. (g) Labyrinthine pattern at $\epsilon = 1.16$ and $\eta = 0$. (h) Localized labyrinthine pattern at $\epsilon = 1.165$ [114].
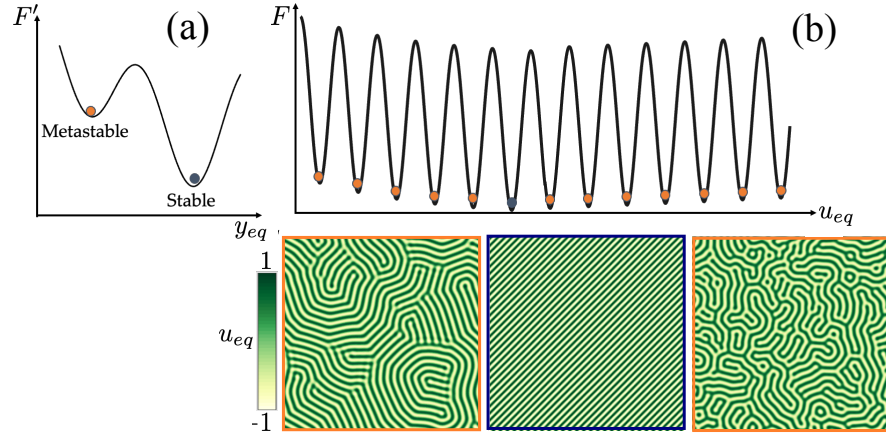
Figure 2.9: Schematical of metastable states in Eq. (2.8). (a) Usual picture of a metastable state as a local minimum and a stable state as a global minimum of a free energy F' depending on an equilibrium variable y_{eq}. (b) Schematical representation of the energy landscape F of Eq. (2.8) showing that labyrinthine patterns (orange) are metastable states and stripe patterns (blue) are stable states.

2.4.   Vegetation self-organization

Self-organized structures emerge in plant ecology, where stressed vegetation biomass can self-organize when resources, such as water or nutrients, are limited [8, 44, 45, 46, 47, 48, 49, 33]. Under these arid conditions, the plant community displays coherent distributions, which are maintained by facilitative and competitive processes involving plants, resources and the environment [44]. These distributions, whose wavelengths range from centimeter to kilometer

scales, are frequently referred to as vegetation patterns, which can be observed in satellite or aerial images of arid or semi-arid regions (some examples are shown in Fig. 2.10).
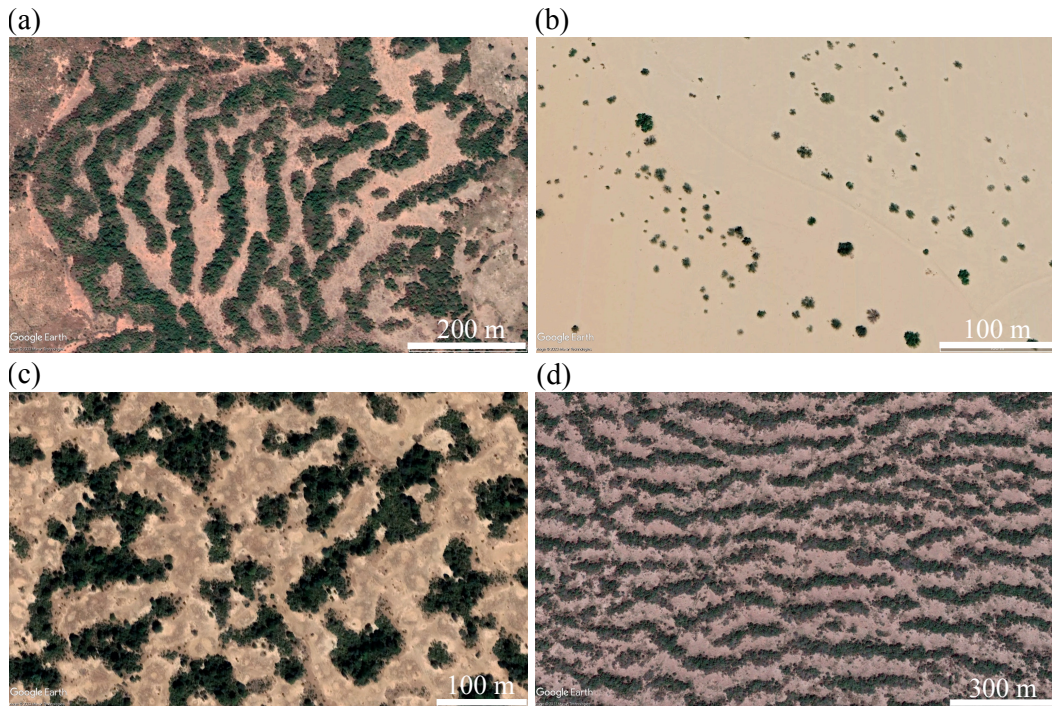
Figure 2.10: Satellite images of vegetation patterns. (a) Niger (12°36'29.76" N 3°00'47.77" E), (b) Namibia (17°39'07.19" S 12°36'22.79" E), (c) Sudan (11°08'23.59" N 27°50'48.33" E), and (d) Sudan (11°05'42.77" N, 28°22'13.15" E). All the images were retrieved from Google Earth software [115].

The formation of vegetation patterns in arid and semi-arid regions has motivated the scientific community to explore different modeling approaches and explanations for this phenomenon [116, 44, 32, 117, 118, 119, 120, 121]. In this dissertation (Chapters 5, 6, and 7), we concentrate on the pioneer modeling approach proposed in Ref. [44], which explains the emergence of vegetation patterns from the perspective of symmetry-breaking instabilities of homogeneous covers in arid or semi-arid environments. Particularly, the plant community behavior is addressed by an interaction-redistribution approach, where the biomass density $c = c(\mathbf{r}, t)$ at space point $\mathbf{r} = (x, y)$ and time t evolves following a logistic equation that includes nonlocal interactions of the biomass [56]

$$\partial_t c = c(1 - c)M_f(\mathbf{r}) - \mu c M_c(\mathbf{r}) + D M_d(\mathbf{r}). \tag{2.12}$$

This is an integrodifferential equation where the constituents of the extended system interact not only through local interactions occurring within a small area but through spatially broader mechanisms mediated by nonlocal functions. The first term in the right-hand side of Eq. (2.12) models the rate at which biomass increases and eventually saturates. The nonlocal function $M_f(\mathbf{r}) = \exp[\chi_f \int d\mathbf{r}' \phi_f(\mathbf{r}', L_f)c(\mathbf{r} + \mathbf{r}')]$ accounts for interactions facilitating growth, regulated by an intensity χ_f. These effects are controlled by the kernel function ϕ_f, whose range of influence is of the order of the plant's aerial structure L_f (size of the canopy or crown). The second term in the right-hand side of Eq. (2.12) represents the biomass death processes.

$M_c(\mathbf{r}) = \exp[\chi_c \int d\mathbf{r}'\phi_c(\mathbf{r}', L_c)c(\mathbf{r} + \mathbf{r}')]$ accounts for interactions enhancing biomass decay with an intensity χ_c. The parameter μ is a measure of the mortality-to-growth rate ratio of plants in the absence of interaction with others, which can be seen as resource scarcity or aridity [44, 117]. This negative feedback acts over distances of the order of the root length L_c with an intensity χ_c and is controlled by the kernel function ϕ_c. A cooperative measure of the ecological system can be introduced as $\chi_f - \chi_c$. The last term in Eq. (2.12) incorporates seeds dispersion with a diffusion parameter D, where $M_d(\mathbf{r}) = \int d\mathbf{r}'\phi_d(\mathbf{r}')[c(\mathbf{r} + \mathbf{r}') - c(\mathbf{r})]$, and $\phi_d(\mathbf{r}')$ accounts for the biomass transport between positions $\mathbf{r}$ and $\mathbf{r}'$. The shape of the kernel or weighting functions depends on the system under study. For example, for isotropic two-dimensional landscapes, Gaussian and exponential type of kernels are suitable enough for qualitative modeling. Equation (2.12) exhibits uniform covers, a bare soil state, and patterns as equilibria [44].

The integrodifferential Eq. (2.12) close to a Lifshitz point, where the bistability is between a uniform vegetation cover and bare soil, and the symmetry breaking instability is suffered by the uniform cover, can be reduced to a partial differential equation. The reduced model reads [45, 56]

$$\partial_t b = -\eta b + \kappa b^2 - b^3 + (\nu - \gamma b)\nabla^2 b - \alpha b\nabla^4 b, \qquad (2.13)$$

where $b = b(\mathbf{r}, t)$ is the state variable associated to the biomass density. The parameters η and κ are the deviations of the aridity and cooperativity critical parameters, respectively. ν and γ are linear and nonlinear diffusion coefficients, respectively. The last term is a nonlinear hyperdiffusion controlled by α. The parameters $\{\nu, \gamma, \alpha\}$ depend on the strength of the competitive feedback, the seed's diffusion, and the shape of the kernels ϕ_f, ϕ_c, and ϕ_d [54]. The model Eq. (2.13) has three homogeneous states; the bare state $b = 0$, and $b_\pm = (\kappa \pm \sqrt{\kappa^2 - 4\eta})/2$. The $b_\pm$ equilibria are connected by a saddle-node bifurcation at $\eta_{sn} = \kappa^2/4$ with κ positive. The uniform solution b_- is always unstable. For small aridity, the vegetated state b_+ is stable. When the aridity is increased the uniform cover suffers a spatial instability. This spatial instability with critical wavelength $\lambda_c = 2\pi\sqrt{2\alpha/(\gamma - \nu/b_c)}$ occurs at $\eta \equiv \eta_c$, where η_c satisfies the implicit condition $4\alpha b_c^2(2b_c - \kappa) = (\gamma b_c - \nu)^2$ with $b_c \equiv b_+(\eta_c)$. The generic sequence of patterns following the increment of the aridity level is: gaps–stripes/labyrinths–spots, and has been predicted using various pattern-forming ecological models. The first paper that discusses the sequence was [45] in 1999. Later on, the sequence was analyzed from reaction-diffusion models in 2001 [46] and 2002 [47]. Besides periodic, other aperiodic and localized vegetation patterns have been reported [50, 51, 52, 53, 54, 122]. Well-documented localized vegetation patterns are the fairy circles [55, 56, 57, 58, 59, 60, 61, 62]. Other alternative hypotheses for the spatial structure of vegetation self-organization have been explored, such as random patterns and power-law distributions of patch sizes [120, 121].

2.5. Chiral nematic liquid crystals

2.5.1. Nematic liquid crystals

Liquid crystals are a state of matter with intermediate physical properties between liquids and solids [63]. This exotic material was discovered by Friedrich Reinitzer [123] when he was studying the thermal behavior of crystals of cholesterol derivatives. In particular, he observed two phase transitions (two melting points) while heating the sample. One year later, these organic materials exhibiting mesomorphic phases (intermediate states) were coined as liquid

crystals by the physicist Otto Lehmann [124]. To chemically generate liquid crystals, strongly elongated molecules or groups of molecules are needed. From a modeling perspective, the particular shape of these objects motivates the introduction of new degrees of freedom, such as the orientation of these non-spherical molecules [63].

In 1922, Georges Friedel introduced the names of three different liquid crystal phases: nematics, smectics, and cholesterics [125]. In this dissertation, we mainly focus on the latter. Nevertheless, we briefly introduce the nematic, or thread-like [126], phase because cholesterics are generally created by doping a nematic liquid crystal with a chiral molecule. Nematics behave as anisotropic fluids showing a preferred alignment in one direction. They are positionally disordered, but orientationally ordered [63]. Figure 2.11(a) shows a small organic molecule, p-azoxyanisole, which from a steric point of view is a rigid rod as depicted schematically in Figure 2.11. When increasing temperature, the material undergoes the two melting transitions described by Friedrich Reinitzer. First, a highly ordered phase (Fig. 2.11(b)) is heated until it reaches the nematic phase (Fig. 2.11(c)), where the remaining orientational order can be distinguished by defining the privileged direction $\vec{n}$, the nematic director. Further heating the system results in the melting of the sample, and the liquid phase emerges (Fig. 2.11(d)). Other molecules or multicomponents, such as MBBA, 5CB, and E7 (see Fig. 2.12 for the molecular representation of the latter), present these macroscopic behaviors when temperature is increased. In this dissertation, we work with liquid crystals undergoing transitions only triggered by temperature variations, that is, thermotropic systems.

The transition from the nematic phase to the isotropic (or liquid) phase can be qualitatively seen as an order-disorder transition [127]. This change in the symmetry of the system can be formally described by a suitable order parameter. In the case of an ideal nematic phase, where molecules are oriented on average in a common direction $\vec{n}$, the system is uniaxial and can be characterized by the macroscopic tensor order parameter [63]
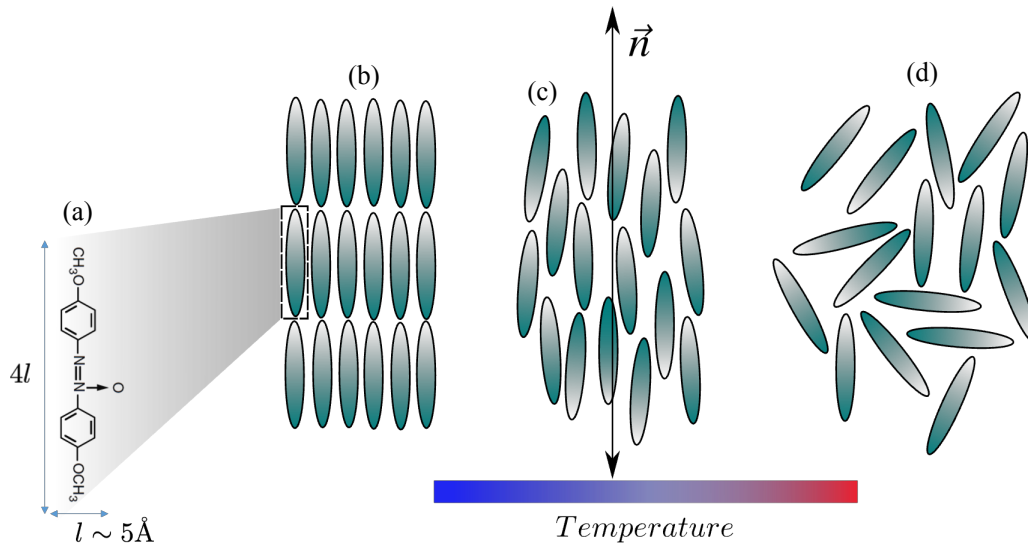
Figure 2.11: Thermotropic liquid crystal exhibiting a nematic phase. (a) Organic molecule p-azoxyanisole (PAA). (b) Ordered crystal phase. (c) The nematic phase is characterized by the nematic director $\vec{n}$. (d) Disordered liquid phase. The green rods are a schematic representation of the organic molecules. The temperature bar indicates low temperatures (blue) and high temperatures (red).

$$Q_{\alpha\beta} = Q(T)\left(n_\alpha n_\beta - \frac{1}{3}\delta_{\alpha\beta}\right), \tag{2.14}$$

where α and β label the three components $\{x, y, z\}$ of the director $\vec{n}$, and $\delta_{\alpha\beta}$ is the Kronecker delta. The tensor $Q_{\alpha\beta}$ is symmetric and fulfills the symmetry $\vec{n} \to -\vec{n}$ (no orientation). The amplitude $Q(T)$ depends on the temperature T of the system and has been used as an order parameter in the Landau-de Gennes theory to reveal the first-order transition between the nematic and the isotropic phase [127].
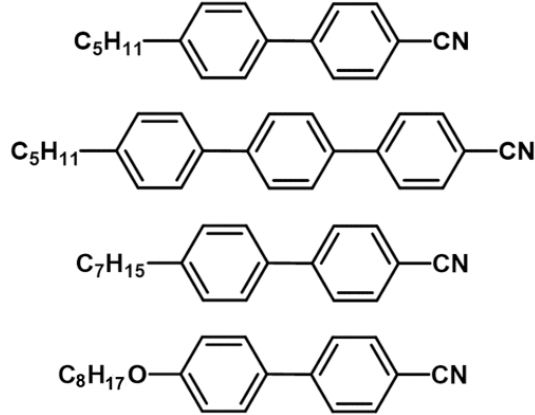
Figure 2.12: Multicomponent nematic liquid crystal E7. Pure components from the top panel to the bottom panel: 4-cyano-4'-n-pentyl-1,1'- biphenyl (5CB-51%); 4-cyano-4"-n-pentyl- 1,1' ,1" -terphenyl (5CT-8%); 4-cyano-4'- n-heptyl-1,1'- biphenyl (7CB-25%); 4-cyano-4'-n-octyloxy-1,1'- biphenyl (8OCB-16%).

2.5.2. Continuum theory: Frank-Oseen free energy

The uniaxial alignment discussed above is highly ideal and is sustained from a hypothetical situation where the nematic liquid crystal is isolated. For example, liquid crystals are used in cell phones subjected to boundaries and voltage variations [128]. These external ingredients cause deformations of the nematic alignment making the tensor $Q_{\alpha\beta}$ space dependent. These deformations can be studied with a continuum theory supposing that the spatial variations occur over distances much larger than the size of the molecules [63]. In this weakly distorted regime, a valid assumption is that locally the properties of the material are still uniaxial, then the amplitude of the tensor order parameter $Q_{\alpha\beta}$ remains constant, and only the reorientation of the nematic director vector $\vec{n}(\vec{r})$, with $\vec{r} = \{x, y, z\}$ a positional vector, governs the dynamics. The elastic distortions of $\vec{n}$ can be characterized by the Frank-Oseen free energy [129, 130]

$$F_{ed} = \int \left[\frac{K_1}{2}(\nabla \cdot \vec{n})^2 + \frac{K_2}{2}(\vec{n} \cdot \nabla \wedge \vec{n})^2 + \frac{K_3}{2}(\vec{n} \wedge \nabla \wedge \vec{n})^2\right] d\vec{r}. \tag{2.15}$$

Notice that this free energy is invariant under the change $\vec{n} \to -\vec{n}$, invariant under rotations, and is related to a centrosymmetric material. The first deformation mode is splay $\nabla \cdot \vec{n}$, which captures the tilt inward or outward of the director $\vec{n}$ in its perpendicular plane. The energetic cost associated with this distortion is measured by the splay constant K_1. The

second mode is twist $\vec{n} \cdot \nabla \wedge \vec{n}$, which indicates how $\vec{n}$ varies in a right-hand or left-hand way with respect to the perpendicular plane of $\vec{n}$. The elastic constant associated with the twist mode is K_2. The third mode is bend $\vec{n} \wedge \nabla \wedge \vec{n}$, which accounts for the variations of $\vec{n}$ along its direction, and its associated elastic constant is K_3 [131]. Figure 2.13 shows the values of the elastic constants of E7 together with their temperature dependence. The free energy (2.15) only considers bulk terms, and this is accurate while surface terms remain neglectable (e.g., strong anchoring conditions [63]). When surface terms are important (e.g., soft anchoring), saddle-splay distortions must be considered [132].
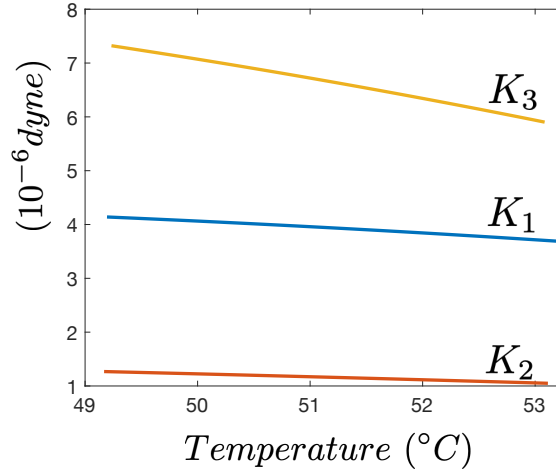
Figure 2.13: Temperature dependence of the elastic constants of E7. The chart is adapted from Ref. [133].

2.5.3. Chiral nematic liquid crystals

Chirality is the absence of mirror symmetry. In 1894, Lord Kelvin used the term for the first time [134]:

"I call any geometrical figure, or group of points, 'chiral', and say that it has chirality if its image in a plane mirror, ideally realized, cannot be brought to coincide with itself".

Chiral nematic liquid crystals (CNLCs) can be created by doping a nematic liquid crystal with chiral molecules [63, 64, 65]. The molecule employed in this dissertation is called EOS12 (see Fig. 2.14), which has been synthetized by the Liquid Crystal Group from the Universidad de Concepción [66]. The addition of the chiral dopants can induce a spontaneous twist deformation in the nematic phase creating a helical structure [63, 67, 64]. Figure 2.15 shows schematically the emergence of the cholesteric phase [63]. The main feature of this phase is the characteristic length of the helix, known as *cholesteric pitch p_o*, which corresponds to the distance required for one full rotation of the nematic director vector $\vec{n}(\vec{r})$. In a dilute limit, the pitch is equal to β/c, where β is the rotatory power of the cholesteric [135, 136], and c is the concentration of the dopant [63]. The pitch is the mesoscopic manifestation of the molecular chirality [137].
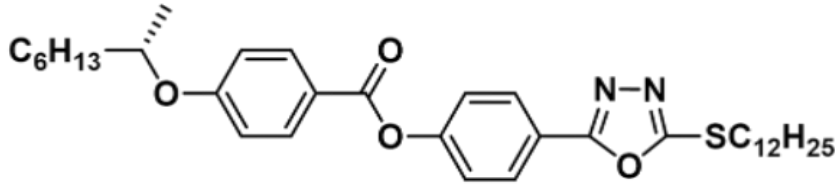
Figure 2.14: EOS12 molecule; (S)–(4–(5–dodecylthio–1,3,4–oxadiazole–2–yl) phenyl 4'–(1"–methylheptyl–oxy)benzoate).
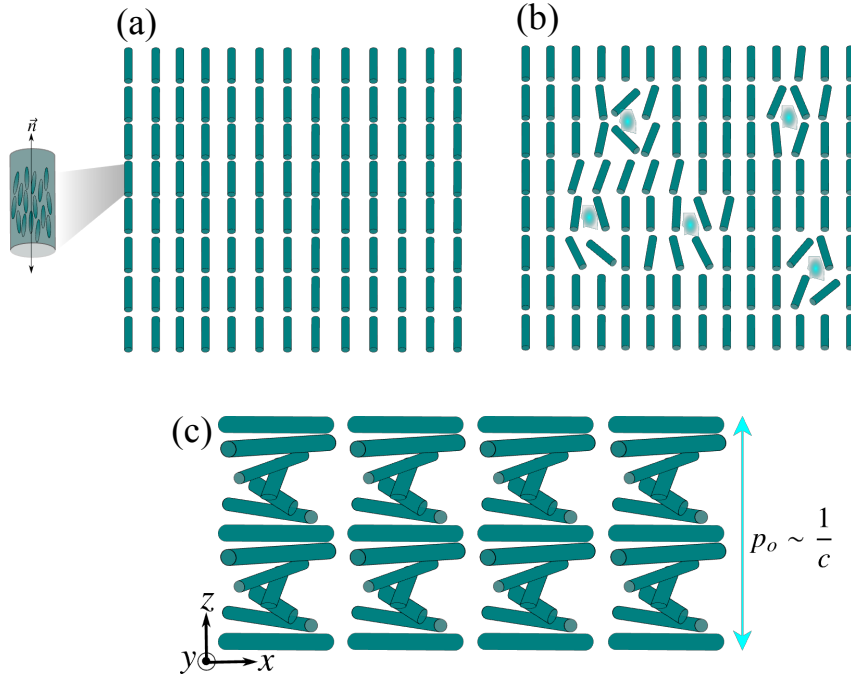
Figure 2.15: The schematic emergence of a cholesteric phase. (a) Nematic phase undistorted, where the green cylinders define a local nematic director $\vec{n}$. (b) Doping of the nematic phase with a non-centrosymmetric material, represented by sky-blue objects. (c) Cholesteric phase with a pitch p_o indicating its inverse relationship with the concentration c of the chiral dopant.

When subjected to homeotropic anchoring in a cell of thickness d (the molecules arrive perpendicular to the plane of the cell), the helical phase gets frustrated, so that given a critical degree of frustration, which is measured in terms of the ratio d/p_o, the system transitions to an unwound (nematic) metastable state (see Fig. 2.16(a)). This state is purely geometric and is sustained by the competition between the pitch, geometric effects introduced by the cell thickness, and elasticity [68, 69, 64]. The twisted or winded structure can be recovered by applying a voltage, a temperature difference, or changing the thickness to the cell in the unwound state [64]. The cholesteric phase is characterized by the spatial variations of the director field (see Fig. 2.16(b)). In general, the reappearance of the twisted phase is in the form of a translationally invariant configuration (TIC) or in the form of cholesteric fingers of type 1 (CF1). The TIC phase is characterized by a twist along the cell thickness $\vec{n}(z)$ (see Fig. 2.16(c)), and the CF1 by a director field of the general form $\vec{n}(x, y, z)$ (see Fig. 2.16(d)). In directional growth experiments with voltage, other types of cholesteric fingers (CF2, CF3, and CF4) have been observed [138].

The recovery of the twisted structure can be described by the minimization of the Frank-Oseen free energy (2.15) with an additional chiral term $2K_2\pi\vec{n}\cdot\nabla\wedge\vec{n}/p_o$, breaking the mirror symmetry in the system [63]. Note that the cholesteric pitch needs to be big, compared to the molecular scale, so the supposition of uniaxiality remains valid [67]. The minimization process describes the evolution of the director, $\gamma d\vec{n}/dt = -\delta F_{ed}/\delta\vec{n}$ while maintaining its unitary norm [139], and reads

$$
\begin{aligned}
\gamma\frac{d\vec{n}}{dt} =\ & K_3[\nabla^2\vec{n} - \vec{n}(\vec{n}\cdot\nabla^2\vec{n})] + (K_3 - K_1)[\vec{n}(\vec{n}\cdot\nabla)(\nabla\cdot\vec{n}) - \nabla(\nabla\cdot\vec{n})] \\
& + (K_2 - K_3)[2(\vec{n}\cdot\nabla\wedge\vec{n})\{\vec{n}(\vec{n}\cdot\nabla\wedge\vec{n}) - \nabla\wedge\vec{n}\} + \vec{n}\wedge\nabla(\vec{n}\cdot\nabla\wedge\vec{n})] \\
& + \frac{4\pi K_2}{p}[-\nabla\wedge\vec{n} + \vec{n}(\vec{n}\cdot\nabla\wedge\vec{n})],
\end{aligned}
$$

$$(2.16)$$

where γ is a rotational viscosity constant, and the homeotropic boundary conditions $\vec{n}(x, y, z = 0) = \hat{z}$ and $\vec{n}(x, y, z = d) = \hat{z}$ are considered during the evolution.
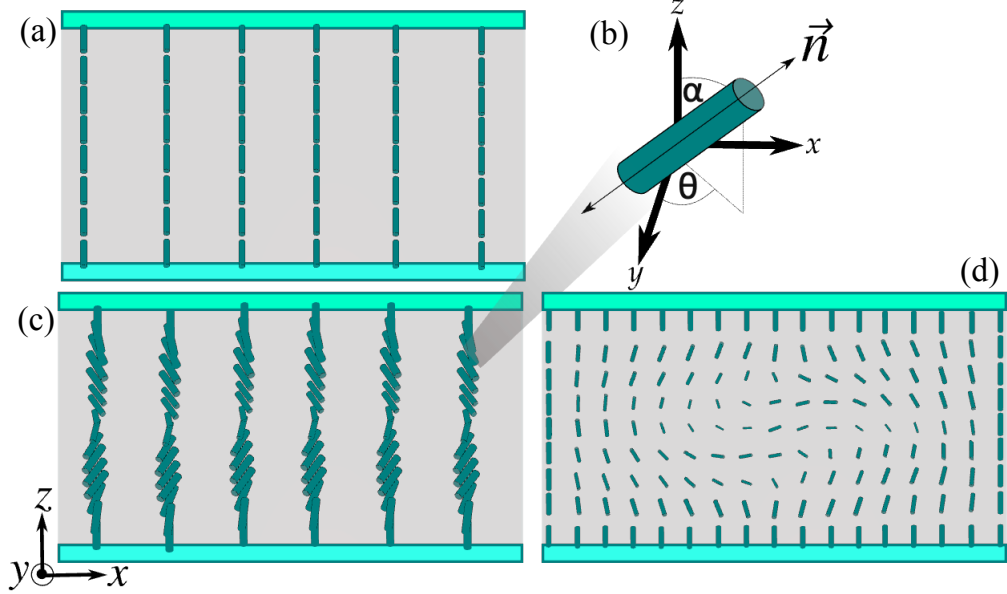
Figure 2.16: Schematic representation of the nematic director within a cell of thickness d with homeotropic boundary conditions. (a) Nematic phase induced by homeotropic anchoring. (b) Representation of the nematic director $\vec{n}$ as tubes in a spherical coordinate system. The angle α represents the tilt of $\vec{n}$ from the z-axis and θ corresponds to the angle between the x-axis and the projection of $\vec{n}$ in the plane $x - y$. (c) Translationally invariant configuration (TIC) is characterized by a uniform twist parallel to the cell thickness. (d) Director distribution of the cross-section of a cholesteric finger of type I. In this case, spatial modulations of $\vec{n}$ are in z and in the plane $x - y$. This director representation is adapted from [140].

During the minimization dynamics, the experimental setup to monitor the emergence of the cholesteric phase triggered by temperature is depicted in Fig. 2.17(a). The thermal setup (1-3) consists of a thermal chamber operating under a Peltier effect controlled by a computer. The optical setup (4-9*) is the usual Polarized Optical Microscopy (POM), which exploits the birefringence of the liquid crystals to observe their beautiful textures [65]. The polarizer

(P) and analyzer (A) are crossed, giving no transmittance of light when the liquid crystal is in the nematic phase. Figure 2.17(b) highlights, schematically, that inside the thermal chamber is the liquid crystal cell (see Figure 2.17(c)). The cholesteric phase is obtained by heating a liquid crystal mixture of E7 with EOS12 inside the cell (with thickness $d = 7$ μm and treated with homeotropic boundary conditions). This recovery of the winded phase is related to the decrease of the cholesteric pitch, which depends inversely on the temperature [65], relieving the geometrical frustration $d/p(T)$ of the system.
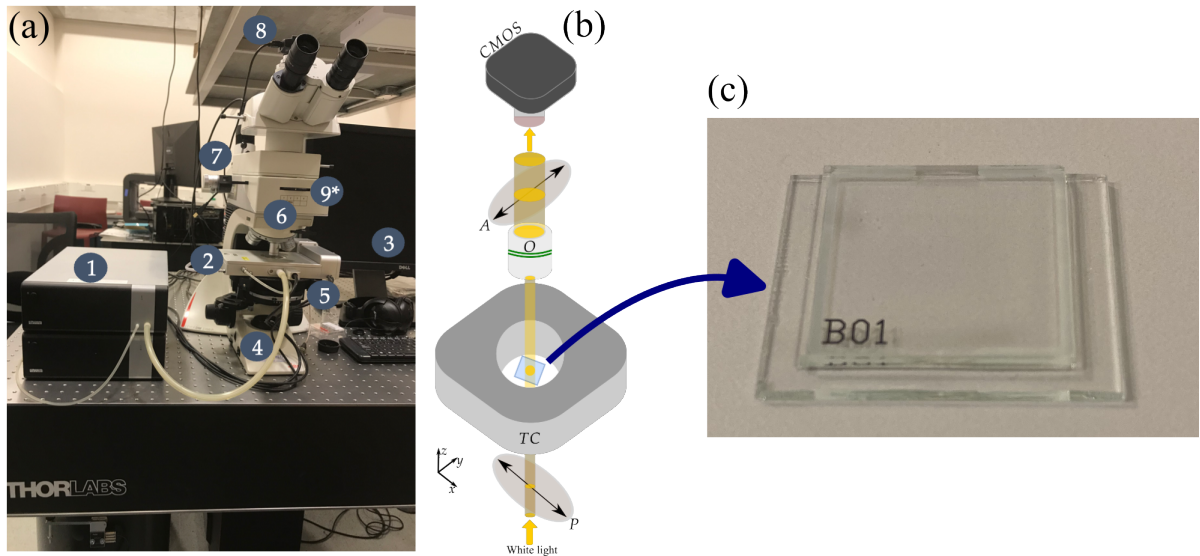
Figure 2.17: Experimental setup. (a) 1) LinkamT95-PE hot stage, 2) Thermal chamber (TC), 3) Linkam software, 4) Lamp, 5) Polarizer (P), 6) Objectives (O), 7) Analyzer (A), 8) CMOS camera, 9*) Quarter-wave plate. (b) Schematic drawing of the experiment highlighting the (c) liquid crystal cell (Instec) inside the thermal chamber.

Chapter 3

Labyrinthine pattern transitions (Physical Review Research 2, 042036)

The spontaneous emergence of self-organized dissipative structures out of a homogeneous state has been observed in many out-of-equilibrium systems, including biology, chemical reaction-diffusion systems, fluid mechanics, nonlinear optics, and laser physics [3, 141, 11]. The loose of stability of a homogenous state against spatial dependent perturbations is a symmetry-breaking instability. Near this transition, the emerging patterns are simple, such as stripes, hexagons, squares, and superlattices [19, 141, 18, 20, 21]. The simplicity is synonymous of trivial symmetry, which is manifested in the few modes needed to describe these patterns [141, 18]. Far from the critical point, the structures start to be complex, that is, they display non-trivial symmetries.

Labyrinthine patterns are one of the complicated spatial structures arising far from primary spatial instabilities. Without loose of generality, let us discuss the spatial structure of labyrinths by means of a simple SH equation. It is well-known that labyrinths are characterized by a powdered ring-like global Fourier spectrum as shown in Figure 3.1(a) [24]. Nevertheless, this description is exhibited by disordered patterns in general. Figure 3.1(b) shows a disordered hexagonal pattern exhibiting a powdered ring spectrum in its global transform. In this chapter, we will show that a precise labyrinth's definition needs a local description in addition to a global characterization. Indeed, when performing local Fourier transforms in windows of size $\propto \lambda_c$ (red-framed boxes in Figure 3.1) a distinction between labyrinths and disordered hexagons can be established.

The ring-like feature of the spectrum of labyrinths can be loosely understood as a a combination of local stripes (two diametrically opposed peaks in Fourier space) in different directions, while the powdered feature is related to the presence of defects in the pattern. These defects reconcile discrepancies in orientation (connect the different stripes) and local wavelength [19, 141, 18]. Figure 3.2 shows the typical local (dislocations and disclinations) and extended (phase and amplitude walls) defects of an equilibrium two-dimensional labyrinthine pattern in the SH equation [25]. Being a signature of the labyrinthine patterns, we think defects are worthy of being considered as an order parameter to describe the transition from simple patterns (for example, stripes with no defects) to complex patterns, such as labyrinths. To measure defects, we introduce the orientational field $\theta(x, y)$ of the local stripe patterns following the ideas introduced in Ref. [142] (see Figure 3.2). This local analysis filters the wavelength of the labyrinthine pattern to distinguish the scalar field $\theta(x, y)$ as shown in Figs. 3.3(a) and 3.3(b). By a visual inspection, it is easy to see (for the top panel at least)

that the discontinuities in the orientational field are related to the defects in the labyrinthine pattern. A way to characterize these jumps is by a local winding number of the orientational field: $\oint \theta(x,y)dxdy/2\pi$. Because of the complexity of the labyrinthine patterns in the SH equation, it is necessary to introduce a threshold (th) in the local winding number to decide if a region is defective or not. Following this idea, we implement the field

$$W(x,y) = \begin{cases} 1, & \text{if } \oint \theta(x,y)dxdy/2\pi \geq th \\ 0, & \text{otherwise} \end{cases}, \qquad (3.1)$$

which is used to compute the density of defects $f_d = \int_0^L \int_0^L W(x,y)dxdy/L^2$. This density allows us to characterize labyrinthine transitions, and their emergence as a freezing of defects dynamics (see Fig. 3.4).
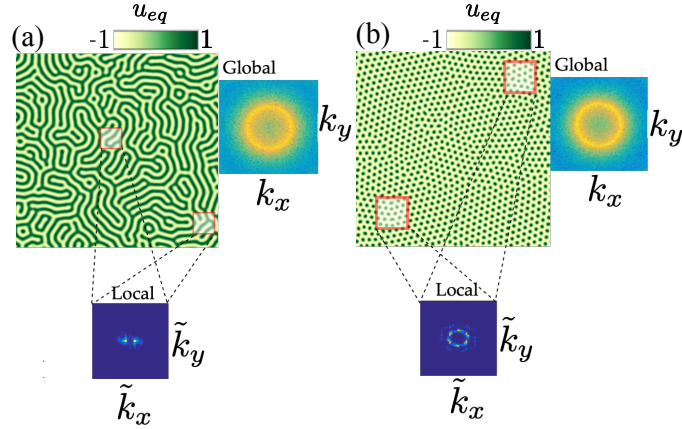
Figure 3.1: Global and local spatial structures of (a) a labyrinthine and (b) a hexagonal pattern. Both patterns are equilibria of the gSH equation with $\epsilon = 0.02$, $\eta = 0$, and $\epsilon = -0.25$, $\eta = -0.1$, respectively.
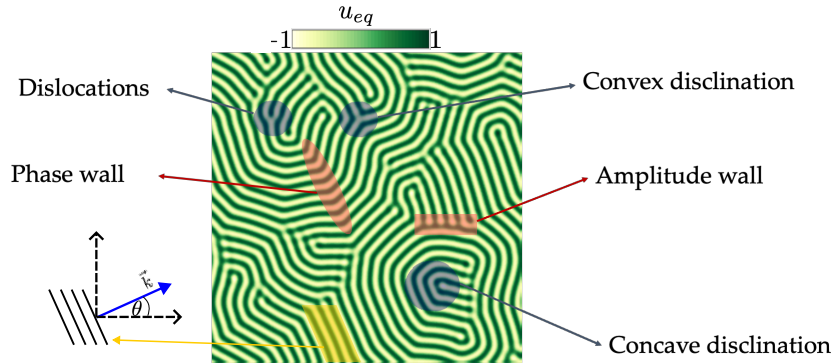
Figure 3.2: "Anatomy" of a two-dimensional labyrinthine pattern u_{eq} of the SH equation with $\epsilon = -0.15$ (adapted from Ref. [25]). Local defects (concave and convex disclinations, and dislocations) are highlighted in blue. Extended defects (phase and amplitude walls) are highlighted in red. The shaded yellow region indicates a local stripe pattern described by it wavevector $\vec{k}$ and an orientation $\theta(x,y)$.
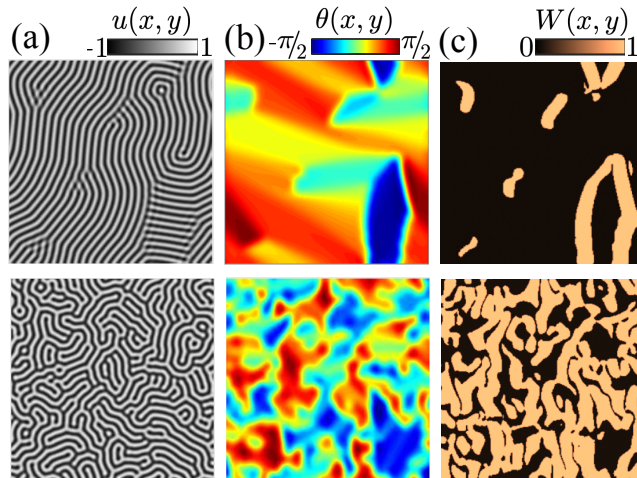
Figure 3.3: Method to determine the density of defects of a labyrinthine pattern. (a) Equilibria labyrinthine patterns of SH equation with $\epsilon = -0.18$ (top panel) and $\epsilon = 0.02$ (bottom panel). (b) Orientational field of the labyrinths. (c) $W(x,y)$ field of the complex patterns.

We note that defects are also observed in the region of parameters where stripe patterns are stable. However, as the defects cost energy, the system always seeks the annihilation of defects. When labyrinths are not too complicated (near $\epsilon = \epsilon_c = -0.25$ in the SH equation with $\nu = 1$), the variational dynamics of the SH equation is characterized by defects annihilation. An example of this complicated dynamics is depicted in Fig. 3.5, where important events are highlighted.
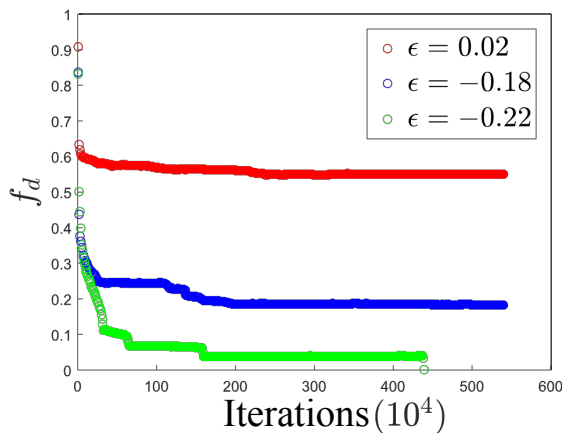
Figure 3.4: Temporal evolution of the density of defects in direct numerical simulations of the SH equation (with $\nu = 1$) with different values of ϵ. It can be seen that equilibria for large ϵ, far from the primary instability $\epsilon_c = -0.25$, have a non-zero f_d. Near ϵ_c, the defects can be annihilated, giving rise to perfect stripe patterns $f_d = 0$.

In this chapter, we investigate the structure, emergence, transitions, and disappearance of labyrinthine patterns in the SH equation. We introduce the windowed average Fourier transform to describe labyrinths locally and define them unambiguously. Additionally, we propose the existence of three different types of labyrinths–fingerprint, glassy, and scurfy–based on their defect density, correlation length, competition against the homogeneous solutions, and

free energy.
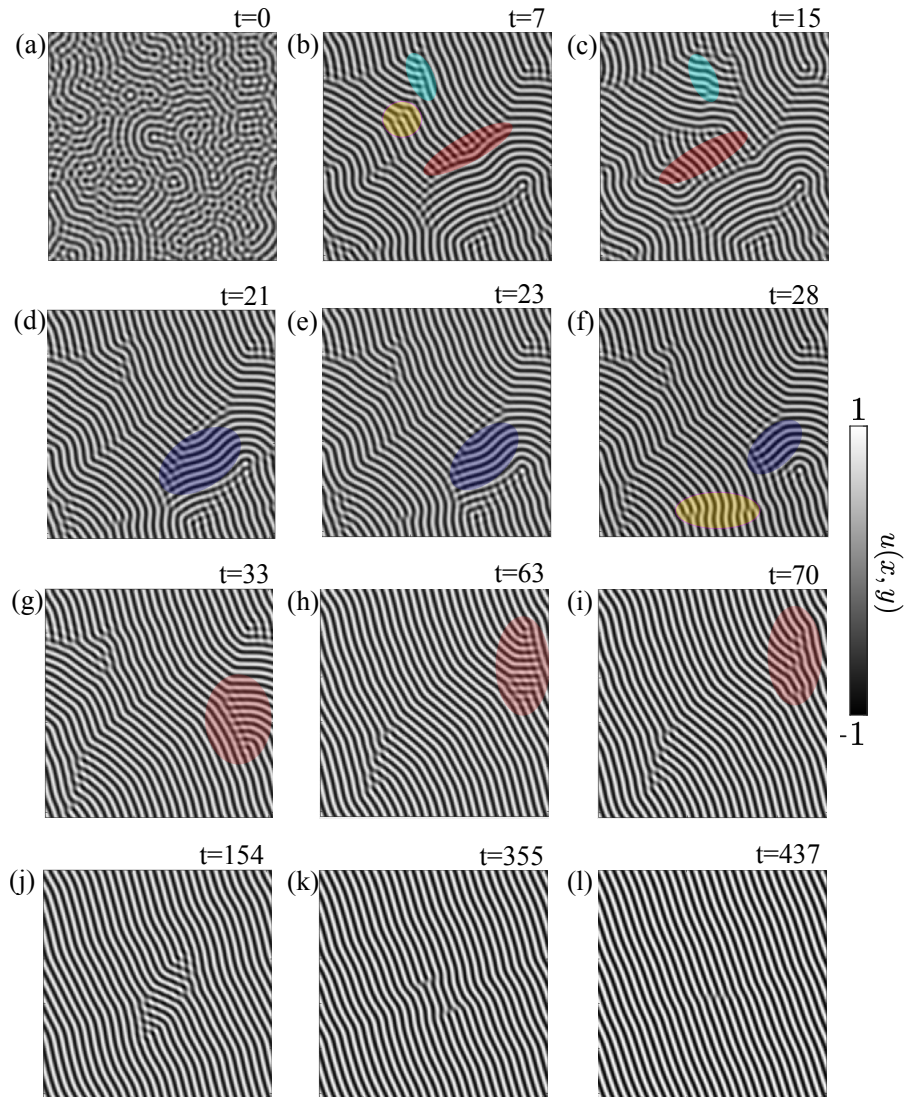
Figure 3.5: Temporal snapshots of numerical integrations of the SH equation (with $\nu = 1$) at $\epsilon = -0.22$ starting from the unstable state $u = 0$ with a small perturbation of white noise. The times t are in arbitrary units. (a) The dominant wavelength λ_c starts to dominate the pattern against all the other wavelengths excited by white noise. (b) Well-defined labyrinthine pattern with characteristic defects: dislocations (shaded yellow and shaded sky blue regions) and an amplitude wall (shaded red region). (c) Quickly, nearby dislocations annihilated (shaded yellow region from (b)), others moved (shaded sky blue), and the amplitude wall (shaded red) also moved as one orientation of stripes started to be selected by the system. The snapshots (d)-(g) summarize the disappearance of a local stripe orientation (shaded blue), while (f)-(g) displays the annihilation of dislocations (shaded yellow). The snapshots (g)-(i) describe the transformation of an amplitude wall (shaded red) into a chain of dislocations. The final snapshots (j)-(l) display the slow annihilation of dislocations governing the asymptotic dynamics. After a long time from (l), the minimization of the curvature (undulations along the stripes) gives rise to perfect stripe patterns.

27

Labyrinthine patterns transitions

S. Echeverría-Alar ● and M. G. Clerc ●

Departamento de Física and Millenium Institute for Research in Optics, Facultad de Ciencias Físicas y Matemáticas,
Universidad de Chile, Casilla 487-3, Santiago, Chile

Macroscopic systems with injection and dissipation of energy exhibit intricate dissipative structures. Labyrinthine patterns are disordered spatial structures arising into homogeneous media that show a short-range order. Here, we investigate the stability properties, classification, and transitions of labyrinthine patterns. Based on a prototype pattern forming model, we characterize the existence of three types of labyrinthine patterns—fingerprint type, glassy, and scurfy—and reveal the bifurcation diagram. The defects density, free energy, structure factor, and correlation length are used as order parameters.

Nature is full of patterns such as dunes, animal fur, fish skin, snowflakes, pigmentation on mollusk shells, fir waves, mountain ripples, and clouds, which have attracted attention due to their regularities or irregularities that generate the diversity of forms [1–5]. All these physical systems correspond to macroscopic systems with injection and dissipation of energy. Out-of-equilibrium systems are characterized in general by exhibiting pattern formation as a result of spontaneous spatial breaking symmetry of a homogeneous state [1–5]. Near this transition, the observed equilibrium patterns are generally striped, hexagonal, square, and superlattice. A unified strategy to describe the emergence and dynamics of these simple patterns is the amplitude equations of critical modes [1–5]. By increasing energy injection, pattern forming systems exhibit more complex patterns, characterized by a large number of defects. Indeed, far from the primary spatial instabilities, disordered patterns arise into homogeneous media. An example of these types of complex patterns is the so-called labyrinthine patterns. Figure 1 shows examples of labyrinthine patterns observed in nature. These patterns have been observed in mussel beds [6], cardiovascular calcification [7], phytomass [8], microemulsions [9], fish skin [10], fluid convection [11], Langmuir monolayer [12], magnetic fluids [13], chemical reactions [14], and cholesteric liquid crystals [15], to mention a few. Hence, labyrinthine patterns are a robust phenomenon of nature. Intuitively, in all the aforementioned systems, the observed patterns are denominated labyrinths. However, a precise definition is not available. A proposition of a labyrinthine pattern is a spatial state that shows a short-range order and a powdered spatial spectrum [16]. Notwithstanding the above, when one considers a hexagonal structure with defects, it satisfies the previous definition and is not an intuitive labyrinth

structure. The previous definition can be amended by specifying that a single wave number characterizes short-range order. The characterization of different types of labyrinth patterns, their properties as a state of equilibrium, and transitions between them has not been established.

The purpose of this Rapid Communication is to describe different types of labyrinthine patterns and characterize the transitions between them. Based on a prototype pattern forming model, the Turing-Swift-Hohenberg equation, we characterize the existence of three types of labyrinthine patterns (*fingerprint-type*, *glassy*, and *scurfy*) and reveal their transitions. The defects density, free energy, structure factor, and correlation length are used as order parameters. Fingerprint-type labyrinths arise as a result of the emergence of bound states between defects. This is a supercritical transition, which precedes freezing of the coarsening process that characterizes striped patterns [17]. When increasing the bifurcation parameter, the transition between the fingerprint-type and glassy patterns is of the second-order type, which is detected by means of the correlation length. The structure factor allows us to characterize the transition between glassy and scurfy labyrinthine patterns. Free energy allows us to envisage the complex organization of the different labyrinthine patterns.

Let us consider a prototype model of pattern formation, the dimensionless Turing-Swift-Hohenberg equation [18]. This model equation accounts for the dynamics of a real order parameter deduced originally to describe the pattern formation on Rayleigh-Bénard convection [18,19], which reads

$$\partial_t u = \epsilon u - u^3 - \nu\nabla^2 u - \nabla^4 u, \tag{1}$$

with $u = u(x, y, t)$ a real scalar field, and x, y, and t are spatial coordinates, and time, respectively. ϵ is the bifurcation parameter. The parameter ν stands for the diffusion coefficient ($\nu < 0$); when this parameter is positive ($\nu > 0$), it induces an antidiffusion process. Notice that the above model is the simplest isotropic, reflection symmetry, and nonlinear equation that presents patterns and localized states [2]. In the last decade, it has been established that Eq. (1) had already been
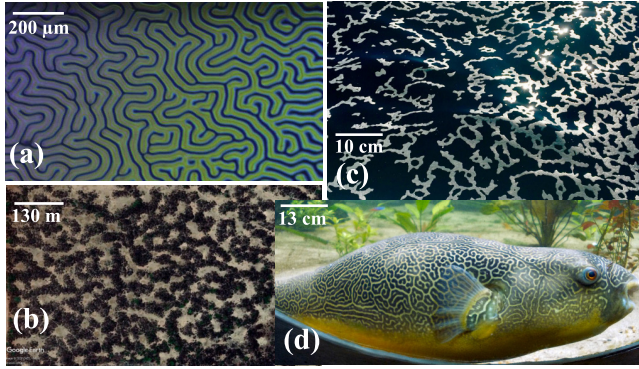
FIG. 1. Labyrinthine patterns. (a) Chiral liquid crystal labyrinthine pattern (courtesy of Gregorio Gonzalez). (b) Vegetation patterns observed in Niger using Google Earth (coordinates 12°27′50.61″ N 3°18′30.76″ E). (c) Seafoam patterns (courtesy of Randall Straka). (d) Giant puffer fish (courtesy of Chiswick Chap).

constructed by Turing, but was unpublished [19]. Note that Eq. (1) was published 23 years after Turing's death [18]. Observe that model equation (1) is of variational nature, that is, $\partial_t u = -\delta\mathcal{F}/\delta u$ where $\mathcal{F}$ is the Lyapunov function

$$\mathcal{F}[u] = \iint \left(-\epsilon\frac{u^2}{2} + \frac{u^4}{4} - \nu\frac{(\nabla u)^2}{2} + \frac{(\nabla^2 u)^2}{2} \right) dx\, dy.$$

(2)

Hence, the dynamics of model equation (1) is characterized by the minimization of the free energy $\mathcal{F}$.

A trivial solution of model equation (1) is the zero solution, $u(x, y, t) = 0$. This solution is stable for $\epsilon < \epsilon_c \equiv -\nu^2/4$. For $\epsilon = \epsilon_c$, the homogeneous solution becomes unstable and gives rise to the emergence of a striped pattern with wavelength $|\vec{k}_c| = \sqrt{\nu/2}$ [2,3]. This spatial supercritical instability is characterized by the emergence of domains of striped patterns with different orientations and the same wavelength. These domains are randomly distributed. Defects that reconcile different pattern orientations separate the domains. These are local disclinations and extended grain boundaries; both of amplitude and phase. Also, dislocations appear that fix local discrepancies in wavelength (see textbook [3], and references therein). The interaction of these defects causes domains to grow over time. This process is self-similar, usually called *coarsening process*, which is characterized by the grain-boundaries perimeter growing as a power law of time $t^{1/3}$ [17]. Note that phase separation in supersaturated solids [20,21] and the formation of localized patterns in optics [22,23] present a coarsening process, which is governed by the same critical exponent. Hence, in a finite-size system, the final equilibrium reached is a striped pattern (monodomain). Figure 2(a) shows the typical observed striped pattern. The orientation of these patterns only depends on the initial condition. The modulus Fourier transform of this type of pattern is characterized by exhibiting two maximums [see the upper inset panel in Fig. 2(a)]. In order to describe the short-range order of the pattern, we introduce *the averaged windowed Fourier transform* by considering a large number of boxes of the same length l, calculating the Fourier transform, rotating the wave-vector space so that a peak of the transformation is
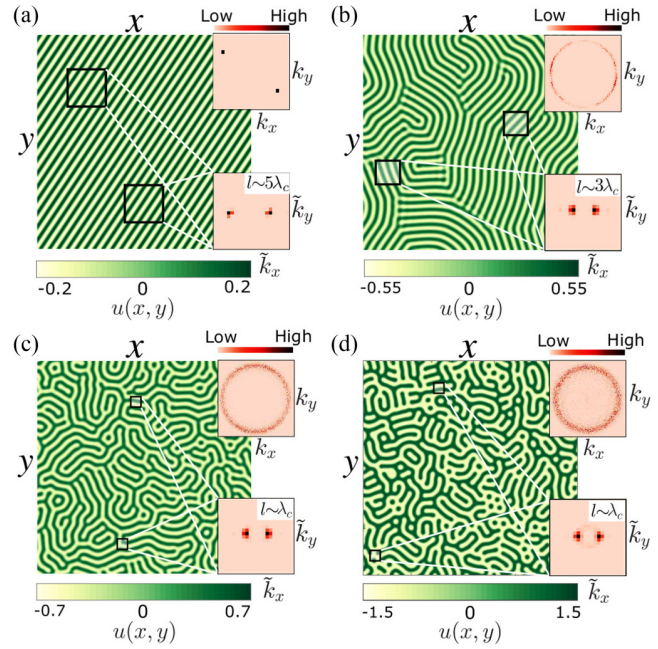
FIG. 2. Equilibrium patterns of the dimensionless Turing-Swift-Hohenberg equation (1) with $\nu = 1$. Surface plots of (a) striped pattern $\epsilon = -0.22$, (b) fingerprint-type labyrinthine pattern $\epsilon = -0.16$, (c) glassy labyrinthine pattern $\epsilon = 0.02$, and (d) scurfy labyrinthine pattern $\epsilon = 1.15$. The upper and lower insets account for the modulus of global and averaged windowed Fourier transforms, respectively. λ_c and l are the critical wavelength ($2\pi/|\vec{k}_c|$) and the size of the window in the averaged windowed Fourier transform, respectively.

always horizontal, and averaging over these transforms. The lower panel of Fig. 2(a) illustrates this transform.

Unexpectedly, when the bifurcation parameter ϵ is increased, the interaction of defects freezes [24], that is, the defects present bound states. In this region of parameters, starting with the zero solution perturbed with a small initial noise, the system exhibits labyrinth solutions as equilibria. Figure 2 shows the different labyrinthine patterns observed in the Turing-Swift-Hohenberg equation. By using the global and averaged windowed Fourier transform, we can verify that the observed patterns are disordered and show a short-range order characterized by a single wave number. All numerical simulations were implemented using a pseudospectral code with the Runge-Kutta order-4 algorithm. In the present study, $u = 0$ with a small random disturbance is always considered as the initial condition.

To verify that the labyrinthine patterns are equilibrium states, we have conducted two analyses. First, monitoring the evolution of free energy over time $\mathcal{F}[u(x, y, t)]$, which should have the tendency to decrease and settle at an asymptotic value. Indeed, the free energy decreases as the defects are annihilated or reach their final position. Figure 3 shows the evolution $\mathcal{F}[u]$ as a function of time. And second, by calculating the linear stability spectrum of the labyrinth solution (cf. upper inset in Fig. 3). Both analyses allow us to conclude that labyrinthine patterns are stable.
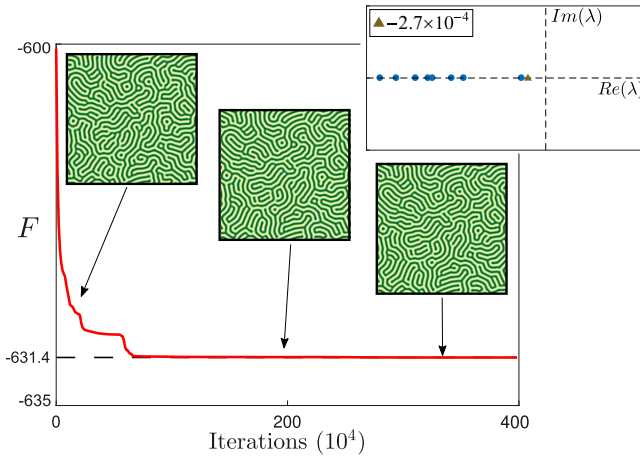
FIG. 3. Temporal evolution of the free energy $\mathcal{F}[u(x, y, t)]$ for a labyrinth state of the Turing-Swift-Hohenberg equation (1) with $\nu = 1$ and $\epsilon = 0.02$. The upper inset corresponds to the linear stability spectrum of the labyrinth solution for large times. The lower insets show the labyrinthine pattern for three different instances.

When defects begin to freeze, $\epsilon = \epsilon_{\text{SFP}}$, the system features large domains of striped patterns mainly separated by amplitude grain boundaries. We have called these structures *fingerprint-like labyrinthine patterns*, due to their similarity to fingerprints. Figure 2(b) shows a fingerprint-type pattern and their respective Fourier transforms. To characterize the emergence of these patterns, we have measured the defects density f_d, based on the orientational field of the pattern [25], as a function of the bifurcation parameter. Figure 4(a) summarizes f_d as a function of the bifurcation parameter. Observe that the transition between fingerprint-type and striped patterns is of a supercritical type and described by a critical exponent $1/2$, as shown by the continuous curve [cf. Fig. 4(a)]. Notice that at this critical point, the striped patterns do not become unstable, and even for higher bifurcation parameters, they coexist with labyrinthine patterns. Likewise, if one calculates the correlation length ξ [26] as a function of the bifurcation parameter [see Fig. 4(a)], we observe that this length diverges in the transition between fingerprint-type and striped patterns with a $-1/2$ power law. When increasing the bifurcation parameter, we observe that the rate of the defects density decreases; particularly from $\epsilon > \epsilon_{\text{FPG}}$, no grain boundaries were observed. Then, the patterns in this region are characterized by presenting a large number of local defects. We have termed this type of pattern as *glassy labyrinths*, due to its amorphous structure. Figure 2(c) shows a typical glassy labyrinthine pattern. The correlation length close to ϵ_{FPG} exhibits a slight local maximum [cf. inset in Fig. 4(a)], which is a peculiarity of glassy-type second-order transitions [27]. To analyze this transition more carefully, we have monitored the time evolution of the correlation length. Figure 4(b) shows the evolution of the correlation length as a function of the bifurcation parameter. From this chart, we infer that the correlation length variations are almost negligible for glassy labyrinthine patterns. Indeed, the glassy state corresponds practically to an instantly frozen state. In brief, the fingerprint-type and glassy labyrinthine patterns can be distinguished by the prevalence
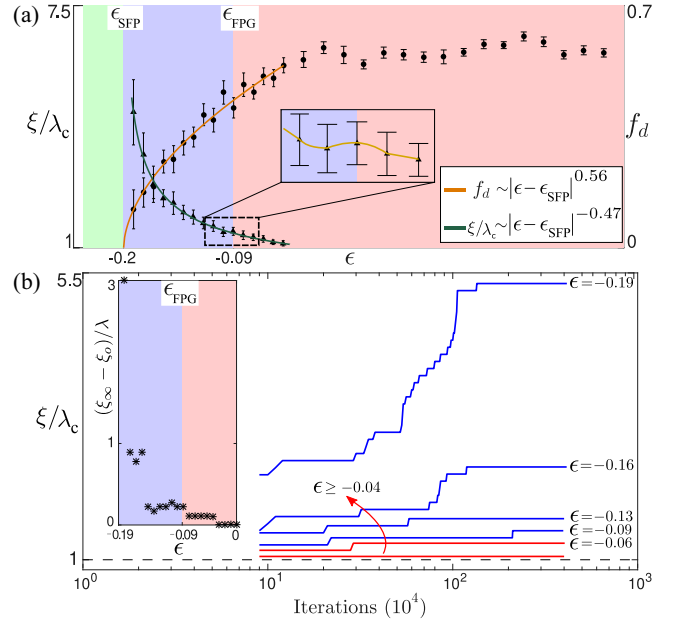
FIG. 4. Bifurcation diagram of labyrinthine patterns. (a) The correlation length ξ and defects density f_d as a function of the bifurcation parameter ϵ. The circles (●) and triangles (△) account for the correlation length and defects density, respectively. The error bars account for the standard deviation obtained after analyzing 50 numerical realizations. ϵ_{SFP} and ϵ_{FPG} account for the transition points between striped and fingerprint-type labyrinthine patterns, and fingerprint-type and glassy labyrinthine patterns, respectively. The solid curves describe the fitting for the defects density and correlation length. The inset accounts for the magnification of the correlation length close to the transition from fingerprint-type to glassy patterns. (b) Temporal evolution of the correlation length ξ as a function of the bifurcation parameter ϵ. The inset shows the initial ξ_0 and equilibrium ξ_∞ correlation length difference as a function of the bifurcation parameter.

of amplitude grain boundaries and the relaxation dynamics to their respective equilibria.

By further increasing the bifurcation parameter, we observe that the glassy patterns maintain the same structure. However, from a critical value, $\epsilon > \epsilon_{\text{GS}}$, we begin to find the appearance of circular spots embedded in the labyrinth pattern. We have called this type of structure *scurfy labyrinthine patterns*. Figure 2(c) shows a typical scurfy labyrinthine pattern. As a result of the presence of spots we are not able to compute the defects density and correlation length. To analyze the emergence of circular spots onto labyrinthine patterns, let us consider the structure factor

$$S(k) = \int_{-\pi}^{\pi} \left| \frac{1}{\sqrt{\pi}} \int u(x, y, t) e^{i\vec{k}\vec{r}} dx \, dy \right| k \, d\theta, \quad (3)$$

where $k = |\vec{k}|$ and θ are the polar coordinate representation of wave-vector space $\vec{k}$. The typical structure factors $S(k)$ for the different labyrinthine patterns are shown in the insets of Fig. 5. Note that for fingerprint-type and glassy patterns only one dominant peak is observed, while for scurfy labyrinthine patterns there are two peaks. This second peak close to $k = 0$ is a consequence of the effect of circular spots and
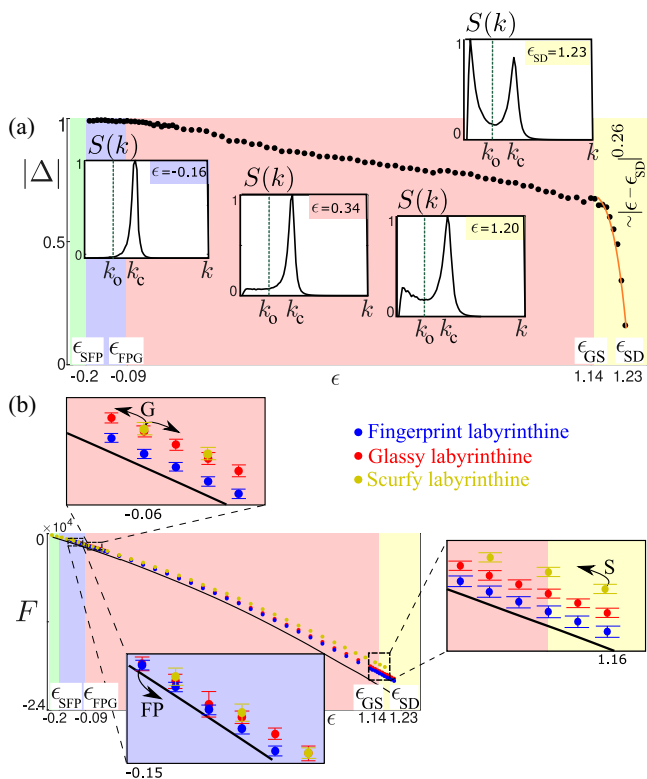
FIG. 5. Characterization of labyrinthine patterns. (a) The normalized area difference between the peaks, $\Delta(\epsilon) \equiv (\int_{k_o}^{\infty} S\,dk - \int_0^{k_o} S\,dk)/\int_0^{\infty} S\,dk$ as a function of the bifurcation parameter. The insets correspond to normalized structure factors at different values of the bifurcation parameter. The continuous curve $\Delta(\epsilon) \approx |\epsilon - \epsilon_{SD}|^{0.26}$ accounts for the fitting obtained for the area difference near the disappearance of the scurfy patterns. ϵ_{GS} and ϵ_{SD} stand for the transition points between glassy and scurfy labyrinths, and scurfy labyrinths and their disappearance, respectively. (b) Free energy $\mathcal{F}$ of the different equilibria as a function of the bifurcation parameter ϵ. The solid curve accounts for the energy of the striped pattern. The circles account for the different labyrinthine patterns (∘ fingerprint-type, ∘ glassy, and ∘ scurfy). The error bars show the standard deviation obtained from 30 realizations. Insets stand for the magnification of the chart in the respective regions.

localized structures. Introducing the normalized area difference between the peaks,

$$\Delta(\epsilon) \equiv \frac{\int_{k_o}^{\infty} S(k)\,dk - \int_0^{k_o} S(k)\,dk}{\int_0^{\infty} S(k)\,dk}, \qquad (4)$$

one can monitor the emergence of the second peak, where k_o is an intermediate wave number between peaks. Figure 5 shows the evolution of the area difference Δ as a function of

ϵ. This indicator presents a sharp decrease at $\epsilon = \epsilon_{GS}$. For $\epsilon_{GS} < \epsilon < \epsilon_{SD}$, we observe scurfy labyrinthine patterns. In this region of parameters, we observe that the labyrinthine patterns coexist with the uniform state and localized structures [28,29]. Hence, ϵ_{GS} accounts for the transition between glassy and scurfy labyrinthine patterns. When $\epsilon > \epsilon_{SD}$, the scurfy labyrinthine patterns become unstable by shrinking, and forming a gas of localized spots. The inverse process, that is, how a labyrinthine pattern is generated deterministically from a localized structure, is well known as invagination [29]. Close to the disappearance point of the labyrinthine patterns, we find $\Delta(\epsilon)$ satisfies a power law 1/4 [see Fig. 5(a)].

The Turing-Swift-Hohenberg model equation (1) is variational. Then, we can use the free energy $\mathcal{F}$ to characterize different equilibria. Figure 5(b) illustrates the free energy $\mathcal{F}$ of the different equilibria as a function of the bifurcation parameter ϵ. From this chart, we conclude that the striped pattern is the most stable state. The fingerprint-type labyrinthine patterns are the most stable labyrinthine state. Note that close to ϵ_{FPG}, the energy of fingerprint-type labyrinths merges with the energy of glassy and scurfy ones. The energy of the glassy labyrinths is always less than the energy of the scurfy labyrinths. Therefore, considering different initial conditions, the system presents a large number of equilibria with varying levels of energy.

In conclusion, out-of-equilibrium systems exhibit complicated disordered patterns. One of the patterns observed in various physical contexts is the so-called labyrinth pattern. We establish these labyrinthine patterns as a spatial state that shows a short-range order characterized by a single wave number and a powdered spectrum. The consideration of a local single wave-number behavior allows the distinction between labyrinths and disordered hexagonal patterns, the latter characterized locally by three wave numbers. Based on a prototype pattern forming model, the Turing-Swift-Hohenberg equation, we investigate the stability properties, classification, and transitions between labyrinthine patterns. The observation of three types of labyrinthine patterns—fingerprint-type, glassy, and scurfy—are established. The density of defects, free energy, structure factor, and correlation length allow us to reveal the bifurcation diagram. The mentioned order parameters, except free energy, together with techniques of global and averaged windowed Fourier transforms can also be used to characterize stationary labyrinths and their transitions in nonvariational systems [16,30].

[1] G. Nicolis and I. Prigogine, *Self-Organization in Non-Equilibrium Systems* (Wiley, New York, 1977).

[2] M. Cross and H. Greenside, *Pattern Formation and Dynamics in Non-Equilibrium Systems* (Cambridge University Press, New York, 2009).

[3] L. Pismen, *Patterns and Interfaces in Dissipative Dynamics* (Springer, Berlin, 2006).

[4] M. I. Rabinovich, A. B. Ezersky, and P. D. Weidman, *The Dynamics of Patterns* (World Scientific, Singapore, 2000).

[5] D. Walgraef, *Spatio-Temporal Pattern Formation: With Examples from Physics, Chemistry, and Materials Science* (Springer Science & Business Media, Berlin, 2012).

[6] Q. X. Liu, P. M. Herman, W. M. Mooij, J. Huisman, M. Scheffer, H. Olff, and J. Van De Koppel, Pattern formation at multiple spatial scales drives the resilience of mussel bed ecosystems, Nat. Commun. **5**, 5234 (2014).

[7] A. Yochelis, Y. Tintut, L. L. Demer, and A. Garfinkel, The formation of labyrinths, spots and stripe patterns in a biochemical approach to cardiovascular calcification, New J. Phys. **10**, 055022 (2008).

[8] J. von Hardenberg, E. Meron, M. Shachak, and Y. Zarmi, Diversity of Vegetation Patterns and Desertification, Phys. Rev. Lett. **87**, 198101 (2001).

[9] I. R. Epstein and V. K. Vanag, Complex patterns in reactive microemulsions: Self-organized nanostructures? Chaos **15**, 047510 (2005).

[10] R. Barrio, C. Varea, J. Aragón, and P. Maini, A two-dimensional numerical study of spatial pattern formation in interacting Turing systems, Bull. Math. Biol. **61**, 483 (1999).

[11] S. W. Morris, E. Bodenschatz, D. S. Cannell, and G. Ahlers, Spiral Defect Chaos in Large Aspect Ratio Rayleigh-Bénard Convection, Phys. Rev. Lett. **71**, 2026 (1993).

[12] Z. Khattari and T. M. Fischer, Shapes of Langmuir monolayer domains in confined geometries, J. Phys. Chem. B **106**, 1677 (2002).

[13] R. E. Rosensweig, M. Zahn, and R. Shumovich, Labyrinthine instability in magnetic and dielectric fluids, J. Magn. Magn. Mater. **39**, 127 (1983).

[14] K. J. Lee, W. McCormick, Q. Ouyang, and H. L. Swinney, Pattern formation by interacting chemical fronts, Science **261**, 192 (1993).

[15] P. Oswald, J. Baudry, and S. Pirkl, Static and dynamic properties of cholesteric fingers in electric field, Phys. Rep. **337** 67 (2000).

[16] M. Le Berre, E. Ressayre, A. Tallet, Y. Pomeau, and L. Di Menza, Example of a chaotic crystal: The labyrinth, Phys. Rev. E **66**, 026203 (2002).

[17] D. Boyer and J. Viñals, Domain coarsening of stripe patterns close to onset, Phys. Rev. E **64**, 050101(R) (2001).

[18] J. Swift and P. Hohenberg, Hydrodynamic fluctuations at the convective instability, Phys. Rev. A **15**, 319 (1977).

[19] J. H. Dawes, After 1952: The later development of Alan Turing's ideas on the mathematics of pattern formation, Hist. Math. **43**, 49 (2016).

[20] M. Lifshitz and V. Slyozov, The kinetics of precipitation from supersaturated solid solutions, J. Phys. Chem. Solids **19**, 35 (1961).

[21] C. Wagner, Theorie der Alterung von Niederschlagen durch Umlösen (Ostwald Reifung), Z. Electrochem. **65**, 581 (1961).

[22] M. Tlidi, P. Mandel, and R. Lefever, Kinetics of Localized Pattern Formation in Optical Systems, Phys. Rev. Lett. **81**, 979 (1998).

[23] M. Tlidi, P. Mandel, M. Le Berre, E. Ressayre, A. Tallet, and L. Di Menza, Phase-separation dynamics of circular domain walls in the degenerate optical parametric oscillator, Opt. Lett. **25**, 487 (2000).

[24] D. Boyer and J. Viñals, Grain boundary pinning and glassy dynamics in stripe phases, Phys. Rev. E **65**, 046119 (2002).

[25] D. A. Egolf, I. V. Melnikov, and E. Bodenschatz, Importance of Local Pattern Properties in Spiral Defect Chaos, Phys. Rev. Lett. **80**, 3228 (1998).

[26] M. C. Cross and D. I. Meiron, Domain Coarsening in Systems Far from Equilibrium, Phys. Rev. Lett. **75**, 11 (1995).

[27] E. Donth, *The glass transition: Relaxation dynamics in liquids and disordered materials* (Springer Science & Business Media, Berlin, 2013), Vol. 48.

[28] K. Ouchi and H. Fujisaka, Phase ordering kinetics in the Swift-Hohenberg Equation, Phys. Rev. E **54**, 3895 (1996).

[29] I. Bordeu, M. Clerc, R. Lefever, and M. Tlidi, From localized spots to the formation of invaginated labyrinthine structures in a Swift–Hohenberg model, Commun. Nonlinear Sci. Numer. Simul. **29**, 482 (2015).

[30] M. Tlidi, R. Lefever, and A. Vladimirov, On vegetation clustering, localized bare soil spots and fairy circles, Lect. Notes Phys. **751**, 381 (2008).

3.1.   Perspectives

The study presented in this chapter was devoted to understanding labyrinthine patterns in the simple framework of the two-dimensional SH equation by introducing a labyrinth's definition and quantitatively describing the transitions between fingerprint, glassy, and scurfy patterns. An interesting future research direction will be to analyze real systems, for example, vegetation labyrinthine-like patterns and liquid crystal textures, and test our findings. Additionally, it will be scientifically appealing to study three-dimensional labyrinthine patterns in the SH equation and try to extend our definitions to higher dimensions. Finally, it is reasonable to think that fingerprint, glassy, and scurfy labyrinthine patterns are not the only labyrinths in nature (other mechanisms can trigger the emergence of non-trivial symmetry patterns, such as branching and invagination processes [23, 64, 143]). Then, it will be interesting to test if the tools used here are enough to reveal the transitions of other types of labyrinths.

Chapter 4

Localized states with nontrivial symmetries: Localized labyrinthine patterns (Physical Review E 105, L012202)

In Chapter 3, we describe the disappearance of the scurfy labyrinthine pattern in the SH equation using as an order parameter a quantitative measure of the competition between the modes $k = 0$ and $k = k_c$, $|\Delta|$ (see Chapter 3 and Fig. 4.1a). The loss of the labyrinthine structure, when increasing ϵ, is governed by the growing of homogeneous domains and the shrinking of isolated stripes (or fingers), which transform into localized structures (black up-triangles in Figs. 4.1b and 4.1c). The inverse process, when decreasing ϵ, is characterized by the elongation of fingers filling all the available space and thus forming a labyrinthine pattern again (see blue down-triangles in Figs. 4.1b and 4.1c). Interestingly, a hysteresis loop connecting the labyrinth and the homogeneous state is revealed and shown in Fig. 4.1b. The coexistence of both equilibria gives the possibility of localized scurfy labyrinthine patterns (see an example in Fig. 4.2). The phenomenon is also manifested in the gSH equation, where the breaking of the reflection symmetry $u \to -u$ allows the localization of localized glassy labyrinthine patterns.
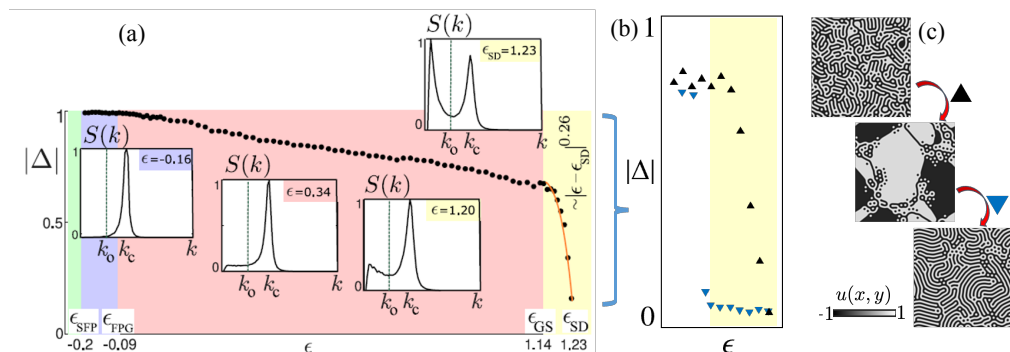
Figure 4.1: Hysteresis loop connecting scurfy labyrinthine patterns and the homogeneous solutions in the SH equation. (a) Disappearance of scurfy labyrinthine patterns in terms of the order parameter $|\Delta|$ (see Chapter 3 for details). (b) Hysteresis loop within the scurfy region. (c) Examples of the disappearance and reappearance of scurfy labyrinthine patterns.
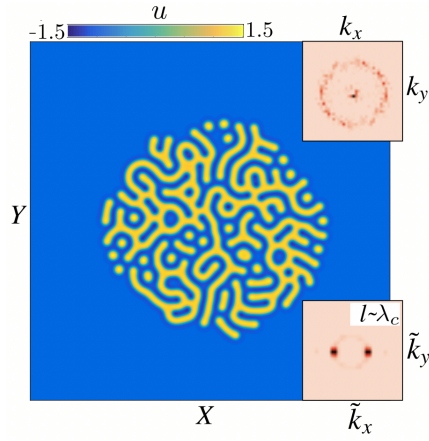
Figure 4.2: Localized labyrinthine pattern of the SH equation with $\epsilon = 1.17$ and $\nu = 1$. The upper and lower insets are the global and local Fourier transforms, which define a labyrinthine pattern. Windows of size $2l$ where used for the averaged windowed Fourier transform.

In this chapter, we show for the first time the possibility of having non-trivial symmetry patterns localized in two and three dimensions. We show that this phenomenon is robust and is presented in various physical systems (vegetation, optics, and chemistry). Furthermore, we give a glimpse of the complex bifurcation diagram exhibited by some stable branches of the localized labyrinthine structures in 2D.

Localized states with nontrivial symmetries: Localized labyrinthine patterns

M. G. Clerc [⬤],[1] S. Echeverría-Alar [⬤],[1] and M. Tlidi[2]

[1]*Departamento de Física and Millennium Institute for Research in Optics, FCFM, Universidad de Chile, Casilla 487-3, Santiago, Chile*
[2]*Faculté des Sciences, Université libre de Bruxelles (U.L.B), CP. 231, 1050 Brussels, Belgium*

The formation of self-organized patterns and localized states are ubiquitous in Nature. Localized states containing trivial symmetries such as stripes, hexagons, or squares have been profusely studied. Disordered patterns with nontrivial symmetries such as labyrinthine patterns are observed in different physical contexts. Here we report stable localized disordered patterns in spatially extended dissipative systems. These two- and three-dimensional localized structures consist of an isolated labyrinth embedded in a homogeneous steady state. Their partial bifurcation diagram allows us to explain this phenomenon as a manifestation of a pinning-depinning transition. We illustrate our findings on the Swift-Hohenberg-type of equations and other well-established models for plant ecology, nonlinear optics, and reaction-diffusion systems.

Spatiotemporal patterning resulting from a symmetry-breaking instability is a central issue in almost all driven far from equilibrium systems [1–3]. Localized structures, dissipative solitons, and localized patterns belong to this field of research. They consist of one or more regions in one state surrounded by a region in a qualitatively different state [4–8]. Spatial localization appears not only in nonlinear systems, but can occur in linear ones such as Anderson localization that arises in inhomogeneous systems [9]. Localized states appear in other classes of experimentally relevant systems such as nonlinear optics and photonics. Spatial localized patterns possess potential applications to all-optical control of light, optical storage, and information processing [6,8].

Localized patterns involving trivial symmetries such as stripes, hexagons, or squares have been abundantly discussed and are by now fairly well understood, including their respective snaking bifurcation diagrams [7,10]. Indeed, these localized patterns involve few Fourier modes. However, localized patterns with nontrivial symmetries have neither been experimentally observed nor documented, nor theoretically predicted. An example of this type of patterning phenomenon is referred to as localized labyrinthine patterns (LLP). They are observed in population biology, such as in vegetation populations, on the skin of animals, or human bodies [cf. Fig. 1]. All these examples show an area, which is not necessarily circular, containing complex spatial structures, a labyrinth, and surrounded by a uniform state. In the vegetation populations, this intriguing phenomenon seems to be stationary (see the Supplementary Material [20]). Extended labyrinthine patterns refer to two-dimensional (2D) or more-dimensional dissipative structures characterized by a circular or spherical powder-like spectrum globally [12], they exhibit a short-range order with a single Fourier mode, and have a finite number of defects [13]. A power spectrum with a powdered ring (sphere)

structure is the main characteristic of patterns with nontrivial symmetries.

In this Letter, we account for the formation of localized patterns with nontrivial symmetries in well-established models from ecology, optics, and reaction-diffusion systems. We illustrate and investigate this phenomenon using a Swift-Hohenberg equation (SHE) [14], which constitutes a well-known paradigm in the study of spatial periodic or localized patterns in spatially extended systems [2]. We show that this model supports static and stable LLP. Considering adequate initial conditions, LLP are generated in the coexistence region between the extended labyrinth and homogenous state. We draw the partial bifurcation diagram showing the stability domain of LLP and their pinning-depinning transitions, where the localized labyrinth exists as a stationary solution. Free energy allows us to study the relative stability analysis. We show numerical evidence of stable three-dimensional localized labyrinthine patterns. Further, within the pinning range of parameters, three LLP with different sizes are generated for a fixed value of the system parameters.

The SHE reads ([14])

$$\partial_t u = \epsilon u - u^3 - \nu \nabla^2 u - \nabla^4 u, \qquad (1)$$

where the real order parameter $u = u(x, y, z, t)$ is an excess scalar field variable measuring the deviation from criticality, ϵ is the control parameter, and ν the (anti) diffusion coefficient for (positive) negative value. The cubic term accounts for the nonlinear response of the system under study. The Laplace operator $\nabla^2 = \partial_{xx} + \partial_{yy} + \partial_{zz}$ acts in the (x, y, z)-Euclidean space and t is time. The last term on the right-hand side, the bi-Laplacian, stands for hyperdiffusion. Equation (1) can also be used to describe 2D systems, where the Laplacian, bi-Laplacian, and the order parameter u are defined in the (x, y)-Euclidean space. The model equation (1) can be rewritten in a variational form as $\partial_t u = -\delta \mathcal{F}/\delta u$, where $\mathcal{F}$ is a
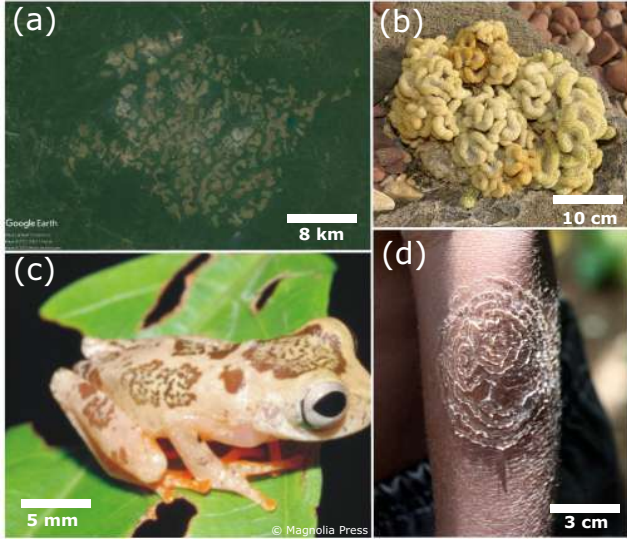
FIG. 1. Snapshots of localized labyrinthine patterns in natural systems. (a) Irregular distribution of vegetation embedded in a uniform vegetated cover observed in central Cameroon using Google Earth software (with ground coordinate 3°58'22.70" N 12°19'05.84" E). (b) Brain cactus (Mammilaria Elongata Cristata) with a contorted tissue (courtesy of David Stang). It is a localized structure in the bare soil background. (c) Pigmented areas composed of stripes and spots in the skin dorsum of a frog (Dendropsophus ozzyi) [11] (reproduced with permission from the copyright holder). (d) Skin lessions of Tinea imbricata disease (courtesy of Michael Marks).

Lyapunov functional or a free energy

$$\mathcal{F} = \int \frac{dx\,dy\,dz}{2}\left(-\epsilon u^2 + \frac{u^4}{2} - \nu(\nabla u)^2 + (\nabla^2 u)^2\right). \quad (2)$$

The variational structure of the SHE (1) indicates that only stationary solutions such as uniform states, spatially periodic, or localized patterns are possible. The SHE (1) is a well-known paradigm for the study of periodic and localized patterns, was first derived in hydrodynamics [14], and later in other fields of natural science, such as chemistry [15], and nonlinear optics [16]. In the last decade, it has been established that Eq. (1) has already constructed by Turing, but was unpublished [17].

Other real SHE was derived for out of equilibrium systems [18,19]

$$\partial_t u = \eta - \epsilon u - u^3 - (\nu - bu)\nabla^2 u - \nabla^4 u - c(\nabla u)^2, \quad (3)$$

where ϵ and η are control parameters; ν, b are diffusion parameters; and c is the nonlinear advection strength. The presence of nonlinear diffusion and nonlinear advection terms, $u\nabla^2 u$ and $(\nabla u)^2$, render Eq. (3) nonvariational. In general, this equation does not admit a Lyapunov functional.

Whether a SHE model is variational or not, numerical simulations of both models, Eqs. (1) and (3) with periodic boundary conditions show evidence of stable stationary localized labyrinthine patterns [see Figs. 2(a) and 2(b)].

To obtain localized labyrinthine patterns, the initial conditions consist of a circular area, of certain diameter d, of a stable labyrinthine pattern in the center of the simulation box, embedded in a uniform background. The evolution towards
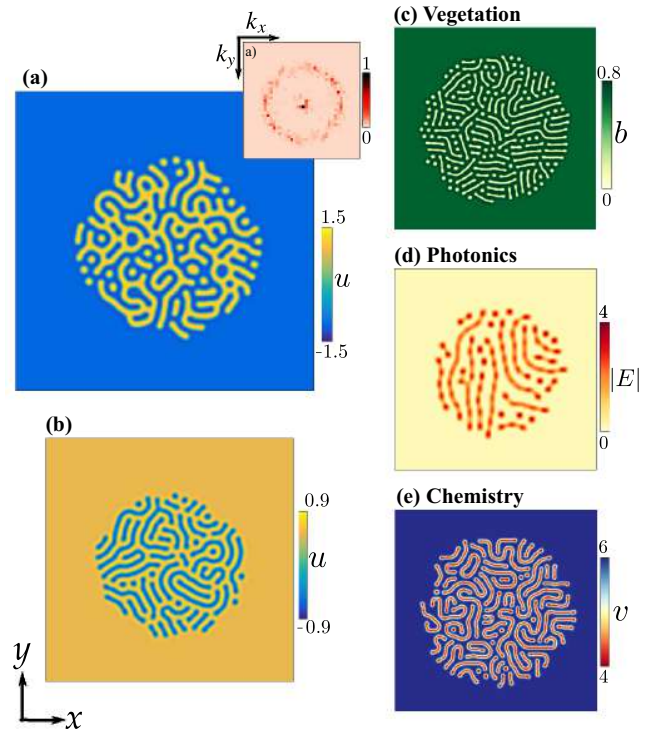
FIG. 2. Stationary localized labyrinthine patterns obtained in different pattern forming models: (a) SHE (1) ($\epsilon = 1.17$, $\nu = 1$); (b) generalized SHE (3) ($\epsilon = 0.2$, $\nu = 1$, $\eta = -0.06$, $b = 0.1$, $c = 0.1$); (c) nonlocal vegetation; (d) passive diffractive resonator; and (e) reaction-diffusion. See the Supplementary Material for more details of models and parameters used in (c), (d), and (e) [20]. The right-upper inset in (a) shows the powder-like ring spectrum of the LLP in the SHE model (1). All the localized structures fulfill the definition of labyrinthine patterns (see Supplementary Material [20] for details).

equilibrium starts with a quick adjustment of the interface mediated by the curvature of the stripe patterns; then there is an accommodation of the stripe patterns in the bulk. To this end, some retraction of stripes in the interface takes place (cf. Video 1 and the stabilization of LLP in the Supplementary Material [20]). The final localized region is not perfectly circular, containing finite segments of deformed stripes separated by spots of the same width, and a high number of defects inherited from the extended labyrinth. These finite-size stripes can be interconnected or not. They support all stripe orientations along the motionless interface separating the labyrinth to the homogeneous steady state, as shown in Fig. 2. Note that localized nontrivial symmetry patterns arise between the critical sizes $d_o \leqslant d \leqslant d_c$ (see the Supplementary Material [20] for details). In addition, the formation of LLP in the above scalar model equations in the form of SHE, additional models are also considered that are experimentally relevant. First, a generic interaction redistribution model describing vegetation pattern formation which is an integrodifferential model equation. This simple modeling approach based on the interplay between short-range and long-range interactions governing plant communities captures localized labyrinthine pattern as shown in Fig. 2(c). Second, broad area photonics devices such as nonlinear resonators subjected to a coherent injected
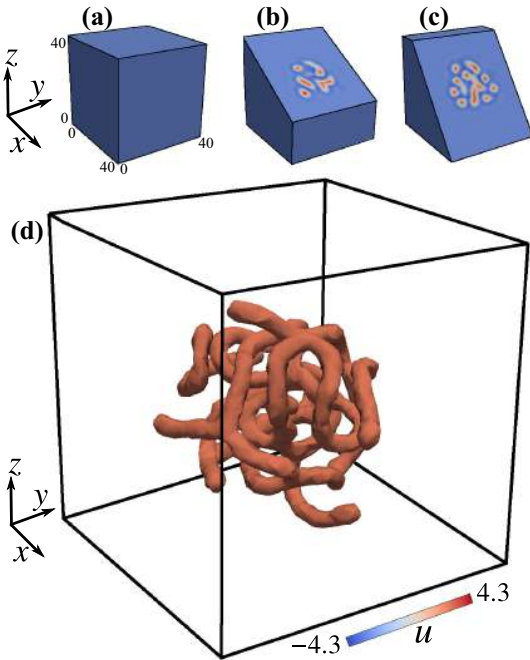
FIG. 3. Three-dimensional localized labyrinthine pattern solution of Eq. (3). (a) Color map of the full simulation, (b) and (c) are color map slices of the localized labyrinthine pattern. (d) Isosurface of the localized labyrinthine pattern with $u = 1.3$. Parameters are $\epsilon = 4.2$, $\nu = 5$, $\eta = -6.8$, $b = 0$, and $c = 0$. The mesh integration is $40 \times 40 \times 40$.

FIG. 4. (a) Bifurcation diagram of homogenous solutions and (b) relative stability analysis of a localized labyrinth in SHE (1) with $\nu = 1$. The uniform $u(x, y) = 0$ state suffers a Turing instability at $\epsilon_{c1} = -0.25$. The uppermost curve (blue) shows the maximum $u(x, y)$ of the different equilibrium patterns [stripe (i), fingerprint-type labyrinth (ii), glassy labyrinth (iii), and scurfy labyrinth (iv)]. At $\epsilon_{c2} = 0.125$, the nonzero homogenous states (HSS-green curves) are unstable to in-homogenous perturbations. In the narrow region limited by $\epsilon_p^- = 1.16$ and $\epsilon_p^+ = 1.19$, where the extended labyrinthine pattern and the uniform solutions coexist, the existence of localized labyrinthine patterns (v) is possible. Free energy $\mathcal{F}$ given by Eq. (2) is computed for an extended labyrinth (EL), the stripe pattern (SP), the homogenous states (HSS), and a localized labyrinthine pattern (LLP) near the pinning region.

beam [see Fig. 2(d)]. In this case, the resulting equation is a complex Ginzburg-Landau-type equation. Finally, a reaction-diffusion model for chemical dynamics, also supports LLP as shown in Fig. 2(e). The description of these models and the values of the parameters are provided in the Supplementary Materials [20]. Similar solutions when using Dirichlet and Neumann boundary conditions are observed. Also, localized labyrinthine patterns are independent of the numerical grid size (see the Supplementary Material [20] for details).

The 2D LLP are robust structures in 2D systems in the various natural system, that is, this phenomenon is observed in different physical systems as shown in Fig. 1 and in the Supplementary Material [20]. It has been shown that the Swift-Hohenberg equation supports three-dimensional (3D) extended patterns with trivial symmetries such as lamellae, body-centered cubic crystals, hexagonally packet cylinders [25–28], and localized patterns [27–29]. Recently, clusters of 3D bullets forming a localized crystal with trivial symmetry were reported [30]. We extend this analysis to 3D nontrivial symmetry patterns and we show the existence of stable 3D localized labyrinthine patterns. They consist of finite-size curved and connected tubes embedded in a homogeneous background. The width of the tubes is half of the critical wavelength at the symmetry-breaking instability. They are obtained by numerical simulations of the generalized SHE Eq. (3) with Neumann boundary conditions along x, y, and z directions. Figure 3 shows a typical 3D localized labyrinthine pattern.

The homogeneous steady states $u_s = 0$ and $u_{s\pm} = \pm\epsilon^{1/2}$ solutions of Eq. (1) undergo symmetry-breaking instabilities at $\epsilon_{c1} = -\nu^2/4$ and $\epsilon_{c2} = \nu^2/8$. At both critical bifurcations points the critical wavelength is $\lambda_c = 2\pi/k_c = 2\sqrt{2}\pi/\sqrt{\nu}$. Indeed, when the linear coefficient of the Laplacian is negative $\nu > 0$, the spontaneous pattern formation process becomes possible thanks to the appearance of a finite band of linearly unstable Fourier modes that triggers the appearance of spatially periodic patterns. The upper cutoff is affected by the bi-Laplacian term, which is always stabilizing for short distances since dispersion is an efficient mixing mechanism. Numerical simulations of the bi-dimensional Eq. (1) in the neighborhood of the critical point $\epsilon = \epsilon_{c1}$ indicate the emergence of extended patterns, as shown in Fig. 4(a). When increasing the control parameter, the sequence of symmetry-breaking transitions fingerprint, glassy, and scurfy labyrinthine patterns are observed [13].

Spatial confinement leading to the formation of localized patterns with nontrivial symmetry occurs in parameter space ($\epsilon > \epsilon_{c2}$), where extended labyrinthine patterns coexist with a homogeneous steady state. Within this hysteresis loop, there generally exists a so-called pinning range of parameters [31], delimited by $\epsilon_p^\pm$, in which LLP can be observed [cf. Fig. 4(a)]. Taking advantage of the variational structure of Eq. (1), we address the problem of the relative stability analysis. We evaluate numerically $\mathcal{F}$, associated with uniform states, extended labyrinth, and LLP. Figure 4(b) summarizes the results. These equilibria correspond to a local or global minimum of Lyapunov functional $\mathcal{F}$ given by Eq. (2). From Fig. 4(b),

we see that the localized labyrinth is more energetically favorable than the extended labyrinth (EL) but less stable than the homogeneous steady state (HSS) and the perfect stripe pattern (SP). The limiting points of the stability region of the localized labyrinth solutions $\epsilon_p^- < \epsilon < \epsilon_p^+$ are similar to the ϵ parameters associated to the interchange of metastability between extended states. The localized labyrinths are stationary and stable patterns since their localized area never expands despite diffusion and never shrinks despite nonlinearity and dissipation.

Localized patterns with trivial symmetry (stripes and hexagons) are organized into a complex diagram following a homoclinic snaking bifurcation [7]. This type of diagram is obtained by a continuation method. The symmetries of the localized structures are relevant for the convergence of this algorithm. However, in the case of LLP there is a lack of continuation algorithms to characterize the full bifurcation diagram. To figure out the existence region of stable LLP, we performed direct numerical simulations of Eq. (1). Figure 5(a) summarizes the results, where we plot

$$||u||^2 = \frac{1}{L_x L_y} \int_0^{L_x} \int_0^{L_y} [u(x,y) - u_{s+}]^2 dx dy, \qquad (4)$$

as a function of the bifurcation parameter. The full bifurcation diagram can be complex, so we display only three branches of LLP obtained with different initial conditions shown in the insets (i), (ii), and (iii) of Fig. 5(a). The maximum amplitude of the three LLPs is the same, but they have different sizes. Varying ϵ from these initial conditions, we obtain the three branches shown in Fig. 5(a). Whatever the initial condition, when increasing the bifurcation parameter the LLP decrease in size, mediated by the shrinking of fingers and accommodation of defects (see the Supplementary Material [20] for details). All LLP disappear close to $\epsilon > \epsilon_p^+$ and the system exhibit a transition towards a mixture of circular localized peaks and dips. Figure 5(b) illustrates this transition, during which we observe the contraction of fingers, which transform to circular peaks or dips. This process correspond to the inverse of the invagination of localized structures [32]. Starting from the initial conditions shown in the insets (i), (ii), and (iii) of Fig. 5(a) and decreasing the bifurcation parameter, we observe an increase in the size of the LLP. Further decreasing $\epsilon < \epsilon_p^-$, we observe a transition to an extended fingerprint-like labyrinthine pattern. This depinning transition mediated by front propagation has the tendency to reduce the number of circular spots and dips, and enhance the invagination process as illustrated in Fig. 5(c).

By varying the control parameter within the pinning region delimited by ϵ_p^- and ϵ_p^+, we see that for a fixed ϵ, and near $\epsilon = \epsilon_p^-$ the sizes of the coexisting LLP are different. However, close to $\epsilon = \epsilon_p^+$ the system reaches more or less the same size. We stress that the position of LLP and their size depends on the initial conditions, and the maximum of the coexisting LLP is essentially constant for fixed values of the system parameters. The number of coexisting LLP with different sizes can be much larger than the three branches shown in the bifurcation diagram displayed in Fig. 5(a).

The localized patterns with trivial symmetries have a well-established bifurcation diagram based on continuation
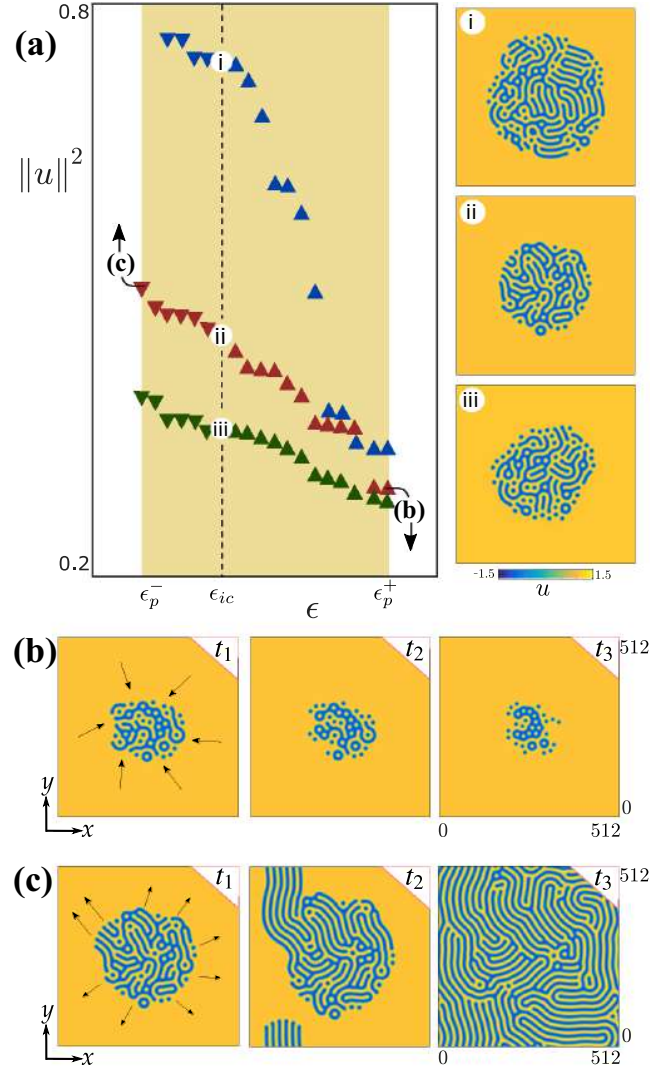
FIG. 5. Three stable branches of LLP and pinning-depinning transitions in the SHE model (1). (a) Plot of $||u||^2$ for three initial conditions (i, ii, and iii) with different sizes (see Fig. 3 in the Supplementary Material [20] for details). The upward (downward) triangles account for the increasing (decreasing) of ϵ, starting from $\epsilon_{ic} = 1.17$. (b) Temporal sequence of the pinning-depinning transition when crossing $\epsilon_p^+ = 1.19$ and (c) $\epsilon_p^- = 1.16$.

methods. However, when dealing with localized patterns with nontrivial symmetries, there are no available algorithms for the continuation to handle this problem. Whether the localized labyrinthine patterns present a homoclinic snaking bifurcation diagram or not remains an open question. The plausibility of spatial varying parameters can be responsible for complex localized patterns. However, our result opens a novel possibility of localized patterns with nontrivial symmetries even in homogenous and isotropic systems. The existence of these types of localized patterns is the consequence of an intricate interplay between pinning, defects, and complex-shaped interface.

[1] P. Glansdorff and I. Prigogine, *Thermodynamic Theory of Sstructure, Stability, and Fluctuations* (Wiley-Interscience, New York, 1971).

[2] M. C. Cross and P. C. Hohenberg, Pattern formation outside of equilibrium, Rev. Mod. Phys. **65**, 851 (1993).

[3] J. D. Murray, *Mathematical Biology: I. An Introduction*, (Springer Science & Business Media, New York, 2007).

[4] O. Descalzi, M. Clerc, S. Residori, and G. Assanto, *Localized States in Physics: Solitons and Patterns* (Springer, New York, 2011).

[5] H. G. Purwins, H. U. Bödeker, and Sh. Amiranashvili, Dissipative solitons, Adv. Phys. **59**, 485 (2010).

[6] M. Tlidi, K. Staliunas, K. Panajotov, A. G. Vladimirov, and M. G. Clerc, Localized structures in dissipative media: From optics to plant ecology, Phil. Trans. R. Soc. A **372**, 20140101 (2014).

[7] E. Knobloch, Spatial localization in dissipative systems, Annu. Rev. Condens. Matter Phys. **6**, 325 (2015).

[8] L. Lugiato, F. Prati, and M. Brambilla, *Nonlinear Optical Systems* (Cambridge University Press, Cambridge, England, 2015).

[9] P. W. Anderson, Absence of diffusion in certain random lattices, Phys. Rev. **109**, 1492 (1958).

[10] P. Coullet, Localized patterns and fronts in nonequilibrium systems, Int. J. Bifurcation Chaos Appl. Sci. Eng. **12**, 2445 (2002).

[11] V. G. D. Orrico, A new "Bat-Voiced" species *Dendrophosus* Fitzinger, 1843 (Anura, Hyliade) from the Amazon Basin, Brazil, Zootaxa **3881**, 4 (2014).

[12] M. Le Berre, E. Ressayre, A. Tallet, Y. Pomeau, and L. Di Menza, Example of a chaotic crystal: The labyrinth, Phys. Rev. E **66**, 026203 (2002).

[13] S. Echeverria-Alar and M. G. Clerc, Labyrinthine patterns transitions, Phys. Rev. Research **2**, 042036(R) (2020).

[14] J. Swift and P. C. Hohenberg, Hydrodynamic fluctuations at the convective instability, Phys. Rev. A **15**, 319 (1977).

[15] M'F. Hilali, G. Dewel, and P. Borckmans, Subharmonic and strong resonances through coupling with a zero mode, Phys. Lett. A **217**, 263 (1996).

[16] M. Tlidi, P. Mandel, and R. Lefever, Localized Structures and Localized Patterns in Optical Bistability, Phys. Rev. Lett. **73**, 640 (1994).

[17] J. H. Dawes, After 1952: The later development of Alan Turing's ideas on the mathematics of pattern formation, Hist. Math. **43**, 49 (2016).

[18] M. G. Clerc, A. Petrossian, and S. Residori, Bouncing localized structures in a liquid-crystal light-valve experiment, Phys. Rev. E **71**, 015205(R) (2005).

[19] G. Kozyreff and M. Tlidi, Nonvariational real Swift-Hohenberg equation for biological, chemical, and optical systems, Chaos **17**, 037103 (2007).

[20] See Supplemental Material at http://link.aps.org/supplemental/10.1103/PhysRevE.105.L012202 for details on the complexity of localized labyrinthine patterns in the models described here [Eqs. (1) and (3)] and in [20] (vegetation, nonlinear optics, reaction-diffusion). Video 1 shows the stabilization process of a localized labyrinthine pattern in the SHE model 1. Discussion of critical size for LLP formation. Details on numerical simulations of LLP in the SHE model 1 with Neumann and Dirichlet boundary conditions and different grid sizes. The growth mechanism along one stable branch of LLP is described. The Supplemental Material includes the references [21–24].

[21] M. Tlidi, R. Lefever, and A. Vladimirov, On vegetation clustering, localized bare soil spots and fairy circles, Lect. Notes Phys. **751**, 381 (2008).

[22] J. von Hardenberg, E. Meron, M. Shachak, and Y. Zarmi, Diversity of Vegetation Patterns and Desertification, Phys. Rev. Lett. **87**, 198101 (2001).

[23] M. Le Berre, E. Ressayre, and A. Tallet, Why does a Ginzburg-Landau diffraction equation become a diffusion equation in the passive ring cavity?, Quantum Semiclass. Opt. **7**, (1995).

[24] E. C. Edblom, M. Orban, and I. R. Epstein, A new iodate oscillator: The Landolt reaction with ferrocyanide in a CSTR, J. Am. Chem. Soc. **108**, 2826 (1986).

[25] U. Thiele, A. J. Archer, M. J. Robbins, H. Gomez, and E. Knobloch, Localized states in the conserved Swift-Hohenberg equation with cubic nonlinearity, Phys. Rev. E **87**, 042915 (2013).

[26] H. G. Lee, A semi-analytical Fourier spectral method for the Swift–Hohenberg equation, Comput. Math. Appl. **74**, 1885 (2017).

[27] K. Staliunas, Three-Dimensional Turing Structures and Spatial Solitons in Optical Parametric Oscillators, Phys. Rev. Lett. **81**, 81 (1998).

[28] M. Tlidi and P. Mandel, Three-Dimensional Optical Crystals and Localized Structures in Cavity Second Harmonic Generation, Phys. Rev. Lett. **83**, 4995 (1999).

[29] I. Bordeu and M. G. Clerc, Rodlike localized structure in isotropic pattern-forming systems, Phys. Rev. E **92**, 042915 (2015).

[30] S. S. Gopalakrishnan, K. Panajotov, M. Taki, and M. Tlidi, Dissipative Light Bullets in Kerr Cavities: Multistability, Clustering, and Rogue Waves, Phys. Rev. Lett. **126**, 153902 (2021).

[31] Y. Pomeau, Front motion, metastability and subcritical bifurcations in hydrodynamics, Phys. D (Amsterdam, Neth.) **23**, 3 (1986).

[32] I. Bordeu, M. G. Clerc, R. Lefever, and M. Tlidi, From localized spots to the formation of invaginated labyrinthine structures in a Swift–Hohenberg model, Comm. Nonlinear Sci. Numer. Simulat. **29**, 482 (2015).

Supplementary Material on "Localized states with non-trivial symmetries: localized labyrinthine patterns"

M. G. Clerc,[1] S. Echeverría-Alar,[1] and M. Tlidi[2]

[1]*Departamento de Física and Millennium Institute for Research in Optics,*
Facultad de Ciencias Físicas y Matemáticas, Universidad de Chile, Casilla 487-3, Santiago, Chile
[2]*Département de Physique, Faculté des Sciences, Université Libre de Bruxelles (U.L.B.),*
CP 231, Campus Plaine, B-1050 Bruxelles, Belgium

I. LOCALIZED LABYRINTHINE PATTERNS

Labyrinthine patterns are disordered spatial structures characterized by a well-defined intrinsic length and presenting a powderlike ring spectrum in Fourier space [1], which signifies their lack of simple symmetry, local behavior of a single wavevector, and a large number of defects [2]. Localized labyrinthine patterns (LLP) arise as the stabilization of a labyrinthine pattern enclosed by a homogenous state. For example, they can be observed in the context of vegetation self-organization as irregular patches embedded in a uniform vegetated cover [cf. Fig. 1]. The localized vegetation labyrinths are robust and stationary, as shown in the temporal sequence of Figure 1, in which no relevant change is observed in a decade. Hence, natural systems can show the coexistence between states with trivial and nontrivial symmetries. Figure 2 shows stationary localized labyrinthine patterns obtained in different pattern forming models. The upper (lower) insets are the modulus of the global (averaged windowed) Fourier transform. From these Fourier transforms, one concludes that the localized patterns are disordered (upper insets) and locally characterized by a single mode (bottom insets).
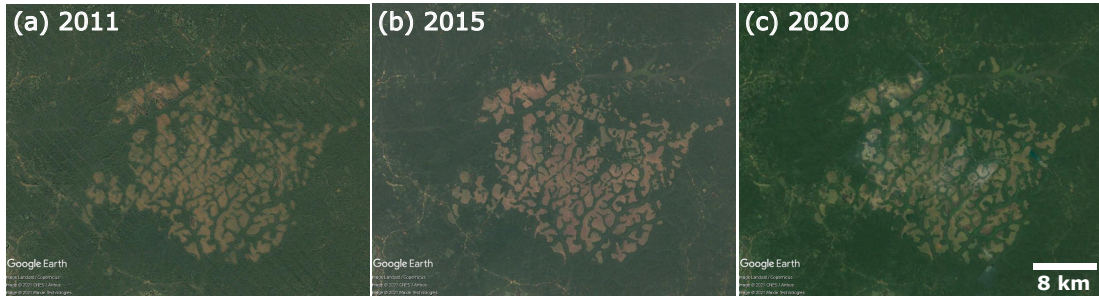
Figure 1: Temporal sequence of snapshots of a localized vegetation labyrinthine pattern. The localized labyrinthine pattern is observed in central Cameroon using Google Earth software (with ground coordinate 3°58'22.70" N 12°19'05.84" E [3]). The images were taken on December of (a) 2011, (b) 2015, and (c) 2020.

II. SWIFT-HOHENBERG MODELS

To shed light in the existence, stabilization, and growth mechanisms of these new localized patterns, we consider the paradigmatic Swift-Hohenberg equation (SHE) [4]

$$\partial_t u = \epsilon u - u^3 - \nu \nabla^2 u - \nabla^4 u, \tag{1}$$

where $u = u(x, y, t)$ is a real scalar field, ϵ is the bifurcation parameter, and $\nu > 0$ is the anti-diffusion coefficient, and a generelization version of the SHE [5, 6]

$$\partial_t u = \eta - \epsilon u - u^3 - (\nu - bu)\nabla^2 u - \nabla^4 u - c(\nabla u)^2, \tag{2}$$

where ϵ and η are control parameters, ν, b are linear and nonlinear diffusion parameters, and c is the nonlinear advection strength. Both models support LLP [see Figs. 2(a) and 2(b)] in a pinning region where the uniform solutions $u_{s\pm} = \pm \epsilon^{1/2}$ coexist with labyrinthine patterns of a critical wavelength $\lambda_c = 2\sqrt{2}\pi/\sqrt{\nu}$.
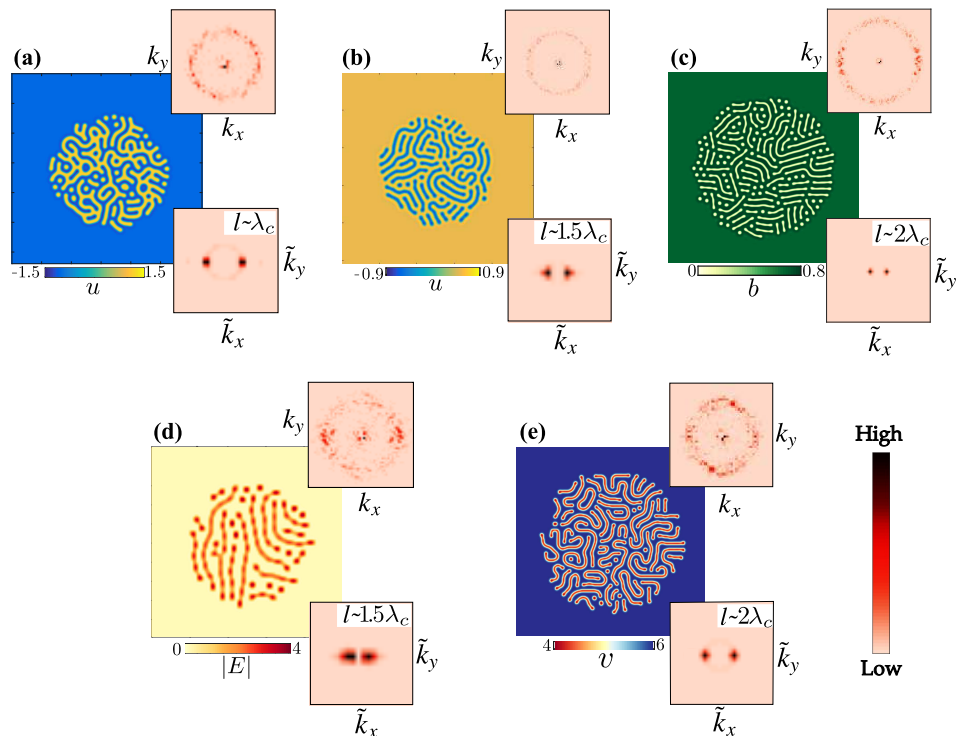
Figure 2: Stationary localized labyrinthine patterns obtained in different pattern forming models: (a) SHE (1) with $\epsilon = 1.17$ and $\nu = 1$, (b) generalized SHE (2) with $\epsilon = 0.2$, $\nu = 1$, $\eta = -0.06$, $b = 0.1$, and $c = 0.1$, (c) Non-local vegetation model Eq. (4) with $L_f = 2.5$, $D = 1$, $\xi_f = 3$, $\xi_c = 1$, $\mu = 1.3$, (d) Passive diffractive resonator equation (8) with $C = 21$, $\theta = -3.8$, and $E_i = 22$, (e) reaction-diffusion model Eq. (10) with $a = 17.16$. The upper (lower) inset is the modulus of global (local) Fourier transform. λ_c and l are the critical wavelength ($2\pi/|\vec{k_c}|$), of the corresponding model, and the size of the window in the averaged windowed Fourier transform, respectively.

III.   OTHER EXPERIMENTALLY RELEVANT SYSTEMS

The existence of stable localized labyrinthine structure is not limited to the large wavelength pattern regime described by the paradigmatic Swift-Hohenberg equation but can be obtained from other experimentally relevant systems. Three examples are chosen across various fields of natural science: (A) vegetation interaction-redistribution model of vegetation dynamics, which can generate patterns even under strictly homogeneous and isotropic environmental conditions. It is grounded on a spatially explicit formulation of the balance between facilitation and competition. Ecosystems experience transitions towards fragmentation of landscapes followed by desertification constitutes a major risk to the biological productivity of degradated zones, (B) nonlinear optical cavity subjected to a coherent injected field, where localized states have been experimentally observed with a possibility for applications in all-optical control of light, optical storage, and information processing, and (C) Chemical reaction-diffusion far from equilibrium systems.

A.   Vegetation interaction-redistribution model

The nonlocal approach, we adopt here focuses on the relationship between the structure of individual plants and the facilitation-competition interactions existing within plant communities. Three types of interactions are considered: the facilitative $M_f(\vec{r}, t)$, the competitive $M_c(\vec{r}, t)$, and the seed dispersion $M_d(\vec{r}, t)$ nonlocal interactions. To simplify further the mathematical modeling, we consider that the seed dispersion obeys a diffusive process $M_d(\vec{r}, t) \approx D\nabla^2 b(\vec{r}, t)$, where D is the diffusion coefficient. We assume in addition that all plants are mature neglecting the allometry, and they

are settled on flat territory $\vec{r} = (x, y)$, assuming isotropic environmental conditions. The interaction-redistribution model reads

$$M_i = exp\left\{\frac{\xi_i}{N_i} \int b(\vec{r} + \vec{r}', t)\phi_i(\vec{r}, t)d\vec{r}'\right\}, \text{ with } \phi_i(\vec{r}, t) = exp(-\vec{r}/L_i) \tag{3}$$

where $i = \{f, c\}$. ξ_i represents the strength of the interaction, N_i is a normalization constant. We assume that their Kernels $\phi_i(\vec{r}, t)$ are exponential functions with L_i the range of their interactions.

A logistic equation with the above mentioned nonlocal interactions leads to the so called vegetation interaction-redistribution model. The spatiotemporal evolution of the normalized biomass density $b(r, t)$ in isotropic environmental conditions reads [7]

$$\partial_t b(\vec{r}, t) = b(\vec{r}, t)[1 - b(\vec{r}, t)]M_f(\vec{r}, t) - \mu b(\vec{r}, t)M_c(\vec{r}, t) + DM_d(\vec{r}, t). \tag{4}$$

The normalization is performed with respect to the total amount of biomass supported by the system. The first two terms in the logistic equation with nonlocal interaction Eq. (4) describe the biomass gains and losses, respectively. The third term models seed dispersion. The aridity parameter μ accounts for the biomass loss and gain ratio. Other approches based on reaction-diffusion type of modelling incorporate water transport by below ground diffusion and/or above ground run-off [8].

The homogeneous steady state solutions of Eq. (4) are: $b_o = 0$ which corresponds to the state totally devoid of vegetation, and the homogeneous cover solutions, which satisfy the equation

$$\mu = (1 - b) \exp \Delta b, \tag{5}$$

with $\Delta = \xi_f - \xi_c$ measures the community cooperativity if $\Delta > 0$ or anti-cooperativity when $\Delta < 0$. The bare state $b_o = 0$ is unstable (stable) $\mu < 1$ ($\mu > 1$) and stable otherwise. The homogeneous cover state with higher biomass density is stable and the other is unstable. These are connected by a saddle node or a tipping point whose coordinates are given by $\{b_{sn} = (\Delta - 1)/\Delta, \mu_{sn} = e^{\Delta-1}/\Delta\}$. The linear stability analysis of the vegetated cover (b_s) with respect to small fluctuations of the form $b(\vec{r}, t) = b_s + \delta b \, exp\{\sigma t + i\vec{k} \cdot \vec{r}\}$ with δb small, yields the dispersion relation

$$\sigma(k) = \left(b_s(1 - b_s)\xi_f - b_s - \frac{b_s(1 - b_s)\xi_c}{(1 + L_c^2 k^2)^{3/2}}\right) e^{\xi_f b_s} - Dk^2. \tag{6}$$

Given the spatial isotropy, the growth rate $\sigma(k)$ is a real quantity. This eigenvalue may become positive for a finite band of unstable modes which triggered the spontaneous amplification of spatial fluctuations towards the formation of periodic structures with a well-defined wavelength $(2\pi/k_c)$. At the symmetry-breaking instability, the value of the critical wavenumber k_c marking the appearance of a band of unstable modes, and hence the symmetry-breaking instability, can be evaluated by two conditions: $\sigma(k_c) = 0$ and $\partial\sigma/\partial k|_{k_c} = 0$. These conditions yield the most unstable mode

$$k_c^2 = \frac{1}{L_c^2}\left[\left(\frac{3b_s e^{\xi_f b_s}(1 - b_s)\xi_c L_c^2}{2D}\right)^{2/5} - 1\right]. \tag{7}$$

This critical wavenumber determines the wavelength of the periodic vegetation pattern $2\pi/k_c$ that emerges from the symmetry-breaking instability. Replacing k_c in the condition $\sigma(k_c) = 0$, we can then calculate the critical biomass density b_c. The corresponding critical aridity parameter μ_c is provided explicitly by the homogeneous steady states Eq. (5). The critical wavelength $(2\pi/k_c)$ determines the half space between stripes in the localized labyrinth, solution of Eq. (4), shown in Fig. 2.

B. Passive nonlinear resonator model

We consider a passive resonator with plane mirrors, filled by a resonant two-level medium without population inversion and driven by a coherent plane-wave injected signal. In the good cavity limit where the medium relaxes much faster than the cavity field, the material variables (the atomic polarization and population difference) are

adiabatically eliminated, and the resulting model equation is a complex Ginzburg-Landau equation of the form

$$\partial_t E = E_i - (1 + i\theta)E - \frac{2CE}{1 + |E|^2} + i\nabla^2 E, \tag{8}$$

where E is the normalized slowly varying complex envelope of the electrical field circulating within the optical cavity, E_i is the input field amplitude, θ is the detuning parameter, and C is a cooperative parameter. The homogenous steady state solutions (E_o) satisfy

$$E_i^2 = \left\{ \left(1 + \frac{2C}{1 + I}\right)^2 + \theta^2 \right\} I, \tag{9}$$

where $I = |E_o|^2$. The emergence of bistability in the model can be established by the conditions $d^2 E_i^2/d^2 I = dE_i^2/dI = 0$. The system exhibits bistability if $C > C_c$, where C_c is solution of $(C_c - 4)(1 + 2C_c^2) = 27\theta^2 C_c^2$, with a critical cavity intensity $I_c = (1 + 2C_c)/(C_c - 1)$. The system exhibits two symmetry-breaking instabilities at $I_T^\pm = C - 1 \pm \sqrt{C^2 - 4C}$. The critical wavenumber at both instabilities is $k_c = \sqrt{-\theta}$. Close to this point a Swift-Hohenberg equation, Eq. (1), has been established [9]. The critical wavenumber defines a critical wavelength $2\pi/k_c$, which is the half space between the stripes observed in the localized labyrinthine pattern, solution of Eq. (8), shown in Fig. 2.

C. Reaction-Diffusion model

Finally, reaction-diffusion systems are models of predilection for the study of dissipative structures and localized states. These models apply not only to chemical open reactors such as continuously stirred tank reactors (CSTR) but also to population dynamics such as population biology and epidemiology. In this context, the symmetry-breaking bifurcation is called the activation-inhibition instability. This bifurcation results from the competition between two-opposite processes: a short-range positive feedback due to an activator that favours the growth of fluctuations and a long-range negative feedback due to an inhibitor that neutralizes the activator's action. We choose the Edblom, Orban, and Epstein (EOE) model [10].

$$\begin{aligned}
\partial_t u &= -uv^2 + av - (1 + b)u + D\nabla^2 u \\
\partial_t v &= uv^2 - (1 + a)v + u + F + \nabla^2 v,
\end{aligned} \tag{10}$$

where the dimensionless variables u and v corresponds to HSO_3 and H^+ concentrations, respectively. a and b are reduced reaction rates, d is the ratio of the diffusion constants of u and v, and F is the dimensionless inflow of hydrogen ions. The homogenous steady states of Eq. (10), u_o and v_o, are solutions of

$$u_o = \frac{av_o}{v_o^2 + 1 + b}$$

$$\frac{av_o^3}{1 + b + v_o^2} - (1 + a)v_o + \frac{av_o}{1 + b + v_o^2} + F = 0. \tag{11}$$

In the case of $b = 1$ and $F = 7.65$ the system exhibits a S-shaped bifurcation diagram with a as the bifurcation parameter. The middle branch is always unstable. In the narrow range $a \in [16.95, 17.04]$ the model displays bistability of homogenous states, characterized by a hysteresis loop. To characterize pattern formation in this chemical model we perform a linear stability analysis. We make perturbations of finite wavenumber around the stable homogenous states, i.e.

$$\begin{pmatrix} u(\vec{r}, t) \\ v(\vec{r}, t) \end{pmatrix} = \begin{pmatrix} u_o \\ v_o \end{pmatrix} + \begin{pmatrix} \delta u \\ \delta v \end{pmatrix} e^{i\vec{k}\cdot\vec{r} + \sigma t}. \tag{12}$$

After introducing Eq. (12) into Eq. (10), we obtain the linearized problem

$$\sigma \begin{pmatrix} \delta u \\ \delta v \end{pmatrix} = \begin{pmatrix} -v_o^2 - 1 - b - Dk^2 & -2u_o v_o + a \\ v_o^2 + 1 & 2u_o v_o - 1 - a - k^2 \end{pmatrix} \begin{pmatrix} \delta u \\ \delta v \end{pmatrix}. \tag{13}$$

We impose $\sigma = \frac{\partial \sigma}{\partial k} = 0$ in the characteristic polynomial equation for σ and obtain the critical wavenumber,

$$k_c^2 = \frac{-v_c^2 - 1 - b + D(2u_c v_c - 1 - a_c)}{2D},\tag{14}$$

together with Eq. (11) the critical point(s) (a_c, v_c) can be obtained. We find, numerically, that in the two stable branches the Turing instability can arise. Note that, close to this critical point a non-variational Swift-Hohenberg model (Eq. (2)) has been established [6]. Eq. (14) defines a critical wavelength $2\pi/k_c$, which is the half space between stripes in the localized labyrinthine pattern in Fig. 2.

IV. INITIAL AND BOUNDARY CONDITIONS, AND GRID INDEPENDENCE OF LOCALIZED LABYRINTHINE PATTERNS

The nucleation process in the SHE model (1) is illustrated in Fig. 3. A circular patch of a diameter d is extracted from the center of a stable labyrinthine pattern. Then, it is embedded in the uniform solution u_{s+} in order to create the initial condition as shown in t_1 in Fig. 3. The localized labyrinthine pattern evolves towards an equilibrium until the temporal evolution of the Lyapunov Functional reaches a plateau, and the stable localized labyrinthine pattern emerges. The step-like descend of the Lyapunov Functional at early stages of the temporal evolution is related to the accomodation of defects in the frustrated labyrinthine pattern [2]. A similar procedure is used to generate the three-dimensional LLP.
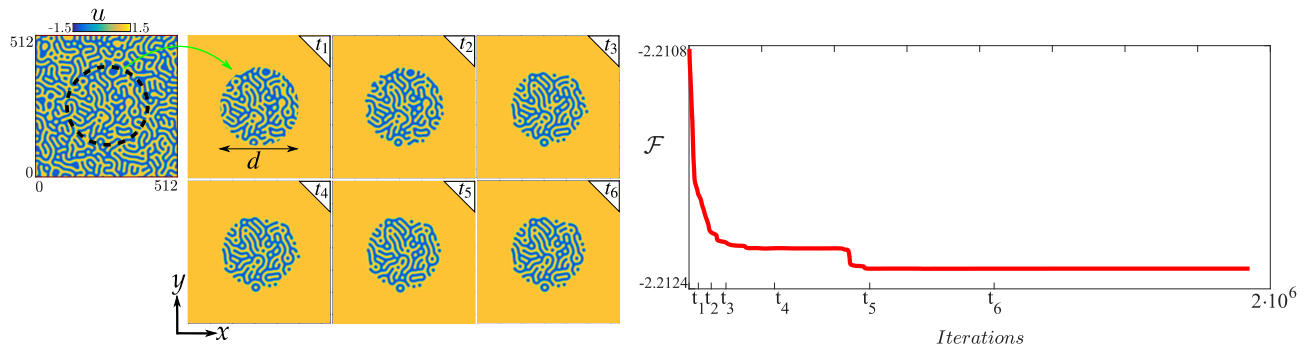
Figure 3: Creation and stabilization of a localized labyrinthine pattern in the SHE (1) with $\epsilon = 1.165$ and $\nu = 1$. The left panel shows an extended labyrinthine pattern in equilibrium. The dashed circle indicates the patch of labyrinthine pattern that is embedded in the uniform solution. The size is $d = 220$. The middle planel accounts for the evolution towards equilibrium of the localized labyrinthine pattern ($t_1 = 1$ to $t_6 = 10^6$, where $t_1 < t_2 < t_3 < t_4 < t_5 < t_6$). The red curve in the right panel shows the minimization of the Lyapunov Functional $\mathcal{F}$ during the stabilization of the localized labyrinthine pattern from the initial condition. See Supplementary Video 1 for the whole evolution.

In the SHE model (1), given an initial condition with a diameter d, LLP emerge as stable patterns when $d \lesssim d_c$. Figure 4 shows the total area of localized labyrinthine patterns $||u||^2$ for different initial conditions, considering the same initial extended labyrinthine pattern. There is a transition between LLP and extended labyrinthine patterns for $d_c \approx 12\lambda_c$. There is a finite size of stripes needed to localized the complex labyrinthine patterns. Also, there is a minimum size $d_o \approx 7\lambda_c$, which gives the minimum amount of wavelengths to form a non-trivial symmetry pattern.

All the two-dimensional localized labyrinthine patterns shown in the main text and here [cf. Fig. 2 and Fig. 3] are obtained using periodic boundary conditions. For completeness, we show that in the SHE model (1) the same localized complex pattern can be seen in numerical simulations using Dirichlet and Neumann boundary conditions [see Fig. 5]. All of these disordered localized patterns are obtained using the procedure described above. Also, we perform numerical simulations in the SHE model (1) varying the numerical grid discretization, Δx, to show the numerical robustness of LLP. These localized patterns are displayed in Fig. 6.
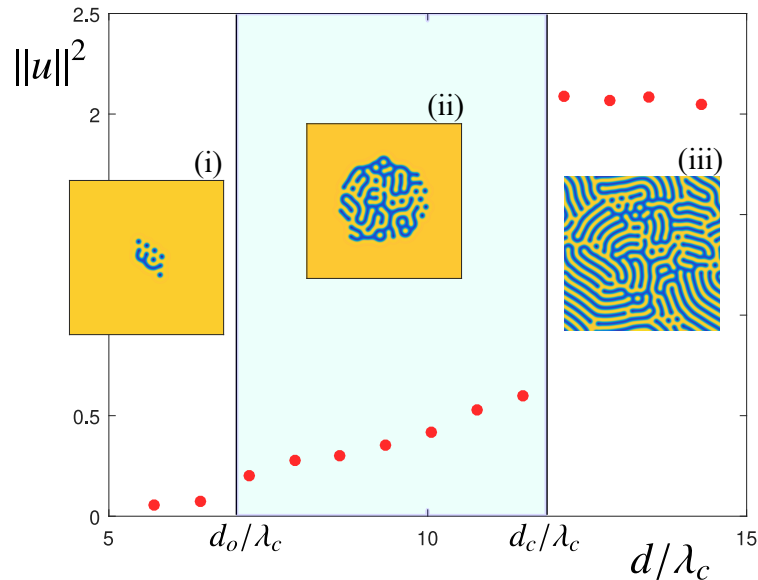
Figure 4: Transitions between (i) localized trivial symmetry patterns, (ii) localized non-trivial symmetry patterns, and (iii) extended labyrinthine patterns in the SHE model (1) with $\epsilon = 1.164$ and $\nu = 1$. $||u||^2$ is the area of the localized non-trivial symmetry patterns. The light blue shaded region accounts for the localized patterns with different degree of non-trivial simmetries exist. $d_o \approx 7\lambda_c$ and $d_c \approx 12\lambda_c$.
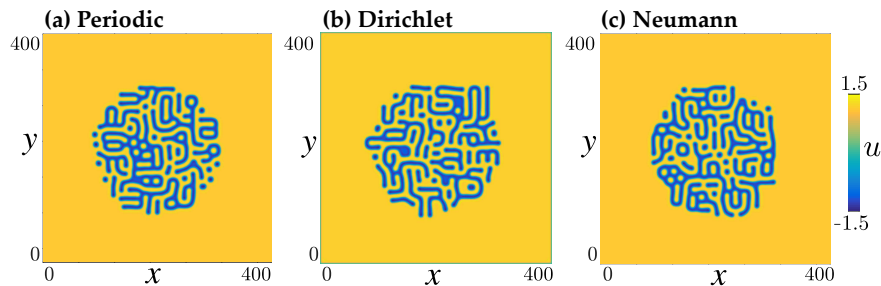
Figure 5: Different boundary conditions for the numerical simulations of localized labyrinthine patterns in the SHE (1) with $\epsilon = 1.175$ and $\nu = 1$. Periodic (a), Dirichlet (b), and Neumann (c) boundary conditions. The diameter of the initial condition is $d = 180$.
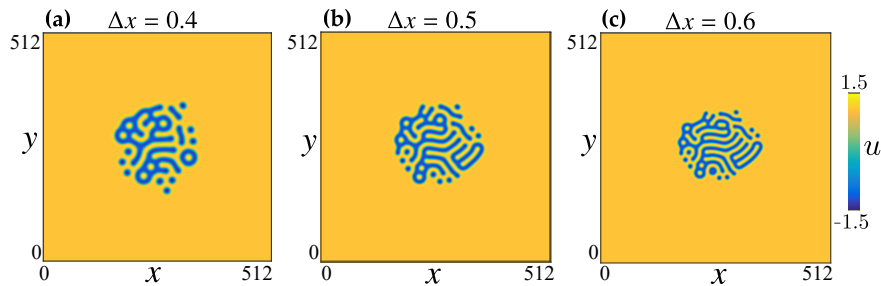
Figure 6: Localized labyrinthine patterns with different space discretizations Δx the SHE model (1) with $\epsilon = 1.162$ and $\nu = 1$. (a) $\Delta x = 0.4$, (b) $\Delta x = 0.5$, and (c) $\Delta x = 0.6$. The initial diameter is $d = 200$.

V.   GROWTH MECHANISM OF LOCALIZED LABYRINTHINE PATTERNS IN THE SWIFT-HOHENBERG EQUATION

Localized labyrinthine patterns, in the SHE model (1), are stable inside the pinning region delimited by ϵ_p^- and ϵ_p^+ as shown in Fig. 7, in which the square of the area supported by the localized labyrinthine patterns $||u||^2$ is plotted as a function of the bifurcation parameter ϵ. When varying ϵ within this region, transitions between different LLP

are possible due to shrinking or expansion of fingers (at the interface or inside the labyrinthine structure), and the accommodation of defects. Likewise, this shrinking process is accompanied by the appearance of circular spots and the disappearance of local domains of stripe patterns. Figure 7 shows four LLP along one stable branch generated by decreasing/increasing ϵ, starting from $\epsilon = \epsilon_{ic}$ [inset (i) in Fig. 7].
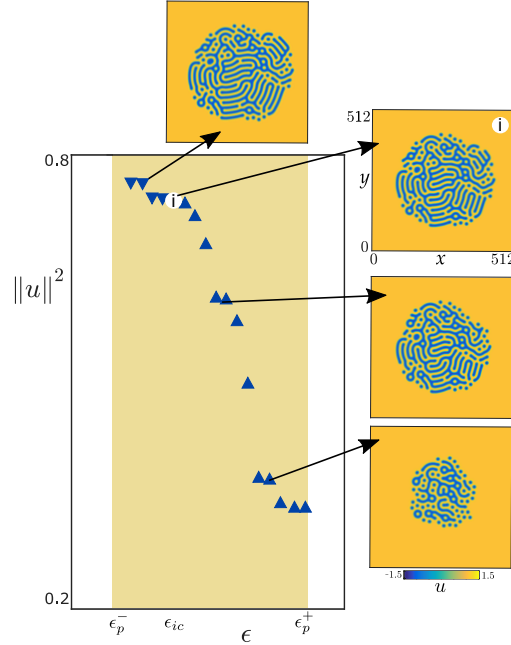
Figure 7: Localized labyrinthine patterns in the SHE model (1) along one stable branch (blue curve). The yellow shaded area with boundaries $\epsilon_p^- = 1.16$ and $\epsilon_p^+ = 1.19$ is the pinning region. Starting from the LLP in (i) at $\epsilon_{ic} = 1.17$, the bifurcation parameter is increased (upward triangles) and decreased (downward triangles).

[1] M. Le Berre, E. Ressayre, A. Tallet, Y. Pomeau, and L. Di Menza, Example of a chaotic crystal: The labyrinth, Phys. Rev. E **66**, 026203 (2002).

[2] S. Echeverria-Alar and M.G. Clerc, Labyrinthine patterns transitions, Phys. Rev. Research **2**, 042036(R) (2020).

[3] https://earth.google.com/web/search/3+58%2722.70%22+N+12+19%2705.84%22+E/@4.01617577,
12.34456541,712.00876556a,54068.64445182d,35y,-24.30467639h,3.78631196t,-0r/data=
CmAaNhIwGV1WF6alyA9AIRBcQMP2oihAKhwzIDU4JzIyLjcwIiBOIDEyIDE5JzA1LjgOIiBFGAIgASImCiQJRQp2zmWCDcARPzR0a9_
ADcAZXVIWd8BLPkAh6rEWsxw7PkA

[4] J. Swift and P.C. Hohenberg, Hydrodynamic fluctuations at the convective instability, Phys. Rev. A **15**, 319 (1977).

[5] M.G. Clerc, A. Petrossian, and S. Residori, Bouncing localized structures in a liquid-crystal light-valve experiment, Phys. Rev. E **71**, 015205 (2005).

[6] G. Kozyreff and M. Tlidi, Nonvariational real Swift-Hohenberg equation for biological, chemical, and optical systems, Chaos **17**, 037103 (2007).

[7] M. Tlidi, *et al. Lect. Notes Phys.* **751**, 381 (2008).

[8] J. von Hardenberg, E. Meron, M. Shachak, and Y. Zarmi, Diversity of Vegetation Patterns and Desertification, Phys Rev Lett **87** 198101 (2001).

[9] M. Le Berre, E. Ressayre, and A. Tallet, Why does a Ginzburg-Landau diffraction equation become a diffusion equation in the passive ring cavity?, A. Quantum Semiclass Opt **7**, (1995).

[10] E.C. Edblom, M. Orban, and I. R. Epstein, A New Iodate Oscillator: The Landolt Reaction with Ferrocyanide in a CSTR, J. Am. Chem. Soc. **108**, 2826 (1986).

4.1.   Perspectives

In this article, we have conceived the concept of localization of a non-trivial symmetry pattern. We believe that these spatial structures are a consequence of a complicated interplay between the pinning of defects in the bulk of the pattern and its complex-shaped interface. An interesting research avenue is to fully discover the bifurcation diagram of the localized labyrinthine patterns. As we have performed direct numerical simulations of the SH equation, we only have access to the stable equilibria. Then, the unstable branches of the labyrinthine patterns are hidden from us. Nowadays, sophisticated numerical continuation algorithms are used to reveal the unstable branches of localized solutions with trivial symmetries [144, 145, 146, 147, 148]. However, in the case of localized labyrinthine patterns, we think the problem is significantly more complicated as the presence of defects and curvature are synonymous with having various degrees of freedom to destabilize the labyrinths. Future work could be aimed to elaborate continuation algorithms for non-trivial symmetry patterns.

Chapter 5

Localised labyrinthine patterns in ecosystems (Scientific reports 11, 18331)

The formation of vegetation patterns in arid and semi-arid regions has motivated the scientific efforts of ecologists, engineers, biologists, mathematicians, and physicists [116, 44, 32, 117, 118, 119]. Until today, the question of how vegetation biomass self-organizes to survive under adverse climate conditions is a matter of debate [149]. In this and the following two chapters, we will contribute to this discussion by mainly focusing on localized and extended labyrinthine vegetation patterns.

In the previous chapter, we showed that in a well-established vegetation model [44, 50, 117, 56] localized labyrinthine patterns are stable. In the present chapter, we analyze satellite images from Google Earth [115] and discover that localized labyrinthine-like patterns are seen in different parts of the world (Central Cameroon, Southwest Niger, and Western Australia). Indeed, these localized patterns are a robust phenomenon. Furthermore, we perform numerical integrations of other types of vegetation models, such as non-local and reaction-diffusion equations, and conclude that the localized labyrinthine patterns are model-independent.

scientific reports

Check for updates

OPEN

Localised labyrinthine patterns in ecosystems

M. G. Clerc[1], S. Echeverría-Alar [1]✉ & M. Tlidi[2]

Self-organisation is a ubiquitous phenomenon in ecosystems. These systems can experience transitions from a uniform cover towards the formation of vegetation patterns as a result of symmetry-breaking instability. They can be either periodic or localised in space. Localised vegetation patterns consist of more or less circular spots or patches that can be either isolated or randomly distributed in space. We report on a striking patterning phenomenon consisting of localised vegetation labyrinths. This intriguing pattern is visible in satellite photographs taken in many territories of Africa and Australia. They consist of labyrinths which is spatially irregular pattern surrounded by either a homogeneous cover or a bare soil. The phenomenon is not specific to particular plants or soils. They are observed on strictly homogenous environmental conditions on flat landscapes, but they are also visible on hills. The spatial size of localized labyrinth ranges typically from a few hundred meters to ten kilometres. A simple modelling approach based on the interplay between short-range and long-range interactions governing plant communities or on the water dynamics explains the observations reported here.

The appearance of order and structures that involve nonequilibrium exchanges of energy and/or matter have been widely observed in many natural systems including fluid mechanics, optics, biology, ecology, and medicine[1–6]. Vegetation populations and vegetation patterns belong to this field of research. Being often undetectable at the soil level, large-scale vegetation patterns have been first observed thanks to the usability of aerial photographs in the early fifties[7]. They appear as extended bands of vegetation alternating periodically with vegetated areas and unvegetated bands. These large-scale botanical organisations have been reported in many semi-arid and arid ecosystems of Africa, Australia, America, and Asia. It is now widely admitted that the origin of these large scale botanical organisations is attributed to a nonequilibrium symmetry-breaking instability leading to the establishment of stable periodic spatial patterns. Extended and periodic vegetation pattern arising in semi-arid and arid ecosystems has been the subject of numerous studies and is by now fairly well-understood issue (see recent overviews[8–10] and references therein).

Vegetation patterns are not always periodic and extended in space. They can be spatially localised and aperiodic consisting of isolated or randomly distributed patches on bare soil[11–13] or gaps embedded in a uniform vegetation cover[14,15]. They are generated in a regime where the homogeneous cover coexists with periodic vegetation patterns. The interaction between well-separated patches is always repulsive[16,17] while for gaps the interaction alternates between attractive and repulsive depending on the distance separating gaps[14,17]. The localised patches has a more or less circular shape. However, for a moderate aridity condition, the circular shape can exhibit deformation followed by splitting of a single into two new patches. Newer patches will in their turn exhibit deformation and self-replication[18–20] until the system reaches a periodic distribution of patches that occupies the whole space available in landscapes[19,20]. This process leading to spotted periodic patterns can be seen as warnings of ecosystem degradation and may lead to outcome of vegetation recovery. Besides patches self-replication, circular spots can exhibit deformation leading to the formation of arcs and spirals like in isotropic and uniform environmental conditions[21]. The vegetation spirals are not waves since they do not rotate[21].

In this work, we unveil a new type of vegetation pattern consisting of a localised labyrinth embedded either in a homogeneous cover or surrounded by bare soil. This phenomenon is observed in Africa and Australia by remote sensing imagery. An example of such a botanical self-organisation phenomenon is shown in Fig. 1. They consist of either an irregular distribution of vegetation surrounded by a uniform cover (see Fig. 1a, b), or by a bare state (Fig. 1c, d). We show that localised labyrinths embedded in a uniform cover can be stable even if the environment is isotropic and their formation does not depend on the topography. However, when a localised labyrinth is surrounded by a bare state, they can expand or shrink. We analyse this phenomenon by using three

[1]Departamento de Física and Millennium Institute for Research in Optics, Facultad de Ciencias Físicas y Matemáticas, Universidad de Chile, Casilla 487-3, Santiago, Chile. [2]Département de Physique, Faculté des Sciences, Université Libre de Bruxelles (U.L.B.), CP 231, Campus Plaine, 1050 Brussels, Belgium. ✉email: sebastianecheverria@ug.uchile.cl
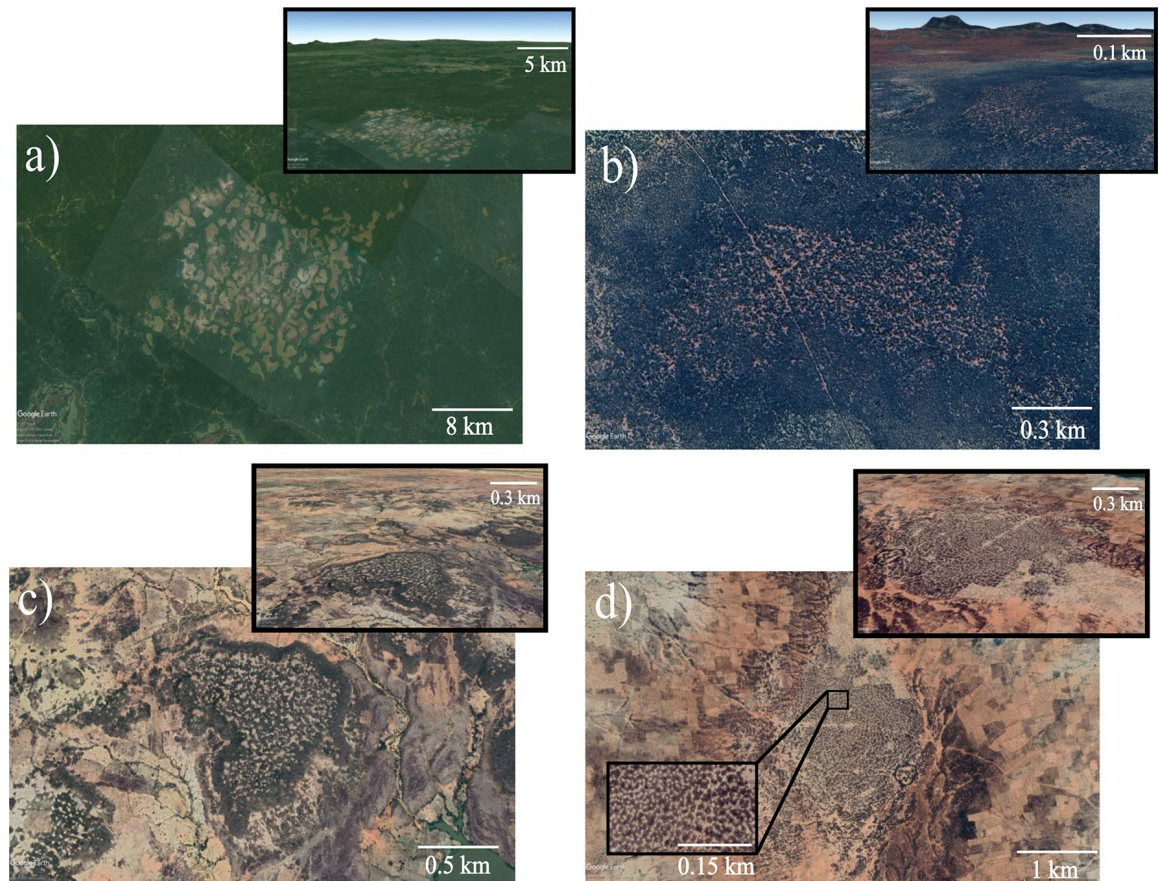
Figure 1. Localised labyrinth vegetation patterns. Top views of (**a**) Central Cameroon (3° 59′ 22.05″ N 12° 17′ 20.99″ E), (**b**) Western Australia (29° 33′ 36.16″ S 117° 15′ 32.60″ E), (**c**) and (**d**) Southwest Niger (12° 34′ 45.10″ N 2° 41′ 28.71″ E and 12° 22′ 6.72″ N 3° 28′ 39.35″ E, respectively). The inset (**d**) show a zoom of the characteristic labyrinth pattern. All the images were retrieved from Google Earth software (https://earth.google.com/web/) with a resolution of 1920 × 1080 pixels (total areas of (**a**) 196.5 km^2, (**b**) 7.4 km^2, (**c**) 12.3 km^2, and (**d**) 24.6 km^2). The satellite images were taken on 17 of February, 2021; 22 of September, 2018; 15 of November, 2016; and 12 of February, 2020, respectively. The upper-right insets show the localised patterns to emphasize the topography of the landscape.

well-known self-organisation vegetation models, which support localised labyrinths. We show that localised labyrinths are permanent structures, and they can be observed worldwide involving a range of species and spatial scales. We interpret this phenomenon as a spatial compromise between the extended labyrinth that occupies the whole space available and stable homogeneous states. More precisely, the mechanism leading to their formation is attributed to the pinning-depinning transition that takes place in a parameter space where models exhibit bistability between extended disordered pattern and homogeneous cover.

Field observations of localised labyrinths

Localised labyrinths observed in nature are large-scale self-organisation patterns. They are satellite images from Africa and Australia obtained by the use of Google Earth software. The landscape of Central Cameroon (zone of forest-savanna mosaic[22]), shown in Fig. 1a, displays contrasted phases of bare and densely vegetated areas with well-defined scale and symmetry surrounded by more or less uniform woodland. The climate in the zone where we observe the localised labyrinth is humid, with annual averaged precipitation of 1800 mm[23]. The annual averaged of potential evapotranspiration is between 1500 and 1600 mm[24]. The localised labyrinth we observe in Western Australia (see Fig. 1b) consists of localised woodland embedded in the shrubland of Mulga Bush (Acacia Aneura)[25]. In this zone the climate is arid, where the mean annual precipitation is 250 mm[26] and the mean annual potential evapotranspiration is between 1200 and 1300 mm[27]. Besides, the localised labyrinth can be surrounded by bare zones as shown in landscapes of Southwest Niger in a brush-grass Savanna zone[28] (Fig. 1c, d). In this region the climate is semi-arid, the mean annual rainfall is 605 mm, in between June and September[29], and the annual mean potential evapotranspiration near this zone is 1900 mm[30]. All the climate data is summarized in Table 1 in Methods section. Sparsely populated or bare areas alternate with dense vegetation irregular bands or patches made of microchloa Indica. The field observations suggest that localised labyrinthine structures are formed both in a flat landscape and with topographic variation (see Fig. 2). By their spatial regularity, by their spatial scales ranging from a few hundred meters to ten kilometres, as well as by the composition of their vegetation (tree, shrubs, herbs, and grasses), localised labyrinthine patterns are permanent structures, and they
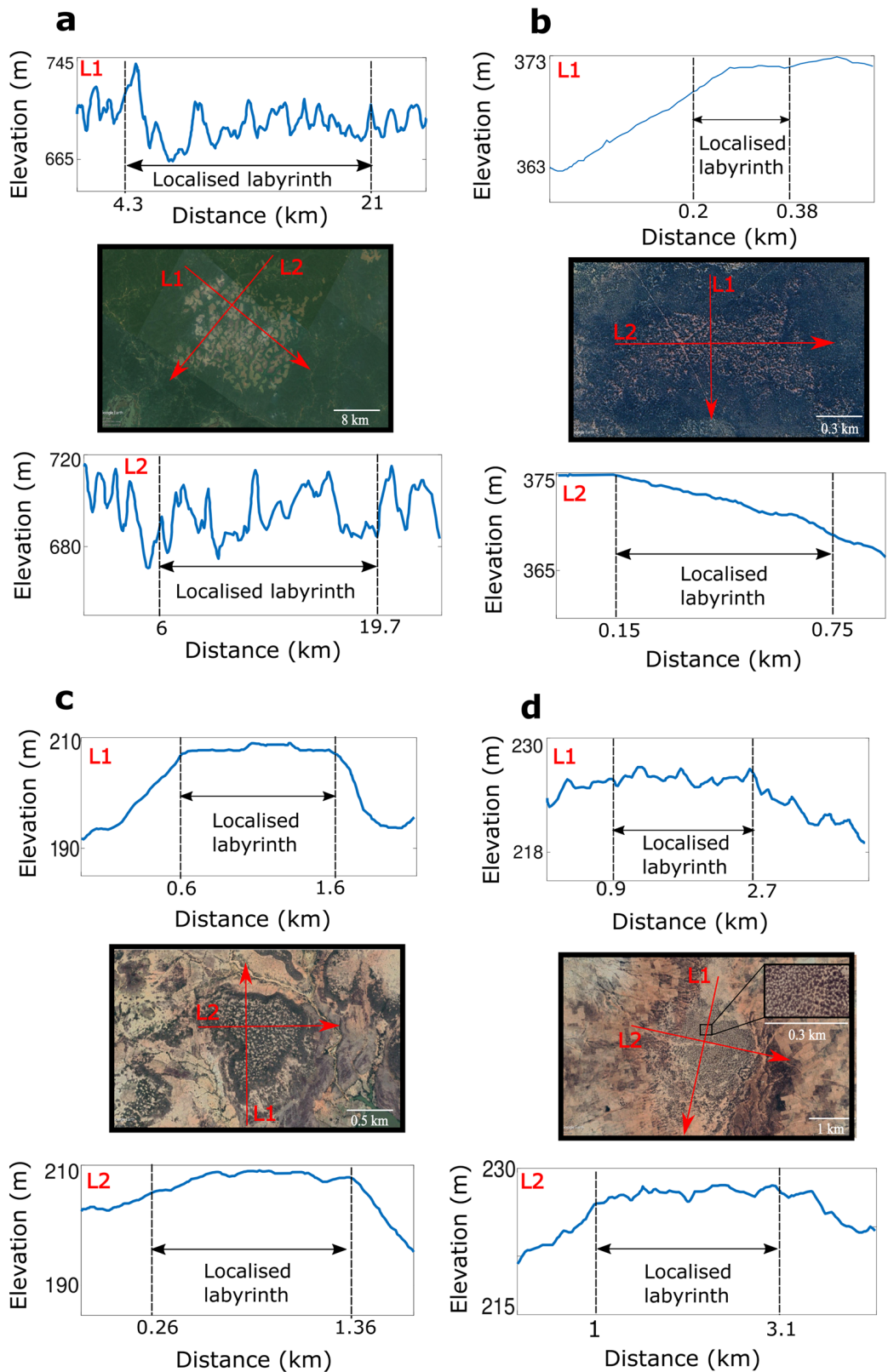
Figure 2. Elevation profiles of the localised labyrinths observed in nature (Fig. 1). They were obtained using Google Earth software (https://earth.google.com/web/). In each zone two elevation profiles are shown for two arbirtary cross-sections (L1 and L2). (**a**) The localised labyrinth in central Cameroon has large fluctuations in height ranging from 665 to 745 m. The homogenous cover that surrounds the localised labyrinth also has fluctuations in height of the same order. The size of the major axis of the localised pattern is 16.7 km. (**b**) In Western Australia the localised labyrinth is in a gentle slope (0.8%), the size of its major axis is 0.6 km. (**c**) and (**d**) shows the elevation profiles of the localised labyrinths in Southwest Niger. Both patterns are in small hills of about 10 m, surrounded by a bare state. These localised labyrinths emerge in plain terrains. The sizes of the major axes are 1.0 km and 2.0 km, respectively. See the "Methods" section for details on the accuracy of the elevation data.

can be observed even in non-arid climates. They have neither been observed nor reported. Understanding their formation and maintenance is an important ecological issue.

The mechanism underlying the emergence of the localised labyrinth can be captured by using self-organisation mathematical models that can explain vegetation pattern formation within a unified conceptual framework. In this respect, two approaches will be used. The first is based on the relationship between the plants' aerial-subterranean structures, the facilitative and competitive feedbacks which act at the community level, and the plants' spatial propagation by seed dispersion[31,32]. The second approach incorporates explicitly water transport by below ground diffusion and/or above ground run-off[33–35]. These models are in reasonable agreement with the field observations[36–38].

Mathematical modelling of ecosystems

The absence of the first principles for biological systems in general, and in particular for vegetation populations where phenomena are interconnected makes their mathematical modelling complex. The theory of vegetation pattern formation rests on the self-organisation hypothesis and symmetry-breaking instability that provoke the fragmentation of the uniform cover. The symmetry-breaking instability takes place even if the environment is isotropic[31,33,35]. This instability may be an advection-induced transition that requires the pre-existence of the environment anisotropy due to the topography of the landscape[34,39,40]. Generally speaking, this transition requires at least two feedback mechanisms having a short-range activation and a long-range inhibition. In this respect, we consider three different vegetation models that are experimentally relevant systems: (i) the generic interaction-redistribution model describing vegetation pattern formation which incorporates explicitly the facilitation, competition and seed dispersion nonlocal interactions (ii) the local nonvariational partial differential model described by a nonvariational Swift–Hohenberg type of model equation, and (iii) the reaction–diffusion system that incorporate explicitely water transport.

The interaction-redistribution approach. *The integrodifferential model.* This approach consists of considering a well-known logistic equation with nonlocal plant-to-plant interactions. Three types of interactions are considered: the facilitative $M_f(\mathbf{r}, t)$, the competitive $M_c(\mathbf{r}, t)$, and the seed dispersion $M_d(\mathbf{r}, t)$ nonlocal interactions. To simplify further the mathematical modelling, we consider that the seed dispersion obeys a diffusive process $M_d(\mathbf{r}, t) \approx \nabla^2 b(\mathbf{r}, t)$, with D the diffusion coefficient, b the biomass density, and $\nabla^2 = \partial^2/\partial x^2 + \partial^2/\partial y^2$ is the Laplace operator acting in the (x,y) plane. The interaction-redistribution reads

$$M_i = exp\left\{ \frac{\xi_i}{N_i} \int b(\mathbf{r} + \mathbf{r}', t)\phi_i(r, t)d\mathbf{r}' \right\}, \text{ with } \phi_i(r, t) = exp(-r/L_i) \tag{1}$$

where $i = f, c$. ξ_i represents the strength of the interaction, N_i is a normalisation constant. We assume that their Kernels $\phi_i(r, t)$ are exponential functions with L_i the range of their interactions. The facilitative interaction $M_f(\mathbf{r}, t)$ favouring vegetation development. They involve the accumulation of nutrients in the neighbourhood of plants, the reciprocal sheltering of neighbouring plants against climatic harshness which improves the water budget in the soil. The range of the facilitative interaction L_f operates on the crown size. The competitive interaction operates over a length L_c and involves the below-ground structures, i.e., the rhizosphere. In nutrient-poor or/and in water-limited territories, lateral spreading may extend beyond the radius of the crown. This extension of roots relative to their crown size is necessary for the survival and the development of the plant in order to extract enough nutrients and/or water from the soil. When incorporating these nonlocal interactions in the paradigmatic logistic equation, the spatiotemporal evolution of the normalised biomass density $b(\mathbf{r}, t)$ in isotropic environmental conditions reads[14]

$$\partial_t b(\mathbf{r}, t) = b(\mathbf{r}, t)[1 - b(\mathbf{r}, t)]M_f(\mathbf{r}, t) - \mu b(\mathbf{r}, t)M_c(\mathbf{r}, t) + D\nabla^2 b(\mathbf{r}, t). \tag{2}$$

The normalisation is performed with respect to the total amount of biomass supported by the system. The first two terms in the logistic equation with nonlocal interaction Eq. (2) describe the biomass gains and losses, respectively. The third term models seed dispersion. The aridity parameter μ accounts for the biomass loss and gain ratio, which depends on water availability and nutrients soil distribution, topography, etc. The homogeneous cover solutions of Eq. (2) are: $b_o = 0$ which corresponds to the state totally devoid of vegetation, and the homogeneous cover solutions satisfy the equation

$$\mu = (1 - b) \exp(\Delta b), \tag{3}$$

with $\Delta = \xi_f - \xi_c$ measures the community cooperativity if $\Delta > 0$ or anti-cooperativity when $\Delta < 0$. The bare state $b_o = 0$ is unstable (stable) $\mu < 1(\mu > 1)$. The homogeneous cover state with higher biomass density is stable and the other is unstable. These solutions are connected by a saddle-node or a tipping point whose coordinates are given by $\left\{ b_{sn} = (\Delta - 1)/\Delta, \mu_{sn} = e^{\Delta - 1}/\Delta \right\}$. The linear stability analysis of vegetated cover (b_s) with respect to small fluctuations of the from $b(\mathbf{r}, t) = b_s + \delta b\, exp\{\sigma t + i\mathbf{k} \cdot \mathbf{r}\}$ with δb small, yields the dispersion relation

$$\sigma(k) = \left(b_s(1 - b_s)\xi_f - b_s - \frac{b_s(1 - b_s)\xi_c}{(1 + L_c^2 k^2)^{3/2}} \right) e^{\xi_f b_s} - Dk^2. \tag{4}$$

Given the spatial isotropy, the growth rate $\sigma(k)$ is a real quantity. This eigenvalue may become positive for a finite band of unstable modes which triggered the spontaneous amplification of spatial fluctuations towards the formation of periodic structures with a well-defined wavelength. At the symmetry-breaking instability the value of the critical wavenumber k_c marking the appearance of a band of unstable modes, and hence the symmetry-breaking

instability, can be evaluated by two conditions: $\sigma(k_c) = 0$ and $\partial\sigma/\partial k|_{k_c} = 0$. These conditions yield the most unstable mode

$$k_c^2 = \frac{1}{L_c^2}\left[\left(\frac{3b_s e^{\xi_f b_s}(1-b_s)\xi_c L_c^2}{2D}\right)^{2/5} - 1\right]. \tag{5}$$

This critical wavenumber determines the wavelength of the periodic vegetation pattern $2\pi/k_c$ that emerges from the symmetry-breaking instability. Replacing k_c in the condition $\sigma(k_c) = 0$, we can then calculate the critical biomass density b_c. The corresponding critical aridity parameter μ_c is provided explicitly by the homogeneous steady states Eq. (3).

Local model: a nonvariational Swift–Hohenberg model. The integrodifferential equation (2) can be reduced by means of a multiple-scale analysis to a simple partial differential equation, in the form of nonvariational Swift–Hohenberg equation. This reduction has been performed in the neighbourhood of the critical point associated with the nascent bistability[14,32]. The coordinates of the critical point are: the biomass density $b_c = 0$, the cooperativity parameter $\Delta_c = 1$, and the aridity parameter $\mu_c = 1$. These coordinates are obtained from Eq. (3) by satisfying the double condition $\partial\mu/\partial b_s = 0$ and $\partial^2\mu/\partial b_s^2 = 0$. To apply a multiple-scale analysis it is necessary to define a small parameter that measures the distance from criticality and expand b, μ, and Δ in the Taylor series around their critical values. The symmetry-breaking instability should be close to that critical point. To fulfil this condition, we must consider a small diffusion coefficient in order to include the symmetry-breaking instability in the description of the dynamics of the biomass density. This reduction is valid in the double limit of nascent bistability and close to the symmetry-breaking instability. In this double limit, the time-space evolution of biomass density obeys a non-variational Swift–Hohenberg model[14]

$$\partial_t u(\mathbf{r},t) = -u(\mathbf{r},t)(\eta - \kappa u(\mathbf{r},t) + u(\mathbf{r},t)^2) + [\nu - \gamma u(\mathbf{r},t)]\nabla^2 u(\mathbf{r},t) - \alpha u(\mathbf{r},t)\nabla^4 u(\mathbf{r},t), \tag{6}$$

where η and κ are, respectively, the deviations of the aridity and cooperativity parameters from their values at the critical point. The linear and nonlinear diffusion coefficients ν, γ, and α depend on the shape of kernels[17]. In addition to the bare state $u = 0$, the homogeneous covers obey

$$u_{\pm} = \frac{\kappa \pm \sqrt{\kappa^2 - 4\eta}}{2}, \tag{7}$$

where the two homogeneous solutions $u_{\pm}$ are connected through the saddle-node bifurcation $\{u_{sn} = \kappa/2, \eta_{sn} = \kappa^2/4\}$, with $\kappa > 0$. The solution u_- is always unstable even in the presence of small spatial fluctuations. The linear stability analysis of vegetated cover (u_+) with respect to small spatial fluctuations, yields the dispersion relation

$$\sigma(k) = u_+(\kappa - 2u_+) - (\nu - \gamma u_+)k^2 - \alpha u_+ k^4. \tag{8}$$

Imposing $\partial\sigma/\partial k|_{k_c} = 0$ and $\sigma(k_c) = 0$, the critical mode can be determined

$$k_c = \sqrt{\frac{\gamma - \nu/u_c}{2\alpha}}, \tag{9}$$

where u_c satisfies $4\alpha u_c^2(2u_c - \kappa) = (2\gamma u_c - \nu)^2$. The corresponding aridity parameter η_c can be calculated from Eq. (7).

The reaction–diffusion approach.

The second approach explicitly adds the water transport by below ground diffusion. The coupling between the water dynamics and the plant biomass involves positive feedbacks that tend to enhance water availability. Negative feedbacks allow for an increase in water consumption caused by vegetation growth, which inhibits further biomass growth.

The modelling considers the coupled evolution of biomass density $b(\mathbf{r}, t)$ and groundwater density $w(\mathbf{r}, t)$. In its dimensionless form, this model reads[33]

$$\frac{\partial b}{\partial t} = \frac{\gamma w}{1 + \omega w}b - b^2 - \theta b + \nabla^2 b, \tag{10}$$

$$\frac{\partial w}{\partial t} = p - (1 - \rho b)w - w^2 b + \delta\nabla^2(w - \beta b). \tag{11}$$

The first term in the first equation describes plant growth at a constant rate (γ/ω) that grows linearly with w for dry soil. The quadratic nonlinearity $-b^2$ accounts for saturation imposed by poor nutrients soil. The term proportional to θ accounts for mortality, grazing or herbivores. The mechanisms of dispersion are modelled by a simple diffusion process. The groundwater evolves due to a precipitation input p. The term $(1 - \rho b)w$ in the second equation accounts for the evaporation and drainage, that decreases with the presence of vegetation. The term $w^2 b$ models the water uptake by the plants due to the transpiration process. The groundwater movement follows the Darcy's law in unsaturated conditions; that is, the water flux is proportional to the gradient of the water matric potential[41]. The matric potential is equal to w, under the assumption that the hydraulic diffusivity

	Precipitation (mm)	Potential evapotranspiration (mm)	Aridity index	Classification
Central Cameroon	1800	1500–1600	1.1–1.2	Humid
Western Australia	250	1200–1300	0.1–0.2	Arid
Southwest Niger	605	1900	0.3	Semi-arid

Table 1. Mean annual precipitation, potential evapotranspiration, and aridity index of the regions where localised labyrinthine patterns are observed. For more details on the meteorological data see the references given in the text.

is constant[41]. To model the suction of water by the roots, a correction to the matric potential is included; $-\beta b$, where β is the strength of the suction.

Results

Localised labyrinthine vegetation pattern. In our analysis, we focus on the simplest vegetation model that has been derived from the interaction-redistribution approach, namely the non-variational Swift–Hohenberg Eq. (6) described above. This model is appropriate to describe the space-time dynamics of the biomass under resource-limited landscapes such as nutrient limitation or water deprivation. In this case, the average biomass density is low comparing the carrying capacity closed-packing density of unstressed vegetation. The simulated stationary localised vegetation labyrinth is shown in Fig. 3a. Moreover, to confirm the field observation and to show that this phenomenon is model-independent, we conducted numerical simulations of the other two models, the integrodifferential (Eq. (2)) based on the facilitative, competitive, and seed dispersion interactions; and the reaction–diffusion type that explicitly incorporates water transport (Eq. (11)). The results are shown in Fig. 3b and 3c. The parameters used to simulate the different localised labyrinths are listed in Tables 2, 3, and 4 in the "Methods" section. The localised labyrinth consists of one spatially disordered state surrounded by a qualitatively different state. Note that the localised labyrinthine patterns shown in Fig. 3 do not have a round shape. The fact that this shape is not round is attributed to the presence of defects in the disordered pattern since they modify the interface energy. Investigations of fronts propagation between labyrinths and homogeneous states mediated by defects are missing in the literature. The interface separating these two states is stationary leading to a fixed size of a localised labyrinth. It neither grows and invades the uniform cover nor shrinks. The stabilization of localised labyrinth is attributed to the interface pinning phenomenon[42,43]. This phenomenon is characterized by an interface that connects a homogeneous state and a periodic one, which is motionless on a finite region of parameters, pinning range. This pinning effect occurs due to the competition between a global energy symmetry breaking between states that favors the interface propagate in one direction and the spatial modulations that block the interface by introducing potential barriers[42].

To determine the stability domain of the localised labyrinth, we establish the bifurcation diagram shown in Fig. 4a, where we plot the biomass density as a function of the aridity parameter η. The aridity refers not only to water scarcity but can be also attributed to the nutrient-poor soil. When the aridity is low obviously the uniform vegetated state is stable (blue line) and the bare state (broken line) is unstable. When the aridity parameter is further increased, the homogeneous cover becomes unstable with respect to small fluctuations. Above this symmetry-breaking instability, several branches of solutions emerge sub-critically for $\eta < \eta_c$. Example of vegetation patterns that appears follows the well-known sequence made sparse vegetation spots that can be either periodic or localised in space (see i, Fig. 4a), banded vegetation (see ii, Fig. 4a) or a periodic distribution of localised patches setting on the bare state (see iii, Fig. 4a).

An extended labyrinthine pattern can be generated subcritically as indicated by the red line in the bifurcation diagram (see Fig. 4a). The situation which interests us requires that this extended labyrinth exhibits a coexistence with the uniform vegetated state. The coexistence between these two qualitatively different states is the prerequisite condition for the formation of a stable localised labyrinth. However, this condition is necessary but not sufficient, the interface separating these two states exhibits a pinning phenomenon[42]. Indeed, as shown in the inset of Fig. 4a, there exists a finite range of the aridity parameter often called the pinning zone $\eta_p^- < \eta < \eta_p^+$, where localised labyrinthine patterns are stable. Examples of localised labyrinth obtained by numerical simulations for fixed values of the control parameters are shown in Fig. 4a (iv, v, vi). The motionless interface is not necessarily circular, and contains bands perpendicular to it and circular patches. Similar bifurcation diagram is obtained from the integrodifferential model (see Fig. 4b).

Finally, we discuss the situation where the aridity is not homogenous due to the topography. For this purpose, we choose a top hat-like shape for the aridity parameter as shown in Fig. 5a. In this case, numerical simulations of the integrodifferential model Eq. (2) show a stable localised labyrinthine pattern (see Fig. 5a). Note that the localised labyrinthine structures surrounded by bare soil shown in Fig. 1c, d are unstable since the interface propagates. The interface can not be pinned in the absence of spatial oscillations around the bare state. Oscillations around this state are unphysical since the biomass density is a positive defined quantity. However, when the aridity parameter possesses an inverted top hat-like shape, it is possible to pin the interface (see Fig. 5b). In this case, the localised labyrinthine pattern is surrounded by a mosaic extended state, and the mechanism of stabilization is rather due to the inhomogeneity of the aridity parameter.

Deppining mechanism. The spatial location of the localised labyrinth immersed in the bulk of the stable uniform vegetated state depends on the initial condition considered. When ecosystems operate out of the pin-
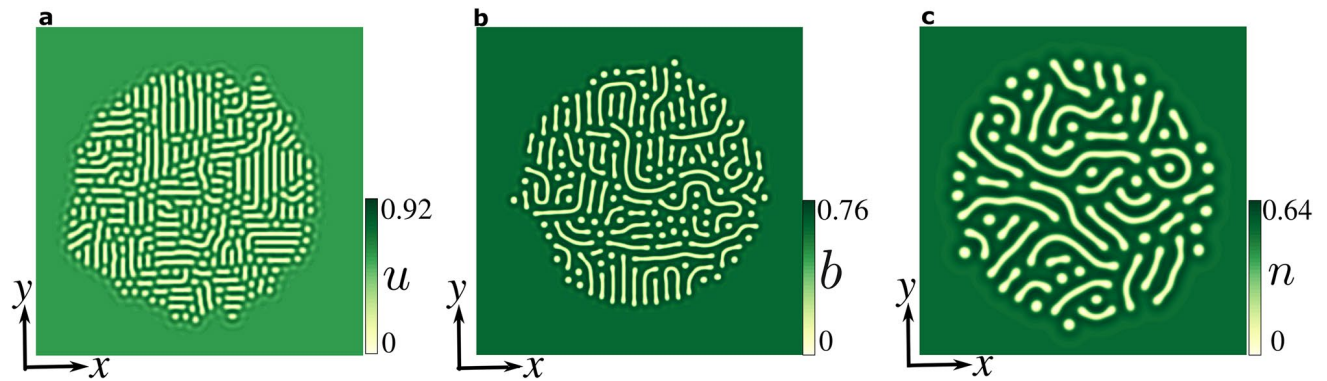
Figure 3. Numerical observations of localised labyrinths. The model-independent structure is observed in (**a**) a non-variational Swift–Hohenberg model, (**b**) integrodifferential non-local model, and (**c**) reaction–diffusion model. In the three cases the labyrinth is supported by a uniform vegetated state. The parameters used in each model are listed in the "Methods" section. From numerical simulations, the figure was created using Inkscape 1.0 (https://inkscape.org/release/inkscape-1.0/).

Cooperativity (κ)	ν	γ	α	Time step (Δt)	Space step (Δx)
0.6	0.011	0.5	0.125	0.05	0.8

Table 2. List of parameter values of the simulations of the non-variational Swift–Hohenberg equation, shown in Fig. 3a (200×200 grid, $\eta = 1.01$), Fig. 4a (120×120 grid, [i, ii, iii] with space step $\Delta x = 0.5$), and Fig. 6 (120×120 grid).

Competition length (L_c)	Diffusion (D)	Facilitation strength (ξ_f)	Competition strength (ξ_c)	Time step (Δt)	Space step (Δx)
2.5	1	3	1	0.1	0.8

Table 3. List of parameter values of the simulations of the integrodifferential model, shown in Fig. 3b (512×512 grid, $\mu = 1.301$), Fig. 4b (256×256 grid), and Fig. 5 (256×256 grid).

γ	ω	θ	p	ρ	δ	β	Time step (Δt)	Space step (Δx)
1.45	1.5	0.2	0.7	1.5	100	2.7	0.001	0.6

Table 4. List of parameter values of the simulation of the reaction–diffusion model, shown in Fig. 3c (512×512 grid).

ning zone, the interface separating the labyrinth and the homogeneous cover propagates due to the depinning transition (see Fig. 6a, b). In this case, depending on the aridity level, the interface propagates from one stable state to another The transition is different when moving the aridity parameter slowly or abruptly. In the second type of variation, when $\eta < \eta_p^-$, the homogeneous cover invades the system, while when $\eta > \eta_p^+$, the localised labyrinth survives but it is now embedded by a periodic distribution of gaps (see Fig. 6b).

Conclusions

In this paper we have reported for the first time evidence of localised labyrinthine vegetation patterns observed on satellite images from Africa and Australia. We have shown that these localised structures are robustly consisting of either an irregular distribution of vegetation surrounded by a uniform cover or on the contrary surrounded by a bare state. We have shown that the formation of localized labyrinthine patterns is not specific to particular plants or soils. We have found localised labyrinths in ecosystems on flat landscapes and hills. Three relevant models which undergo localised vegetation labyrinthine patterns have been considered; (i) vegetation interaction-redistribution model of vegetation dynamics, which can generate patterns even under strictly homogeneous and isotropic environmental conditions. It is grounded on a spatially explicit formulation of the balance between facilitation and competition. Ecosystems experience transitions towards landscape fragmentation of landscapes (ii) the nonvariational Swift–Hohenberg model that can be derived from the model (i) in the long-wavelength pattern forming regime, and (iii) reaction–diffusion model that incorporates explicitly water transport. We have shown that all these models despite their mathematical structure support the phenomenon
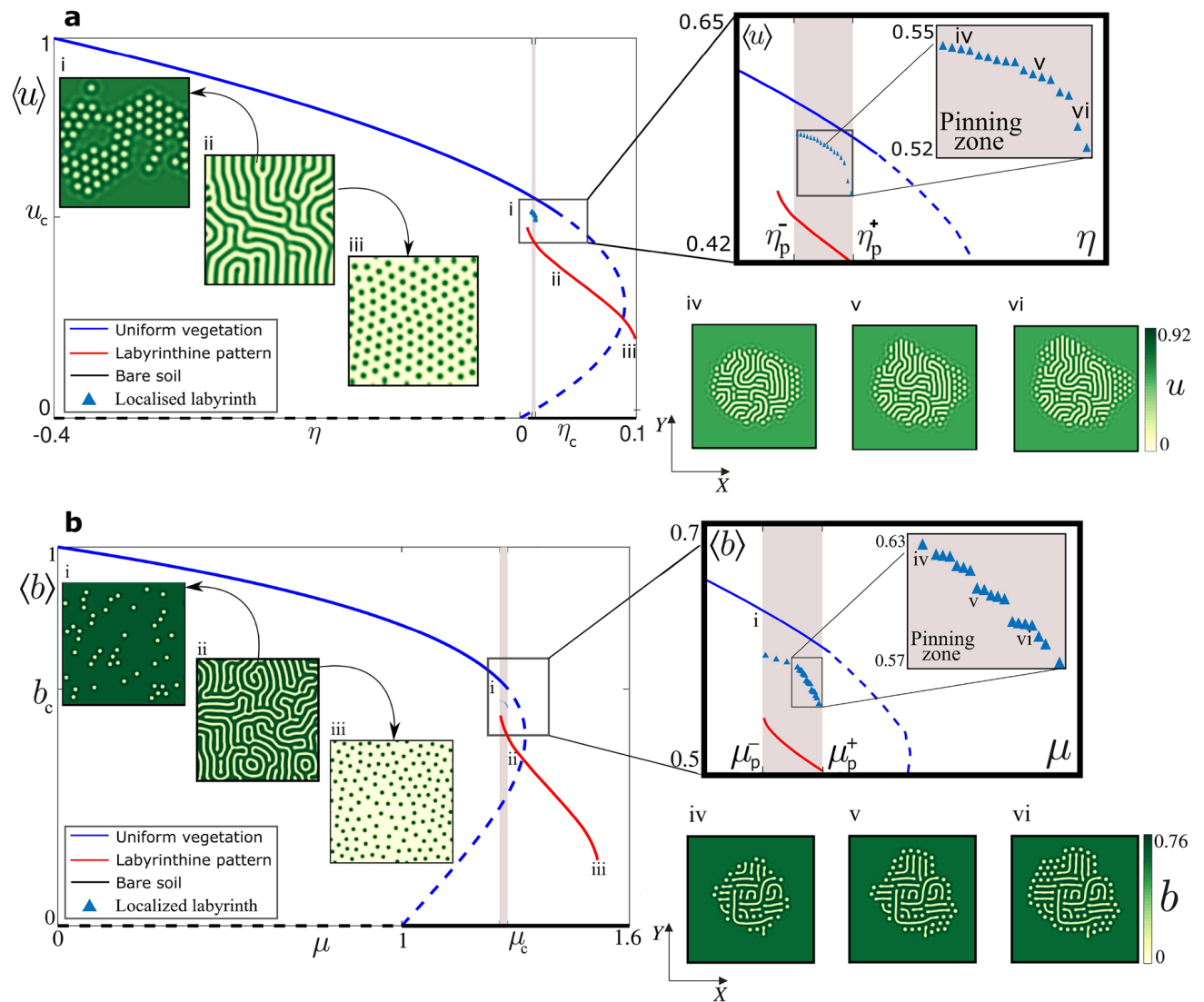
Figure 4. Bifurcation diagram of vegetation models. (**a**) the non-variational Swift–Hohenberg model, and (**b**) the integrodifferential model. Gaps (i), labyrinths (ii), and spots (iii) is the standard sequence of patterns in vegetation models. $\langle u \rangle$ and $\langle b \rangle$ stands for the average biomass in each model. The solid curves indicate where the bare soil or uniform vegetation cover are stable, whereas the segmented curves indicate where these states are unstable. In (**a**), the critical point ($\eta_c = 0.038$, $u_c = 0.53$) stands for the instability threshold where the uniform vegetated cover loses stability to a modulated state. In a narrow region, between $\eta_p^- = 0.010$ and $\eta_p^+ = 0.013$, where there is a multistability of states (labyrinth, uniform vegetation, bare soil) the emergence of localized labyrinths is possible. In (**b**), ($\mu_c = 1.309$, $b_c = 0.62$) and $\mu_p^- = 1.2950$, $\mu_p^+ = 1.3044$. The insets with the pinning zones enlarged show the existence of a family of localized labyrinths (triangles) with different average biomasses. The insets (iv), (v), and (vi) show different localized labyrinthine patterns [(**a**) and (**b**)]. The other parameters are provided in the "Methods" section. From numerical simulations, the figure was created using Inkscape 1.0 (https://inkscape.org/release/inkscape-1.0/).

of the localised labyrinth. We have established their bifurcation diagram and identified a parameter region, where we have observed a coexistence between a homogeneous cover and an extended labyrinthine structure which are both linearly stable. Within it, there exist a pinning zone of parameters where localised labyrinthine vegetation patterns have been generated as a stable pattern. Note however that localised labyrinth is determined by the initial condition, while their maximum peak biomass remains constant for a fixed value of the system parameters. This phenomenon results from front pinning between qualitatively different coexisting vegetation states. Outside of the pinning region, we have shown that the localised labyrinth either shrink and leads to the formation of regular distribution of circular spots or expand leading to the formation of an extended labyrinth. Finally, we have investigated the formation of localised labyrinth on a hill by considering an inhomogenous aridity parameter. This forcing acts as a trapping potential for the labyrinthine pattern. Owing to its general character, robust localised labyrinthine structures observed and predicted in our analysis should be observed in other systems of various fields of natural science such as fluid mechanics, optics, and medicine.

We have documented for the first time the phenomenon of localised vegetation labyrinth by remote observations, using the Google Earth computer program, and numerical simulations of three different theoretical models
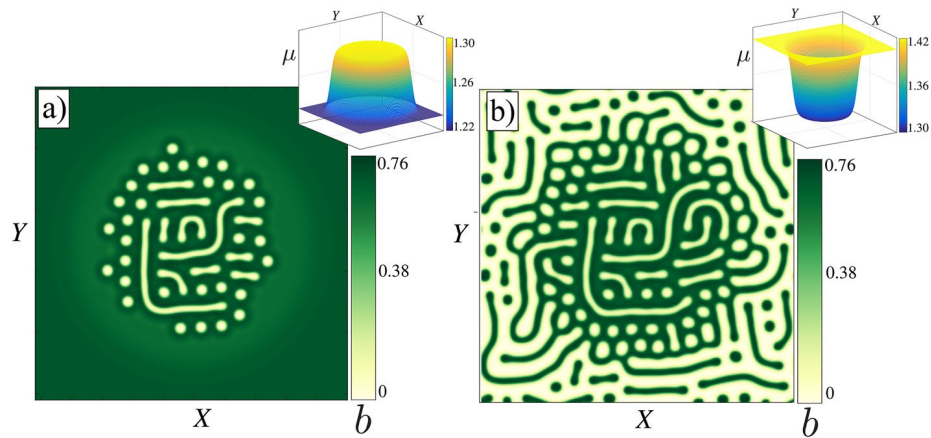
Figure 5. Localised labyrinthine patterns generated by inhomogenous aridity in the integrodifferential model. The spatially forced pattern can be supported by (**a**) the vegetated state (top hat-like shape μ parameter), and (**b**) the bare state (inverted top hat-like shape μ parameter). From numerical simulations, the figure was created using Inkscape 1.0 (https://inkscape.org/release/inkscape-1.0/).

which are based on ecologically realistic assumptions. These models provide a clear explanation of how nonlinear plant-plant interactions and the effects of plants on soil water can be crucial in determining the spatial distribution of plant communities. It is far from the scope of this contribution to provide parameters assessment and comparison between the theoretical predictions and the field observations. Work in this direction is in progress.

Extended and localised vegetation labyrinthine patterns opens a whole new area of research in self-organisation in vegetation pattern formation, where field observations will be fundamental to establish a connection with the concepts developed in this work.

Methods

Google Earth data.   The satellite images (cf. Fig. 1) are retrieved from the open-access program Google Earth (see the link https://earth.google.com/web/ and information there), courtesy of CNES/Airbus, Landsat/Copernicus, and Maxar Technologies (Fig. 1a), and CNES/Airbus (see Fig. 1b–d).

The elevation profiles in Fig. 2 are obtained from Google Earth. This software uses digital elevation data from the Shuttle Radar Topography Mission at a resolution of 30 m[44,45]. The error, at a 90% confidence level, associated to the absolute height data is less than 6 m for the territories considered here (Africa and Australia)[44].

Climate data.   Localised labyrinthine patterns are observed in Central Cameroon (Fig. 1a), Western Australia (Fig. 1b), and Southwest Niger (Fig. 1c, d). The climate types of these regions are humid, arid, and semi-arid, respectively. The climatic classification is based on the aridity index (see Table 1), which is the ratio of mean annual precipitation and potential evapotranspiration[46]. Note that the aridity index is small (big) when the aridity parameter (η or μ), defined in the interaction-redistribution approach subsection, is big (small).

Numerical simulations data.   Numerical simulations of models under consideration were solved in square grids with Runge-Kuttta 4 time integrator. The spatial derivatives were approximated using finite difference scheme with a three point stencil using periodic boundary conditions. In the integrodifferential simulation, the convolution integrals were solved in Fourier space through DFT algorithms. The detail of the parameters used in the numerical simulations are listed in the Tables below.

Generation of numerical localised labyrinthine patterns.   The localised labyrinthine patterns are initialised in a region of parameters where the uniform vegetation cover and the labyrinthine pattern coexist, in particular, in a pinning zone (see Fig. 4). The initial condition consists of a circular patch of labyrinthine pattern in the centre of the simulation box, embedded in a homogenous background (see Fig. 7). After a transient accommodation of the biomass field, the stable localised labyrinth emerges. The dynamics towards equilibrium in the integrodifferential model Eq. (2) is resumed in Fig. 7 and the Supplementary Video S1.

Computation of the bifurcation diagrams.   The bifurcation diagrams in Fig. 4 were determined with analytical and direct numerical integration techniques of the governing equations. The blue and black curves account for the vegetated state and the bare one, respectively. The curves are solid when the corresponding state is stable, and broken if unstable. The critical points in which the different states change their stability are determined by linear analysis, detailed in the interaction-redistribution approach subsection.

The red curve is the stable branch of labyrinthine patterns, and it is determined by direct numerical integration of the governing equations (using the algorithm explained above). Starting from a vegetated state with a small amplitude noise perturbation, in the region where the uniform vegetation state is unstable, a stable labyrinthine pattern can emerge (see (ii) in Fig. 4). The stability range of the labyrinth state, that is (i) and (iii) in
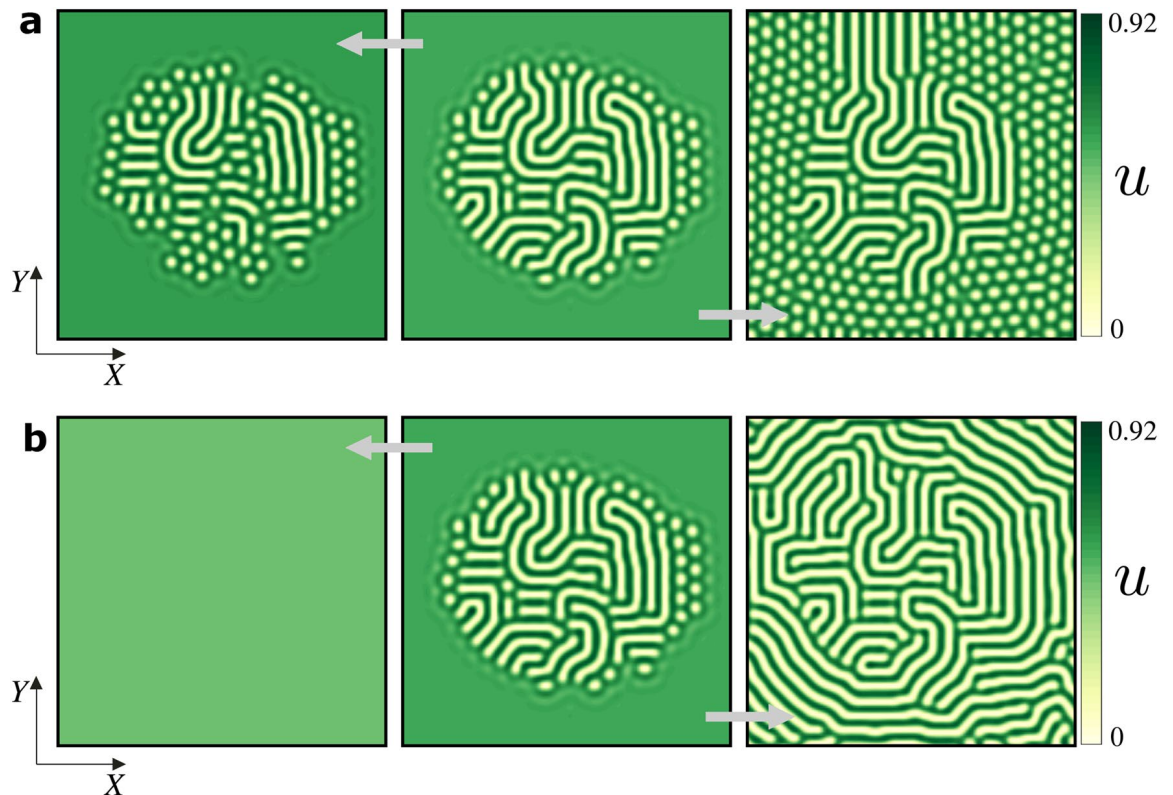
Figure 6. Deppining transitions of a localised labyrinth state ($\eta = 0.0102$) in a non-variational Swift–Hohenberg model. This state is shown in the middle panel of (**a**) and (**b**). The localised pattern destabilize when crossing the pinning region boundaries when varying slowly (**a**) or abruptly (**b**) the aridity parameter. In the first case (**a**), when decreasing η the localized labyrinth loses its internal structure due to shrinking of stripes (left panel, $\eta = 0.007$), and when increasing η some stripes begin to grow at the interface of the localized labyrinth and a hexagon pattern starts to invade the uniform cover (right panel, $\eta = 0.016$) . In the second case (**b**), when decreasing η all the stripes and patches of sparse vegetation disappear in favor of a uniform vegetated cover (left panel, $\eta = -0.03$), and when increasing η the vegetated cover becomes unstable and stripes emerge. This process transform the localised labyrinth into an extended one (right panel, $\eta = 0.05$). The other parameters are provided in the "Methods" section. From numerical simulations, the figure was created using Inkscape 1.0 (https://inkscape.org/release/inkscape-1.0/).

Fig. 4, are found by decreasing/increasing the aridity parameter starting from the labyrinthine pattern (see the black arrows in Fig. 4).

The blue triangles account for the stable branch of the localised labyrinthine pattern. The initial condition is a stable localised labyrinth state (cf. state (iv) in Fig. 4). The aridity is decreased until the localised labyrinthine pattern becomes a localised hexagonal pattern, which determines the left boundary of the pinning region (η_p^- or μ_p^-). On the other hand, the right boundary of the pinning region (η_p^+ or μ_p^+) is determined by increasing the aridity until the localised labyrinthine pattern invades all the system (see Fig. 6).
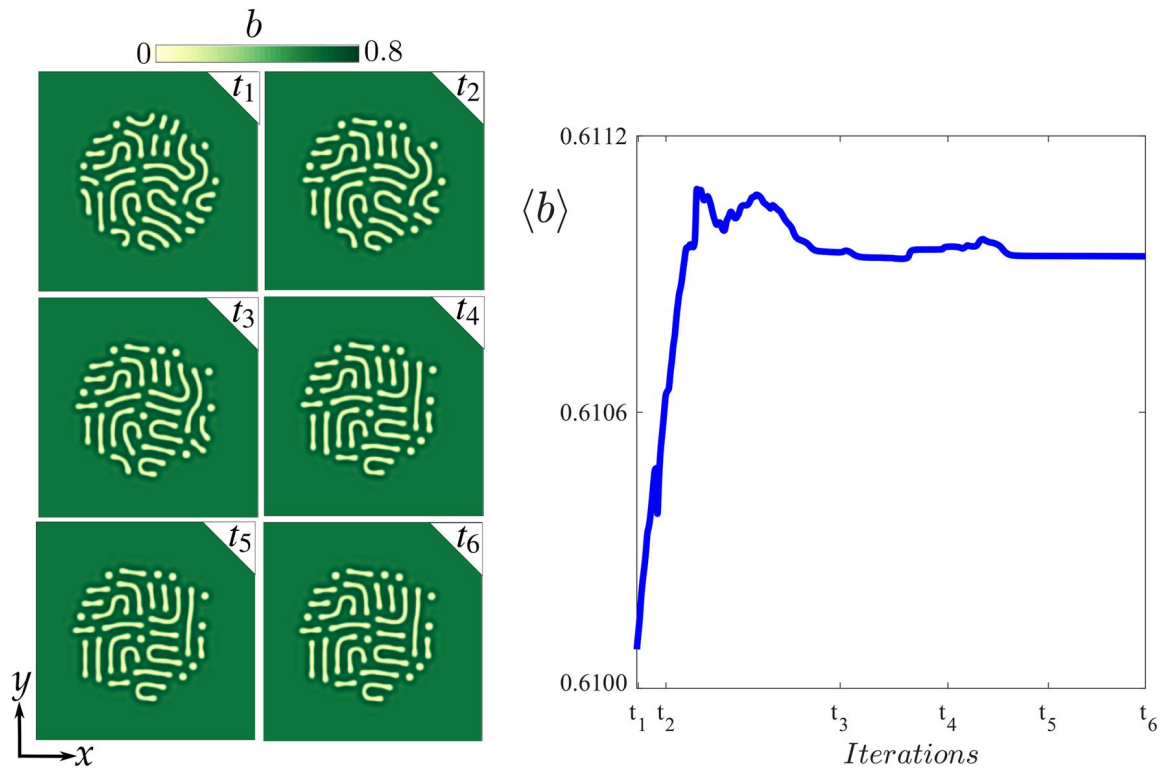
Figure 7. Initialization and stabilization of localised labyrinthine pattern in the integrodifferential model Eq. (2). The aridity parameter is $\mu = 1.3$. The other parameters are summarized in Table 3 on "Methods" section. The sequence $t_1 = 1$ to $t_6 = 4 \cdot 10^5$ accounts for the evolution towards equilibrium of the localised labyrinthine pattern, starting from a circular patch of a labyrinth state embedded in a vegetated background (t_1). The curve in the right shows the evolution of the average biomass density $\langle b \rangle$, that is the double integral of the two dimensional biomass field b divided by the area of the simulation box (see the Integrodifferential model subsection). The stable labyrinthine pattern is reached in $t_5 \approx 10^5$ iterations of the RK4 time integrator, when there is no change in $\langle b \rangle$. From numerical simulations, the figure was created using Inkscape 1.0 (https://inkscape.org/release/inkscape-1.0/).

References

1. Cross, M. C. & Hohenberg, P. C. Pattern formation outside of equilibrium. *Rev. Mod. Phys.* **65**, 851 (1993).
2. Murray, J. D. Mathematical biology. In *Biomathematics* Vol. 19 (Springer, 1989).
3. Akhmediev, N. & Ankiewicz, A. (eds) *Dissipative Solitons: From Optics to Biology and Medicine. Lecture Notes in Physics* Vol. 751 (Springer, 2008).
4. Tlidi, M., Staliunas, K., Panajotov, K., Vladimirov, A. G. & Clerc, M. G. Localized structures in dissipative media: From optics to plant ecology. *Philos. Trans. R. Soc. A* **372**, 20140101 (2014).
5. Yochelis, A., Gilad, E., Nishiura, Y., Silber, M. & Uecker, H. Special issue: Advances in pattern formation. *Physica D* **415**, 132769 (2021).
6. Clerc, M. G., Coullet, P., Rojas, R. G. & Tlidi, M. Introduction to focus issue: Instabilities and nonequilibrium structures. *Chaos* **30**, 110401 (2020).
7. Macfadyen, W. A. Soil and vegetation in British Somaliland. *Nature* **165**, 121 (1950).
8. Ridolfi, L., D'Odorico, P. & Laio, F. *Noise-Induced Phenomena in the Environmental Sciences* (Cambridge University Press, 2011).
9. Meron, E. *Nonlinear Physics of Ecosystems* (CRC Press, Taylor & Francis Group, 2015).
10. Kéfi, S. & Couteron, P. Spatiotemporal patterns as indicators of approaching critical transitions. *Ecol. Ind.* **94**, 491 (2018).
11. Lejeune, O., Tlidi, M. & Couteron, M. Localized vegetation patches: A self-organized response to resource scarcity. *Phys. Rev. E* **66**, 010901(R) (2002).
12. Rietkerk, M., Dekker, S. C., Ruiter, P. C. & van de Koppel, J. Self-organized patchiness and catastrophic shifts in ecosystems. *Science* **305**, 1926 (2004).
13. Meron, E., Yizhaq, H. & Gilad, E. Localized structures in dryland vegetation: Forms and functions. *Chaos* **17**, 037109 (2007).
14. Tlidi, M., Lefever, R. & Vladimirov, A. On vegetation clustering, localized bare soil spots and fairy circles. *Lect. Notes Phys.* **751**, 381 (2008).
15. Tarnita, C. E. *et al.* A theoretical foundation for multi-scale regular vegetation patterns. *Nature* **541**, 398 (2017).
16. Berríos-Caro, E., Clerc, M. G., Escaff, D., Sandivari, C. & Tlidi, M. On the repulsive interaction between localised vegetation patches in scarce environments. *Sci. Rep.* **10**, 5740 (2020).
17. Tlidi, M., Berríos-Caro, E., Pinto-Ramo, D., Vladimirov, A. G. & Clerc, M. G. Interaction between vegetation patches and gaps: A self-organized response to water scarcity. *Physica D* **414**, 132708 (2020).
18. Meron, E., Gilad, E., von Hardenberg, J., Shachak, M. & Zarmi, Y. Vegetation patterns along a rainfall gradient. *Chaos, Solitons & Fractals* **19**, 367 (2004).

19. Bordeu, I., Clerc, M. G., Couteron, P., Lefever, R. & Tlidi, M. Self-replication of localized vegetation patches in scarce environments. *Sci. Rep.* **6**, 33703 (2016).
20. Tlidi, M., Bordeu, I., Clerc, M. G. & Escaff, D. Extended patchy ecosystems may increase their total biomass through self-replication. *Ecol. Ind.* **94**, 534 (2018).
21. Tlidi, M. *et al.* Observation and modelling of vegetation spirals and arcs in isotropic environmental conditions: Dissipative structures in arid landscapes. *Philos. Trans. R. Soc. A (Lond.)* **376**, 20180026 (2018).
22. Mermoz, S., Le Toan, T., Villard, L., Réjou-Méchain, M. & Seifert-Granzin, J. Biomass assessment in the Cameroon savanna using ALOS PALSAR data. *Remote Sens. Environ.* **155**, 109 (2014).
23. Manetsa, V. *Étude multi-échelles des précipitations et du couvert végétal au Cameroun: Analyses spatiales, tendances temporelles, facteurs climatiques et anthropiques de variabilité du NDVI* (Doctoral dissertation) (Université de Bourgogne, 2011).
24. Africa Energy Unit. *Understanding the Impact of Climate Change on Hydropower: The Case of Cameroon* (Africa Energy Unit, 2014).
25. Beard, J. S. The vegetation survey of western Australia. *Vegetation* **30**, 3 (1975).
26. England, M., Ummenhofer, C. & Santoso, A. Interannual rainfall extremes over southwest western Australia linked to Indian Ocean climate variability. *J. Clim.* **19**, 1948–1969 (1948).
27. Chiew, F., Wang, Q. J. & McConachy, F. Evapotranspiration maps for Australia. In *Hydrology and Water Resources Symposium* (2002).
28. Wallace, J. S. & Holwill, C. J. Soil evaporation from tiger-bush in south-west Niger. *J. Hidrol.* **188**, 426 (1997).
29. Casse, C. *et al.* Potential of satellite rainfall products to predict Niger river flood events in Niamey. *Atmos. Res.* **163**, 162 (2015).
30. Ashaolu, E. & Iroye, K. Rainfall and potential evapotranspiration patterns and their effects on climatic water balance in the Western Lithoral hydrological zone of Nigeria. *Ruhuna J. Sci.* **9**, 2 (2018).
31. Lefever, R. & Lejeune, O. On the origin of tiger bush. *Bull. Math. Biol.* **59**, 263 (1997).
32. Lejeune, O. & Tlidi, M. A model for the explanation of vegetation stripes (tiger bush). *J. Veg. Sci.* **10**, 201 (1999).
33. von Hardenberg, J., Meron, E., Shachak, M. & Zarmi, Y. Diversity of vegetation patterns and desertification. *Phys. Rev. Lett.* **87**, 198101 (2001).
34. Klausmeier, C. A. Regular and irregular patterns in semiarid vegetation. *Science* **284**, 1826 (1999).
35. HilleRisLambers, R., Rietkerk, M., van den Bosch, F., Prins, H. H. T. & de Kroon, H. Vegetation pattern formation in semi-arid grazing systems. *Ecology* **82**(50), 50 (2001).
36. Barbier, N., Couteron, P., Lefever, R. & Deblauwe, V. Spatial decoupling of facilitation and competition at the origin of gapped vegetation patterns. *Ecology* **89**, 1521 (2008).
37. Couteron, P. *et al.* Plant clonal morphologies and spatial patterns as self-organized responses to resource-limited environments. *Philos. Trans. R. Soc. A (Lond.)* **372**, 20140102 (2014).
38. Getzin, S. *et al.* Adopting a spatially explicit perspective to study the mysterious fairy circles of Namibia. *Ecography* **38**, 1 (2015).
39. Okayasu, T. & Aizawa, Y. Systematic analysis of periodic vegetation patterns. *Prog. Theor. Phys.* **106**, 705 (2001).
40. Sherratt, J. A. An analysis of vegetation stripe formation in semi-arid landscapes. *J. Math. Biol.* **51**, 183 (2005).
41. Hillel, L. *Introduction to Environmental Soil Physics* (Academic Press, 2004).
42. Pomeau, Y. Front motion, metastability and subcritical bifurcations in hydrodynamics. *Physica D* **23**, 3 (1986).
43. Haudin, F. *et al.* Driven front propagation in 1D spatially periodic media. *Phys. Rev. Lett.* **103**, 128003 (2009).
44. Farr, T. G. *et al.* The shuttle radar topography mission. *Rev. Geophys.* **45**, 2 (2007).
45. El-Ashmawy, K. L. A. Investigation of the accuracy of google earth elevation data. *Artif. Satt.* **51**, 3 (2016).
46. United Nations Environment Programme. (World Atlas Desertification, 1992).

Acknowledgements

Author contributions

M.G.C. and M.T. designed the research. S.E.-A. conducted numerical simulations and the data analysis. All authors worked on the theoretical description and drafted the paper, and contributed to the overall scientific interpretation and edited the manuscript.

Competing interests

The authors declare no competing interests.

Additional information

Supplementary Information The online version contains supplementary material available at https://doi.org/10.1038/s41598-021-97472-4.

Correspondence and requests for materials should be addressed to S.E.-A.

Reprints and permissions information is available at www.nature.com/reprints.

Publisher's note Springer Nature remains neutral with regard to jurisdictional claims in published maps and institutional affiliations.

5.1.   Perspectives

In this investigation, we elucidated the existence of localized complex vegetation patterns in different sites around the world. We reproduce these observations by modeling the distribution of vegetation biomass with different theoretical perspectives [44, 32, 50, 117, 56]. Additionally, we show numerically how an inhomogeneous aridity parameter localize labyrinthine patterns. An appealing perspective will be to obtain on-site measurements to know the natural conditions at which ecosystems privilege the existence of localized labyrinthine patterns instead of extended labyrinths.

Chapter 6

Vegetation covers phase separation in inhomogeneous environments (Chaos, Solitons & Fractals 163, 112518)

Until now, well-established vegetation mathematical models based on the interactions between plants have been successful in qualitatively reproducing the vegetation self-organization observed in arid and semi-arid ecosystems [116, 44, 32, 117, 118, 150]. Nevertheless, the regularity of the patterns obtained by numerical integration of mathematical models is perfect (see Chapter 5), which is not the case for real patterns subjected to heterogeneous conditions. The causes of heterogeneities are frequently related to changes in interannual precipitation, occurrences of fire, topographic variations, inhomogeneous grazing, soil depth distribution, and soil-moisture islands [151, 152, 153, 154, 119, 155, 48, 156, 157]. It makes sense to infer that one or more of the aforementioned heterogeneities control the irregularities in vegetation patterns. For example, the topography can be estimated from satellite data (see a site of Niger in Fig. 6.1).
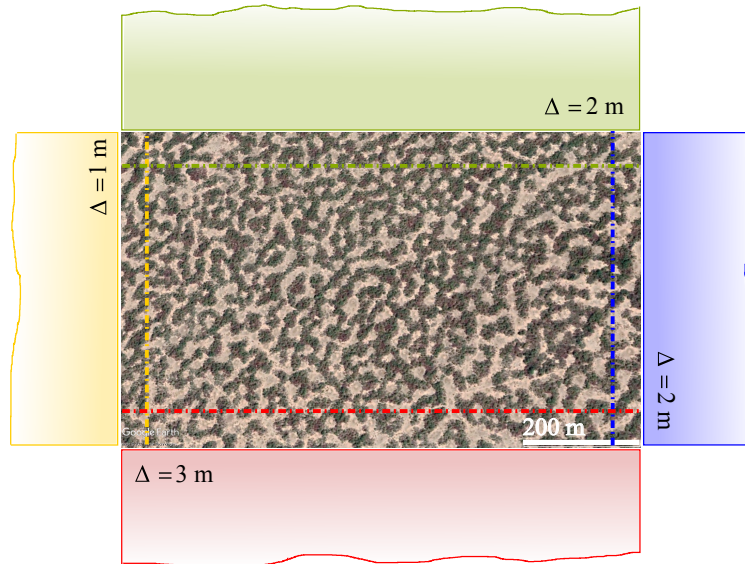
Figure 6.1: Satellite image of a vegetation pattern in Niger (12°27'50.58" N 3°18'30.76" E). The insets correspond to elevation profiles along the dotted lines. The value of Δ indicates the difference between the maximum and minimum height.

In this chapter, we suppose that topographic static fluctuations (see a site of Niger in Fig. 6.1 for illustration) can affect the resource distribution in vegetated ecosystems. Particularly, we include inhomogeneities by promoting an aridity parameter to be space dependent. We characterize the effects of these heterogeneities in the selection of equilibria, by computing Fourier transforms and correlation functions, and in the transition between a bare state and a uniform cover. Moreover, we discuss the invasion of a vegetation front in an inhomogeneous environment from the perspective of coarsening dynamics.

Vegetation covers phase separation in inhomogeneous environments

D. Pinto-Ramos [a],[*],[1], S. Echeverría-Alar [a],[1], M.G. Clerc [a],[1], M. Tlidi [b],[1]

[a] *Departamento de Física and Millennium Institute for Research in Optics, Facultad de Ciencias Físicas y Matemáticas, Universidad de Chile, Casilla 487-3, Santiago, Chile*
[b] *Faculté des Sciences, Université libre de Bruxelles (ULB), CP. 231, 1050 Brussels, Belgium*

ABSTRACT

Vegetation patterns in arid and semi-arid ecosystems as a self-organized response to resource scarcity is a well-documented issue. Their formation is often attributed to the symmetry-breaking type of instability. In this contribution, we focus on a regime far from any symmetry-breaking instability and consider a bistable regime involving uniformly vegetated covers and a bare state. We show that vegetation populations exhibit non-random two-phase structures where high biomass density regions are separated by sparsely covered areas or even bare soil. These structures are referred to as phase separation vegetation covers. We provide observations of this phenomenon in Gabon, Angola, Argentina, and Mexico. The inhomogeneities in environmental conditions are crucial to explain the origin of phase separation vegetation covers. We derive a simple equation from ecologically relevant models to explain various field observations. The bifurcation diagrams obtained from this model allow us to prove that inhomogeneity in the aridity parameter is a source of resilience for vegetation covers, avoiding collapsing towards a bare state. We characterize the natural observations and the equilibria from the model by using Fourier transform technique, spatial autocorrelation analysis, and size distribution of patches analysis.

1. Introduction

The fragmentation of landscapes and loss of biological production in drylands, which leads to desertification as a result of climate change and longer drought periods, is one of the world's most pressing environmental challenges. This fragmentation is typically accompanied by a non-equilibrium symmetry breaking instability, even when the topology of the landscapes is flat [1,2]. The patterns that emerge from the symmetry-breaking instability is generically called vegetation patterns. The 'tiger bush' is a well-known example that was first seen in the early 1940s thanks to the development of aerial photography [3]. Since this discovery, several modeling approaches have been proposed to explain the origin of these patterns, ranging from cellular-automata models [4], integrodifferential equations [1], reaction–diffusion equations [5–8], to spatially stochastic models [9, 10]. The later approach focuses on how environmental randomness can be used to create symmetry-breaking transitions that lead to the formation of vegetation patterns. Besides tiger bush other spatially periodic vegetation patterns have been reported such as hexagons [1,2,11,12], and labyrinths [2,12].

Vegetation patterns are not always periodic. They can be localized in space [13–17], found close to the symmetry-breaking instability. In [18,19], it is established how two well separated isolated patches interact in one- and two-dimensions. As one moves out from the patch center, the patch tail monotonically decays, whereas localized gaps have a damped oscillatory tail. Depending on how far apart the

gaps are, the interaction can be either attractive or repulsive [20]. Localized patches may exhibit a curvature instability that causes the self-replication phenomenon [21,22] or the emergence of arcs and spirals [23].

Nonperiodic vegetation patterns in a regime far from any symmetry-breaking instability can be observed in nature. These structures emerge spontaneously from random perturbations of the unstable homogeneous steady state that separates the two stable states forming a bistable system. This phenomenon is referred as phase separation. Growth of spatial domains of different phases whose dynamics is governed by power law in systems with conserved and nonconserved order parameters is a well documented issue [24–26]. This phenomenon has been studied in a variety of out-of-equilibrium systems, including polymer chemistry [27,28], material science [29], optical systems [30–33] and cell biology [34]. However, the topic of phase separation in ecosystems caused by environmental inhomogeneity has received little attention.

Examples of phase separation in ecosystems are shown in Fig. 1. These are satellite photos, retrieved from Google Earth software, of vegetation coverage in different regions. Near the African coast, the landscapes of Gabon (see Fig. 1a) and Angola (see Fig. 1b) show distinct patches of bare soil and planted areas of various sizes and forms. Scattered vegetated and non-vegetated areas are seen in the hilly regions of Argentina (see Fig. 1c) and Mexico (see Fig. 1d). It is seen that the vegetation distribution in all these places is inhomogeneous. Modeling

---
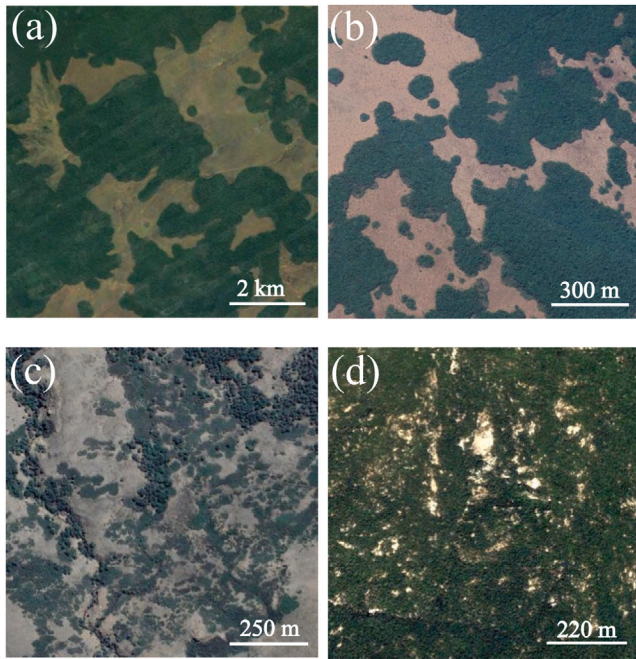
Fig. 1. Vegetation pattern phase separation. Top views of (a) Gabon, Africa (2° 44' 08.42" S, 10° 12' 28.37" E), (b) Angola, Africa (6° 19' 39.10" S, 12° 35' 25.98" E), (c) Argentina, South America (40° 58' 17.21" S, 71°16' 03.76" O), and (d) Mexico, North America (29° 04' 25.99" N, 110° 11' 19.27" O).

approaches in vegetation ecosystems do not exhibit heterogeneous non-periodic self-organization as equilibrium. The spatial characterization of such vegetation states and the transitions between them have not been explored.

We propose a unified description for non-homogeneous and non-periodic vegetation covers, vegetation pattern phase separation. We show that the inhomogeneous vegetation covers are equilibrium states of the ecosystem under inhomogeneous environment. We demonstrate how the inclusion of inhomogeneities in the parameters plays a crucial part in explaining the wide range of distinct observed equilibria. We observe that the vegetation spatial organization is characterized by a power-law distribution in Fourier space and an exponential decay in the spatial correlation. Finally, a power law for the early temporal evolution of the total biomass is numerically inferred .

Following an introduction, Section 2 shows the characterization of the spatial self-organization of the satellite images in Fig. 1. In Section 3, we present a straightforward Fisher–Kolmogorov–Petrovskii–Piskunov (FKPP) type model with inhomogeneous environmental conditions and explore the dynamics of phase separation vegetation covers. The study of equilibria and the coarsening dynamics of homogeneous states are discussed in Sections 4 and 5, respectively. In Section 5.2, we examine how the coarsening dynamics are impacted by an inhomogeneous environment by avoiding collapse to the bare state. The paper is concluded in Section 6. A detailed derivation of the FKPP equation from the generic interaction redistribution model and the reaction–diffusion water and biomass model is included in the Appendix section.

2. Spatial characterization of field observations

To characterize vegetation phase separation patterns shown in Fig. 1, we evaluate their Fourier spectrum and their spatial autocorrelation. The results are shown in Fig. 2, where the Fourier spectrum $|F(q)|^2$, as a function of the radial wavevector q, is depicted in Fig. 2(a_1, b_1, c_1, d_1). All satellite images taken from Gabon, Angola, Argentina, and Mexico unexpectedly possess a power-law decaying tail connecting
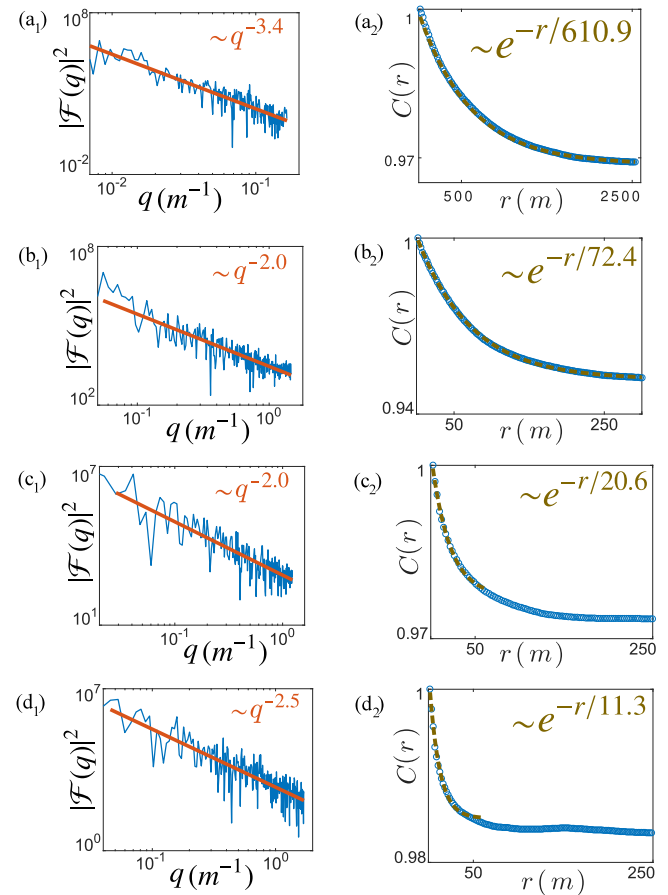
Fig. 2. Fourier spectra and spatial autocorrelations. The blue dots and the blue lines represent the real data from the vegetation images of Fig. 1. (a_1, b_1, c_1, and d_1) correspond to the Fourier spectrum of Gabon, Angola, Argentina, and Mexico vegetation patterns, respectively. The red line in the Fourier space illustrates the power-law behavior of the tail in the radial direction q. The exponents range from 2.0 to 3.4. The R^2 values of the linear fittings are (a_1) 0.79, (b_1) 0.77, (c_1) 0.69, and (d_1) 0.70, respectively. (a_2, b_2, c_2, and d_2) are autocorrelations corresponding to Gabon, Angola, Argentina, and Mexico vegetation patterns, respectively. The characteristic correlation lengths l are (a_2) l = 610.9 m, (b_2) l = 20.6 m, (c_2) l = 11.3 m, and (d_2) l = 72.4 m. They are obtained by fitting the exponential law $Be^{-r/l}$ to the real data, where B is a positive constant. The R^2 value of all the exponential fittings is 0.99. (For interpretation of the references to color in this figure legend, the reader is referred to the web version of this article.)

a range of spatial scales in the wavevector space. In this figure, the linear fitting is indicated by red line. At the very least, this eliminates the possibility of a wavelength selection process leading to the formation of periodic vegetation patterns. Besides, each vegetation photograph of Fig. 1 is accompanied by spatial autocorrelation function $C(r)$ as a function of a distance r [see Fig. 2(a_2)]. The vegetation structures have a spatial autocorrelation characterized by an exponential decay behavior until an asymptotic value is reached. Up until great distances, Gabon shown in Fig. 2(a_2) and Angola shown in Fig. 2 (b_2) exhibit an exponential behavior. At small distances, the exponential decay is truncated in Argentina and Mexico as shown in Fig. 2(c_2) and Fig. 2(d_2), respectively. The exponential decay is represented by fitting curves of the form $\sim e^{-r/l}$ of the autocorrelation data [see brown dashed lines in panels of Fig. 2(a_2, b_2, c_2, d_2)]. The correlation length is denoted by l, which describes the local vegetation pattern phase-separation of a well defined mean patch size. In fact, a closer look at the vegetation covers in Fig. 1 reveals nonperiodic behavior, leaving aside the explanation of spontaneous symmetry-breaking mechanisms.

The Fourier spectra together with spatial autocorrelations indicated that the vegetation patterns observed in Africa and America reported in

Fig. 1 do not emerge spontaneously from symmetry-breaking instability but rather from phase separation mechanism. Independent of the region of the planet, and type of soil and vegetation (bushes, patches, shrubs, trees), we observe a power-law in Fourier space and an exponential decay of the autocorrelation function. In the next sections, we introduce a model and provide an explanation to the field observations.

3. Phase separation dynamics for biomass

We adopt a continuous time and space description of the biomass density $b(x, y, t)$ at space coordinates $\mathbf{r} = (x, y)$ and time t. Theory of vegetation patterns based on the non-local FKPP equation has been reported in [35–37]. In this contribution, we consider the paradigmatic local FKPP [38,39] model equation describing the population dynamics of individuals with the inclusion of small inhomogeneities in the growth parameter

$$\partial_t b = -\left(\eta + \sqrt{\Gamma}\xi(\mathbf{r})\right)b + \kappa b^2 - b^3 + D\nabla^2 b. \tag{1}$$

This simple model is derived from the nonlocal FKPP equation, and from reaction–diffusion water biomass model (see the Appendix). The parameter η measures the linear growth ($\eta < 0$) or decay ($\eta > 0$) of vegetation population. η increases as the aridity of the environment increases; κ measures the net effect of facilitative versus competitive interactions, and b^3 is the nonlinear saturation. The last term describes diffusion with coefficient D and $\nabla^2 = \partial_{xx} + \partial_{yy}$ is the bidimensional laplacian operator. The degree of aridity described by the parameter η of an environment is related with on-site evapotranspiration process [40]. A spatial distribution of this process can arise naturally due to different type of soil, diverse plant groups, and topographic variations [41]. The function $\xi(\mathbf{r})$ models these environmental inhomogeneities and Γ measures the intensity of them.

Let us briefly recall that Eq. (1) can be stated in gradient form

$$\partial_t b = -\frac{\delta F}{\delta b},$$
$$F \equiv \int d\mathbf{r} \left(\eta(\mathbf{r})\frac{b^2}{2} - \kappa\frac{b^3}{3} + \frac{b^4}{4} + \frac{D}{2}(\nabla b)^2\right), \tag{2}$$

where $\eta(\mathbf{r}) = \eta + \sqrt{\Gamma}\xi(\mathbf{r})$. Then, it is well-known that the system Eq. (1) will reach an equilibrium minimizing the potential F.

In what follows, we focus on the effects of independent inhomogeneities in space. In this case, the function $\xi(\mathbf{r})$ is generated by a delta-correlated gaussian random process of zero mean. In the absence of inhomogeneities, i.e., $\Gamma = 0$, the model for vegetation Eq. (1) was derived from ecologically relevant models (see the Appendix). It has also been derived from a variety of physical systems, including liquid crystals [42], flame combustion [43], fiber Kerr resonators [44], passive Kerr cavity [45], and electrical circuits [46], to mention a few.

Eq. (1) for $\Gamma = 0$ supports domain walls [47] (or bistable fronts) separating the two stable equilibrium states $b_{h1} = (\kappa + \sqrt{\kappa^2 - 4\eta})/2$ and $b_{h2} = 0$. One important aspect of equilibria, is that for positive values of κ there exist a tipping – or saddle node – point at $b_s = \kappa/2$ and $\eta_s = \kappa^2/4$. As one crosses the critical aridity $\eta = \eta_s$, this bifurcation, which is defined by the annihilation of two equilibria, causes dramatic changes in the system [48], well documented as catastrophic shift in ecology.

The dynamics of Eq. (1) in the simple case of homogeneous environmental conditions, is characterized by front propagation. Straightforward calculations lead to a propagation speed of the fronts proportional to the difference of energy of the homogeneous states. Neglecting the curvature effects for the domain propagation, the speed of walls reads (see the textbook [47] and reference therein)

$$v_{walls}(b_{h1} \rightarrow b_{h2}) \equiv v_0 \propto F(b_{h2}) - F(b_{h1}), \tag{3}$$
$$F(b) \equiv \eta\frac{b^2}{2} - \kappa\frac{b^3}{3} + \frac{b^4}{4}. \tag{4}$$

In homogeneous environmental conditions where η is a constant, the dynamics leads to either a uniform vegetated cover or a state totally
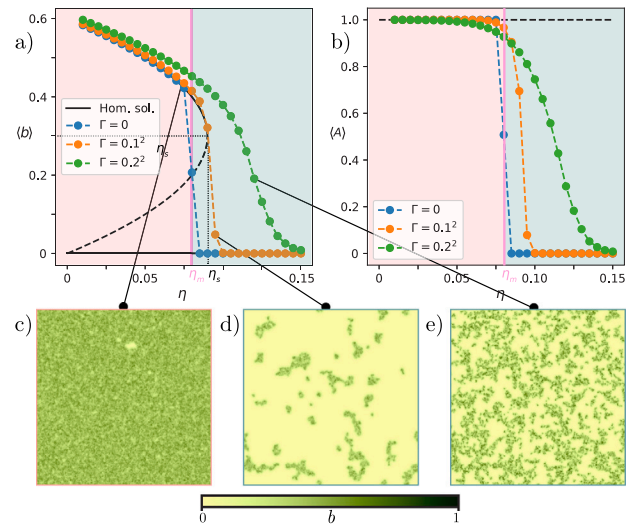
Fig. 3. The bifurcation diagram of Eq. (1) for parameters $\kappa = 0.6$ and $D = 0.1$, showing the different behaviors for different Γ values. (a) Bifurcation diagram for the averaged biomass $\langle b \rangle$. (b) Bifurcation diagram for the area fraction $\langle A \rangle$. (c), (d) and (e) show examples of the different equilibria exhibited in the bifurcation diagram. (For interpretation of the references to color in this figure legend, the reader is referred to the web version of this article.)

devoid of vegetation. This approximation cannot explain the wide range of vegetation patterns depicted in Fig. 1. It is then necessary, to include inhomogeneities in the environmental conditions, such as the aridity, which will explain the field observation as we will see in the next section.

4. Equilibrium states analysis

In this section, we discuss equilibria of Eq. (1) first in the homogeneous parameter $\Gamma = 0$ case, and then when $\Gamma \neq 0$, considering both delta-correlated and spatial correlated inhomogeneities.

4.1. Homogeneous case $\Gamma = 0$

Starting from random initial conditions $b_i(\mathbf{r}, 0)$ around the unstable vegetated state, one can introduce the averaged biomass $\langle b \rangle \equiv \sum_{i=1}^{N} \int d\mathbf{r}\, b_i(\mathbf{r}, T)/NL^2$, where N is the number of realizations and T is the time to reach equilibrium. $\langle b \rangle$ exhibits an abrupt change when increasing the aridity parameter η as shown by the blue dotted curve in Fig. 3(a). There exist a single point called the Maxwell point and denoted by $\eta = \eta_m$, where front solutions of Eq. (1) are stationary, i.e., when the two stable homogeneous steady states have the same energy. For $\eta < \eta_m$, b_{h1} has the lowest free energy density, whereas for $\eta > \eta_m$, $b_{h2} = 0$ is the preferred state. Figs. 3(b) illustrates the bifurcation diagram for the mean biomass $\langle b \rangle$ and the biomass area fraction $\langle A \rangle \equiv \sum_{i=1}^{N} \int d\mathbf{r}\, A_i(\mathbf{r}, T)/NL^2$, respectively. The latter is defined using the binarized biomass field A_i for different initial conditions b_i as

$$A_i(\mathbf{r}, T) \equiv \begin{cases} 1 & \text{if } b_i(\mathbf{r}, T) \geq b_s = \kappa/2, \\ 0 & \text{if } b_i(\mathbf{r}, T) < b_s = \kappa/2. \end{cases} \tag{5}$$

The biomass area fraction corresponding to the case $\Gamma = 0$ is indicated by the blue dotted curve in Fig. 3(b). Without inhomogeneities, numerical simulations of Eq. (1) for a long time evolution, reach either a uniform cover state or a state totally devoid of vegetation. These equilibrium biomass covers correspond to an area fraction one or zero in Fig. 3(b), respectively. Therefore, vegetation patterns and phase separation vegetation covers are excluded in this case.
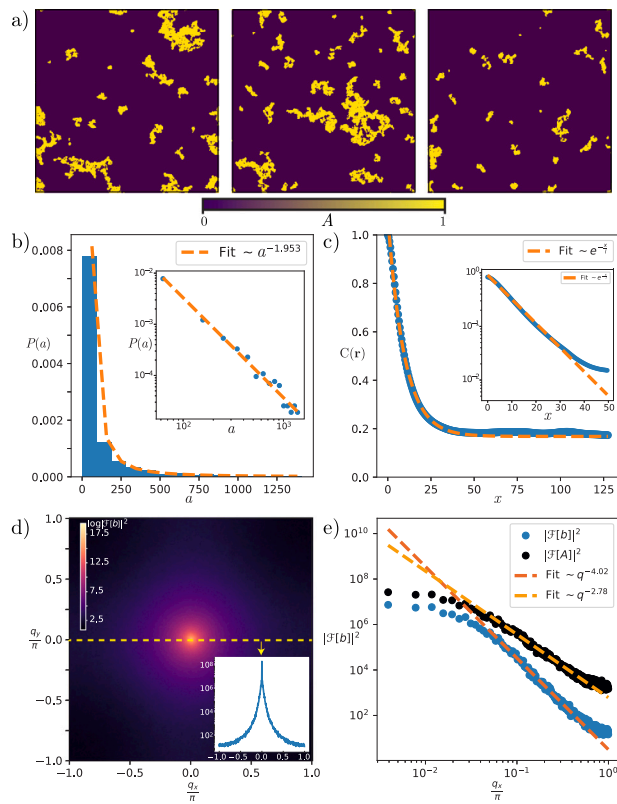
Fig. 4. Statistical analysis of a low area fraction equilibrium for parameters $\kappa = 0.6$, $D = 0.1$, $\eta = 0.95$, and $\Gamma = 0.01$. (a) Examples of equilibrium A fields. (b) Probability density of patch area $P(a)$ with a power law fit and its logarithmic scale graph in the inset. (c) Autocorrelation function of the b field, showing an exponential fit and a semi logarithmic scale graph in the inset. (d) Averaged absolute value of the Fourier transform of b in semi logarithmic scale (for contrast purposes). (e) Logarithmic scale graph for the tail of the Fourier transform with power law fits for the A and b fields. (For interpretation of the references to color in this figure legend, the reader is referred to the web version of this article.)

4.2. Inhomogeneous $\Gamma \neq 0$ and non-correlated $\xi(\mathbf{r})$ case

When the aridity parameter is inhomogeneous $\Gamma \neq 0$, numerical simulations of Eq. (1), using different random initial conditions and different realizations of $\xi(\mathbf{r})$, show there is no abrupt change in the mean biomass for large enough Γ. Fig. 3(a) show this smooth transition (see orange and green curves). In this case, the transition is rather continuous avoiding a catastrophic shift in the ecosystem.

Contrarily to the homogeneous case, the system can reach phase separation vegetation covers as shown in Figs. 3(c, d, e). Now, the system is characterized by the coexistence of disordered patches of vegetation and bare soil. According to the bifurcation diagram in Fig. 3(b), equilibrium biomass covers can have an area fraction other than zero or one. Note that states with low area fraction ($\langle A \rangle \ll 1$) are found above the Maxwell point ($\eta > \eta_m$) (cf. Figs. 3(d) and 3(e)). However, states with high area fraction ($1 - \langle A \rangle \ll 1$) are only found below the Maxwell point ($\eta < \eta_m$), as shown in Fig. 3(c).

Inhomogeneities can prevent plants from collapsing to bare ground. It is important to notice that even for entirely uncorrelated inhomogeneities, one can recognize the spatial structures seen in vegetation (see Fig. 1), and predicted by the FKPP Eq. (1). One can identify the location and size of patches by using ImageJ software [49], which has been applied to the field A. Fig. 4(a) shows examples of the field A for different realizations of the numerical simulations. It is interesting to note that the probability distribution of patch sizes $P(a)$, where a is the area of a biomass patch, follows a power law as shown in Fig. 4(b). This $P(a)$ behavior is in line with some measurement for small patch
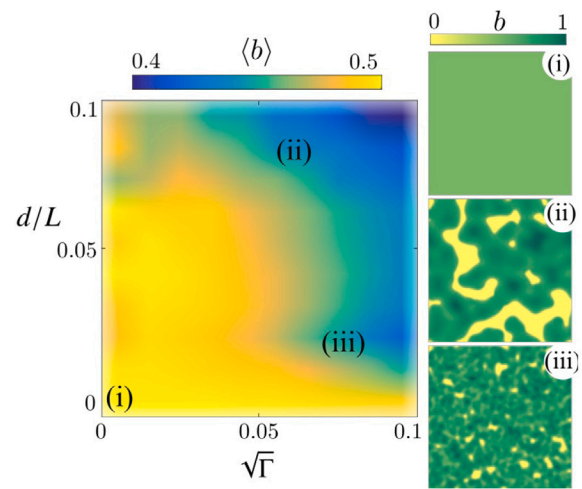
Fig. 5. Steady state averaged biomass $\langle b \rangle$ from Eq. (1) with spatially correlated inhomogeneities. The surface-plot show the average biomass $\langle b \rangle$ for different values of the intensity $\sqrt{\Gamma}$ and the degree of correlation d/L of the inhomogeneities. d is the correlation length of the $\xi(\mathbf{r})$ function, obtained by fitting an exponential law to the autocorrelation $C(\mathbf{r})$ of $\xi(\mathbf{r})$, and L is the size of the simulation box. All the correlated $\xi(\mathbf{r})$ were created with the reaction–diffusion process ($\epsilon = 0.1$). (i) $d/L = 0$ and $\sqrt{\Gamma} = 0$, (ii) $d/L = 0.03$ and $\sqrt{\Gamma} = 0.08$, and (iii) $d/L = 0.08$ and $\sqrt{\Gamma} = 0.07$ correspond to different equilibria obtained in Eq. (1). The biomass b is normalized to 1 in the three insets. (For interpretation of the references to color in this figure legend, the reader is referred to the web version of this article.)

sizes that have been documented in the literature [50]. In addition, as shown in Figs. 4(d) and 4(e), the tails of the Fourier transform of the $b_i(\mathbf{r}, T)$ and $A_i(\mathbf{r}, T)$ fields both follow a power law, typical of complex systems [51,52]. This Fourier space structure translates into a well-defined correlation function with an exponential decay for equilibrium states produced by the model Eq. (1), as shown in Fig. 4(c). We compare the outcomes of numerical simulations of the model equation with the satellite photos provided in Fig. 1 thanks to these straightforward analysis tools.

4.3. Inhomogeneous $\Gamma \neq 0$ and correlated $\xi(\mathbf{r})$ case

In what follows, we address the problem of considering the effects of inhomogeneities that are spatially correlated. To have spatially correlated inhomogeneities, let us consider an initial delta correlated function $\xi(\mathbf{r})$, to go through a simple reaction–diffusion process

$$\partial_s \xi(\mathbf{r}) = -\epsilon \xi(\mathbf{r}) + \nabla^2 \xi(\mathbf{r}), \tag{6}$$

where ϵ is a positive relaxational constant, and s parametrizes the evolution of $\xi(\mathbf{r})$. We extract different temporal stages of this evolution. In this way, we obtain inhomogeneity functions with a degree of spatial correlation, which is characterized by the dimensionless parameter d/L. d is the correlation length and L is the system size. After, we normalize the correlated functions $\xi(\mathbf{r}, s)$ between $[-1, 1]$ in order to control the inhomogeneities in Eq. (1) with the inhomogeneity level intensity Γ. Fig. 5 shows the averaged biomass $\langle b \rangle$ from Eq. (1) for different values of the inhomogeneity intensities Γ and correlation lengths d of the inhomogeneities $\xi(\mathbf{r})$. When increasing d, $\langle b \rangle$ decreases (see insets (ii) and (iii) in Fig. 5) in comparison to the homogeneous case shown in the inset (i) of Fig. 5. This is related to the coherent patches of bare soil that can coexist with the vegetated state thanks to incorporating a correlated inhomogeneity function $\xi(\mathbf{r})$. The addition of the spatial correlation can capture more smooth vegetation distributions, which are comparable to the satellite images of Gabon and Angola (cf. Figs. 1(a) and 1(b), respectively).
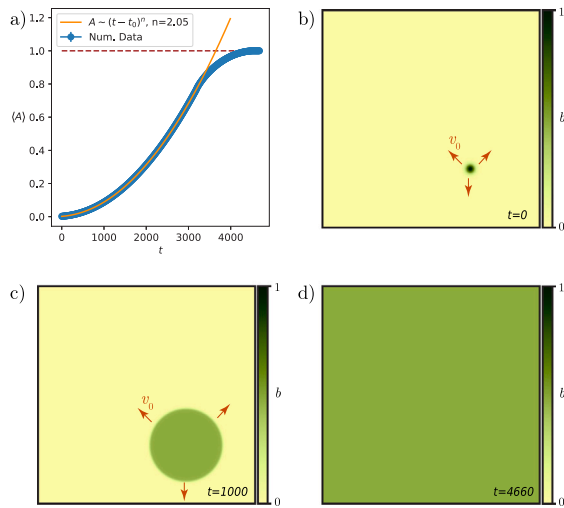
Fig. 6. Biomass propagation in homogeneous landscape. (a) The blue dots are the temporal evolution of the area cover for numerical simulations of Eq. (1), with parameters $\kappa = 0.6$, $D = 0.1$, $\eta = 0.02$, and $\Gamma = 0$. The orange indicates the theoretical prediction from Eq. (9). (b), (c), and (d) are different stages of propagation, showing that homogeneous conditions favor circular patches and full cover at equilibrium. (For interpretation of the references to color in this figure legend, the reader is referred to the web version of this article.)

5. Coarsening dynamics

In the last section, we analyze the early temporal evolution of the biomass density field $b(x, y, t)$ that leads to the equilibrium states discussed previously.

5.1. Coarsening in homogeneous environment

From the front or wall speed Eq. (3), one can infer the temporal evolution for the total cover of the biomass b as depicted in Fig. 6(a). For this, consider that a localized portion of vegetation (patch) is placed on bare ground $b = 0$, as shown in Fig. 6(b). Then, the interface propagates, as seen in Figs. 6(c) and 6(d), with an approximated speed of v_0 (see Section 3 and Eq. (3)). Thus, the characteristic size of the patch increases linearly with time t as

$$\langle L_{patch} \rangle \sim v_0 t. \tag{7}$$

Then, it is straightforward to introduce the total biomass and the area of a patch A_{patch} by

$$b_{total} \sim b_{h1} \langle L_{patch} \rangle^2 \equiv b_{h1} \langle A_{patch} \rangle. \tag{8}$$

From this, one can easily see that

$$\langle A_{patch} \rangle \sim t^n, \tag{9}$$

with $n = 2$. The previous expression is valid for a single patch in space neglecting curvature effects. Otherwise, front interactions and curvature effects alter the simple dynamics of the front. Fig. 6 (a) shows perfect agreement with this simple theory by fitting Eq. (9) to the numerical data.

More interesting is the natural nucleation of multiple patches after an initial perturbation. Initializing the system with random initial conditions, small deviations from the critical exponent $n = 2$ are expected due to multiple patch nucleation, as seen in Figs. 7(a) and (b) for early times. Figs. 7(c) to 7(f) show the temporal evolution of the nucleation of patches. Note that as one gets closer to the Maxwell point, the interaction between walls becomes stronger, and we expect larger deviations from the naive exponent $n = 2$. Unexpectedly, a crossover between exponents $n = 2$ and $n = 3$ is observed for low area fractions $\langle A \rangle$ with the former dominating the early time dynamics.
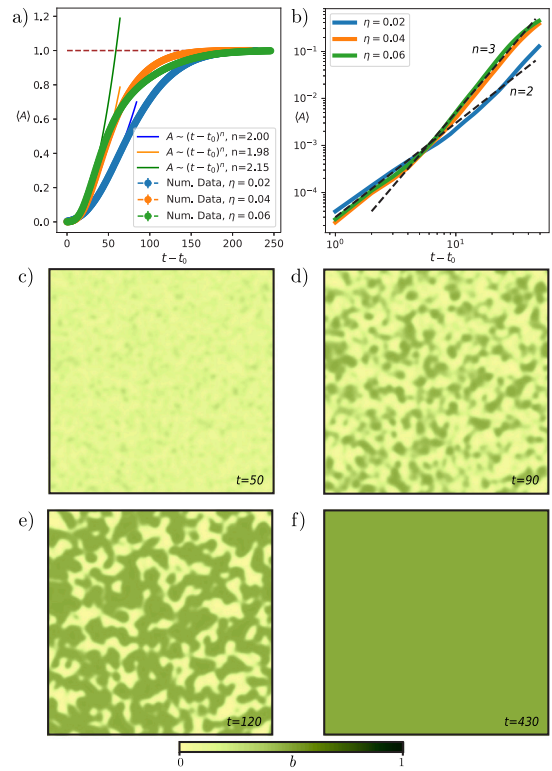
Fig. 7. Temporal dynamics of multiple patch growth in homogeneous landscape. (a) and (b) exhibit the temporal dynamics following power laws in time for the vegetation area cover, calculated from numerical simulation data of Eq. (1) with parameters $\kappa = 0.6$, $D = 0.1$, and $\Gamma = 0$. (c), (d), (e) and (f) show different stages of temporal evolution with coarsening dynamics. (For interpretation of the references to color in this figure legend, the reader is referred to the web version of this article.)

5.2. Coarsening in an inhomogeneous environment

In the case $\Gamma \neq 0$, fronts can suffer from a pinning phenomenon [53], explaining the amorphous shapes we can observe as equilibrium states. Pinning phenomenon has been studied in several fields of physics, appearing naturally in discrete systems such as crystal lattices [54], and pattern forming systems [55]. Spatially modulated parameters could also induce pinning phenomenon as observed in liquid crystal devices [56] or granular media [57].

For the temporal dynamics, fronts will be highly coupled to the external inhomogeneities imposed, putting in doubt the validity of Eq. (7). Surprisingly, coarsening dynamics for low area fractions were observed, although with a different exponent n compared with the homogeneous case, as seen in Fig. 8.

One can see that inhomogeneities increase the characteristic exponent for the area cover growth, from $n = 2$ to $n = 4$. Indeed, it is observed that inhomogeneities dramatically accelerate evolution towards the equilibrium state, reaching an almost full cover approximately fifty times faster compared to the homogeneous case $\Gamma = 0$ case.

6. Conclusions

We have reported satellite photos showing phase separation vegetation covers, obtained from Google Earth software in different landscapes of Africa and America. We have characterized vegetation phase separation patterns by establishing their Fourier spectra and spatial autocorrelations. We have demonstrated that these patterns, independent of the plant involved and the type of soil in which they are observed, exhibit a generic power-law in Fourier space and exponential decay of the autocorrelation function. Thanks to this investigation, we were able
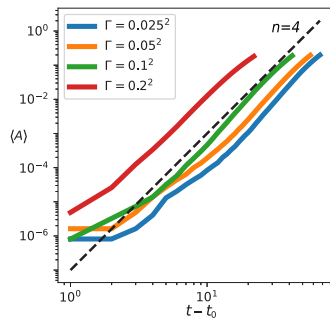
Fig. 8. Effect of inhomogeneities on early temporal evolution. The area cover of vegetation shows a different exponent for its temporal dynamics, from numerical simulations of Eq. (1) with delta correlated $\xi(\mathbf{r})$, parameters $\kappa = 0.6$, $D = 0.1$, $\eta = 0.02$. (For interpretation of the references to color in this figure legend, the reader is referred to the web version of this article.)

to rule out the symmetry-breaking mechanism caused by the formation of periodic vegetation patterns.

We have derived a simple equation, the local FKPP, as a paradigm for the studying of population dynamics, from the generic interaction redistribution model, and the reaction–diffusion water and biomass model. We have demonstrated that environmental inhomogeneities are necessary to account for the phase separation patterns observed in vegetation. Numerical simulations for a long time evolution showed that the model Eq. (1) without inhomogeneities cannot support phase separation vegetation covers.

Simple static indicators such as patch size distributions, spatial Fourier transform analysis, and correlation functions analysis reveal the presence of inhomogeneities. Additionally, we propose dynamical indicators given by the coarsening power-law exponents for the early time evolution of vegetation covers.

More importantly, inhomogeneities are shown to be a source of resilience for vegetation covers. We demonstrated that enough inhomogeneities allowed to avoid collapsing towards a bare state, shedding light on mechanisms to preserve arid ecosystems from the global warming process and long drought periods.

Declaration of competing interest

The authors declare that they have no known competing financial interests or personal relationships that could have appeared to influence the work reported in this paper.

Data availability

Data will be made available on request.

Acknowledgments

Appendix

A.1. Nonlocal FKPp model

The nonlocal FKPP model for vegetation population reads [20,35]

$$\partial_t b = b(1 - b)m_f(\mathbf{r}) - \mu b m_c(\mathbf{r}) + D m_D(\mathbf{r}), \tag{10}$$

$$m_{f,c} = \exp(\chi_{f,c} \int d\mathbf{r}' \phi_{f,c}(\mathbf{r}')b(\mathbf{r} + \mathbf{r}')), \tag{11}$$

$$m_D = \int d\mathbf{r}' \phi_D(\mathbf{r}') \left[b(\mathbf{r} + \mathbf{r}') - b(\mathbf{r}) \right], \tag{12}$$

where b corresponds to the biomass density field, following a logistic growth depending on the neighboring biomass with m_f. Mortality has a base rate μ enhanced by competition feedback through m_c. The seed dispersion is described by the last term in the rhs of Eq. (10). The nonlocal terms Eqs. (11) and (12) correspond to a weighted sum of the biomass with kernels $\phi_{f,c,D}(\mathbf{r}')$. These kernels are decaying functions of the distance between interacting plants, and are assumed to be radially symmetric. They model facilitative (f), competitive (c), and seed dispersion (D) processes. The strength of the competitive and facilitative interactions are χ_f and χ_c, respectively. Whereas D is the intensity of seed dispersion.

We perform a weak nonlinear analysis in Eq. (10). First, note the critical parameter $\mu = \mu_c = 1$ at which the bare soil state $b = 0$ changes its stability. The curve defining the non-trivial homogeneous equilibria is $0 = (1 - b)\exp(\chi_f b) - \mu \exp(\chi_c b)$, and has two positive solutions for $\chi_f - \chi_c \geq 1$. These solutions collapse to the $b = 0$ state at $\chi_f - \chi_c = 1$ and $\mu = \mu_c$. Let us explore the vicinity of the onset of bistability by introducing a small parameter ϵ ($\epsilon \ll 1$) that describes the distance from criticality as

$$\mu = \mu_c + \epsilon^2 \eta, \tag{13}$$

$$\chi_f - \chi_c = 1 + \epsilon \kappa. \tag{14}$$

A linear analysis of Eq. (10) around $b = 0$ with finite wavevector perturbation $b = A \exp(i\mathbf{q} \cdot \mathbf{r} + \lambda t)$ leads to the characteristic equation $\lambda(\mathbf{q}) = 1 - \mu + D(\hat{\phi}_D(\mathbf{q}) - 1)$, where $\hat{\phi}_D(\mathbf{q})$ is the Fourier transform of $\phi_D(\mathbf{r})$. Remembering that the kernels are normalized, it follows that $\hat{\phi}_{f,c,D}(\mathbf{q} = 0) = 1$. Moreover, as the kernels are radially symmetric the expansion for large wavelength perturbation reads $\hat{\phi}_D(\mathbf{q}) \approx 1 + \partial_{q_x q_x}\hat{\phi}_D(\mathbf{0})\mathbf{q}^2/2 + \cdots$, having at dominant order the band of unstable modes $\Delta q^2 = (\mu - 1)/(D\partial_{q_x q_x}\hat{\phi}_D(\mathbf{0})/2) \sim \epsilon^2$. Then, we propose the ansatz

$$b = \epsilon A(T = \epsilon^2 t, \mathbf{R} = \epsilon \mathbf{r}) + \epsilon^2 W^{[2]} + \epsilon^3 W^{[3]} + \cdots, \tag{15}$$

where $W^{[n]}$ correspond to nonlinear corrections of order ϵ^n. Additionally, we expand the integral terms, provided that the kernels in Eqs. (11) and (12) decay faster than an exponential, as

$$\int d\mathbf{r}' \phi_{f,c,D}(\mathbf{r}')b(\mathbf{r} + \mathbf{r}') \approx b(\mathbf{r}) + \frac{\nabla^2 b}{4} \int d\mathbf{r}' \phi_{f,c,D}(\mathbf{r}')\mathbf{r}'^2 + \cdots$$

By replacing this expansion and Eqs. (13), (14), (15) in Eq. (10) a hierarchy of equations at different orders in ϵ are found. Orders ϵ and ϵ^2 satisfy automatically the solvability condition, and at ϵ^3 order we get the equation

$$\partial_T A = -\eta A + \kappa A^2 - A^3/2 + D_e \nabla^2 A, \tag{16}$$

where

$$D_e = \frac{D}{4} \int d\mathbf{r}' \phi_D(\mathbf{r}')\mathbf{r}'^2. \tag{17}$$

In this way, with a renaming and scaling of variables and parameters in Eq. (16), we recover the local FKPP Eq. (1).

A.2. Water and biomass model

Another popular approach to explain the vegetation pattern formation proposed in the literature is based on water transport [5–8]. When biomass and water interact, vegetation ecosystems can be modeled by a pair of coupled reaction–diffusion equations. A general approach when considering sloped territory was provided in [5]. A model considering the possible bistability between bare soil and populated state reads [58]

$$
\begin{aligned}
\partial_t b &= b(1-b)w(1+\gamma b)^2 - \mu b + D\nabla^2 b, \\
\partial_t w &= p - w - \sigma b w(1+\gamma b)^2 + \nabla^2 w.
\end{aligned}
\tag{18}
$$

Where b and w correspond to the biomass and ground water density fields, respectively. γ characterizes the increase of biomass production with water consumption. The parameter μ represents the mortality rate and D accounts for the dispersal by seeds. The parameter p models the mean water input to the system, and σ weights the water lost by consumption of the biomass.

We can derive a normal form equation for long wavelength perturbations near the onset of bistability. Let us consider the linear dynamics around the bare soil state as $(b,w) = (0,p) + \delta A \vec{v}\exp(i\mathbf{q}\cdot\mathbf{r}+\lambda t)$, with $\delta A \ll 0$, the jacobian reads

$$
J = \begin{pmatrix} p - \mu - Dq^2 & 0 \\ -\sigma p & -1 - q^2 \end{pmatrix},
\tag{19}
$$

which has eigenvalues $\lambda_s(q) = -1 - q^2$ and $\lambda_u(q) = p - \mu - Dq^2$. The eigenvalue λ_u can change of sign at $\mu_c = p$ and the equilibrium point changes its stability. The corresponding band of unstable modes is $\Delta q^2 = (p-\mu)/D$. thus, close to the instability of the bare soil solution $p = \mu$, slow spatial variations domain the dynamics ($\Delta q^2 \to 0$). We use a multiple time–space scale analysis to establish a simple normal form model Eq. (1). We choose a small parameter ϵ which measure the distance from the critical point $p = \mu$ as

$$
p = \mu - \epsilon^2 \eta,
\tag{20}
$$

then, $\Delta q^2 \sim \epsilon^2$. The non-trivial homogeneous equilibria read $w_1 = \mu/\left[(1-b)(1+\gamma b)^2\right]$ and $w_2 = p/\left[1+\sigma b(1+\gamma b)^2\right]$. The onset of bistability condition reads $\partial_b w_1|_{b=0} = \partial_b w_2|_{b=0}$, giving the critical relation $\sigma_c = 2\gamma - 1$. Thus, we perturb around this condition as

$$
\sigma = 2\gamma - 1 - \epsilon\kappa.
\tag{21}
$$

To perform a weak nonlinear analysis, we consider the ansatz

$$
\begin{pmatrix} b \\ w \end{pmatrix} = \begin{pmatrix} 0 \\ p \end{pmatrix} + \epsilon A(T,\mathbf{R})\vec{v}_1 + \epsilon^2 \vec{W}^{[2]} + \epsilon^3 \vec{W}^{[3]} + \cdots
\tag{22}
$$

where the slow time scale is $T = \epsilon^2 t$, and the space scale is $\mathbf{R} = \epsilon\mathbf{r}$. We insert the previous expressions for b and w, and expansions Eqs. (20), (21) in Eq. (18), and solve the linear problems for the unknown functions $\vec{W}^{[n]}$ corresponding to nonlinear corrections of order ϵ^n.

At order ϵ, one has

$$
0 = \begin{pmatrix} 0 & 0 \\ -\sigma_c p & -1 \end{pmatrix} A\vec{v}_1,
\tag{23}
$$

which gives the eigenvector at instability

$$
\vec{v}_1 = \begin{pmatrix} 1 \\ -\sigma_c p \end{pmatrix}.
\tag{24}
$$

At order ϵ^2, one finds

$$
0 = \begin{pmatrix} 0 & 0 \\ -\sigma_c p & -1 \end{pmatrix} \vec{W}^{[2]} + A^2\begin{pmatrix} 0 \\ -\sigma_c p \end{pmatrix},
\tag{25}
$$

which is solved for

$$
\vec{W}^{[2]} = A^2\begin{pmatrix} 0 \\ -\sigma_c p \end{pmatrix}.
\tag{26}
$$

Finally, at order ϵ^3, we get the following linear inhomogeneous problem

$$
\begin{aligned}
\vec{v}_1\partial_T A = &\begin{pmatrix} 0 & 0 \\ -\sigma_c p & -1 \end{pmatrix}\vec{W}^{[3]} + A\begin{pmatrix} -\eta \\ 0 \end{pmatrix} + pA^2\begin{pmatrix} \kappa \\ 0 \end{pmatrix} + \\
&pA^3\begin{pmatrix} -3\gamma^2 \\ -\sigma_c(\gamma^2 - 2\gamma\sigma_c - \sigma_c) \end{pmatrix} + \nabla^2 A\begin{pmatrix} D \\ -\sigma_c p \end{pmatrix}.
\end{aligned}
\tag{27}
$$

Introducing the inner product $\langle \vec{f}|\vec{g}\rangle \equiv \sum_i f_i g_i$, we search for the kernel of the adjoint of the linear operator acting on $\vec{W}^{[3]}$, which is

$$
v^* = \begin{pmatrix} 1 \\ 0 \end{pmatrix}.
$$

Then, for a linear problem of the form $Ax = b$, solutions exist whenever $\langle \ker(A^\dagger)|b\rangle = 0$. Applying the solvability condition to solve Eq. (27), we get

$$
\partial_T A = -\eta A + p\kappa A^2 - 3\gamma^2 p A^3 + D\nabla^2 A.
\tag{28}
$$

By a renaming and scaling of variables and parameters, we recover the local FKPP Eq. (1).

References

[1] Lefever R, Lejeune O. On the origin of tiger bush. Bull Math Biol 1997;59(2):263–94.
[2] Lejeune O, Tlidi M. A model for the explanation of tiger bush vegetation stripes. J Veg Sci 1999;10:201–8.
[3] Macfadyen W. Vegetation patterns in the semi-desert plains of British somaliland. Geogr J 1950;116(4/6):199–211.
[4] Thiery J, d'Herbès J-M, Valentin C. A model simulating the genesis of banded vegetation patterns in Niger. J Ecol 1995;497–507.
[5] Klausmeier CA. Regular and irregular patterns in semiarid vegetation. Science 1999;284(5421):1826–8.
[6] HilleRisLambers R, Rietkerk M, van den Bosch F, Prins HH, de Kroon H. Vegetation pattern formation in semi-arid grazing systems. Ecology 2001;82(1):50–61.
[7] von Hardenberg J, Meron E, Shachak M, Zarmi Y. Diversity of vegetation patterns and desertification. Phys Rev Lett 2001;87(19):198101.
[8] Okayasu T, Aizawa Y. Systematic analysis of periodic vegetation patterns. Progr Theoret Phys 2001;106(4):705–20.
[9] D'Odorico P, Porporato A, Runyan CW. Dryland ecohydrology. Vol. 9. Springer; 2006.
[10] D'Odorico P, Laio F, Ridolfi L. Patterns as indicators of productivity enhancement by facilitation and competition in dryland vegetation. J Geophys Res Biogeosciences 2006;111(G3).
[11] Lejeune O, Tlidi M, Lefever R. Vegetation spots and stripes: dissipative structures in arid landscapes. Int J Quantum Chem 2004;98(2):261–71.
[12] Rietkerk M, Boerlijst MC, van Langevelde F, HilleRisLambers R, de Koppel Jv, Kumar L, et al. Self-organization of vegetation in arid ecosystems. Amer Nat 2002;160(4):524–30.
[13] Lejeune O, Tlidi M, Couteron P. Localized vegetation patches: a self-organized response to resource scarcity. Phys Rev E 2002;66(1):010901.
[14] Rietkerk M, Dekker SC, De Ruiter PC, van de Koppel J. Self-organized patchiness and catastrophic shifts in ecosystems. Science 2004;305(5692):1926–9.
[15] Vladimirov A, Lefever R, Tlidi M. Relative stability of multipeak localized patterns of cavity solitons. Phys Rev A 2011;84(4):043848.
[16] Fernandez-Oto C, Tlidi M, Escaff D, Clerc M. Strong interaction between plants induces circular barren patches: fairy circles. Phil Trans R Soc A 2014;372(2027):20140009.
[17] Clerc MG, Echeverría-Alar S, Tlidi M. Localised labyrinthine patterns in ecosystems. Sci Rep 2021;11(1):1–12.
[18] Berríos-Caro E, Clerc MG, Escaff D, Sandivari C, Tlidi M. On the repulsive interaction between localised vegetation patches in scarce environments. Sci Rep 2020;10(1):1–8.
[19] Tlidi M, Berríos-Caro E, Pinto-Ramo D, Vladimirov A, Clerc MG. Interaction between vegetation patches and gaps: A self-organized response to water scarcity. Physica D 2020;414:132708.
[20] Tlidi M, Lefever R, Vladimirov A. On vegetation clustering, localized bare soil spots and fairy circles. In: Dissipative solitons: from optics to biology and medicine. Springer; 2008, p. 1–22.
[21] Bordeu I, Clerc MG, Couteron P, Lefever R, Tlidi M. Self-replication of localized vegetation patches in scarce environments. Sci Rep 2016;6(1):1–11.
[22] Tlidi M, Bordeu I, Clerc MG, Escaff D. Extended patchy ecosystems may increase their total biomass through self-replication. Ecol Indic 2018;94:534–43.
[23] Tlidi M, Clerc M, Escaff D, Couteron P, Messaoudi M, Khaffou M, et al. Observation and modelling of vegetation spirals and arcs in isotropic environmental conditions: dissipative structures in arid landscapes. Phil Trans R Soc A 2018;376(2135):20180026.

[24] Domb C. Phase transitions and critical phenomena. Elsevier; 2000.

[25] Allen SM, Cahn JW. A microscopic theory for antiphase boundary motion and its application to antiphase domain coarsening. Acta Metall 1979;27(6):1085–95.

[26] Meron E. Pattern formation in excitable media. Phys Rep 1992;218(1):1–66.

[27] Flory PJ. Thermodynamics of high polymer solutions. J Chem Phys 1942;10(1):51–61.

[28] Bates FS. Polymer-polymer phase behavior. Science 1991;251(4996):898–905.

[29] Wang Z, Gao K, Kan Y, Zhang M, Qiu C, Zhu L, et al. The coupling and competition of crystallization and phase separation, correlating thermodynamics and kinetics in OPV morphology and performances. Nature Commun 2021;12(1):1–14.

[30] Tlidi M, Mandel P, Lefever R. Kinetics of localized pattern formation in optical systems. Phys Rev Lett 1998;81:979–82.

[31] Tlidi M, Mandel P, Le Berre M, Ressayre E, Tallet A, Di Menza L. Phase-separation dynamics of circular domain walls in the degenerate optical parametric oscillator. Opt Lett 2000;25(7):487–9.

[32] Tlidi M, Le Berre M, Ressayre E, Tallet A, Di Menza L. High-intensity localized structures in the degenerate optical parametric oscillator: comparison between the propagation and the mean-field models. Phys Rev A 2000;61(4):043806.

[33] Gomila D, Colet P, Oppo G-L, San Miguel M. Stable droplets and growth laws close to the modulational instability of a domain wall. Phys Rev Lett 2001;87(19):194101.

[34] Boeynaems S, Alberti S, Fawzi NL, Mittag T, Polymenidou M, Rousseau F, et al. Protein phase separation: a new phase in cell biology. Trends Cell Biol 2018;28(6):420–35.

[35] Lefever R, Turner JW. A quantitative theory of vegetation patterns based on plant structure and the non-local F–KPP equation. C R Méc 2012;340(11–12):818–28.

[36] Dornelas V, Colombo EH, López C, Hernández-García E, Anteneodo C. Landscape-induced spatial oscillations in population dynamics. Sci Rep 2021;11(1):1–11.

[37] Piva G, Colombo E, Anteneodo C. Interplay between scales in the nonlocal FKPP equation. Chaos Solitons Fractals 2021;153:111609.

[38] Fisher RA. The wave of advance of advantageous genes. Ann Eugen 1937;7(4):355–69.

[39] Kolmogorov AN. A study of the equation of diffusion with increase in the quantity of matter, and its application to a biological problem. Moscow Univ Bull Math 1937;1:1–25.

[40] Middleton N, Thomas D. World atlas of desertification. Arnold, Hodder Headline, PLC; 1997.

[41] Mauser W, Schädlich S. Modelling the spatial distribution of evapotranspiration on different scales using remote sensing data. J Hydrol 1998;212:250–67.

[42] De Gennes P-G, Prost J. The physics of liquid crystals. (83). Oxford University Press; 1993.

[43] Clavin P. Dynamic behavior of premixed flame fronts in laminar and turbulent flows. Prog Energy Combust Sci 1985;11(1):1–59.

[44] Coen S, Tlidi M, Emplit P, Haelterman M. Convection versus dispersion in optical bistability. Phys Rev Lett 1999;83:2328–31.

[45] Odent V, Tlidi M, Clerc MG, Glorieux P, Louvergneaux E. Experimental observation of front propagation in a negatively diffractive inhomogeneous Kerr cavity. Phys. Rev. A 2014;90:011806.

[46] Murray JD. Mathematical biology: I. an introduction. third ed.. New York, NY: Springer; 2002.

[47] Pismen LM. Patterns and interfaces in dissipative dynamics. Springer Science & Business Media; 2006.

[48] Strogatz SH. Nonlinear dynamics and chaos: with applications to physics, biology, chemistry, and engineering. CRC Press; 2018.

[49] Abràmoff MD, Magalhães PJ, Ram SJ. Image processing with ImageJ. Biophotonics Int 2004;11(7):36–42.

[50] Maestre FT, Escudero A. Is the patch size distribution of vegetation a suitable indicator of desertification processes? Ecology 2009;90(7):1729–35.

[51] Bak P. How nature works: the science of self-organized criticality. Springer Science & Business Media; 1996.

[52] Sornette D. Critical phenomena in natural sciences: chaos, fractals, selforganization and disorder: concepts and tools. Springer Science & Business Media; 2006.

[53] Clerc M, Falcon C, Tirapegui E. Additive noise induces front propagation. Phys Rev Lett 2005;94(14):148302.

[54] Braun OM, Kivshar YS. The Frenkel-Kontorova model: concepts, methods, and applications. Springer Science & Business Media; 2013.

[55] Pomeau Y. Front motion, metastability and subcritical bifurcations in hydrodynamics. Physica D 1986;23(1–3):3–11.

[56] Alfaro-Bittner K, Castillo-Pinto C, Clerc MG, González-Cortés G, Jara-Schulz G, Rojas RG. Front propagation steered by a high-wavenumber modulation: Theory and experiments. Chaos 2020;30(5):053138.

[57] Jara-Schulz G, Ferré MA, Falcón C, Clerc MG. Noise-induced kink propagation in shallow granular layers. Chaos Solitons Fractals 2020;134:109677.

[58] Meron E. Nonlinear physics of ecosystems. CRC Press Boca Raton, FL; 2015.

6.1.   Perspectives

In this chapter, we have shown the effects of spatial heterogeneities in the homogeneous equilibria of a population model. Particularly, inhomogeneities are shown to be a source of resilience for vegetation landscapes. We demonstrated that inhomogeneities can avoid a critical collapse into a bare state. A future research direction is to explore the effect of heterogeneous environmental conditions, following the framework developed in this chapter, in the (de)stabilization of more complicated equilibria, such as hexagonal, stripe, and labyrinthine patterns.

Chapter 7

Effect of heterogeneous environmental conditions on labyrinthine vegetation patterns (Physical Review E 107, 054219)

In the previous chapter, we studied the effect of spatial heterogeneities in the homogeneous equilibria of a population model related to plant communities in harsh environments. Now, we would like to investigate the effect of heterogeneities in the labyrinthine-like structures observed in different regions of Africa (cf. Figure 7.1). The simple question driving this analysis is: Can we extend the ideas of labyrinthine patterns of Chapter 3 in real systems, where heterogeneities are the rule rather than the exception?

In this chapter, we will include spatial heterogeneities in a local model of vegetation dynamics (2.13) by promoting the aridity parameter η to be spatial dependent, and study its effects in labyrinths (see different equilibria in Fig. 7.2). We discover that perfect labyrinths are persistent below critical heterogeneous conditions, depending on the intensity level and degree of correlation of the heterogeneities. After these conditions are reached, perfect labyrinths transform into imperfect labyrinthine patterns. This transition is revealed by employing global spatial analysis techniques (Fourier transforms and structure factor function) and by extending the windowed Fourier transform tool (see Chapter 3) to the case where a zero mode is active. We think the imperfect labyrinthine patterns are the structures observed in Fig. 7.1; that is, the labyrinths observed in real landscapes are a combination of symmetry-breaking instabilities of uniform covers and the underlying heterogeneities.
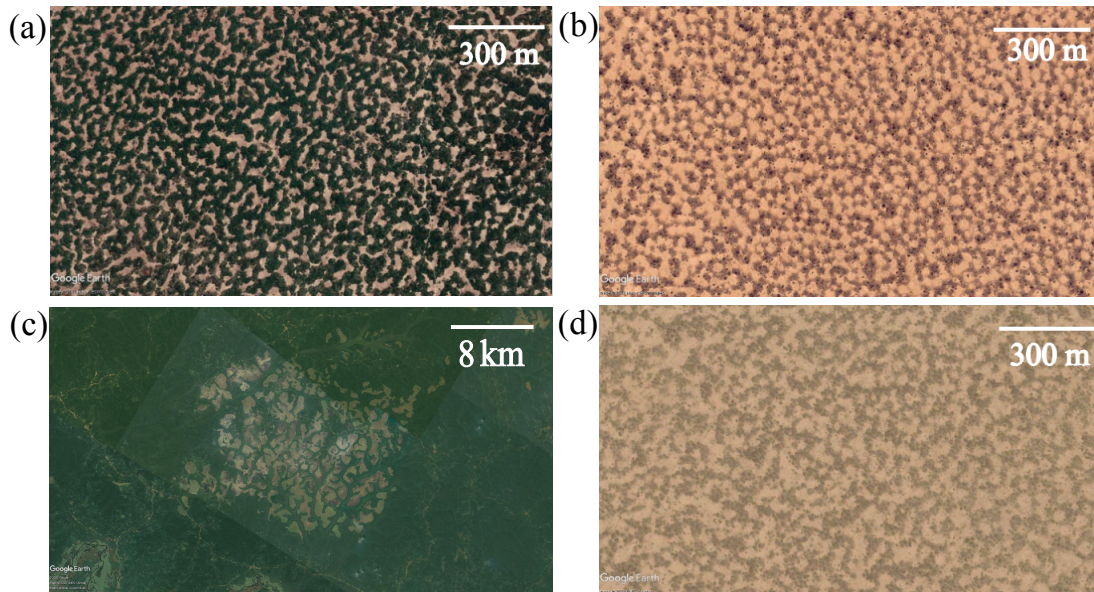
Figure 7.1: Satellite images of labyrinthinelike vegetation patterns in (a) Niger (12°27'50.58" N 3°18'30.76" E), (b) Sudan (11°18'26.07" N 27°57'58.62" E), (c) Cameroon (3°59'22.05" N 12°17'20.99" E), and (d) Senegal (15°20'48.72" N, 14°43'07.17" O). All the images were retrieved from Google Earth software [115].
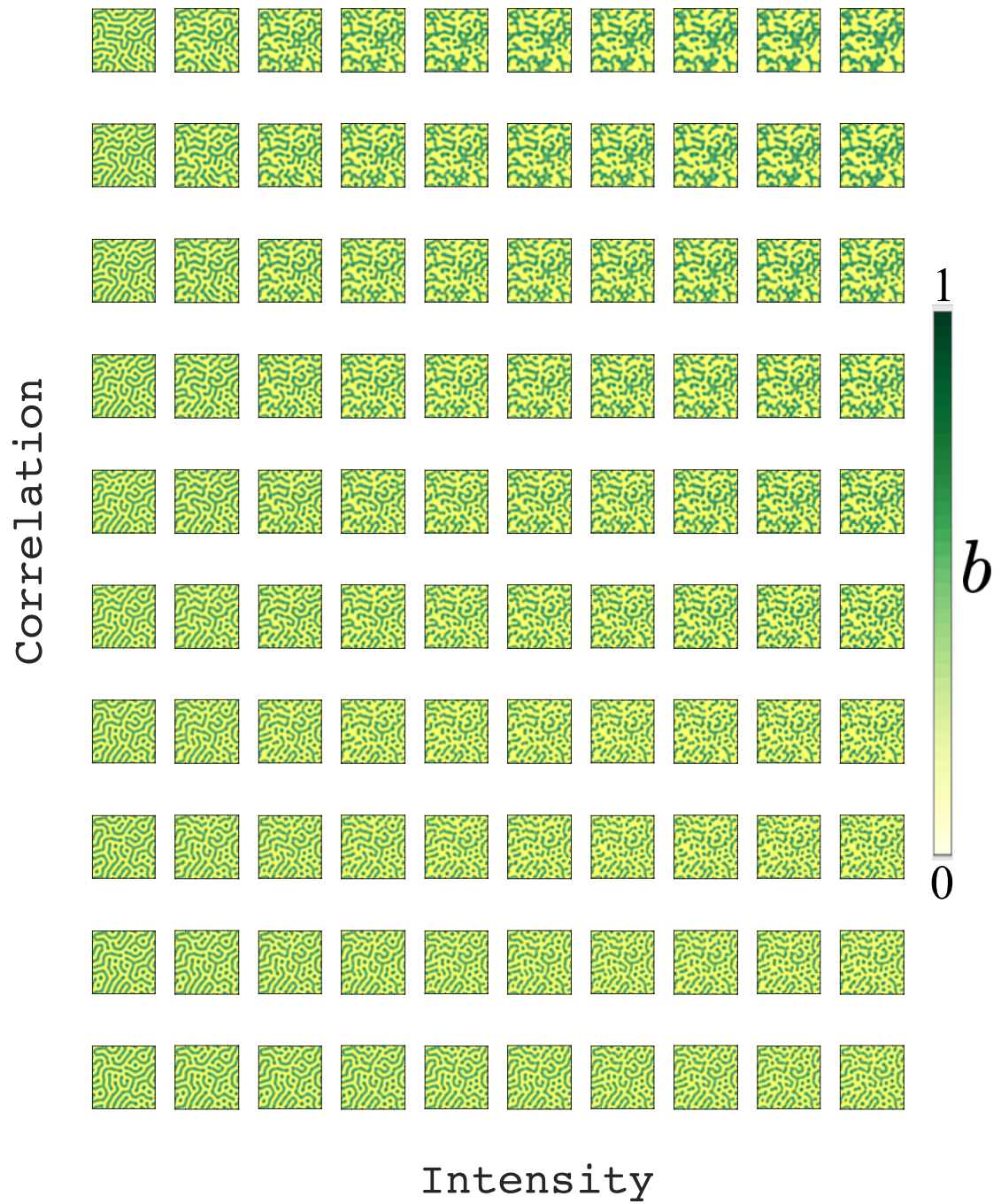
Figure 7.2: Numerical integrations of Eq. (2.13) with $\kappa = 0.6$, $\nu = 0.01$, $\gamma = 0.5$, and $\alpha = 0.125$, showing different labyrinthinelike textures for different intensity levels (increasing from left to right) and degrees of correlation (increasing from bottom to top) of the heterogeneities. The simulations are performed in squared boxes of size 240×240.

Effect of heterogeneous environmental conditions on labyrinthine vegetation patterns

S. Echeverría-Alar [●],[1] D. Pinto-Ramos [●],[1] M. Tlidi,[2] and M. G. Clerc [●][1]

[1]*Departamento de Física and Millennium Institute for Research in Optics, FCFM, Universidad de Chile, Casilla 487-3, Santiago, Chile*
[2]*Faculté des Sciences, Université libre de Bruxelles (U.L.B), CP 231, 1050 Brussels, Belgium*

Self-organization is a ubiquitous phenomenon in Nature due to the permanent balance between injection and dissipation of energy. The wavelength selection process is the main issue of pattern formation. Stripe, hexagon, square, and labyrinthine patterns are observed in homogeneous conditions. In systems with heterogeneous conditions, a single wavelength is not the rule. Large-scale self-organization of vegetation in arid environments can be affected by heterogeneities, such as interannual precipitation fluctuations, fire occurrences, topographic variations, grazing, soil depth distribution, and soil-moisture islands. Here, we investigate theoretically the emergence and persistence of vegetation labyrinthine patterns in ecosystems under deterministic heterogeneous conditions. Based on a simple local vegetation model with a space-varying parameter, we show evidence of perfect and imperfect labyrinthine patterns, as well as disordered vegetation self-organization. The intensity level and the correlation of the heterogeneities control the regularity of the labyrinthine self-organization. The phase diagram and the transitions of the labyrinthine morphologies are described with the aid of their global spatial features. We also investigate the local spatial structure of labyrinths. Our theoretical findings qualitatively agree with satellite images data of arid ecosystems that show labyrinthinelike textures without a single wavelength.

I. INTRODUCTION

Self-organization is a universal feature of out-of-equilibrium systems and is of common occurrence in many fields of nonlinear science [1–4]. The spontaneous emergence of self-organized dissipative structures out of a homogeneous state has been observed in many out-of-equilibrium systems, including biology, chemical reaction-diffusion systems, fluid mechanics, nonlinear optics, and laser physics [1–3]. On the one hand, these systems are subjected to a balance between a nonlinear effect and a transport or a spatial coupling process. On the other hand, they are subjected to a continuous injection and dissipation of energy. The balance between these processes triggers the emergence of dissipative structures with an intrinsic macroscopic scale [2,5,6], which corresponds to a spontaneous symmetry-breaking instability. Over the past decades, extensive research has been done to understand the origins of simple patterns, such as stripes, hexagons, and squares, from a theoretical point of view [2,7]. However, nontrivial symmetry patterns, i.e., labyrinths, have gotten little attention due to their complicated structure, rich in spatial defects [8,9]. Recently, an attempt to characterize this ubiquitous phenomenon has introduced a quantitative definition of *ideal* labyrinthine patterns [10], which satisfy the following: (i) the disordered patterns are characterized globally by a powdered ring Fourier spectrum, and (ii) the spatial structures are described locally by a single wave mode. The *ideal* adjective refers to labyrinths with a single dominant characteristic wavelength, which are observed in controlled physical contexts, e.g., ferrofluids, chemical reactions, cholesteric liquid crystals, block copolymers, metal nanosurfaces, and ferroelectric thin films [11–16].

Self-organized structures arise in plant ecology, where stressed vegetation biomass can self-organize when resources, such as water or nutrients, are limited [17–24]. Under these arid conditions, the plant community displays coherent distributions, which are maintained by facilitative and competitive processes involving plants and the environment [18]. These distributions, whose wavelengths range from centimeter to kilometer scales, are frequently referred to as vegetation patterns. Starting from a uniform cover, as the aridity level is increased, the first pattern that appears consists of a periodic spatial distribution of gaps followed by labyrinths and then spots. This generic sequence has been predicted using various pattern-forming ecological models. The first paper that discusses the sequence was [19] in 1999. Later on, the sequence was analyzed from reaction-diffusion models in 2001 [20] and 2002 [21]. The sequence gaps-stripes/labyrinths-spots as a function of the aridity has been empirically studied in an arid region of Sudan [24]. There, the term labyrinth was used to describe disordered vegetation bands in a flat surface [20–25]. Besides periodic, other aperiodic and localized vegetation patterns have been reported [26–31]. Well-documented localized vegetation patterns are the fairy circles [32–39]. Localized vegetation patterns can exhibit curvature instabilities leading either to the self-replication phenomenon [40,41], or the formation of arcs and spirals [42]. Other alternative hypotheses for the spatial structure of vegetation self-organization have been explored, such as random patterns and power-law distributions of patch sizes [43,44].

In ecological systems, the presence of spatial and/or temporal heterogeneities may influence the self-organization of plant communities. The causes of heterogeneities are frequently related to variations in interannual precipitation,
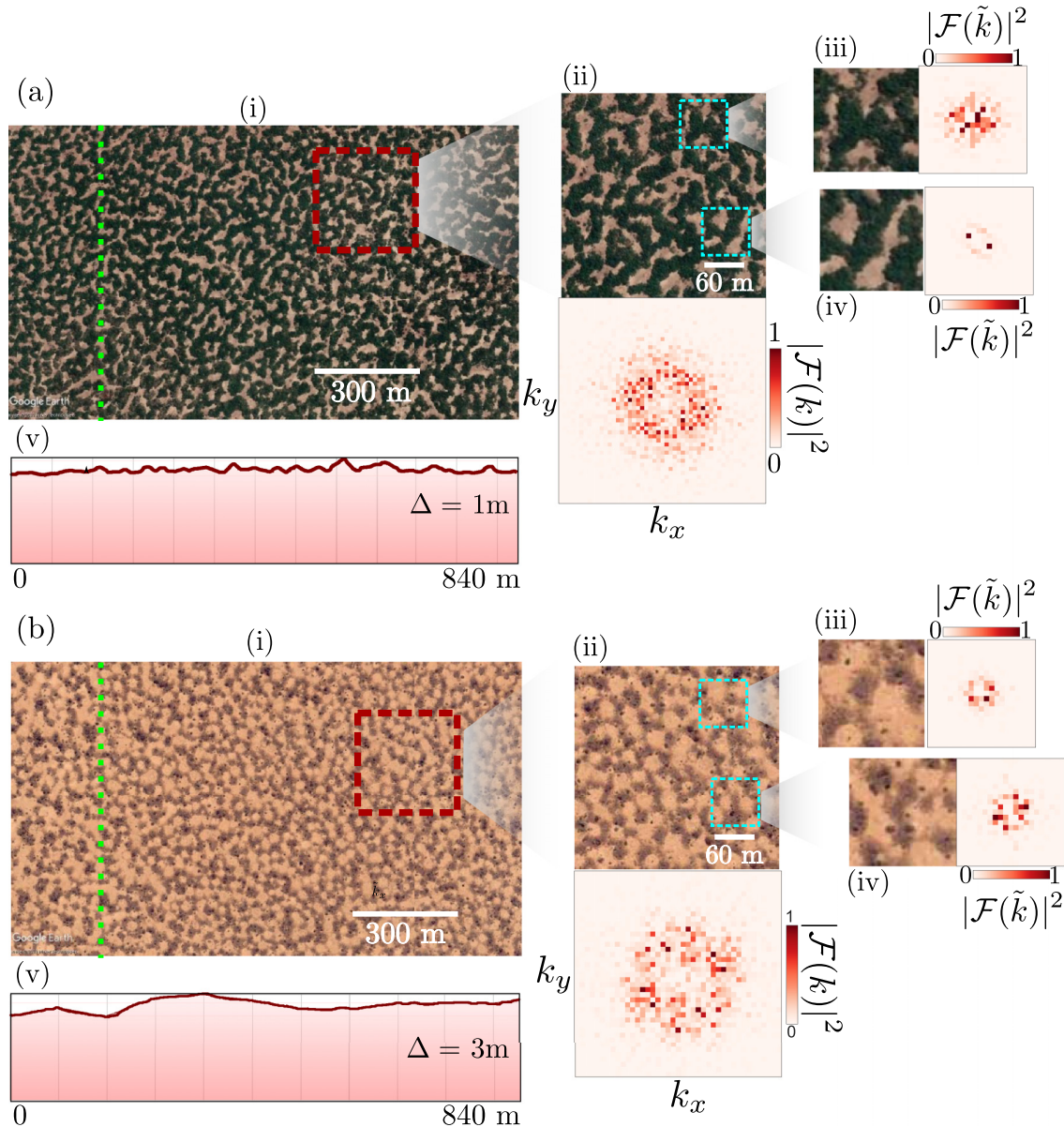
FIG. 1. Satellite images of vegetation labyrinths. Self-organization of vegetation observed in (a)(i) Niger (12°27′50.58″ N 3°18′30.76″E) and (b)(i) Sudan (11°18′26.07″ N 27°57′58.62″E). The (ii) insets display a zoom of images in (i) and are characterized by their Fourier transform $|\mathcal{F}(k)|^2$. The (iii) and (iv) insets are local regions of the images in (ii) accompanied by their local Fourier transforms $|\mathcal{F}(\tilde{k})|^2$. The (v) insets correspond to elevation profiles along the green dotted lines in (i). The value of Δ indicates the difference between the maximum and the minimum height. The vegetation snapshots and elevation profiles were retrieved from Google Earth Pro software.

occurrences of fire, topographic changes, grazing, soil depth distribution, and soil-moisture islands [22,45–49]. It makes sense to infer that one or more of the aforementioned heterogeneities control the irregularities in vegetation patterns (see the labyrinthinelike structures in Fig. 1). In the majority of the ecological mathematical models, these heterogeneous effects are not included, resulting in far too ideal vegetation patterns, or are approached by stochastic processes in time [46,47,49,50] or space [51]. To our knowledge, the role of deterministic heterogeneities in forming different labyrinthinelike vegetation patterns and controlling their possible transitions has not been addressed. Understanding the conditions under which heterogeneous labyrinths arise is

relevant from an ecological perspective as it sheds light on the self-organization of vegetation in isotropic real ecosystems (Fig. 1). Furthermore, the study of these types of vegetation self-organization can contribute to the discussion on how heterogeneities in arid or semiarid systems can avoid catastrophic shifts [27,51,52], which corresponds to abrupt transitions between a vegetated cover and bare soil, by establishing irregular vegetation mosaics.

In this article, we investigate theoretically the role of deterministic heterogeneities in shaping labyrinthinelike vegetation patterns as equilibria in arid and semiarid landscapes. For this purpose, we use a well-established model for vegetation biomass, where the effects of heterogeneities are modeled

as spatial variations around a mean aridity parameter. The heterogeneities are controlled by their intensity and degree of correlation. Different equilibria are numerically observed after the temporal evolution of the biomass. These vegetation patterns are characterized by their structure factor and their spatial Fourier transform at a global and local scale. These tools allow us to differentiate between perfect and imperfect labyrinths, and disordered self-organization. We construct a phase diagram and show that a minimum intensity level and/or degree of correlation are needed to observe imperfect labyrinthine patterns. This equilibrium qualitatively resembles the labyrinthinelike patterns observed in nature (Fig. 1). Finally, we discuss a possible implementation of our classification in natural landscapes.

II. LABYRINTHINELIKE PATTERNS IN ECOSYSTEMS

It is crucial to identify whether plants have structures resembling labyrinths to assess if they fulfill the definition of a labyrinth proposed recently [10]. Figures 1(a i) and 1(b i) show two examples of labyrinthinelike self-organized structures in Niger and Sudan, respectively. These vegetation images can be characterized by their Fourier spectrum at different scales as shown in insets (ii), (iii), and (iv) of Fig. 1. The insets (ii) exhibit the disordered feature of the self-organization at a global scale. The Fourier transform is nearly isotropic and highly scattered, involving several wave vectors (powderlike ring spectrum). The insets (iii) and (iv) of Fig. 1 show the spatial behavior at a local scale. The local Fourier transforms do not show a dominant single wave vector pair structure. Specifically, two diametrally opposed peaks are not visible in the local two-dimensional Fourier transform, and more complex structures are exhibited. As a result, neither the landscapes of Niger nor of Sudan meet the criteria for a perfect labyrinthine pattern [10]. We attribute the departure from the ideal pattern to the presence of heterogeneities in the regions shown in Fig. 1. The insets (v) in Figs. 1(a) and 1(b) display the topographic variations of the terrain in Niger and Sudan, respectively. Indeed, the topography is a source of spatial heterogeneity for the vegetation local self-organization [53–55]. In the following, we suppose that these topographic fluctuations affect the resource distribution on the Niger and Sudan landscapes.

III. THEORETICAL MODELING APPROACH

We choose to model the emergence of vegetation patterns from the perspective of symmetry-breaking instabilities of homogeneous covers in arid or semiarid environments [18]. Particularly, we use an interaction-redistribution approach for plant community behavior, where the biomass density $c = c(\mathbf{r}, t)$ at space point $\mathbf{r} = (x, y)$ and time t evolves following a logistic equation that includes nonlocal interactions of the biomass [33]:

$$\partial_t c = c(1 - c)M_f(\mathbf{r}) - \mu c M_c(\mathbf{r}) + D M_d(\mathbf{r}). \quad (1)$$

The first term on the right-hand side (rhs) of Eq. (1) models the rate at which biomass increases and eventually saturates. The nonlocal function $M_f(\mathbf{r}) = \exp[\chi_f \int d\mathbf{r}' \phi_f(\mathbf{r}', L_f) c(\mathbf{r} + \mathbf{r}')]$ accounts for interactions facilitating growth, regulated by
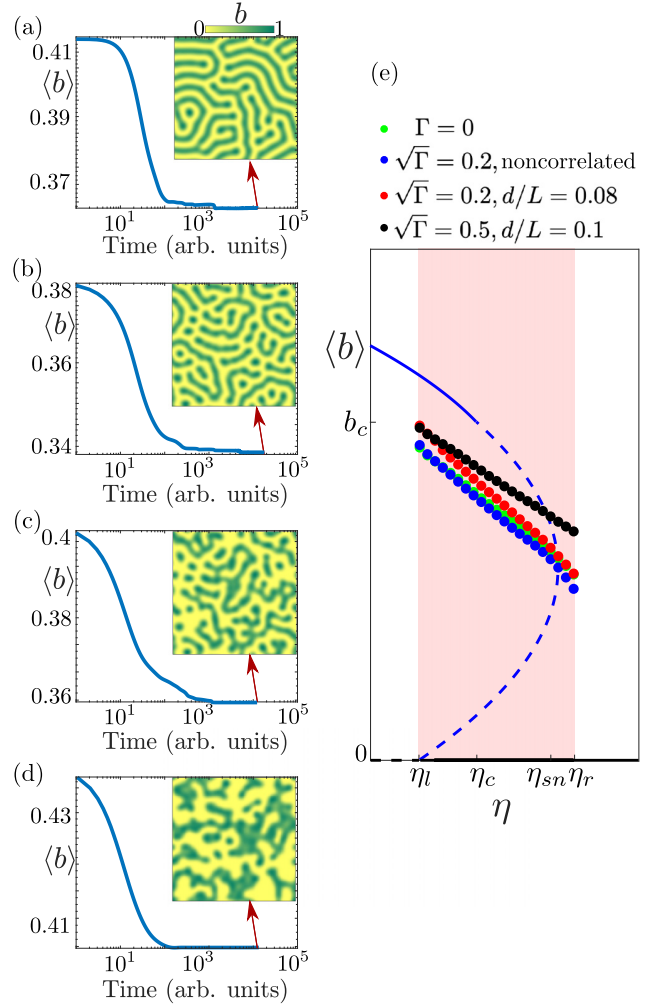
FIG. 2. Equilibrium patterns of Eq. (2) in a square domain of size $L = 240$ (arb. units) with $\kappa = 0.6$, $\nu = 0.011$, $\gamma = 0.5$, and $\alpha = 0.125$. The temporal evolutions of the spatially averaged biomass $\langle b \rangle$ are displayed for the (a) homogeneous case $\Gamma = 0$, and the inhomogeneous cases $\Gamma \neq 0$ considering both (b) noncorrelated and (c),(d) correlated heterogeneities. The insets show the respective equilibria. (e) Bifurcation diagram of Eq. (2). The black lines correspond to the bare state and the blue curves account for the uniform vegetated state in the homogeneous case $\Gamma = 0$. The continuous (broken) lines indicate that these analytical solutions are stable (unstable). In the shaded region, limited by η_l and η_r, the labyrinthine patterns in homogeneous conditions are stable. In this subfigure, $\langle b \rangle$ is the mean value over 30 random initial conditions around b_+.

an intensity χ_f. These effects are controlled by the kernel function ϕ_f, whose range of influence is of the order of the plant's aerial structure L_f. The second term on the rhs of Eq. (1) represents the biomass death processes. $M_c(\mathbf{r}) = \exp[\chi_c \int d\mathbf{r}' \phi_c(\mathbf{r}', L_c) c(\mathbf{r} + \mathbf{r}')]$ accounts for interactions enhancing biomass decay with an intensity χ_c. The parameter μ is a measure of the mortality-to-growth rate ratio of plants in the absence of interaction with others, which can be seen as resource scarcity or aridity [18,56]. This negative feedback acts over distances of the order of the root length L_c with an intensity χ_c and is controlled by the kernel function

ϕ_c. A cooperative measure of the ecological system can be introduced as $\chi_f - \chi_c$. The last term in Eq. (1) incorporates seeds dispersion with a diffusion parameter D, where $M_d(\mathbf{r}) = \int d\mathbf{r}' \phi_d(\mathbf{r}')[c(\mathbf{r} + \mathbf{r}') - c(\mathbf{r})]$, and $\phi_d(\mathbf{r}')$ accounts for the biomass transport between positions $\mathbf{r}$ and $\mathbf{r}'$.

The integrodifferential equation (1), close to the double limit of nascent bistability (between uniform vegetation cover and bare soil) and the symmetry-breaking instability of the uniform cover, can be reduced to a partial differential equation. The reduced model reads [19,33]

$$\partial_t b = -\eta b + \kappa b^2 - b^3 + (\nu - \gamma b)\nabla^2 b - \alpha b \nabla^4 b, \quad (2)$$

where $b = b(\mathbf{r}, t)$ is the state variable associated to the biomass density close to nascent bistability. The parameters η and κ are the deviations of the aridity and cooperativity critical parameters, respectively. ν and γ are linear and nonlinear diffusion coefficients, respectively. The last term is a nonlinear hyperdiffusion controlled by α. The parameters $\{\nu, \gamma, \alpha\}$ depend on the strength of the competitive feedback, the seed's diffusion, and the shape of the kernels ϕ_f, ϕ_c, and ϕ_d [30]. The model equation (2) has three homogeneous states: the bare state $b = 0$ [black line in Fig. 2(d)] and $b_\pm = (\kappa \pm \sqrt{\kappa^2 - 4\eta})/2$ [blue line in Fig. 2(d)]. The $b_\pm$ equilibria are connected by a saddle-node bifurcation at $\eta_{sn} = \kappa^2/4$ with κ positive. The uniform solution b_- is always unstable. For small aridity, the vegetated state b_+ is stable. When the aridity is increased the uniform cover suffers a spatial instability. This spatial instability with critical wavelength $\lambda_c = 2\pi\sqrt{2\alpha/(\gamma - \nu/b_c)}$ occurs at $\eta \equiv \eta_c$, where η_c satisfies the implicit condition $4\alpha b_c^2(2b_c - \kappa) = (\gamma b_c - \nu)^2$ with $b_c \equiv b_+(\eta_c)$. Hence, the homogeneous cover b_+ is unstable to patterns within the range $\eta_c \leqslant \eta \leqslant \eta_{sn}$ [see Fig. 2(d)]. By fixing the parameters $\{\kappa, \nu, \gamma, \alpha\}$ in Eq. (2), labyrinthine patterns are stable within the aridity range $[\eta_l, \eta_r]$ as shown in Fig. 2(d).

To model the effect of heterogeneities in the labyrinths of Eq. (2), in principle, we must promote all parameters to be spatially dependent; that is, one should consider five functions $[\eta(\mathbf{r}), \kappa(\mathbf{r}), \alpha(\mathbf{r}), \nu(\mathbf{r}), \gamma(\mathbf{r})]$, which makes the theoretical and numerical studies cumbersome. To shed light on the effect of heterogeneities in the labyrinthine patterns, we promote the aridity parameter to be spatially dependent $\eta(\mathbf{r})$ and keep the other parameters homogeneous. Hence, in the following analysis, we focus on the model equation (2) with heterogeneous aridity $\eta(\mathbf{r}) = \eta + \sqrt{\Gamma}\xi(\mathbf{r})$, where η accounts for the mean aridity. This average value is inside the aridity range $[\eta_l, \eta_r]$. $\xi(\mathbf{r})$ models the spatial variations with zero mean value $\langle\xi(\mathbf{r})\rangle = 0$ and intensity level Γ. The heterogeneities $\xi(\mathbf{r})$ can be spatially independent (delta correlated) or correlated. To obtain a spatially correlated function $\xi(\mathbf{r})$ characterized by a correlation length d, we consider a relaxation diffusive process with a random initial condition, which evolves until a given time [57]. Note that the results presented below are qualitatively similar if all parameters are spatially dependent.

IV. RESULTS

Let us introduce the spatially averaged biomass $\langle b \rangle \equiv \int_0^L \int_0^L b(\mathbf{r}, t)dx\,dy/L^2$, where L^2 is the system size. The charts

in the left panel of Fig. 2 show the temporal evolution to equilibrium for $\langle b \rangle$ according to Eq. (2) starting from the vegetated state b_+ in the symmetry-breaking regime $\eta_c \leqslant \eta \leqslant \eta_{sn}$. Figure 2(a) corresponds to the homogeneous case, $\Gamma = 0$, exhibiting an ideal labyrinthine pattern. Figure 2(b) represents the noncorrelated spatial variations, while Figs. 2(c) and 2(d) show the spatially correlated cases. In these cases, the striped structure of the labyrinthine pattern becomes locally distorted. Figure 2(e) shows the bifurcation diagram of Eq. (2). The labyrinthinelike patterns (dotted plots) are characterized by their averaged biomass $\langle b \rangle$. The green dotted curve indicates a branch of an ideal labyrinthine pattern when $\Gamma = 0$, which is stable in the range $\eta_l \leqslant \eta \leqslant \eta_r$. By increasing the aridity level, the labyrinth exhibits a transition to a mosaic of localized spots at $\eta > \eta_r$. When decreasing the aridity parameter, the labyrinthine pattern becomes clusters of hexagonal gaps at $\eta < \eta_l$ [31]. The blue dotted curve represents the stable branch of a vegetation pattern when $\Gamma \neq 0$ and ξ is noncorrelated. The red and black dotted curves are the stable branches of labyrinthinelike patterns under correlated heterogeneous conditions. We note that the impact of heterogeneities in the averaged biomass is not always strong [see red and blue dots in Fig. 2(e)]. Thus, other types of spatial tools are needed to understand and differentiate the labyrinthinelike equilibria of Eq. (2).

To characterize labyrinthine equilibria under homogeneous ($\Gamma = 0$) and heterogeneous ($\Gamma \neq 0$) conditions, we consider first the aridity distributions depicted in Fig. 3, and next we concentrate on the biomass densities $b_{eq}(\mathbf{r})$ shown in Fig. 4. We analyze the spatial structure of these aridities and biomass equilibria employing the Fourier transform amplitude $|\mathcal{F}(\mathbf{k})|^2 = |\int g(\mathbf{r})e^{i\mathbf{k}\cdot\mathbf{r}}dx\,dy|^2$ and the structure factor $S(k) = \int_{-\pi}^{\pi} |\mathcal{F}(\mathbf{k})|k\,d\theta$, where $\mathbf{k} = (k\cos\theta, k\sin\theta)$, and $g(\mathbf{r})$ can be either $b_{eq}(\mathbf{r})$ or $\eta(\mathbf{r})$. The homogeneous and noncorrelated heterogeneous aridity distributions are characterized by a delta and a noisy flat $|\mathcal{F}(\mathbf{k})|^2$, respectively [see Figs. 3(a) and 3(b)]. The spatially correlated aridities have a nontrivial $S(k)$ shape associated with their coherent distribution [cf. Figs. 3(c) and 3(d)].

Let us now have a look at the biomass densities $b_{eq}(\mathbf{r})$ displayed in the top panels of Fig. 4. These equilibria are obtained by numerical simulations of the model equation (2) in square boxes. The spatial profiles of the aridity $\eta(\mathbf{r})$ used in these numerical simulations are the same as those in Fig. 3. Under homogeneous conditions, the biomass density exhibits a *perfect* labyrinthine pattern. The corresponding spectrum and the structure factor are shown in Fig. 4(a). From this figure, we see that the spectrum has a powdered ringlike shape and the structure factor presents a well-defined peak at $k = k_c$ [see Fig. 4(a)]. The finite width in the structure factor is attributed to the defects size and local variations of the wavevector [9]. The powdered ringlike shape indicates no preferred direction since the system is isotropic in the (x, y) plane. The full width at half maximum of $S(k)$ for the labyrinth in Fig. 4(a) is $w \approx 0.15k_c$. It is obtained by fitting a Lorentzian squared curve to the structure factor [58,59]. We define $w_h = k_c \pm w/2$ as the characteristic wavevector range of the perfect labyrinthine pattern, which emerges from a symmetry-breaking instability in Eq. (2). Figure 4(b) shows an equilibrium in the case of $\Gamma \neq 0$ and delta-correlated $\xi(\mathbf{r})$.
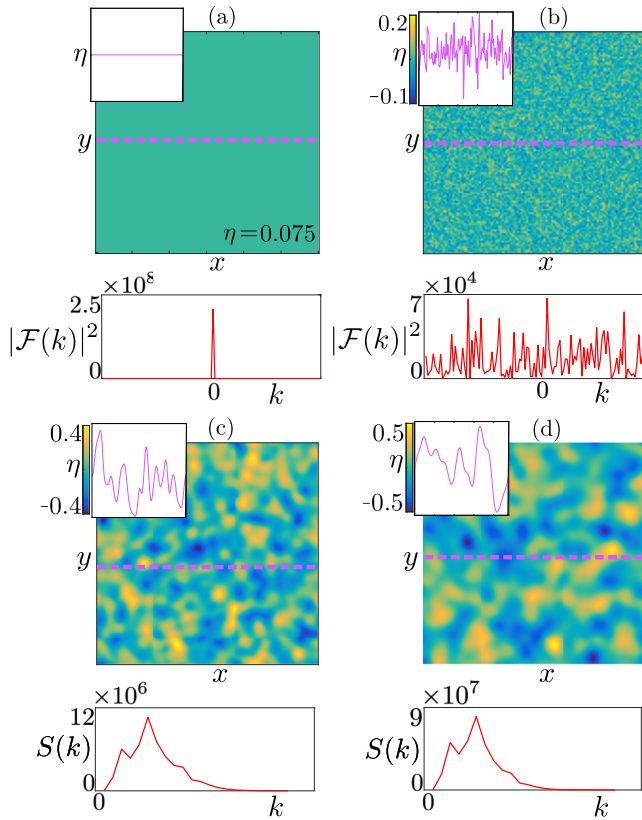
FIG. 3. Spatial distributions of the aridity parameters $\eta(\mathbf{r}) = \eta + \sqrt{\Gamma}\xi(\mathbf{r})$ with $\eta = 0.075$. In the top panels, the aridity distributions are shown. The insets correspond to an arbitrary one-directional cut represented by dashed pink lines. The lower panels illustrate the spatial structure of the distributions by their Fourier transform amplitude $|\mathcal{F}(\mathbf{k})|^2$ or structure factor $S(k)$. Other parameters are (a) $\Gamma = 0$; (b) $\sqrt{\Gamma} = 0.2$, $d/L = 0$; (c) $\sqrt{\Gamma} = 0.2$, $d/L = 0.08$; and (d) $\sqrt{\Gamma} = 0.5$, $d/L = 0.1$.

FIG. 4. Spatial characterization of the equilibria from Eq. (2) with $\kappa = 0.6$, $\nu = 0.011$, $\gamma = 0.5$, $\alpha = 0.125$, and $\eta = 0.075$. The top panels in each subfigure display the steady-state vegetated covers from the model equation (2) considering the aridity profiles $\eta(\mathbf{r})$ depicted in Fig. 3, respectively. The blue and yellow curves of the bottom panels indicate the normalized structure factor $\bar{S}(k) \equiv S(k)/S_h(k_c)$, and $\bar{S}_h(k) \equiv S_h(k)/S_h(k_c)$, respectively. $S_h(k)$ is the structure factor in the homogeneous case. The insets in the bottom panels correspond to the Fourier transform $|\mathcal{F}(k)|^2$ of the solutions from Eq. (2). The wavevector $\hat{k}$ illustrates the maximum of $\bar{S}(k)$ when heterogeneities are present.

In this case, the labyrinth does not exhibit long fingers as in the homogeneous case due to the proliferation of local spots. Indeed, the heterogeneities introduce local disturbances in the wavevector reflected in the widening of $S(k)$ [cf. blue curve and inset in the bottom panel of Fig. 4(b)]. When the heterogeneities are sufficiently intense ($\sqrt{\Gamma} = 0.2$) and correlated ($d/L = 0.08$), the perfect labyrinthine pattern loses its structure and blobs of vegetation or bare soil emerge [see Fig. 4(c)]. In this aridity level, the maximum of the structure factor $\hat{k}$ lies outside w_h [cf. blue curve in the bottom panel of Fig. 4(c)]. We define this shift in $\hat{k}$ as a transition from perfect labyrinths ($|\hat{k} - k_c| < w_h$) to *imperfect labyrinthine patterns* ($|\hat{k} - k_c| > w_h$). When further increasing the correlation and the intensity level of the heterogeneities ($\sqrt{\Gamma} = 0.5$ and $d/L = 0.1$), the labyrinthine pattern is almost completely lost. A few vegetated fingers coexist with homogeneous islands of vegetation and bare soil [see the top panel in Fig. 4(d)]. As seen in the bottom panel of Fig. 4(d), the peak of the structure factor exhibits a significant shift (from $\hat{k} = 0.9k_c$ to $\hat{k} = 0.55k_c$) toward the center of the spectrum. Moreover, the global Fourier spectrum loses its powdered ring shape [see the inset in the bottom panel of Fig. 4(d)]. In this regime, the spatial profiles

of the aridity and the biomass density are strongly correlated [see the lower panels of Fig. 3(d) and Fig. 4(d), respectively]. We have termed this spatial structure as *disordered self-organization*.

A phase diagram is generated using numerical simulations of Eq. (2), as shown in Fig. 5(a). The diagram depicts the existence and stability domains of three types of vegetation structures: perfect and imperfect labyrinths and disordered self-organization. We can see that perfect labyrinthine patterns can persist for different combinations of $\sqrt{\Gamma}$ and d/L. Given a minimum intensity level value $\sqrt{\Gamma}$ or degree of correlation d/L, the perfect labyrinths bifurcate to imperfect labyrinthine patterns. When heterogeneities are strong enough, the system exhibits disordered self-organization. We stress that the transition between different labyrinthinelike textures can be triggered solely by $\sqrt{\Gamma}$ or d/L [cf. dashed arrows in Fig. 5(a)]. For example, Fig. 5(b) show the variation of $\hat{k}/k_c$ by fixing $d/L = 0.08$ and moving $\sqrt{\Gamma}$. The insets (i)–(iii) along the diagram illustrate the change in $\bar{S}(k)$ and $\hat{k}$ as the biomass
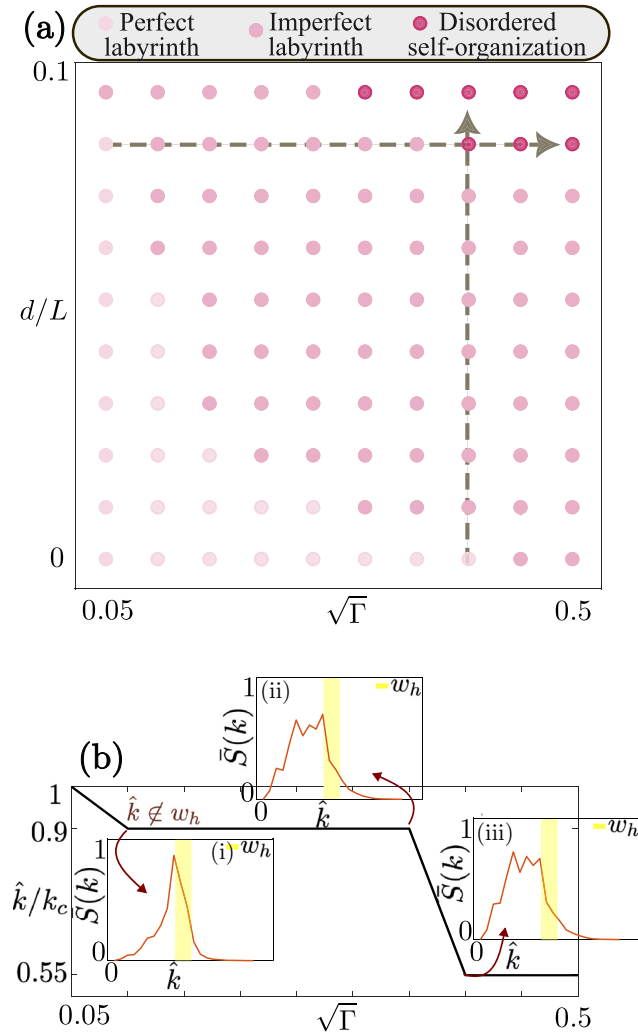
FIG. 5. Phase diagram of vegetation patterns in heterogeneous environments. (a) Phase diagram of the global spatial structure of Eq. (2) with $\kappa = 0.6$, $\nu = 0.011$, $\gamma = 0.5$, $\alpha = 0.125$, and $\eta = 0.075$ as a function of the intensity level $\sqrt{\Gamma}$ and the degree of correlation d/L. The different phases are perfect labyrinthine patterns ($\hat{k} \approx k_c$), imperfect labyrinthine patterns ($\hat{k} \approx 0.9k_c$), and disordered self-organizations ($\hat{k} \approx 0.55k_c$). The dashed gray arrows illustrate possible transition paths between the equilibria. (b) Transition triggered by changing the intensity of the heterogeneities $\sqrt{\Gamma}$ given a correlation $d/L = 0.8$ in the aridity distribution. The insets (i)–(iii) show the normalized structure factor $\bar{S}(k)$ and its peak position $\hat{k}$. The yellow rectangle depicts the characteristic wavevector range w_h of the labyrinth with $\Gamma = 0$.

FIG. 6. Phase diagram of the local structure of labyrinthine patterns from Eq. (2) with $\kappa = 0.6$, $\nu = 0.0113$, $\gamma = 0.5$, $\alpha = 0.125$, and $\eta = 0.075$. (a) Colormap of the local two-mode fraction ϕ_2 for different intensity level Γ and correlation d/L of the heterogeneities $\xi(\vec{r})$. The segmented yellow lines separate the three regions of Fig. 5: (i) perfect labyrinthine patterns, (ii) imperfect labyrinthine patterns, and (iii) disordered self-organization. (b) Spatial division of a steady-state vegetation pattern, with $\sqrt{\Gamma} = 0.4$ and $d/L = 0.04$ (☆), in windows of size $2.3\lambda_c$. (c) Local Fourier transform $|\mathcal{F}(\tilde{k})|^2$ of each window. The orange borders in (b) and (c) indicate that the local pattern fulfills the criteria of being dominantly a stripe.

departures from the perfect labyrinths. The transition between imperfect labyrinths and disordered self-organization [(ii) → (iii)] resembles the disappearance of scurfy labyrinthine patterns in a variational Swift-Hohenberg model [10].

In what follows, we further numerically characterize the labyrinthinelike equilibria using local Fourier transforms. This statistical tool allows us to investigate the self-organization process at small spatial scales. Ideal labyrinthine patterns, for instance, are characterized by their local striped behavior. This feature can be extracted through the averaged

windowed Fourier transform [10]. The procedure consists of dividing the labyrinthine patterns into N windows of size s, calculating each window's Fourier transform, and then performing a projective average in Fourier space. The result is a single wave mode (stripe) local Fourier spectrum. The critical step is to choose the adequate size s. It has to be small enough to lose the pattern's isotropy and sufficiently big to account for the labyrinth wavelength. Then, the safe choice is $s \approx 2\lambda_c$. Here, we compute the local Fourier transform of the patterns obtained from Eq. (2) in windows of size

TABLE I. Summary of the sensitivity analysis. The sensitivity indices $Si(\phi_2^{pi})$ and $Si(\phi_2^{id})$ are associated to the transition fractions ϕ_2^{pi} and ϕ_2^{id}, respectively.

	η	κ	ν	γ	α	s	th
Original value	0.085	0.6	0.01	0.5	0.125	$2.3\lambda_c$	0.8
$Si(\phi_2^{pi})$	0.10	0.09	0.11	0.07	0.14	0.16	0.26
$Si(\phi_2^{id})$	0.33	0.17	0.12	<0.01	0.23	0.11	0.21

$s = 2.3\lambda_c$ because L/s is an integer number. As a consequence of imperfect labyrinths and disordered self-organizations, the projective average process is not a good approach. To amend this, we introduce the three largest values of the local Fourier transforms $\mathcal{F}_1 \geqslant \mathcal{F}_2 \geqslant \mathcal{F}_3$. We define a local window to be dominantly a stripe if $\mathcal{F}_1 = \mathcal{F}_2$ (dominated by two peaks, i.e., a stripe) and $\mathcal{F}_3 \leqslant 0.8\mathcal{F}_1$. The threshold (th = 0.8), which takes into account the defects of the labyrinths, is selected to maximize the fraction $\phi_2 = N_s/N$ of the labyrinthine pattern under homogeneous conditions. N_s is the number of windows exhibiting stripes.

Figure 6(a) shows the fraction ϕ_2 for different combinations of the intensity level Γ and degree of correlation d/L of the heterogeneities. Additionally, the dashed yellow lines indicate the transitions related to the global spatial structure of the biomass density (see Fig. 5). We note that the transition from perfect labyrinths to imperfect labyrinths is marked by $\phi_2^{pi} = 0.61 \pm 0.06$. As well, imperfect labyrinths become disordered self-organizations when $\phi_2^{id} = 0.30 \pm 0.02$. Figures 6(b) and 6(c) illustrate the local structure and the windowed Fourier transform of an imperfect labyrinthine pattern with $N_s = 6$ as depicted by the orange squares. We note that the transitions in the $(\sqrt{\Gamma}, d/L)$ parameter space depend on the choices of $[\eta, \kappa, \gamma, \alpha, \nu]$. Hence, we highlight that a suitable model parametrization is needed for extending our classifications to natural landscapes.

To test the robustness of our predictions against modeling decisions, we have performed a sensitivity analysis by changing in $\pm 10\%$ the original values of the parameters chosen to observe labyrinths in Eq. (2), the window size s, and the threshold th. When varying the window length, we use the same number of windows N as in the original case by overlapping the windows or by not considering the boundaries of the simulation boxes. To evaluate the sensitivity, the simple sensitivity index $Si(h) = |1 - h_{\min}/h_{\max}|$ is used, where $h_{\min}$ and $h_{\max}$ are a model output when a parameter was decreased or increased, respectively [60]. Values closer to 1 indicate high sensitivity, while $Si(h) < 0.01$ means no sensitivity to variations. We consider the averaged fractions ϕ_2^{pi} and ϕ_2^{id} as model outputs with sensitivity indices $Si(\phi_2^{pi})$ and $Si(\phi_2^{id})$, respectively (see Table I). The transitions from perfect to imperfect labyrinths and imperfect labyrinths to disordered self-organizations are always observed when varying the parameters in Table I.

The sensibility analysis shows that ϕ_2^{id} is sensible to the mean aridity parameter η, which is related to the system being near the boundaries η_l and η_r (see Fig. 2). Additionally, this transition is highly affected by the spatial coupling parameter α and could be related to changes in λ_c. Table I suggests that

both ϕ_2^{pi} and ϕ_2^{id} are sensible to the threshold th, which can be attributed to a wrong counting of the N_s values.

V. DISCUSSION AND CONCLUSIONS

We have investigated the effect of heterogeneous conditions on a pattern-forming ecological model of semiarid and arid landscapes. We have considered a well-known model based on the relationship between the vegetation biomass and the facilitation-competition interactions operating within plants. We have further simplified the analysis by focusing on a reduced model, Eq. (2), and we have restricted our study to a single species that accounts for most of the biomass. Motivated by topographic variations along labyrinthinelike self-organization in Niger and Sudan, we have modeled the heterogeneities as a spatial-dependent aridity parameter. The spatial fluctuations act around a mean aridity value with a certain intensity level. These variations can be correlated with a given correlation length.

By increasing the intensity level and the correlation length of the aridity heterogeneities, we have shown evidence of imperfect labyrinthine patterns and disordered self-organizations. These equilibria of Eq. (2) qualitatively resemble the real labyrinthinelike vegetation patterns observed in satellite images of arid and semiarid landscapes. Furthermore, we have found that perfect labyrinthine patterns are persistent until a critical degree of heterogeneity is reached, where they become imperfect labyrinths. Further increasing the heterogeneities, the spatial structure of the imperfect labyrinth is eventually lost to a disordered self-organization, which is governed by the spatial distribution of the aridity. Based on the peak's position and width of the global structure factor, we have characterized the transitions between equilibria and built a phase diagram. A windowed Fourier transform is used to measure the departure from perfect labyrinthine patterns as a function of heterogeneities.

An interesting future research is the identification of perfect labyrinths, imperfect labyrinths, and disordered self-organizations in real ecosystems by applying the tools and modeling introduced here. To achieve this natural classification, on-site measurements in arid environments populated by labyrinthinelike vegetation patterns will be needed to validate the application of the reduced model, Eq. (2), and to verify if the model parameters are realistic or not. It will be crucial to determine the parameters η and α, as they significantly impact the transitions between labyrinthinelike vegetation patterns. For example, if the labyrinthinelike landscapes of Niger and Sudan (Fig. 1) are well described by model equation (2) and the parameters chosen are characteristic of these particular places, our classification could be applied by extending the local analysis presented here. In fact, our modeling can be used to identify the threshold th for the Sudan and Niger regions in Fig. 1. We hypothesize that these labyrinths are imperfect; that is, they are sustained by a minimum level of spatially correlated heterogeneity, and are the consequence of a combination of a symmetry-breaking instability and heterogeneous environmental conditions. Moreover, *in situ* observations of topography and resource distribution could reveal if a more complex way to incorporate heterogeneities

is needed or if our straightforward approach, based on the intensity level and degree of correlation, is sufficient and reasonable.

Our theoretical findings can be used with other modeling approaches to obtain more realistic labyrinthine patterns, such as reaction-diffusion systems where water dynamics is included explicitly [20,21]. Additionally, our classification can also be applied in different scientific contexts where labyrinths are experimentally observed. For example in fluid mechanics, liquid crystals, optics, biology, and chemistry [61–65], where the sources of heterogeneity are diverse (e.g., thermal fluctuations, experimental imperfections, boundary conditions, inhomogeneous forcing, material defects).

[1] G. Nicolis and I. Prigogine, *Self-Organization in Non-Equilibrium Systems* (Wiley, New York, 1977).

[2] M. Cross and H. Greenside, *Pattern Formation and Dynamics in Non-Equilibrium Systems* (Cambridge University Press, New York, 2009).

[3] J. D. Murray, *Mathematical Biology: I. An Introduction* (Springer, New York, 2002).

[4] R. V. Solé and J. Bascompte, *Self-Organization in Complex Ecosystems. (MPB-42)* (Princeton University Press, Princeton, NJ, 2006).

[5] A. M. Turing, The chemical basis of morphogenesis, Philos. Trans. R. Soc. London, Ser. B **237**, 37 (1952).

[6] I. Prigogine and R. Lefever, Symmetry breaking instabilities in dissipative systems. II, J. Chem. Phys. **48**, 1695 (1968).

[7] R. Hoyle and R. B. Hoyle, *Pattern Formation: An Introduction to Methods* (Cambridge University Press, Cambridge, UK, 2006).

[8] T. Passot and A. C. Newell, Towards a universal theory for natural patterns, Phys. D (Amsterdam, Neth.) **74**, 301 (1994).

[9] M. Le Berre, E. Ressayre, A. Tallet, Y. Pomeau, and L. Di Menza, Example of a chaotic crystal: The labyrinth, Phys. Rev. E **66**, 026203 (2002).

[10] S. Echeverría-Alar and M. G. Clerc, Labyrinthine patterns transitions, Phys. Rev. Res. **2**, 042036(R) (2020).

[11] R. E. Rosensweig, M. Zahn, and R. Shumovich, Labyrinthine instability in magnetic and dielectric fluids, J. Magn. Magn. Mater. **39**, 127 (1983).

[12] K. J. Lee, W. McCormick, Q. Ouyang, and H. L. Swinney, Pattern formation by interacting chemical fronts, Science **261**, 192 (1993).

[13] P. Oswald and P. Pieranski, *Nematic and Cholesteric Liquid Crystals: Concepts and Physical Properties Illustrated by Experiments* (CRC, Boca Raton, FL, 2005).

[14] S. Park, Manipulating the sequences of block copolymer patterns on corrugated substrates, Polymer **180**, 121726 (2019).

[15] A. Nakhoul, C. Maurice, M. Agoyan, A. Rudenko, F. Garrelie, F. Pigeon, and J.-P. Colombier, Self-organization regimes induced by ultrafast laser on surfaces in the tens of nanometer scales, Nanomaterials **11**, 1020 (2021).

[16] P. Kavle, J. A. Zorn, A. Dasgupta, B. Wang, M. Ramesh, L.-Q. Chen, and L. W. Martin, Strain-driven mixed-phase domain architectures and topological transitions in $Pb_{1-x}Sr_x TiO_3$ thin films, Adv. Mater. **34**, 2203469 (2022).

[17] W. Macfadyen, Soil and vegetation in British Somaliland, Nature (London) **165**, 121 (1950).

[18] R. Lefever and O. Lejeune, On the origin of tiger bush, Bull. Math. Biol. **59**, 263 (1997).

[19] O. Lejeune and M. Tlidi, A model for the explanation of tiger bush vegetation stripes, J. Veg. Sci. **10**, 201 (1999).

[20] J. von Hardenberg, E. Meron, M. Shachak, and Y. Zarmi, Diversity of Vegetation Patterns and Desertification, Phys. Rev. Lett. **87**, 198101 (2001).

[21] M. Rietkerk, M. C. Boerlijst, F. van Langevelde, R. HilleRisLambers, J. v. de Koppel, L. Kumar, H. H. Prins, and A. M. de Roos, Self-organization of vegetation in arid ecosystems, Am. Nat. **160**, 524 (2002).

[22] V. Deblauwe, N. Barbier, P. Couteron, O. Lejeune, and J. Bogaert, The global biogeography of semi-arid periodic vegetation patterns, Global Ecol. Biogeogr. **17**, 715 (2008).

[23] F. Borgogno, P. D'Odorico, F. Laio, and L. Ridolfi, Mathematical models of vegetation pattern formation in ecohydrology, Rev. Geophys. **47**, RG1005 (2009).

[24] V. Deblauwe, P. Couteron, O. Lejeune, J. Bogaert, and N. Barbier, Environmental modulation of self-organized periodic vegetation patterns in Sudan, Ecography **34**, 990 (2011).

[25] L. Mander, S. C. Dekker, M. Li, W. Mio, S. W. Punyasena, and T. M. Lenton, A morphometric analysis of vegetation patterns in dryland ecosystems, R. Soc. Open Sci. **4**, 160443 (2017).

[26] O. Lejeune, M. Tlidi, and P. Couteron, Localized vegetation patches: A self-organized response to resource scarcity, Phys. Rev. E **66**, 010901(R) (2002).

[27] M. Rietkerk, S. C. Dekker, P. C. De Ruiter, and J. van de Koppel, Self-organized patchiness and catastrophic shifts in ecosystems, Science **305**, 1926 (2004).

[28] E. Meron, H. Yizhaq, and E. Gilad, Localized structures in dryland vegetation: Forms and functions, Chaos **17**, 037109 (2007).

[29] P. Couteron, F. Anthelme, M. Clerc, D. Escaff, C. Fernandez-Oto, and M. Tlidi, Plant clonal morphologies and spatial patterns as self-organized responses to resource-limited environments, Philos. Trans. R. Soc. A **372**, 20140102 (2014).

[30] M. Tlidi, E. Berríos-Caro, D. Pinto-Ramo, A. Vladimirov, and M. G. Clerc, Interaction between vegetation patches and gaps: A self-organized response to water scarcity, Phys. D (Amsterdam, Neth.) **414**, 132708 (2020).

[31] M. G. Clerc, S. Echeverría-Alar, and M. Tlidi, Localised labyrinthine patterns in ecosystems, Sci. Rep. **11**, 18331 (2021).

[32] M. Van Rooyen, G. Theron, N. Van Rooyen, W. Jankowitz, and W. Matthews, Mysterious circles in the Namib desert: Review of hypotheses on their origin, J. Arid. Environ. **57**, 467 (2004).

[33] M. Tlidi, R. Lefever, and A. Vladimirov, On vegetation clustering, localized bare soil spots and fairy circles, Lect. Notes Phys. **751**, 381 (2008).

[34] N. Juergens, The biological underpinnings of Namib desert fairy circles, Science **339**, 1618 (2013).

[35] M. D. Cramer and N. N. Barger, Are Namibian "fairy circles" the consequence of self-organizing spatial vegetation patterning? PLoS One **8**, e70876 (2013).

[36] C. Fernandez-Oto, M. Tlidi, D. Escaff, and M. Clerc, Strong interaction between plants induces circular barren patches: Fairy circles, Philos. Trans. R. Soc. A **372**, 20140009 (2014).

[37] D. Escaff, C. Fernandez-Oto, M. G. Clerc, and M. Tlidi, Localized vegetation patterns, fairy circles, and localized patches in arid landscapes, Phys. Rev. E **91**, 022924 (2015).

[38] S. Getzin, K. Wiegand, T. Wiegand, H. Yizhaq, J. von Hardenberg, and E. Meron, Adopting a spatially explicit perspective to study the mysterious fairy circles of Namibia, Ecography **38**, 1 (2015).

[39] C. E. Tarnita, J. A. Bonachela, E. Sheffer, J. A. Guyton, T. C. Coverdale, R. A. Long, and R. M. Pringle, A theoretical foundation for multi-scale regular vegetation patterns, Nature (London) **541**, 398 (2017).

[40] I. Bordeu, M. G. Clerc, P. Couteron, R. Lefever, and M. Tlidi, Self-replication of localized vegetation patches in scarce environments, Sci. Rep. **6**, 33703 (2016).

[41] M. Tlidi, I. Bordeu, M. G. Clerc, and D. Escaff, Extended patchy ecosystems may increase their total biomass through self-replication, Ecol. Indic. **94**, 534 (2018).

[42] M. Tlidi, M. Clerc, D. Escaff, P. Couteron, M. Messaoudi, M. Khaffou, and A. Makhoute, Observation and modelling of vegetation spirals and arcs in isotropic environmental conditions: Dissipative structures in arid landscapes, Philos. Trans. R. Soc. A **376**, 20180026 (2018).

[43] S. Kéfi, M. Rietkerk, C. L. Alados, Y. Pueyo, V. P. Papanastasis, A. ElAich, and P. C. De Ruiter, Spatial vegetation patterns and imminent desertification in Mediterranean arid ecosystems, Nature (London) **449**, 213 (2007).

[44] F. Meloni, G. M. Nakamura, C. R. Granzotti, and A. S. Martinez, Vegetation cover reveals the phase diagram of patch patterns in drylands, Phys. A (Amsterdam, Neth.) **534**, 122048 (2019).

[45] P. Adler, D. Raff, and W. Lauenroth, The effect of grazing on the spatial heterogeneity of vegetation, Oecologia **128**, 465 (2001).

[46] P. D'Odorico, F. Laio, and L. Ridolfi, Vegetation patterns induced by random climate fluctuations, Geophys. Res. Lett. **33**, L19404 (2006).

[47] P. D'Odorico, F. Laio, A. Porporato, L. Ridolfi, and N. Barbier, Noise-induced vegetation patterns in fire-prone savannas, J. Geophys. Res. **112**, G02021 (2007).

[48] T. E. Franz, E. G. King, K. K. Caylor, and D. A. Robinson, Coupling vegetation organization patterns to soil resource heterogeneity in a central Kenyan dryland using geophysical imagery, Water Resour. Res. **47**, W07531 (2011).

[49] I. Rodriguez-Iturbe, Z. Chen, A. C. Staver, and S. A. Levin, Tree clusters in savannas result from islands of soil moisture, Proc. Natl. Acad. Sci. USA **116**, 6679 (2019).

[50] K. Pal, S. Deb, and P. S. Dutta, Tipping points in spatial ecosystems driven by short-range correlated noise, Phys. Rev. E **106**, 054412 (2022).

[51] P. Villa Martín, J. A. Bonachela, S. A. Levin, and M. A. Muñoz, Eluding catastrophic shifts, Proc. Natl. Acad. Sci. USA **112**, E1828 (2015).

[52] M. Scheffer, S. Carpenter, J. A. Foley, C. Folke, and B. Walker, Catastrophic shifts in ecosystems, Nature (London) **413**, 591 (2001).

[53] J. Greenwood, The development of vegetation patterns in Somaliland protectorate, Geogr. J. **123**, 465 (1957).

[54] C. Montana, The colonization of bare areas in two-phase mosaics of an arid ecosystem, J. Ecol. **80**, 315 (1992).

[55] B. Bookhagen and D. W. Burbank, Topography, relief, and TRMM-derived rainfall variations along the Himalaya, Geophys. Res. Lett. **33**, L08405 (2006).

[56] O. Lejeune, M. Tlidi, and R. Lefever, Vegetation spots and stripes: Dissipative structures in arid landscapes, Int. J. Quantum Chem. **98**, 261 (2004).

[57] D. Pinto-Ramos, S. Echeverría-Alar, M. G. Clerc, and M. Tlidi, Vegetation covers phase separation in inhomogeneous environments, Chaos, Solitons & Fractals **163**, 112518 (2022).

[58] M. C. Cross and D. I. Meiron, Domain Coarsening in Systems Far from Equilibrium, Phys. Rev. Lett. **75**, 2152 (1995).

[59] T. Galla and E. Moro, Defect formation in the Swift-Hohenberg equation, Phys. Rev. E **67**, 035101(R) (2003).

[60] S. Echeverría, M. B. Hausner, N. Bambach, S. Vicuña, and F. Suárez, Modeling present and future ice covers in two antarctic lakes, J. Glaciol. **66**, 11 (2020).

[61] J. Gollub, A. McCarriar, and J. Steinman, Convective pattern evolution and secondary instabilities, J. Fluid Mech. **125**, 259 (1982).

[62] M. Seul and D. Andelman, Domain shapes and patterns: The phenomenology of modulated phases, Science **267**, 476 (1995).

[63] Q.-X. Liu, P. M. J. Herman, W. M. Mooij, J. Huisman, M. Scheffer, H. Olff, and J. van de Koppel, Pattern formation at multiple spatial scales drives the resilience of mussel bed ecosystems, Nat. Commun. **5**, 5234 (2014).

[64] A. Pandey, J. D. Scheel, and J. Schumacher, Turbulent superstructures in Rayleigh-Bénard convection, Nat. Commun. **9**, 2118 (2018).

[65] Y. Soupart and P. Aguilera-Rojas (private communication).

7.1. Perspectives

The present chapter was devoted to analyzing the stabilization of perfect labyrinths, imperfect labyrinths, and disordered self-organizations in a local vegetation model (2.13) with a spatial dependent aridity parameter. An interesting future research is the identification of perfect labyrinths, imperfect labyrinths, and disordered self-organizations in real ecosystems by applying the framework introduced in this study. To achieve this classification, on-site measurements in arid environments populated by labyrinthine-like vegetation patterns will be needed to validate the application of the reduced model Eq. (2.13) and to verify if the model parameters are realistic or not. Moreover, in-situ observations of topography and resource distribution could reveal if a more complex way to incorporate heterogeneities is needed or if our straightforward approach is sufficient and reasonable.

As a final remark, we note that our theoretical findings can be applied using other modeling approaches, such as reaction-diffusion systems, where water dynamics is included explicitly [46, 47] as shown in Fig. 7.3.
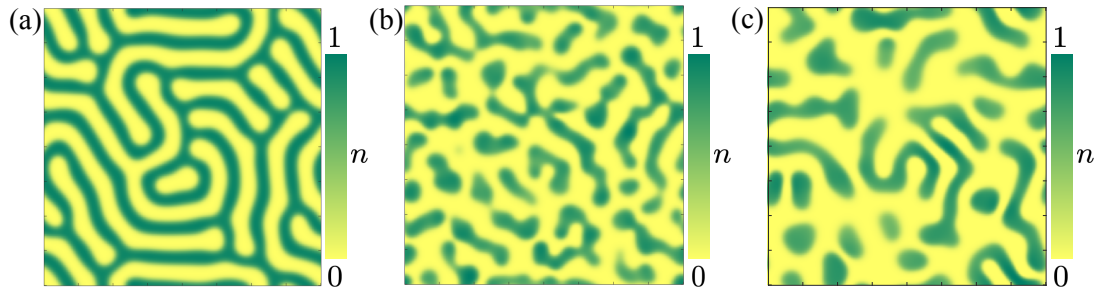
Figure 7.3: Numerical integrations of Eqs. (1) and (2) from Reference [46], considering the mortality parameter μ to be space dependent. (a) Perfect labyrinthine pattern. (b) Imperfect labyrinthine pattern. (c) Disordered self-organization. The field n accounts for the vegetation biomass. The simulations are performed in squared boxes of size 400×400.

Chapter 8

Localized dissipative vortices in chiral nematic liquid crystal cells (Physical Review Research 4, L022021)

In the previous chapter, we have studied the emergence of labyrinthinelike patterns in an inherently inhomogeneous real system. In this and the following two chapters, we will investigate the appearance of perfect labyrinthine patterns in a controlled experiment (almost a homogenous real system) of chiral nematic liquid crystals under geometrical frustration. A distinctive feature of these labyrinths is that they are not consequence of a spatial symmetry-breaking instability, which has been the rule of the labyrinthine patterns studied in this dissertation so far. Interestingly, to our knowledge, they emerge through two growth modes of cholesteric fingers of type 1 (CF1): invagination and tip-splitting [64]. In this and the next chapter, we will focus only on the tip-splitting process.

In the context of frustrated chiral nematic liquid crystals, the developing of labyrinthine patterns occurs near the winding/unwinding transition when a critical degree of frustration is reached [158, 36, 72, 37] and the twisted phase of the cholesterics is recovered. Figure 8.1(a) shows the appearance of a CF1 in an unwound background at the temperature-triggered transition, highlighting their asymmetric tips (rounded and pointed). As time evolves ($t_4 > t_3 > t_2 > t_1$), the finger grows by straightening its pointed tip while producing some side branches, and by the ramification of their rounded tips (tip-splitting instability) [140, 158, 36, 72, 37]. Eventually, the pointed tip merges with the cholesteric interface of another cholesteric finger, and all the rounded tips fill the sample by the splitting of their tips giving rise to a perfect labyrinthine pattern (t_4). We note that upon cooling the sample, fingers retract, and the frustrated unwound phase is the equilibrium again. Now, let us take a closer look at the merging process of pointed tips of CF1 by inspecting the particular case illustrated in Fig. 8.2. The figure shows the usual invasion of the cholesteric phase by tip-splitting of rounded tips and the straight elongation of pointed tips (see the red arrows in t_1). However, a peculiarity is that two *domains*, created by successive ramifications of a starting CF1, close themselves through their pointed tips (see the pink path closing from t_2 to t_3) creating a closed loop of CF1. Starting from this texture, the dynamics when decreasing temperature is not only governed by the retraction of fingers, but also by the collapse of CF1 loops into chiral bubbles (cf. Fig 8.3) [159, 74, 160]. These localized twisted objects allow us to control the emergence of cholesteric labyrinthine patterns and avoid the creation of pointed tips. Figure. 8.4 displays the creation of a labyrinthine pattern, where cholesteric fingers grow

from chiral bubbles when the temperature is increased.
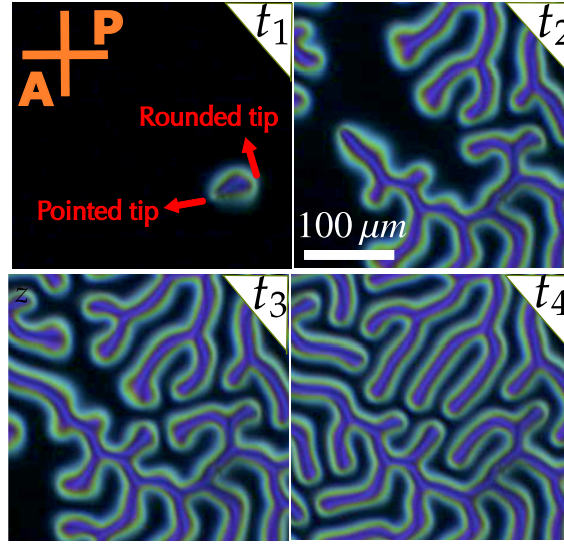
Figure 8.1: Sequence of temporal snapshots of the creation of a labyrinthine pattern ($t_4 > t_3 > t_2 > t_1$). At t_1, the appearance of a cholesteric finger of type 1 marks the onset of the winding transition. Subsequent snapshots illustrate the space-filling dynamics of the fingers, showing, in particular, a merging event between a pointed tip and a cholesteric interface at t_3. The snapshots were taken at $T = 51.7°C$, and the confinement ratio of the sample is $d/p = 0.7$.
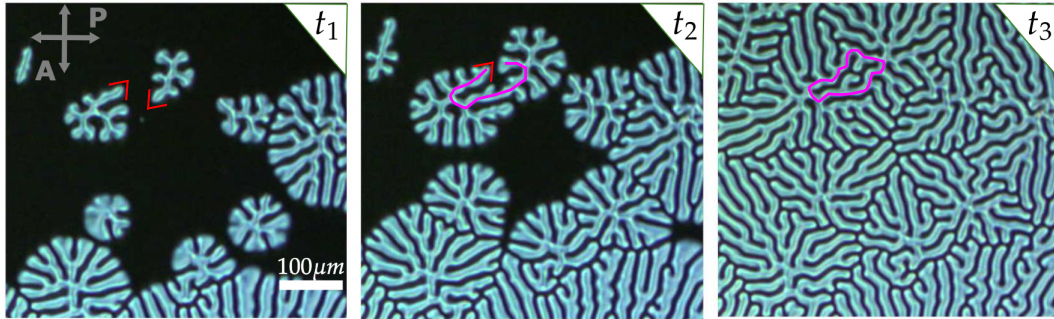
Figure 8.2: Sequence of temporal snapshots of the creation of a cholesteric labyrinthine pattern ($t_3 > t_2 > t_1$) showing the generation of a closed loop of CF1. The red arrows indicate the pointed tips of fingers, and the pink path illustrates the closing of the loop (from t_2 to t_3) due to two merging events. The snapshots were taken at $T = 51.3°C$, and the confinement ratio of the sample is $d/p < 26.6$.

The first step of our investigation is to understand the stabilization of chiral bubbles, so then we can study the emergence of labyrinthine patterns from the interface of the localized objects. To achieve our goal, we have proposed a variational amplitude equation based on symmetry arguments, multiscaling and the subcritical nature of the winding/unwinding transition. The model equation reads

$$\partial_t A = \mu A + \beta |A|^2 A - |A|^4 A + \nabla^2 A + \delta \partial_{\eta\eta} \bar{A} + \chi (A \partial_{\bar{\eta}} A - \bar{A} \partial_\eta A), \tag{8.1}$$

where A is a complex parameter accounting for the rotation in the $x - y$ plane, and the tilt from the z axis of the nematic director $\vec{n}$. $\partial_\eta = \partial_x + i\partial_y$ is a differential operator on the complex plane, the Wirtinger derivative [161]. The bifurcation parameter μ measures the distance from the critical transition point. The three first terms on the right-hand side of Eq. (8.1) model a subcritical bifurcation ($\beta > 0$). This transition presents a bistability range within which a Maxwell point exists [91, 92]. The fourth and fifth terms account for the isotropic and anisotropic elastic coupling in the system, respectively [162]. The last term models the mirror symmetry breaking, i.e., chirality [163].
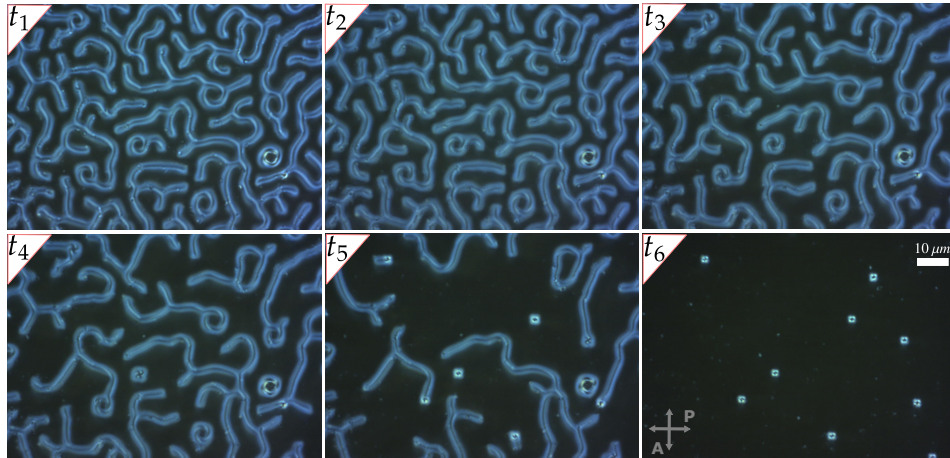
Figure 8.3: Temporal snapshots ($t_6 > t_5 > t_4 > t_3 > t_2 > t_1$) showing the retraction of fingers and the collapse of closed loops CF1 into chiral bubbles. The snapshots were taken at $T = 50.6°C$, and the confinement ratio of the sample is $d/p < 58.8$.
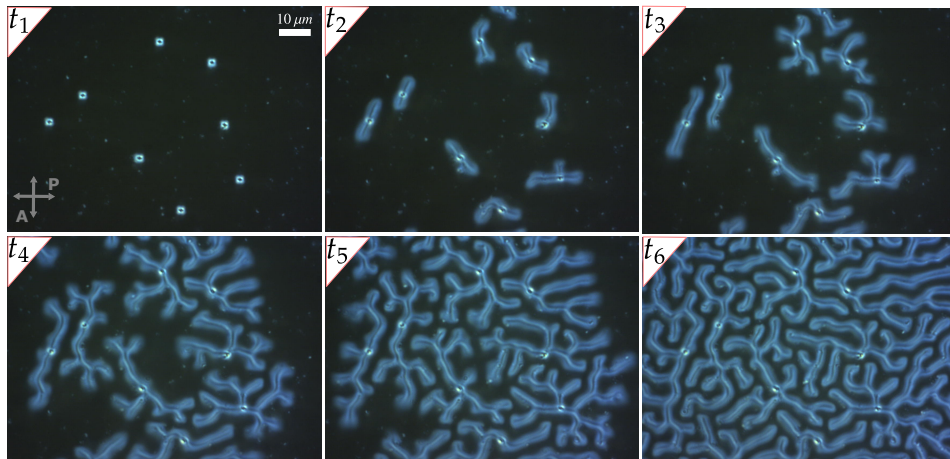
Figure 8.4: Temporal snapshots ($t_6 > t_5 > t_4 > t_3 > t_2 > t_1$) showing the emergence of cholesteric fingers from the interface of chiral bubbles. The dynamics is characterized by the elongation and tip-splitting of the cholesteric fingers. The snapshots were taken at $T = 51.3°C$, and the confinement ratio of the sample is $d/p < 58.8$.

89
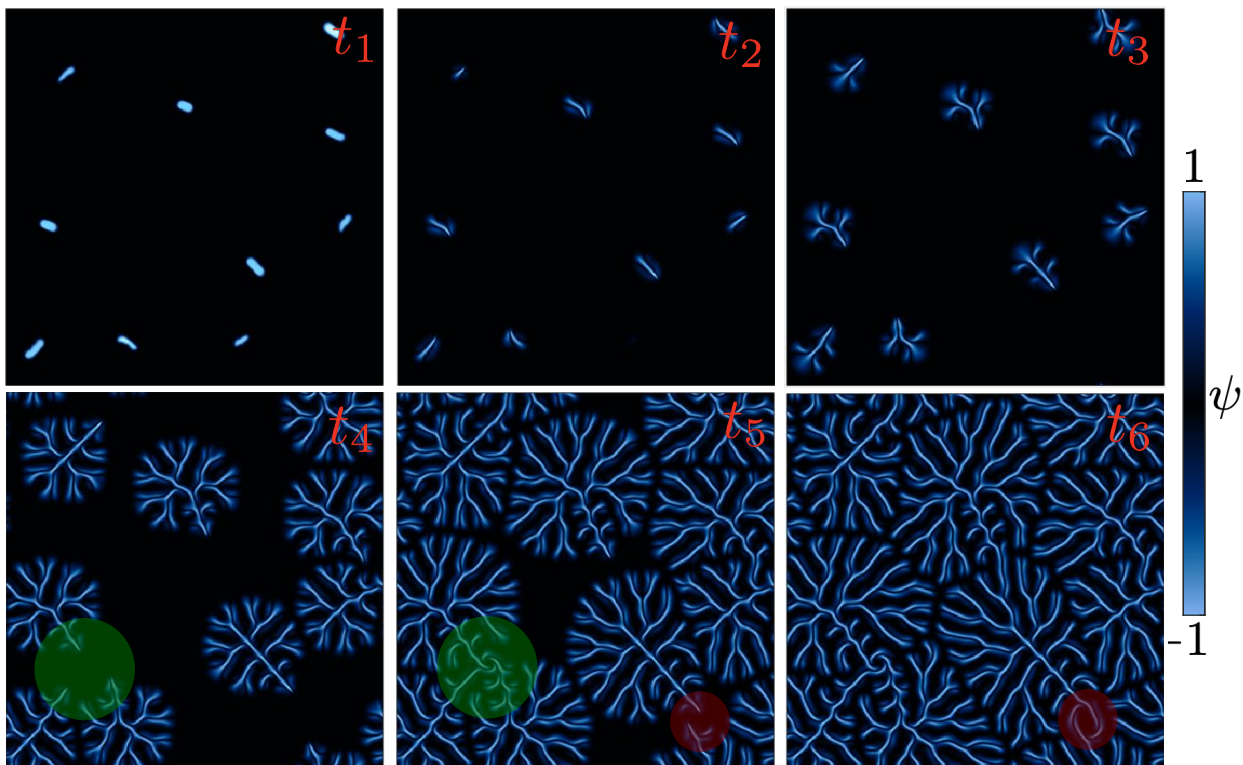
Figure 8.5: Temporal snapshots ($t_6 > t_5 > t_4 > t_3 > t_2 > t_1$) of a numerical integration of Eq. 8.1 with $\delta = 0.1$, $\mu = -0.4$, $\beta = 1$, and $\chi = 2.5$. The figure shows the emergence of a labyrinthine pattern with closed loops from an initial condition t_1 consisting of various perturbations in the real part of the complex field Re(A). The polarized field ψ is defined as $Re(A)Im(A)$. The green (red) shaded region corresponds to a closing event of three (two) domains. The numerical simulation was performed in a box of size 200×200.

Numerical integrations of model (8.1) show good agreement with experiments and allow us to discover more information about the dynamics of fingers and chiral bubbles. Figure. 8.6 describes a numerical experiment reproducing the creation of closed loops of CF1. The dynamics, as in the experiment, is governed by the creation and elongation of fingers with asymmetric tips, where pointed tips advance straight, producing side branches, and the rounded tips are unstable against a tip-splitting mode. The green shaded region, from t_4 to t_5 in Figure. 8.6, illustrates the closing of three domains, while the red shaded region (from t_5 to t_6) shows the closing of two domains. Both events produce closed loops of CF1. Our model also predicts the self-closing of one domain as shown in Fig. 8.6, where a pointed tip meets a side branch created by the same finger giving rise to a closed loop. By changing the parameters μ or χ, the closed loops collapse into localized vortices (cf. Figure. 8.7). The radially symmetric localized solutions, i.e., $A = R(r)e^{i\theta}$ where (r, θ) are polar coordinates, resemble the vortices of Ginzburg-Landau type of equations, where the phase structure ϕ (see Fig. 8.7(b)) exhibits a phase jump at the center of the vortex [164, 165]. However, in this case, the vortex is localized and supported by the background of modulus $|A| = 0$.
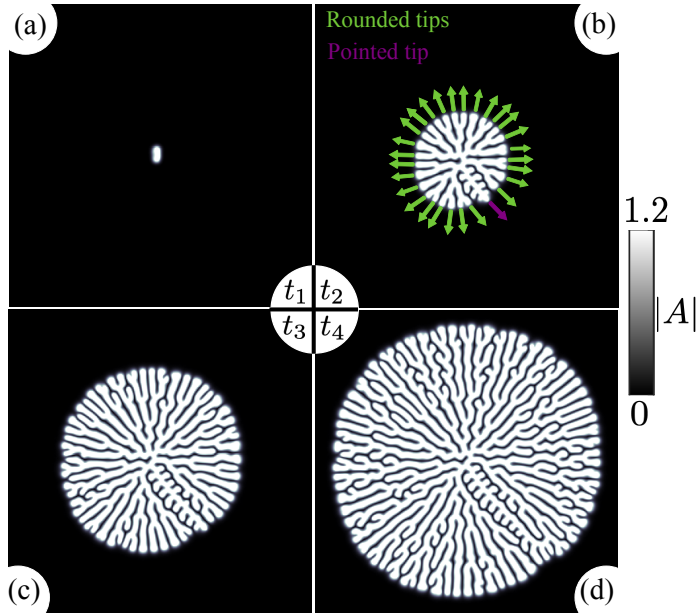
Figure 8.6: Temporal snapshots ($t_4 > t_3 > t_2 > t_1$) of a numerical integration of Eq. 8.1 with $\delta = 0.1$, $\mu = -0.4$, $\beta = 1$, and $\chi = 2.8$. The figure shows the emergence of a labyrinthine pattern with a closed loop from an initial condition t_1 consisting of a perturbation of the real part of the complex field $\mathrm{Re}(A)$ at the center of the system. The polarized field ψ is defined as $Re(A)Im(A)$. The numerical simulation was performed in a box of size 1000×1000.
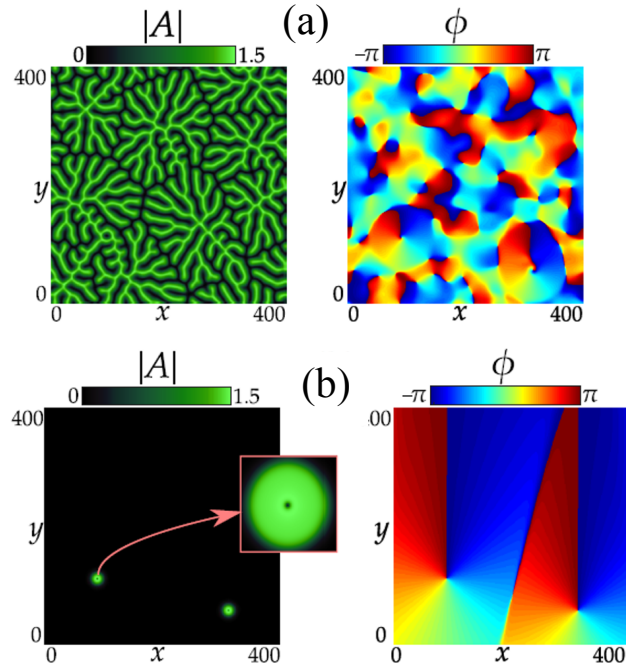
Figure 8.7: Numerical transition from a labyrinthine pattern with closed loops to localized vortices. (a) Labyrinthine pattern at $\chi = 2.5$. (b) Chiral bubble sat $\chi = 2.2$. The other parameters are $\delta = 0.1$, $\mu = -0.4$, and $\beta = 1$. The numerical simulation was performed in a box of size 200×200.

We note that model Eq. (8.1) has numerical chiral bubbles of different sizes as equilibria, where the size can be quantified by the position r_f of the interface between the localized vortex and the homogeneous background (see Figs. 8.8(a) and 8.8(b)). To shed light on the stabilization of the spherulite, we have derived a particle-type model for the core r_f. In this way, we approximate the radial profile as $R_o = (3/4/(1 + e^{\sqrt{3/4}(r-r_f)}))^{1/2}$, which is solution of $\mu R_o + R_o^3 - R_o^5 + \partial_{rr} R_o = 0$ at the Maxwell point $\mu = \mu_{MP}$ [94]. The solid line in Fig. 8.8 accounts for the profile R_o showing a good match with the full profile far from the center of the vortex. We make a weakly nonlinear analysis near μ_{MP} and include the effects of the two-dimensional terms (curvature, topology, and chirality), assuming that $r_f \gg \sqrt{4/3}$. Introducing the ansatz $A = Re^{i(\theta+\phi_o)}$ in Eq. (8.1) and assuming that $\delta \to 0$, we obtain for the real part

$$\partial_t R = \mu R + \beta R^3 - R^5 + \partial_{rr} R + \frac{1}{r_f}\partial_r R - \frac{R}{r_f^2} + 2\chi\frac{R^2}{r_f}, \tag{8.2}$$

and the imaginary part sets the phase jump $\phi_o = 0$. We propose the following ansatz $R = (R_o(r - r_f(t)) + \epsilon W_1(r, r_f(t)) + \epsilon^2 W_2(r, r_f(t)))$, $\mu = \mu_{MP} + \epsilon^2\mu_1$, $\chi = \chi_o + \epsilon\chi_1$, $r_f = \tilde{r}_f/\epsilon$, $\partial_t = \epsilon^3\partial_T$, where we have introduced the small parameter ϵ. At $O(\epsilon^0)$ in Eq. (8.2), the 1D problem $\mu_{MP}R_o + R_o^3 - R_o^5 + \partial_{rr} R_o = 0$ is recovered. At first order in ϵ we have

$$(\mu_{MP} + 3R_o^2 - 5R_o^4 + \partial_{rr})W_1 = \frac{\partial_r R_o}{\tilde{r}_f} + 2\chi_o\frac{R_o^2}{r_f}. \tag{8.3}$$

To solve the inhomogenous equation (8.3), we introduce the inner product $\langle f|g\rangle = \int_{-\infty}^{\infty} fg\,dz$, where $z = r - r_f$. The operator $\mathcal{L} = \mu_{MP} + 3R_o^2 - 5R_o^4 + \partial_{rr}$ is self-adjoint ($\mathcal{L} = \mathcal{L}^\dagger$), and $Ker\{\mathcal{L}\} = \partial_z R_o$. Then, the solvability condition is $\langle \partial_z R_o|(\partial_r R_o + 2\chi_o R_o^2)/\tilde{r}_f\rangle = 0$, which gives $\chi_o = 0.25$. This is the minimum chirality value that allows the existence of the cholesteric bubble, which agrees with numerical observations. At $O(\epsilon^2)$ we get

$$(\mu_{MP}+3R_o^2-5R_o^4+\partial_{rr})W_2 = -\partial_z R_o\partial_T\tilde{r}_f - \mu_1 R_o + \frac{R_o}{\tilde{r}_f^2} - 2\chi_1\frac{R_o^2}{\tilde{r}_f} - \frac{\partial_r W_1}{\tilde{r}_f} - 4\chi_o\frac{R_o W_1}{\tilde{r}_f} - 3R_o W_1^2 + 10R_o^3 W_1^2. \tag{8.4}$$

Following the same procedure as before, we obtain the solvability condition $\langle \partial_z R_o|b_2\rangle = 0$, with b_2 the right hand side of Eq. (8.4), which gives

$$\partial_T\tilde{r}_f = c_1\mu_1 + c_2\frac{\chi_1}{\tilde{r}_f} - \frac{c_3}{\tilde{r}_f^2}, \tag{8.5}$$

where

$$c_1 = -\frac{\langle \partial_z R_o|R_o\rangle}{\langle \partial_z R_o|\partial_z R_o\rangle} > 0, \tag{8.6}$$

$$c_2 = -2\frac{\langle \partial_z R_o|R_o^2\rangle}{\langle \partial_z R_o|\partial_z R_o\rangle} > 0, \tag{8.7}$$

and

$$c_3 = -\frac{\langle\partial_z R_o|R_o\rangle - \langle\partial_z R_o|\partial_r w_1\rangle - 4\chi_o\langle\partial_z R_o|R_o w_1\rangle - 3\langle\partial_z R_o|R_o w_1^2\rangle + 10\langle\partial_z R_o|R_o^3 w_1^2\rangle}{\langle\partial_z R_o|\partial_z R_o\rangle} \approx c_1 > 0.$$

$$(8.8)$$
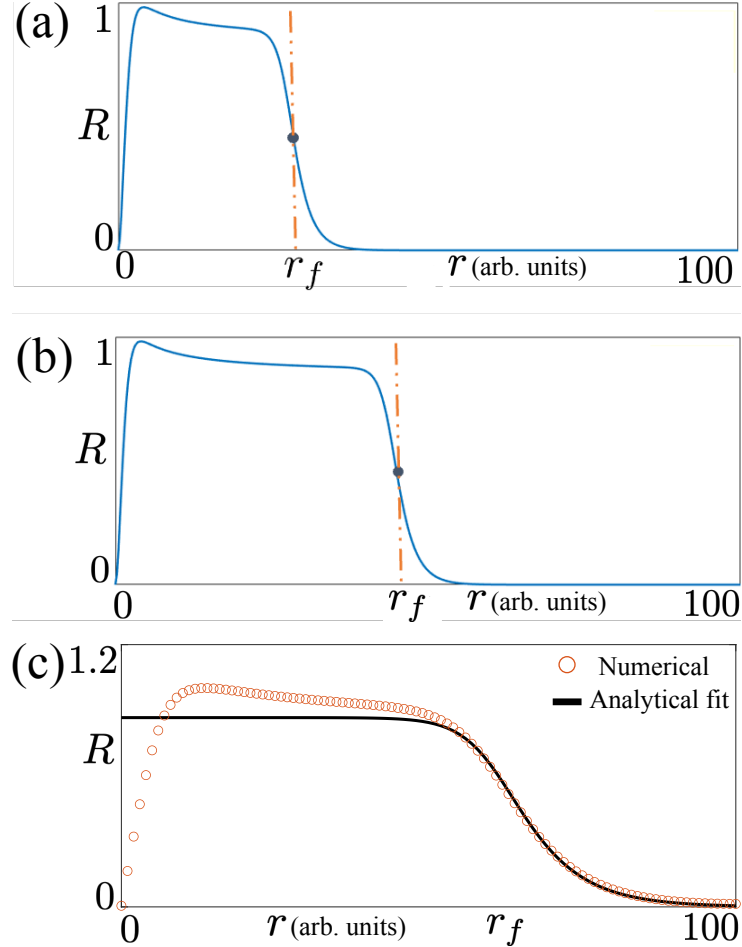
Figure 8.8: Radial profiles $R(r)$ of different localized vortex solution of size r_f with (a) $\mu = -0.19$ and $\chi = 0.3$, (b) $\mu = -0.19$ and $\chi = 0.28$, and (c) $\mu = -0.19$ and $\chi = 0.25$. In (c), the solid black line indicates the analytical fit R_o. All the profiles correspond to numerical integrations of Eq. (8.1) with $\beta = 1$, and $\delta = 0.05$ in squared boxes of size 200×200.

In the article of this chapter, we show the potential of Eq. (8.1) in predicting transitions and cholesteric textures observed in the winding/unwinding temperature-controlled experiment. We explore the appearance and disappearance of the chiral bubble solution by using the zero-dimensional model Eq. (8.5) and discover that a saddle-node bifurcation is responsible for the stabilization of the localized solution. Additionally, we discuss the emergence of cholesteric fingers from the interface of chiral bubbles.

Localized dissipative vortices in chiral nematic liquid crystal cells

M. G. Clerc, G. González-Cortés ◉, and S. Echeverría-Alar ◉
Departamento de Física and Millenium Institute for Research in Optics, Facultad de Ciencias Físicas y Matemáticas,
Universidad de Chile, Casilla 487-3, Santiago, Chile

Solitary waves and solitons have played a fundamental role in understanding nonlinear phenomena and emergent particle-type behaviors in out-of-equilibrium systems. This type of dynamic phenomenon has not only been essential to comprehend the behavior of fundamental particles but also to establish the possibilities of novel technologies based on optical elements. Dissipative vortices are topological particle-type solutions in vectorial field out-of-equilibrium systems. These states can be extended or localized in space. The topological properties of these states determine the existence, stability properties, and dynamic evolution. Under homeotropic anchoring, chiral nematic liquid crystal cells are a natural habitat for localized vortices or spherulites. However, chiral bubble creation and destruction mechanisms and their respective bifurcation diagrams are unknown. We propose a minimal two-dimensional model based on experimental observations of a temperature-triggered first-order winding/unwinding transition of a cholesteric liquid crystal cell and symmetry arguments, and investigate this system experimentally. This model reveals the main ingredients for the emergence of chiral bubbles and their instabilities. Experimental observations have a quite fair agreement with the theoretical results. Our findings are a starting point to understand the existence, stability, and dynamical behaviors of dissipative particles with topological properties.

Dissipative particle-type solutions have been studied in many fields of nonlinear science, ranging from biology, chemistry, to physics (see the reviews [1–4] and references therein). Localized structures are characterized by being supported by a spatially extended stable state. These localized states present features of the particles. Hence, one can characterize them with a family of discrete parameters such as position, amplitude, width, and topological charge. The localized structures generalize the concept of solitons or solitary waves reported in fluid dynamics, nonlinear optics, and Hamiltonian systems [5]. Because of the initial conditions or inherent fluctuations, out-of-equilibrium physical systems exhibit rich dynamics of the localized structures [1–4]. Particle-type solutions with topological charges are well known as *vortices* [6]. In complex fields, vortices are point-like singularities that locally break the rotational symmetry. Namely, zero intensity at the singular point characterizes the vortex with a phase spiraling around it. The number of phase jumps determines the topological charge of the vortex [6]. The spiral rotation sense gives the sign of the charge. Vortices are nucleated and annihilated by pairs between opposite charges due to the conservation of the total topological charge. The Ginzburg-Landau equation is a universal and minimal model that presents vortices [6,7]. This universal model has

been used to describe superconductors, magnetic media, fluids, superfluids, granular matter, liquid crystals, and optical dielectrics, to mention a few [6–10].

Liquid crystals are a natural physical context where extended or localized dissipative vortices can be observed [11]. Extended vortices in nematic liquid crystals are usually called umbilical defects. Topological localized states are the cholesteric bubbles observed in chiral liquid crystals, *spherulites* or *elementary torons* [12–15]. These localized states are characterized by exhibiting localized vorticity with a circular shape surrounded by a homogeneous state without vorticity, when observed under crossed polarizers (see Fig. 1). These cholesteric localized objects and textures also possess a rich three-dimensional structure [15]. The spherulites are usually observed close to the winding/unwinding transition [12–14], which occurs when the helical structure of a chiral nematic liquid crystal develops/frustrates under homeotropic anchoring [16,17]. Topological transitions, nontopological to topological states and vice versa, have previously been observed in liquid crystals [12,18–21]. Although cholesteric bubbles and their transitions have been studied for several decades, their theoretical description, interaction, creation mechanisms, and instabilities have not been completely clarified.

This Letter aims to investigate the emergence, stabilization, and instabilities of chiral bubbles in the context of cholesteric liquid crystal cells subjected to thermal driving. Experimentally, the winding/unwinding transition, triggered by temperature, of a chiral nematic liquid crystal sample is analyzed. We show that this transition is of the first-order type. Different cholesteric textures are observed when changing

---
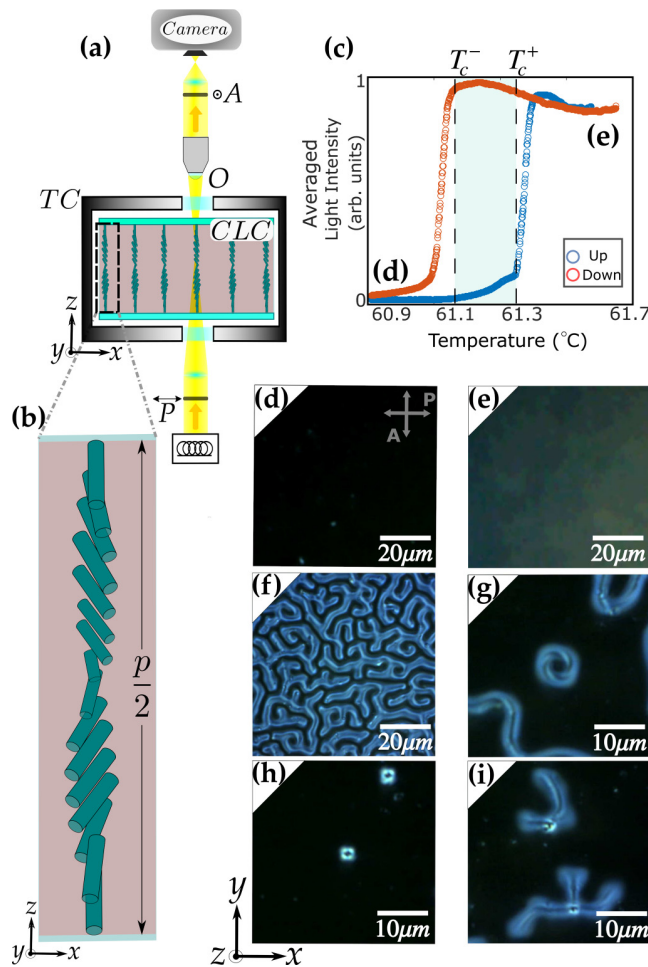
FIG. 1. Cholesteric liquid crystal cell under homeotropic anchoring and crossed polarizers. (a) Schematic representation of the experimental setup. TC represents the thermal chamber. O stands for the objective of the microscope, with magnifications ranging from $20\times$ to $50\times$. P and A are the polarizer and analyzer, respectively. (b) Director representation $\bar{n}$ of the chiral nematic liquid crystal displaying a TIC phase. p is the cholesteric pitch. (c) The subcritical bifurcation between the (d) unwound state and the (e) TIC phase. The light blue shaded region stands for the bistability region. (f) Cholesteric labyrinth. (g) Loop of CF-1. (h) Chiral bubbles. (i) Fingering instability of the localized vortices.

the temperature, such as translational invariant configuration (TIC), modulated TIC, cholesteric fingers of type 1 (CF-1), loops of CF-1, and spherulites. Similar textures have been reported in experiments controlled by applying a voltage to cholesteric liquid crystal cells [12]. Based on the subcritical nature of the observed transition and symmetry arguments, an amplitude equation of the Ginzburg-Landau type is proposed. This minimal two-dimensional model allows us to disclose the phase diagram and the transitions in the system. We establish, theoretically and numerically, the stability region of the chiral bubbles. The combined effect of chirality, interface curvature, and topology allows us to reveal a saddle-node mechanism of the appearance or disappearance of the chiral bubbles. The finger instability of the cholesteric bubbles is characterized by

a modal stability analysis. There is a fair agreement between the experimental observations and the theoretical findings.

Experimental setup. Polarized optical microscopy with a hot stage is a well-known experiment setup that permits the characterization of liquid crystal textures and their transitions (see Ref. [22] and references therein). Figure 1(a) shows a schematic representation of this experiment. This setup is made up of a white light source, which passes through a polarizer P and illuminates a cholesteric liquid crystal (CLC) sample. To control the temperature, the sample is inside a thermal chamber (TC). The transmitted light goes into the objective O and after that passes through another polarizer A. A CMOS camera monitors transmitted light. We consider CLC samples with homeotropic anchoring. The imposition of this boundary condition frustrates the helical structure of the CLC [cf. Fig. 1(b)]. The degree of frustration of this mesophase is quantified by the confinement parameter d/p, where d is the cell thickness and p is the cholesteric pitch [17]. This pitch accounts for the length of rotation of the molecules, and it depends on temperature, and the concentration of chiral molecules [12,22]. The liquid crystal used is a mixture of nematic E7 (Merck) with a chiral molecule EOS-12 [23]. The molecule concentration determines the cholesteric pitch p [11]. The pitch length is determined by the Grandjean-Cano technique [12].

Experimental results. To carry out the study of the winding/unwinding transition of CLC samples, we consider two cells with different concentrations of chiral elements since a higher chiral molecule concentration yields a higher mixture chirality and shorter pitch. The first sample has a dopant concentration of 3 wt % ($p = 21.8\ \mu$m at $T = 57\,^\circ$C) and its thickness is $d = 9\ \mu$m. When varying the temperature, the sample shows a subcritical winding/unwinding transition at $T_c^+ \approx 61.3\,^\circ$C, as depicted in Fig. 1(c). The transmitted light intensity is used to measure the subcritical winding/unwinding transition. The blue (red) curve stands for the increase (decrease) of temperature at a rate of $0.5\,^\circ$C/min. At $T < T_c^- \approx 61.1\,^\circ$C the helical structure of this CLC unwinds completely, and under crossed polarizers a homeotropic texture is observed [see Fig. 1(d)], which is characterized by no transmitted light. When the sample overcomes the critical temperature T_c^+, the uniform helical structure is recovered and a homogeneous coloration is observed on the transmitted light, TIC phase [cf. Fig. 1(e)]. The hysteresis loop between the homeotropic and TIC phase renders the transition of the first-order type. Indeed, the system exhibits a bistability region [see the light blue shaded region in Fig. 1(c)].

The second sample of the CLC mixture contains 25 wt % ($p = 2.6\ \mu$m at $T = 57\ ^\circ$C) of the chiral molecule and thickness $d = 200\ \mu$m. We observe a subcritical bifurcation, however, the scenario changes radically. In this case, at $T > T_c^+ \approx 51.3\,^\circ$C the nucleation of the cholesteric fingers is observed. Rapidly, the rounded tip of the fingers suffers a tip-splitting instability, and the abnormal tip advance and merge with the nearest cholesteric finger, showing similar dynamical behaviors to those reported in Ref. [24]. This process ends in a cholesteric labyrinthine pattern. Figure 1(f) shows a typical observed labyrinthine pattern. The self-merging of the fingers gives rise to CF-1 loops, analogous to those observed with the application of an oscillatory voltage [25]. Upon decreasing

the temperature, the CF-1 retracts and the loops survive [see Fig. 1(g)]. Lowering further, the CF-1 loop collapses into cholesteric bubbles [cf. Fig. 1(h)]. Here, we use the term cholesteric bubble for the localized objects created by this process, which correspond to the *elementary torons* [15]. The transition from CF-1 loops to spherulites is irreversible [14]. When increasing the temperature, the cholesteric fingers appear at the interface of the localized vortices, as shown in Fig. 1(i). This fingering instability has been also observed in electrically driven experiments [26].

Theoretical description. Close to the winding/unwinding transition and in the long-pitch limit $p \gg l$, where l is a typical molecular length, the average molecular orientation of the frustrated chiral nematic liquid crystal state inside a cell of thickness d can be modeled as [27,28]

$$\vec{n} = \begin{pmatrix} \cos\left(\frac{z}{p} + \theta\right) \sin\left[\alpha \sin\left(\frac{\pi z}{d}\right)\right] \\ \sin\left(\frac{z}{p} + \theta\right) \sin\left[\alpha \sin\left(\frac{\pi z}{d}\right)\right] \\ \cos\left[\alpha \sin\left(\frac{\pi z}{d}\right)\right] \end{pmatrix}, \quad (1)$$

where $\vec{n}$ is the liquid crystal director, which accounts for the orientational average of molecules in a small volume element, $\alpha = \alpha(x, y, t)$ is the tilt angle of $\vec{n}$ from the vertical z axis, and $\theta = \theta(x, y, t)$ is the azimuth angle of the director, that is, the angle between the projection of $\vec{n}$ into the x-y plane and the x axis. To characterize the winding/unwinding transition, one can introduce the order parameter $Q \equiv n_z(n_x + in_y)$ [27]. Close to the transition, $\alpha \ll 1$, the order parameter becomes $Q(x, y, z, t) \approx \alpha e^{i(\theta + z/p)} \sin(\pi z/d) = Ae^{iz/p} \sin(\pi z/d)$. The two-dimensional complex amplitude $A(x, y, t) = \alpha e^{i\theta}$ can be used as an order parameter to study the winding/unwinding transition at the middle plane of the cell [27]. This simplification assumes that 3D effects, such as confinement and surface anchoring, are neglectable.

To shed light on the cholesteric textures that emerge in the thermally driven winding/unwinding transition, we propose a phenomenological amplitude equation for A. Based on the subcritical nature of the transition [see Fig. 1(c)], symmetry arguments, and multiscaling, the dimensionless amplitude equation reads

$$\partial_t A = \mu A + \beta |A|^2 A - |A|^4 A + \partial_\eta \partial_{\bar{\eta}} A + \delta \partial_\eta \partial_\eta \bar{A} + \chi (A \partial_{\bar{\eta}} A - \bar{A} \partial_\eta A), \quad (2)$$

where $\partial_\eta = \partial_x + i\partial_y$ is a differential operator on the complex plane, the *Wirtinger derivative*. The bifurcation parameter $\mu \propto T - T_c^+$ measures the distance from the critical temperature. Indeed, μ is a function of temperature, concentration, cholesteric pitch, thickness of the cell, and elastic constants. The three first terms on the right-hand side of Eq. (2) model a subcritical transition ($\beta > 0$). The fourth and fifth terms account for the isotropic and anisotropic elastic coupling in the system, respectively [29]. The last term models the mirror symmetry breaking, i.e., chirality [27]. The model Eq. (2) obeys the scaling $\partial_t \sim \mu$, $\partial_\eta \sim \mu^{1/2}$, $A \sim \mu^{1/4}$, $\chi \sim \mu^{1/4}$, with $\mu \ll 1$ and $\delta \sim O(1)$. The dynamics of Eq. (2) is vari-
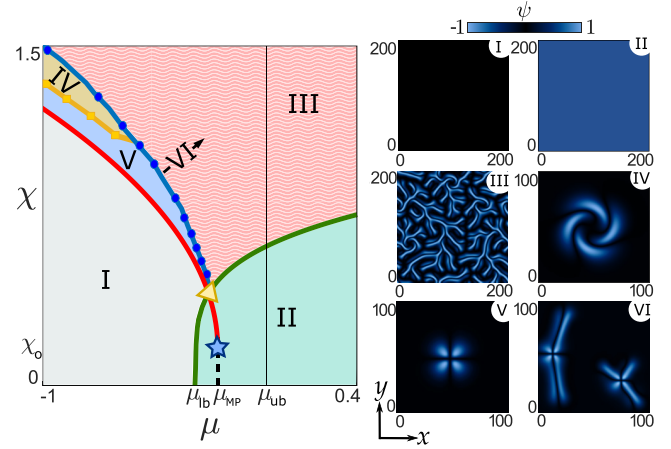
FIG. 2. Phase diagram of model Eq. (2) with $\beta = 1$ and $\delta = 0.05$. $\mu_{lb} = -1/4$ and $\mu_{ub} = 0$ are the limits of the bistability region between A_o and A_T. $\mu_{MP} = -3/16$ is the Maxwell point. The green line accounts for the spatial instability of A_T. The red curve is the saddle-node bifurcation of the localized vortices. The yellow line with □ markers stands for the transition between loops and spherulites. The blue line with ○ markers shows the mode-3 instability of chiral bubbles. $\chi_o = 0.26$ is the minimum value for the existence of spherulites (☆). The △ symbol is the triple point of the system. Regions I, II, III, IV, and V account for the stable zone of uniform state A_o, TIC phase A_T, cholesteric patterns, cholesteric loop, and chiral bubble, respectively. Path VI represents the fingering instability. $\psi = \text{Re}(A)\text{Im}(A)$ is the polarization field. The right panels illustrate the states in the respective regions.

ational, $\partial_t A = -\delta \mathcal{F}[A, \bar{A}]/\delta \bar{A}$, where

$$\mathcal{F} = \iint dx dy \left\{ -\mu |A|^2 - \beta \frac{|A|^4}{2} + \frac{|A|^6}{3} + |\nabla A|^2 + 2\delta \, \text{Re}\left\{ (\partial_\eta \bar{A})^2 \right\} - \chi |A|^2 (\partial_{\bar{\eta}} A + \partial_\eta \bar{A}) \right\} \quad (3)$$

is a Lyapunov functional. Hence, the dynamics of the amplitude Eq. (2) is driven by the minimization of $\mathcal{F}$. A similar amplitude equation to model (2), but supercritical and with terms of different order in the scaling has been used to study the unwinding transition [27].

For $\mu < \mu_{ub} \equiv 0$, the unwound state $A = A_o \equiv 0$ of Eq. (2) is stable (see region I in Fig. 2). When $\mu \geqslant \mu_{ub}$ the zero state is unstable by a subcritical instability and the TIC state $A_T = (1/2 + \sqrt{1/4 + \mu})^{1/2} e^{i\theta_o}$ is stable (see region II in Fig. 2), with θ_o an arbitrary phase. Indeed, the model Eq. (2) presents a bistability region between $A = 0$ and A_T in $\mu_{lb} \leqslant \mu \leqslant \mu_{ub}$ for small chirality. Within this zone there is a Maxwell point μ_{MP}, where $\mathcal{F}[A_T] = \mathcal{F}[A_o]$ [30]. The A_T solution has a spatial instability that gives rise to striped pattern, which is associated with the modulated TIC phase [12]. A linear stability analysis around A_T delivers the critical wave vector $|\vec{k}_c| = \sqrt{[f(\mu) + \delta g(\mu) + 2\chi^2 A_T^2]/(1 - \delta^2)}$, where $f(\mu) = \mu + 2\beta A_T^2 - 3A_T^4$ and $g(\mu) = \beta A_T^2 - 2A_T^4$. The spatial instability curve is obtained by restricting $|\vec{k}_c|$ to be a real quantity (cf. green line in Fig. 2). The critical wavelength is $\lambda_c = 2\pi/|\vec{k}_c|$, which is proportional to the pitch p [12]. For
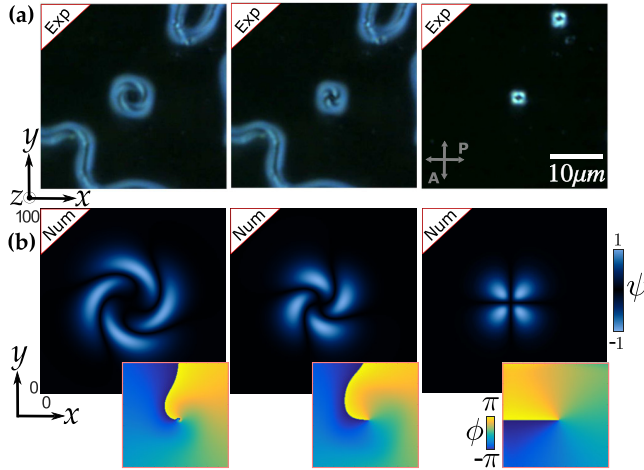
FIG. 3. Transition from CF-1 loops to chiral bubbles. (a) Experimental bifurcation triggered by decrease the temperature in the sample with 25 wt % of chiral dopant. (b) Numerical transition in model Eq. (2) with $\beta = 1$, and $\delta = 0.05$, when parameters change from region IV to V in the phase diagram of Fig. 2. $\psi = \text{Re}(A)\text{Im}(A)$ is the polarization field. ϕ is the phase field. The middle panels are transient states.

high chirality ($\chi > 1.5$), the parameter χ is approximated by $\chi \approx (2\pi/\sqrt{2}A_T)/p$. Hence, χ is interpreted as a qualitative measure of the confinement, and have a temperature dependence through p. Experimentally, a similar bifurcation diagram has been obtained by varying the applied voltage and the confinement parameter (chirality) [26].

Chiral bubble solutions and instabilities. The model Eq. (2) exhibits localized finger states with different tips. When changing parameters, the pointed tips can merge, and the rounded tips exhibit the tip-splitting instability, which is characterized by a flowerlike type of growth [12]. The final equilibrium structure is a labyrinthine pattern with embedded loops (see panel III of Fig. 2 and Video 1 in the Supplemental Material [31]). Entering in the zone IV, the fingers withdraw and only loops survive. Starting from region IV and going into region V, the loop collapses into an axisymmetric localized vortex solution $A(r, \theta) = R(r)e^{i\phi(\theta)}$, where R and ϕ are the modulus and phase, and $\{r, \theta\}$ are the polar coordinates. Figure 3 shows this transition experimentally and numerically. Besides the change in size, the phase field transforms from a nontrivial phase structure into the typical phase jump of a singular point or vortex (spherulites) [19]. This transition has been studied experimentally and numerically from a three-dimensional configuration [32].

In the experiment, when decreasing temperature, the spherulites shrink as depicted in Fig. 4(a). Suddenly, the localized vortex is lost. This out-of-the-blue disappearance is characteristic of a saddle-node bifurcation and is referred to as *ruin* [33]. An analogous transition is observed numerically between regions V and I of Fig. 2. This transition should be accompanied by the divergence of the spherulite residence time τ_r, which is the elapsed time by the vortex before its disappearance, near the saddle-node bifurcation. To shed light on this mechanism, we measure from model Eq. (2) the accumulated area $A_{ac}(\chi) = \int_{t_o}^{\tau_r} \int_0^\infty R(r, t)^2 dr dt$, which is
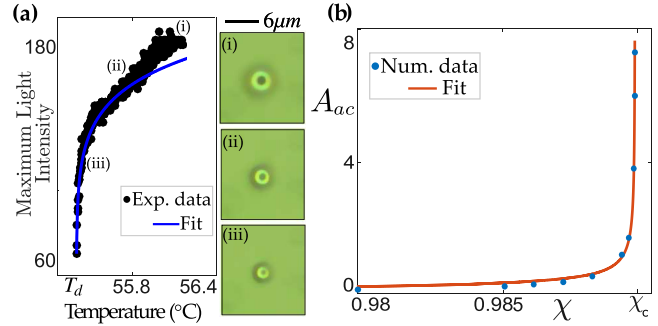
FIG. 4. Disappearance of chiral bubbles. (a) Experimental observation of the spherulite loss in the sample with 25 wt % of chiral dopant. The black dots correspond to the maximum intensity peak of the localized structure when the temperature is decreased from 56.3 °C (i) until the disappearance at $T_d \approx 55.3$ °C. The blue curve is the fit $128(T - T_d)^{0.08}$. The insets shows the spherulite changes under circular polarization. (b) Divergence of A_{ac} at $\chi_c = 0.989$, in Eq. (2) with $\mu = -0.45$, $\beta = 1$, $\delta = 0.05$, and $t_o = 0$. The fit is $A_{ac} = 0.024(\chi_c - \chi)^{-1/2}$, where $\chi_c = 0.9895$.

proportional to τ_r near the bifurcation [34]. The lower limit t_o is an arbitrary reference time. Figure 4(b) summarizes the result. When varying χ, a power law $A_{ac} \propto (\chi_c - \chi)^{-1/2}$ is obtained, rendering the transition of the saddle-node type [33].

In region V of Fig. 2, cholesteric bubbles of different sizes are stable. The main feature of the transition between bubbles is the interface dynamics, with a core r_f, which connects $R = 0$ and $R \approx |A_T|$ [see Fig. 5(a)]. For large bubbles size, the radial profile of the interface is approximated by $R_o = [3/4(1 + e^{\sqrt{3/4}(r-r_f)})]^{1/2}$ at the Maxwell point [35]. Introducing the ansatz $A(r, \theta, t) = R_o[r - r_f(t)]e^{i\theta} + w$, where w is a small correction function, into Eq. (2) with $\beta = 1$ and $\delta \ll 1$, linearizing in w and applying a solvability condition after straightforward calculation, we get

$$\dot{r}_f = c_1 \Delta\mu + \frac{c_2\chi - c_o}{r_f} - \frac{c_1}{r_f^2}, \tag{4}$$
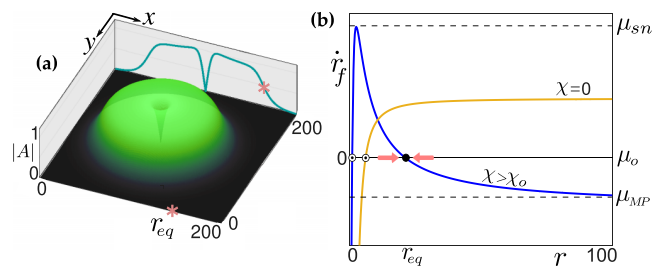
FIG. 5. (a) Chiral bubble observed in model Eq. (2) with $\mu_o = -0.21$, $\chi = 0.4$, $\delta = 0.05$, and $\beta = 1$. The radial profile $|A| = R(r)$ is characterized by the core r_f of the interface. (b) Phase portrait of Eq. (4). The yellow curve accounts for the case $\chi = 0$. The blue curve shows the force $\dot{r}_f$ when $\chi > \chi_o$. The open dots represent unstable solutions. The solid black dot is a stable equilibrium (r_{eq}). μ_{sn} is the saddle-node critical parameter. μ_{MP} is the Maxwell point.

where $c_o = \int_{-\infty}^{\infty} (\partial_z R_o)^2 dz$, $c_1 = -\int_{-\infty}^{\infty} \partial_z R_o R_o dz$, $c_2 = -2\int_{-\infty}^{\infty} \partial_z R_o R_o^2 dz$, $z = r - r_f$, $\Delta\mu = \mu - \mu_{MP}$, and $\dot{r}_f = c_o \partial_t r_f$.

The kinematic Eq. (4) combines energy difference, chirality, curvature, and topology effects, respectively. Figure 5(b) illustrates the kinematic Eq. (4). There are two cases: zero chirality $\chi = 0$ (yellow curve) in which the system only has one unstable state, and $\chi > \chi_o = c_o/c_2$ (blue curve), where the systems exhibit two localized topological states, one unstable and another stable ($r_f = r_{eq}$). Hence, chiral bubbles are a consequence of the presence of the chirality. Likewise, we note that the previous method is only applicable for positive topological charges since the negative one requires considering the transversal dynamics of the interface. The disappearance of the chiral bubble ($\mu = \mu_{sn}$) is mediated by the collision of two equilibria, which indicates a saddle-node bifurcation. The critical curve of this bifurcation is $\chi = \chi_o + 2c_1|\Delta\mu|^{1/2}$ (red line in Fig. 2). Note that at $\mu = \mu_{MP}$ and $\chi = \chi_o$, the chiral bubble is unstable due to the divergence of its size.

In model Eq. (2), the chiral bubble suffers a fingering instability (cf. path VI in the phase diagram of Fig. 2). A numerical linear analysis can be performed to investigate this transition. Introducing the ansatz $A = [R_o + \tilde{R}(r)\cos(m\theta)e^{\lambda_m t}]e^{i[\theta + \tilde{\phi}(r)\sin(m\theta)e^{\lambda_m t}]}$ in Eq. (2), where $\tilde{R}(r)$ and $\tilde{\phi}(r)$ are small perturbations, the modes $m = 1, 2$, and 3 are unstable, where $\lambda_3 > \lambda_2 > \lambda_1 > 0$. Modes with $m > 3$ cannot be treated with the perturbational ansatz given above, due to the appearance of new phase jumps in the complex field. Experimentally, we have not observed these higher modes. The blue line shown in Fig. 2 is the mode-3 instability. This curve allows us to envisage a triple point between a patterned state and two uniform phases (see the triangle in Fig. 2) [36].

In conclusion, the minimal model Eq. (2) allows us to reveal analytically the instabilities of chiral bubbles, namely, saddle-node bifurcation and interfacial instability. Both behaviors are mainly controlled by the chirality χ of the system, which is the manifestation of the inherent twist of the chiral liquid crystal in the middle plane of the cell. Also, the model reproduces other types of cholesteric textures, such as the TIC phase, cholesteric labyrinth, and CF-1 loop. The instabilities and textures have been experimentally observed using polarized optical microscopy. Indeed, there is agreement between the experimental observations and the 2D minimal model Eq. (2). Three-dimensional effects were neglected in this work and could be necessary to describe in more depth the transition from CF-1 loop to the cholesteric bubble. However, the detailed analysis of this transition was out of the scope of this study. Comparisons between the theoretical 2D model and the 3D results in Ref. [32] are in progress. In addition, with our modeling approach, it is possible to visualize and understand other behaviors of cholesteric liquid crystals. For example, nematic umbilical defects undergo structural transitions due to chirality [37], the chiral bubble interaction, and topological labyrinthine pattern propagation. Work is in progress in these directions.

[1] N. Akhmediev and A. Ankiewicz, *Dissipative Solitons: From Optics to Biology and Medicine* (Springer, Heidelberg, 2008), Vol. 751.

[2] H.-G. Purwins, H. U. Bödeker, and S. Amiranashvili, Dissipative solitons, Adv. Phys. **59**, 485 (2010).

[3] O. Descalzi, M. Clerc, S. Residori, and G. Assanto, *Localized States in Physics: Solitons and Patterns* (Springer, Berlin, 2011).

[4] M. Tlidi, K. Staliunas, K. Panajotov, A. G. Vladimirov, and M. G. Clerc, Localized structures in dissipative media: from optics to plant ecology, Phil. Trans. R. Soc. A **372**, 20140101 (2014).

[5] A. C. Newell, *Solitons in Mathematics and Physics* (Society for Industrial and Applied Mathematics, Philadelphia, 1985).

[6] L. M. Pismen, *Vortices in Nonlinear Fields: From Liquid Crystals to Superfluids, from Non-equilibrium Patterns to Cosmic Strings* (Oxford Science, New York, 1999).

[7] I. S. Aranson and L. Kramer, The world of the complex Ginzburg-Landau equation, Rev. Mod. Phys. **74**, 99 (2002).

[8] E. Sandier and S. Serfaty, *Vortices in the Magnetic Ginzburg-Landau Model* (Springer, Boston, 2008).

[9] F. Bethuel, H. Brezis, F. Hélein *et al.*, *Ginzburg-Landau Vortices* (Springer, New York, 1994).

[10] M. C. Cross and P. C. Hohenberg, Pattern formation outside of equilibrium, Rev. Mod. Phys. **65**, 851 (1993).

[11] P. G. de Gennes and J. Prost, *The Physics of Liquid Crystals*, 2nd ed. (Clarendon Press, Oxford, UK, 1993).

[12] P. Oswald and P. Pieranski, *Nematic and Cholesteric Liquid Crystals* (CRC Press, London, 2005).

[13] N. Nawa and K. Nakamura, Observation of forming process of bubble domain texture in liquid crystals, Jpn. J. Appl. Phys. **17**, 219 (1978).

[14] S. Pirkl, P. Ribiere, and P. Oswald, Forming process and stability of bubble domains in dielectrically positive cholesteric liquid crystals, Liq. Cryst. **13**, 413 (1993).

[15] P. J. Ackerman and I. I. Smalyukh, Diversity of Knot Solitons in Liquid Crystals Manifested by Linking of Preimages in Torons and Hopfions, Phys. Rev. X **7**, 011006 (2017).

[16] F. Lequeux, P. Oswald, and J. Bechhoefer, Influence of anisotropic elasticity on pattern formation in a cholesteric liquid crystal contained between two plates, Phys. Rev. A **40**, 3974 (1989).

[17] P. Ribiere, S. Pirkl, and P. Oswald, Electric-field-induced phase transitions in frustrated cholesteric liquid crystals of negative dielectric anisotropy, Phys. Rev. A **44**, 8198 (1991).

[18] I. I. Smalyukh, B. I. Senyuk, P. Palffy-Muhoray, O. D. Lavrentovich, H. Huang, E. C. Gartland, Jr., V. H. Bodnar, T. Kosa, and B. Taheri, Electric-field-induced nematic-cholesteric transition and three-dimensional director struc-

tures in homeotropic cells, Phys. Rev. E **72**, 061707 (2005).

[19] R. Barboza, U. Bortolozzo, M. G. Clerc, S. Residori, and E. Vidal-Henriquez, Optical vortex induction via light–matter interaction in liquid-crystal media, Adv. Opt. Photonics **7**, 635 (2015).

[20] M. G. Clerc, M. Kowalczyk, and V. Zambra, Topological transitions in an oscillatory driven liquid crystal cell, Sci. Rep. **10**, 19324 (2020).

[21] G. Durey, H. R. O. Sohn, P. J. Ackerman, E. Brasselet, I. I. Smalyukh, and T. Lopez-Leon, Topological solitons, cholesteric fingers and singular defect lines in Janus liquid crystal shells, Soft Matter **16**, 2669 (2020).

[22] I. Dierking, *Textures of Liquid Crystals* (Wiley, Hoboken, NJ, 2003).

[23] M. L. Parra, P. I. Hidalgo, and E. Y. Elgueta, Synthesis and mesomorphic properties of oxadiazole esters derived from (*R*)-2-octanol, (*S*)-2-*n*-octyloxypropanol and (2*S*, 3*S*)-2-chloro-3-methylpentanol, Liq. Cryst. **35**, 823 (2008).

[24] P. Ribiere and P. Oswald, Nucleation and growth of cholesteric fingers under electric field, J. Phys. (Paris) **51**, 1703 (1990).

[25] J. Baudry, S. Pirkl, and P. Oswald, Looped finger transformation in frustrated cholesteric liquid crystals, Phys. Rev. E **59**, 5562 (1999).

[26] S. Thiberge, Structures cholestériques et dynamique hors équilibre, Ph.D. thesis, Université de Nice–Sophia Antipolis, 1999.

[27] T. Frisch, L. Gil, and J. M. Gilli, Two-dimensional Landau–de Gennes dynamical model for the unwinding transition of a cholesteric liquid crystal, Phys. Rev. E **48**, R4199 (1993).

[28] P. Oswald, J. Baudry, and S. Pirkl, Static and dynamic properties of cholesteric fingers in electric field, Phys. Rep. **337**, 67 (2000).

[29] T. Frisch, S. Rica, P. Coullet, and J. M. Gilli, Spiral Waves in Liquid Crystal, Phys. Rev. Lett. **72**, 1471 (1994).

[30] R. E. Goldstein, G. H. Gunaratne, L. Gil, and P. Coullet, Hydrodynamic and interfacial patterns with broken space-time symmetry, Phys. Rev. A **43**, 6700 (1991).

[31] See Supplemental Material at http://link.aps.org/supplemental/10.1103/PhysRevResearch.4.L022021 for a video showing the experimental and numerical emergence of labyrinthine patterns from cholesteric fingers.

[32] J.-S. B. Tai, P. J. Ackerman, and I. I. Smalyukh, Topological transformations of Hopf solitons in chiral ferromagnets and liquid crystals, Proc. Natl. Acad. Sci. USA **115**, 921 (2018).

[33] S. H. Strogatz, *Nonlinear Dynamics and Chaos with Student Solutions Manual: With Applications to Physics, Biology, Chemistry, and Engineering* (CRC Press, New York, 2018).

[34] F. del Campo, F. Haudin, R. G. Rojas, U. Bortolozzo, M. G. Clerc, and S. Residori, Effects of translational coupling on dissipative localized states, Phys. Rev. E **86**, 036201 (2012).

[35] M. G. Clerc and C. Falcón, Localized patterns and holesolutions one-dimensional extended systems, Physica A **356**, 48 (2005).

[36] R. M. Hornreich, M. Luban, and S. Shtrikman, Critical Behavior at the Onset of $\vec{k}$-Space Instability on the λ Line, Phys. Rev. Lett. **35**, 1678 (1975).

[37] J. M. Gilli and L. Gil, Static and dynamic textures obtained under an electric field in the neighbourhood of the winding transition of a strongly confined cholesteric, Liq. Cryst. **17**, 1 (1994).

8.1. Perspectives

In this chapter, we have proposed a variational amplitude equation to understand experimental observations of a frustrated chiral nematic liquid crystal. In particular, we have focused on the stabilization of localized vortices. We have shown that chirality and topology, expressed as curvature corrections in the weakly curved front dynamics of chiral bubbles, are the main ones responsible for the appearance and disappearance of the localized objects. Figure 8.9 shows the $\mu - \chi$ phase diagram, where the solid red line is the analytical saddle-node curve obtained in the article of this chapter. Although the agreement between numerical integrations (blue dots) of Eq. (8.1) and theory is good, for sufficiently big χ values, the approximation stops being correct. Obviously, our theoretical interpretation remains valid only near the critical point (μ_{MP}, χ_o); however, an interesting future direction is to include the anisotropic coupling δ and study if its effect amends the prediction of the saddle-node bifurcation for high χ values.
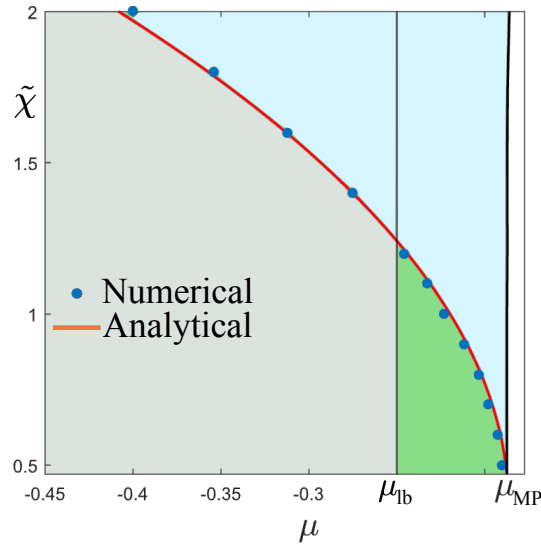
Figure 8.9: Phase diagram of Eq. (8.1) with $\beta = 1$ and $\delta = 0.05$. μ_{lb} is the lower boundary of the bistability range, μ_{MP} is the Maxwell point, and $\bar{\chi} = 2\chi$. The red line (blue dots) indicates the analytical (numerical) saddle-node curve for the localized vortices. The shaded gray region is associated with the homogeneous zero solution, the green shaded region is part of the bistability region between the uniform solutions, and the sky blue shaded region is the zone of stability of modulated solutions such as chiral bubbles, closed loops, fingers, and labyrinths.

Chapter 9

Emergence of disordered branching patterns in confined chiral nematic liquid crystals (Proceedings of the National Academy of Sciences 120, e2221000120)

In the previous chapter, besides revealing the stabilization mechanisms of localized vortices in a model of chiral nematic liquid crystals, we have also learned the predicting ability of the Equation (8.1). In particular, we discussed the emergence of labyrinthine patterns as an interfacial instability of chiral bubbles, where fingers are produced, and their rounded tips exhibit a cascade of tip-splitting events (cf. Fig. 9.1).

In the present chapter, we focus on how the tip-slipping instability develops at cholesteric interfaces and which are the interaction rules that ultimately give rise to the large-scale cholesteric labyrinthine pattern. Using the minimal model (8.1), which is now derived from first principles, we demonstrate the role of chirality in the tip-splitting mechanism and the emergence of the disordered branching pattern with a velocity-curvature equation for the cholesteric interface. We show that during the growth of the chiral fingers, there is a selection principle in the morphology and speed of the rounded tip (see Fig. 9.2). Furthermore, from these analyses, we deduce a small number of crucial interactions that regulate the growth process and show that the topological features of the labyrinthine pattern emerge from stochastic branching and termination events.
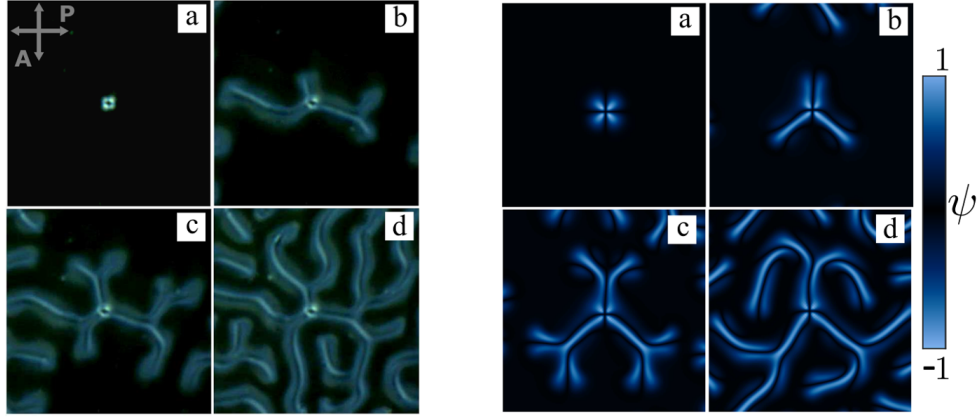
Figure 9.1: Emergence of labyrinthine patterns as a consequence of the instability of chiral bubbles and rounded tips. The left (right) panel shows the experimental (numerical) temporal evolution (a)-(d) of the instability. In the experimental case, the chiral nematic liquid crystal is at $T = 51.3°C$, and the confinement ratio of the sample is $d/p < 58.8$. The numerical integration in the right panel was performed with $\mu = -0.4$, $\chi = 2.5$, $\delta = 0.1$, and $\beta = 1$ in a squared box of size 200×200.
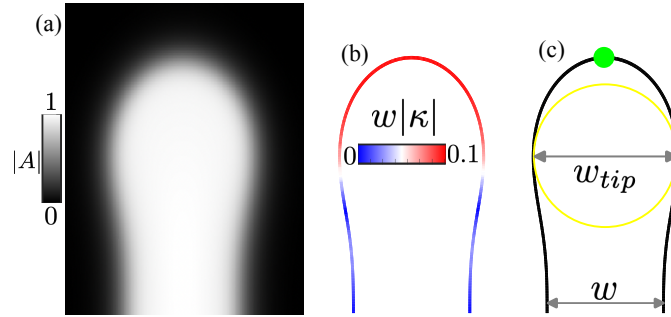
Figure 9.2: Morphology of the rounded tips in model Eq. (8.1). (a) Modulus $|A|$ of a propagating finger with. (b) Normalized curvature distribution $w|\kappa|$ along the interface of the finger. (c) Anatomy of the rounded tip showing the finger width w, and the size of the tip w_{tip} defined as the diameter of the biggest circle (yellow line) that fit in the finger solution. We track the center to estimate the velocity of the finger. When $|\kappa| = 0$ at the furthest point of the rounded tip (green dot), the tip-splitting takes place. The numerical integration was performed with $\mu = -0.4$, $\chi = 2$, $\delta = 0.0$, and $\beta = 1$ in a squared box of size 200×200.

Emergence of disordered branching patterns in confined chiral nematic liquid crystals

Sebastián Echeverría-Alar[a,b,1] (iD), Marcel G. Clerc[a,b] (iD), and Ignacio Bordeu[a] (iD)

Spatial branching processes are ubiquitous in nature, yet the mechanisms that drive their growth may vary significantly from one system to another. In soft matter physics, chiral nematic liquid crystals provide a controlled setting to study the emergence and growth dynamic of disordered branching patterns. Via an appropriate forcing, a cholesteric phase may nucleate in a chiral nematic liquid crystal, which self-organizes into an extended branching pattern. It is known that branching events take place when the rounded tips of cholesteric fingers swell, become unstable, and split into two new cholesteric tips. The origin of this interfacial instability and the mechanisms that drive the large-scale spatial organization of these cholesteric patterns remain unclear. In this work, we investigate experimentally the spatial and temporal organization of thermally driven branching patterns in chiral nematic liquid crystal cells. We describe the observations through a mean-field model and find that chirality is responsible for the creation of fingers, regulates their interactions, and controls the tip-splitting process. Furthermore, we show that the complex dynamics of the cholesteric pattern behaves as a probabilistic process of branching and inhibition of chiral tips that drives the large-scale topological organization. Our theoretical findings are in good agreement with the experimental observations.

liquid crystals | chirality | interface dynamics | branching process

Branching processes are responsible for the formation of a vast number of ramified structures observed in geology, chemistry, biology, and physics (1). In soft matter physics, fingering instability, whereby a flat interface becomes unstable, giving rise to tip splitting, is a well-known mechanism of spatial branching (2–4). Several macroscopic models have been formulated to describe the context-dependent mechanisms of branching (1, 5–7). However, it remains a challenging task to identify the key ingredients that lead to the large-scale branching self-organized patterns in each case.

The rich phenomenology of chiral nematic liquid crystals (CNLCs) renders them an ideal system to study pattern formation and branching (8–11). CNLCs can be created by doping a nematic liquid crystal, characterized by a long-range orientational order, but not a positional one, with chiral molecules (12–14). The addition of chiral dopants can induce a spontaneous twist deformation in the nematic phase, creating a helical structure (12, 13, 15). The main feature of this phase is the characteristic length of the helix, known as cholesteric pitch p, which corresponds to the distance required for one full rotation of the nematic director vector $\vec{n}(\vec{r})$, where $\vec{r} = (x, y, z)$ is a position vector. The pitch is the mesoscopic manifestation of the molecular chirality (16), while the director vector field accounts for the local average orientation of liquid crystal molecules (17, 18). When subjected to homeotropic anchoring in a cell of thickness d, the helical phase gets frustrated, so that given a critical degree of frustration, which is measured in terms of the ratio d/p, the system transitions to an unwound (nematic) metastable state. This state is purely geometric and is sustained by the competition between the pitch, geometric effects introduced by the cell thickness, and elasticity (13, 19, 20). The twisted or winded structure can be recovered by applying a voltage, a temperature difference, or changing the thickness to the cell in the unwound state (13). In general, the reappearance of the twisted phase is in the form of a translationally invariant configuration (TIC) or in the form of cholesteric fingers of type 1 (CF1). The TIC phase is characterized by a twist along the cell thickness $\vec{n}(z)$ (*SI Appendix*, Fig. S1) and the CF1 by a director field of the general form $\vec{n}(x, y, z)$ (Fig. 1 *A–C* and *SI Appendix*, Fig. S1). In directional growth experiments with voltage, other types of cholesteric fingers (CF2, CF3, and CF4) have been observed (21). The recovery of the twisted structure can be described by the minimization of the Frank–Oseen free energy with an additional chiral term (*SI Appendix*) (12). This type of noncentrosymmetric interaction is also modeled in chiral magnets and in particle physics (22, 23).

Significance

Chirality breaks the mirror symmetry and may introduce rich new dynamics to physical systems, as observed in particle physics, condensed matter, chemical, biological, and soft matter systems. Here, we consider a liquid crystal mixed with chiral molecules to explore the role of chirality in driving the destabilization of chiral bubbles and the branching dynamics of cholesteric fingers, as a response to thermal forcing on a confined space. We show that the large-scale organization and topology of the chiral textures emerge from stochastic tip branching and inhibition. Our work provides the means to control the organization of confined cholesteric patterns and paves the way for future studies in chiral systems, such as self-organization in noncentrosymmetric magnets.

Fig. 1. Emergence of branching patterns in cholesteric liquid crystal cells. (*A–D*) and (*J–M*) display the schematic representation of the director field of the CNLC in the midplane of the cell $z = d/2$. The angles α and θ correspond to the tilt angle of $\bar{n}$ from the z-axis and the angle between the x-axis and the projection of $\bar{n}$ in the plane of the cell, respectively. (*A*) shows the CF1 director field on the plane, characterized by a good twist across its (*B*) body and (*C*) rounded tip and a localized bad twist at its (*D*) pointed tip. (*E*) Schematic representation of the experimental setup. (*F*), Steady-state cholesteric branching pattern reached after the tip-splitting dynamics. Evolution of branching patterns through the fingering instability of a cholesteric interface starting at $t_1 = 0.00$ s, which is triggered at (*G*), cholesteric fingers ($t_2 = 5.27$ s; $t_3 = 5.83$ s, $t_4 = 6.63$ s) of type I, (*H*) chiral bubbles ($t_2 = 2.62$ s; $t_3 = 3.20$ s, $t_4 = 3.41$ s), and (*I*), glass beads ($t_2 = 0.88$ s; $t_3 = 1.28$ s, $t_4 = 1.63$ s). The initial conditions from where the cholesteric interfaces were created are (*G*) impurities in the nematic phase, (*H*) closed loop of CF1, and (*I*) glass bead. The branching patterns (t_4) are observed at (*G*), 51.7 °C, (*H*) 51.3 °C, and (*I*) 51.7 °C. The green (purple) arrows in (*G*) illustrate the elongation of the rounded (pointed) tips of CF1. (*J*) depicts the director field of a chiral bubble on the plane, exhibiting a radial (*K*) π-twist from its center to the interface (skyrmion-like). (*L–M*) show a schematic representation of the director field build-up around a glass bead on the plane.

The winding/unwinding transition of chiral nematic liquid crystals has been widely studied from experimental and theoretical perspectives (10, 24–29). Near this transition, the distinctive CF1 appear (Fig. 1 *A–I*) (30). These elongated chiral textures nucleate from the unwound background and may elongate in arbitrary orientations from both ends. (Fig. 1*A* and *SI Appendix*, Fig. S1 for the schematic director fields in the midplane of the cell and in a cross-section along d, respectively.) The CF1 are dissipative soliton-like structures with a well-defined width that is regulated by an in-plane good twist of the nematic director (Fig. 1*B*) (25, 31). The elongation of fingers introduces the good twist in the frustrated sample. Fingers are asymmetric and exhibit two different tips, a rounded and a pointy one. The difference in morphology is associated with the handedness of the nematic director near the tips: The good twist gives rise to rounded tips (Fig. 1*C*), while the bad twist produces pointy ones (Fig. 1*D*) (25). In these frustrated CNLCs, above a critical forcing—of temperature, voltage, or confinement— fingers invade all the system through a branching dynamic. Pointy tips propagate in a straight line, nucleating rounded tips through a side-branching mechanism, and rounded tips become unstable, undergoing tip splitting as they propagate (11, 25, 32). Pointy tips, unlike rounded tips, are not generated during branching

events and quickly reconnect with the cholesteric pattern or merge with impurities in the system (25). A combination of side branching and reconnection of pointy tips gives rise to closed loops of CF1. Closed loops can transform into localized twisted objects (29, 33, 34). These localized structures have been termed elementary torons, in particular, triple-twist toron-1 (35, 36). They exhibit a skyrmion-like structure in the midplane director field (36, 37) (cf. Fig. 1 *J* and *K*). Here, we refer to these elementary torons as chiral bubbles, which have also been termed spherulites (13). While more complex cholesteric textures can arise to alleviate frustration (34–36, 38), in our study, we focus only on CF1 and in the interface of chiral bubbles. Similar to glass beads, chiral bubbles can act as nucleation sites for CF1 avoiding the creation of pointy tips (29, 31), which are energetically unfavorable. Hence, the long-term dynamic of growth is governed by the continuous elongation and splitting of rounded tips, resulting in a disordered branching cover. Despite all the work conducted in frustrated CNLCs, the mechanisms that drive the tip splitting of rounded tips of CF1 and the self-organization of disordered ramified patterns have not yet been studied in detail. In this work, we study how the tip-slipping instability develops at cholesteric interfaces and which are the interaction rules that ultimately give rise to the large-scale

cholesteric branching pattern. For this, we focus on temperature-tuned chiral nematic liquid crystal experiments that allow us to control the transition toward branching and the formation of ramified patterns by heating the system. Using an adequate order parameter and its minimal model, which is derived from first principles, we demonstrate the role of chirality in the tip-splitting mechanism and the emergence of the disordered branching pattern with a velocity–curvature equation for the cholesteric interface. We show that during the growth of the chiral fingers, there is a selection principle in the morphology and speed of the rounded tip, which depends on the forcing of the system. From these analyses, we deduce a small number of crucial interactions that regulate the growth process and show that the topological features of the large-scale pattern emerge from stochastic branching and termination events.

Results

Emergence of Disordered Branching Patterns. To explore the growth of cholesteric branching patterns experimentally (Fig. 1 and *SI Appendix*, Movie S1), we consider two chiral–nematic liquid crystal cells, composed of mixtures of a commercial nematic liquid crystal E7 (Merck) and chiral molecules EOS12 (39), under thermal forcing. The cholesteric pitch p in each sample depends on the EOS12 concentration and on the temperature within the cell (14). The samples were introduced into a thermal chamber and then placed between crossed polarizers (Fig. 1E). In this setup, dark regions correspond to the unwound phase, while birefringent regions (shades of blue) correspond to the cholesteric phase (Fig. 1F). To trigger the emergence of the cholesteric phase, we initialize the experiments at room temperature (20 °C), where the CNLC is in the unwinding state, and increase the temperature at a rate of 0.35 °C min^{-1} until reaching a winding phase. Fig. 1F (cell #1; $T = 51.3\,°C$, $p = 3.4\,\mu m$, $d/p < 58.8$; *Materials and Methods* for details) shows a steady-state of the system, which corresponds to a disordered self-organized labyrinthine pattern (40). This pattern develops mainly from the elongation and splitting of rounded tips that leads to a ramified texture, constituted locally by various connected CF1 pointing in arbitrary directions. The cholesteric fingers may be initially nucleated from impurities in the unwound phase as shown in Fig. 1G (cell #2; $T = 51.7\,°C$, $p = 12.9\,\mu m$, $d/p = 0.7$) or at the cholesteric interface of a chiral bubble, which is created by cooling a closed loop of CF1 (29) (see cell #1 in Fig. 1H), or at the interface of glass beads, as depicted in Fig. 1I (cell #2), where molecular deformations are enhanced (31, 41). Under the experimental conditions considered here, the winding/unwinding transition is characterized by the emergence of CF1 (Fig. 1), instead of the TIC phase, when $d/p \approx 0.7$ and the transition temperature (T_c) is around 50 °C. In previous experiments, the TIC phase emerged subcritically in a mixture of E7 with EOS12 at 3 wt% with $d/p = 0.4$ and $T_c \approx 61.3\,°C$ (29). The texture selection and type of transition are governed by the elastic constants of the CNLC mixture E7-EOS12 and the confinement ratio in the cell (*SI Appendix*) (13). In consequence, in the current experimental setup, CF1 are more stable than the TIC phase.

In cells #1 and #2, the system generally avoids the creation of pointy tips by nucleating rounded tips of CF1 from chiral bubbles or glass beads instead. Therefore, the merging process of pointy tips described in the Introduction section can be neglected. We illustrate schematically the in-plane director field of the chiral bubble (Fig. 1 J–K) and around the glass bead (Fig. 1 L–M) to highlight the similarity between both interfaces and rounded tips (Fig. 1A). In the following, we focus our attention on the

growth of fingers and their rounded tips, which can destabilize and undergo branching.

Before introducing a model to describe the rounded tip dynamic and the subsequent patterning process, we explored whether further qualitative insight into the growth process could be extracted from the spatial organization of the labyrinthine pattern (cell #2 in Fig. 2A). Analysis of the power spectrum of the spatial patterns (Fig. 2B) revealed a characteristic wavelength of $\lambda_c = 14.9\,\mu m$ and powder-like ring spectrum with local order, proper of labyrinthine patterns (Fig. 2 B, *Inset*) (40). Furthermore, the distribution of segment lengths (defined as the distance between two branching points along the cholesteric phase) was well fitted by a gamma distribution (data in Fig. 2C), whose exponential tail suggests that the timing between consecutive branching events is uncorrelated (7). The typical segment length (observed as a kink for short fingers) indicates a short-term memory or maturation process between consecutive branching events of a tip. From the temporal evolution of the branching pattern, we noted that branching events could be inhibited by the neighboring pattern (green arrowheads in Fig. 2D), with some newly formed tips receding in favor of the growth of other, more developed tips (white arrowheads in Fig. 2D). These interactions lead to remodeling of the patterns, further contributing to the disordered self-organization of the patterns.

Altogether, these observations suggest that the dynamic of growth, branching, and inhibition of rounded tips controls the self-organization of the chiral labyrinthine patterns. To understand how these mechanisms arise in the context of CNLCs, in the following, we introduce a Ginzburg–Landau-type model that allows us to relate the interaction mechanisms to the chiral nature of the liquid crystal.

The Chiral–Anisotropic Ginzburg–Landau (CAGL) Model. Close to the winding/unwinding transition and in the long-pitch limit of the chiral nematic liquid crystal, the following model can be derived (*SI Appendix* for details)

$$\partial_t A = \mu A + \beta |A|^2 A - |A|^4 A + \partial_\eta \partial_{\bar\eta} A$$
$$+ \delta \partial_\eta \partial_\eta \bar A + i\chi \left(A\partial_{\bar\eta} A + \bar A \partial_\eta A \right), \qquad [1]$$

where $A(x, y, t) = \alpha e^{i\theta}$ is the complex order parameter close to the transition (26), $\partial_\eta = \partial_x + i\partial_y$ is the Wirtinger derivative, and $\bar A$ is the complex conjugate of A. Here, μ is the bifurcation parameter describing the winding/unwinding transition, while the parameter $\beta = \beta(K_{12}, K_{32}, d/p)$ controls the type of bifurcation, which is subcritical ($\beta > 0$) for the experiments considered here (29). The elastic coupling, characterized by the parameter $\delta = (K_{12} - 1)/2(K_{12} + 1)$ (42), considers both isotropic and anisotropic effects. The last term breaks the mirror symmetry in the plane of the cell and is controlled by the parameter $\chi = \chi(K_{12}, K_{32}, d/p)$. $K_{12} = K_1/K_2$, $K_{32} = K_3/K_2$, where the parameters $\{K_1, K_2, K_3\}$ are the elastic constants of the CNLC (12). The model (1) is variational, i.e., $\partial_t A = -\delta \mathcal{F}[A, \bar A]/\delta \bar A$, where

$$\mathcal{F} = \int\int dxdy \left[-\mu |A|^2 - \beta \frac{|A|^4}{2} + \frac{|A|^6}{3} + |\nabla A|^2 \right.$$
$$\left. + 2\delta Re\left\{ (\partial_\eta \bar A)^2 \right\} - i\chi |A|^2 (\partial_{\bar\eta} A - \partial_\eta \bar A) \right], \qquad [2]$$

is the free energy of the system, which is minimized during the dynamics of Eq. 1.
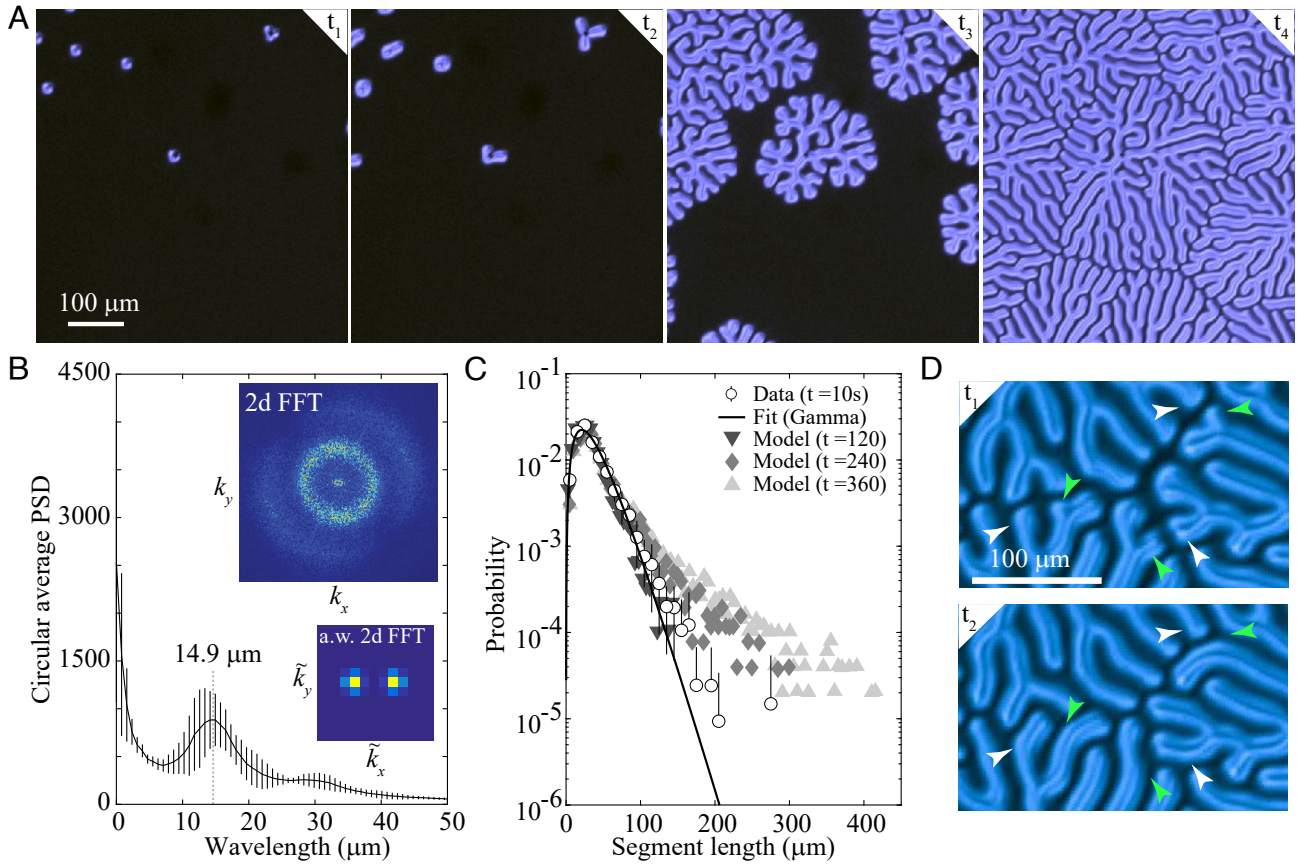
Fig. 2. Tip-branching drives the formation of a cholesteric labyrinthine pattern. (*A*), Time lapse of the destabilization of multiple cholesteric interfaces around glass beads (cell #2 with $d/p = 0.7$) and formation of an extended labyrinthine pattern, at times $t_1 = 3.3$ s, $t_2 = 7.8$ s, $t_3 = 12.2$ s, and $t_4 = 16.7$ s. (*B*), Circular average of the 2D power spectrum (*Inset Top*) of the extended pattern in panel (*A*) at t_4, showing a characteristic wavelength of the cholesteric pattern of $\lambda_C = 14.9$ microns and (*Inset Bottom*) local Fourier transform characterizing the local order in the pattern. (*C*), segment length distribution of the experimental labyrinthine patterns (markers, with errors obtained from 7 independent realizations) and a gamma distribution fit (solid line, for scale and shape parameters), together with the distribution obtained from numerical integration of Eq. **1** at three different times, rescaled by the ratio of the experimental and model wavelengths $\lambda_C/\lambda_{CAGL} \approx 2.3$. (*D*), Two time points ($t_1 < t_2$) of the experiment, showing remodeling of the patterns, where short fingers are inhibited (green arrowheads) allowing other fingers to continue elongating (white arrowheads).

The CAGL Eq. **1** exhibits the same equilibria observed in CNLC experiments: a homeotropic phase $A_o = 0$ (region I in Fig. 3*A*); a translationally invariant configuration (TIC) phase A_T (region II in Fig. 3*A*); a modulated TIC (starting in region II and crossing the green curve into region V or VI in Fig. 3*A*), chiral finger states (region IV in Fig. 3*A*); chiral bubbles (region III in Fig. 3*A*); and cholesteric labyrinths (starting in region IV and crossing the blue curve into region V in Fig. 3*A*) (13, 29). Additionally, the model (1) has a region of bistability of states A_o and A_T ($\mu_{lb} \leq \mu \leq \mu_{ub}$) that contains a Maxwell point μ_{MP}, where both states are energetically equivalent $\mathcal{F}[A_o] = \mathcal{F}[A_T]$ (43). The model also exhibits fingers and tip splitting (*Right* panels of Fig. 3*A*), where fingers nucleate from the homeotropic phase or from a chiral bubble and invade the system through elongation (region IV of Fig. 3*A*) or branching of their rounded tips (region V of Fig. 3*A*). Note that the fingers emerge at $\mu < \mu_{MP}$ (region V in Fig. 3*A*), where the state A_o is more stable than A_T. In brief, the appearance of a finger with a given width is not explained by a modulational instability, as in the case of the modulated TIC phase (13).

To understand the emergence of the chiral fingers from an energy minimization perspective, we first study the properties of an infinite finger in the CAGL Eq. **1**. In the top panel of Fig. 3*B*, the polarized field $\psi(x, y) \equiv \text{Re}(A)\text{Im}(A)$ of the infinite finger solution is shown, together with the horizontal profile of

its modulus R and phase gradient $\partial_x\phi$, where we use the polar representation $A(x, y) = Re^{i\phi}$. The profiles show bell-shaped soliton structures, which are characterized by their heights ($\bar{R}$ and $\bar{\Phi}$) and widths (w and w_ϕ), and can be approximated by $R \approx \bar{R}\text{sech}(x/w)$ and $\partial_x\phi \approx -\bar{\Phi}\text{sech}(x/w_\phi)$, respectively. Introducing these ansatz into the free energy (2), we obtain (*SI Appendix*)

$$\mathcal{F}_{finger} = F_o w + \frac{2(1 + \delta)}{3w}\bar{R}^2 + (1 + \delta)\bar{R}^2\bar{\Phi}^2 I_5(w, w_\phi)$$
$$+ 2\chi\bar{R}^3 I_6(w, w_\phi, \bar{\Phi}) - 2\chi\bar{R}^3\bar{\Phi}I_7(w, w_\phi, \bar{\Phi}), \quad \textbf{[3]}$$

where $F_o = -2\mu\bar{R}^2 - 2\beta\bar{R}^4/3 + 16\bar{R}^6/45$, and I_5, I_6, I_7 are integrals, which depend on the coupling between R, ϕ, and $\partial_x\phi$.

The finger solution is supported by the homogenous state ($\mathcal{F}[A_o] = 0$) if $\mathcal{F}_{finger} < 0$. The energy term F_o is bounded from below $F_o \geq (1.68\sqrt{|\mu|} - 0.67)\bar{R}^4$, which is positive for $\mu < \mu_{MP}$. Hence, the only energetic contribution that stabilizes the finger solution is the chirality, proportional to χ in Eq. **3**, while all the other terms in Eq. **3** act as a nucleation barrier. To find the optimal finger width, we minimize the free energy Eq. **3** with respect to w in the limit $w/L \ll 1$, $w_\phi/L \ll 1$, where L is the length of the finger in the y-direction. As a result of the dependence on the integrals in Eq. **3**, we can only find
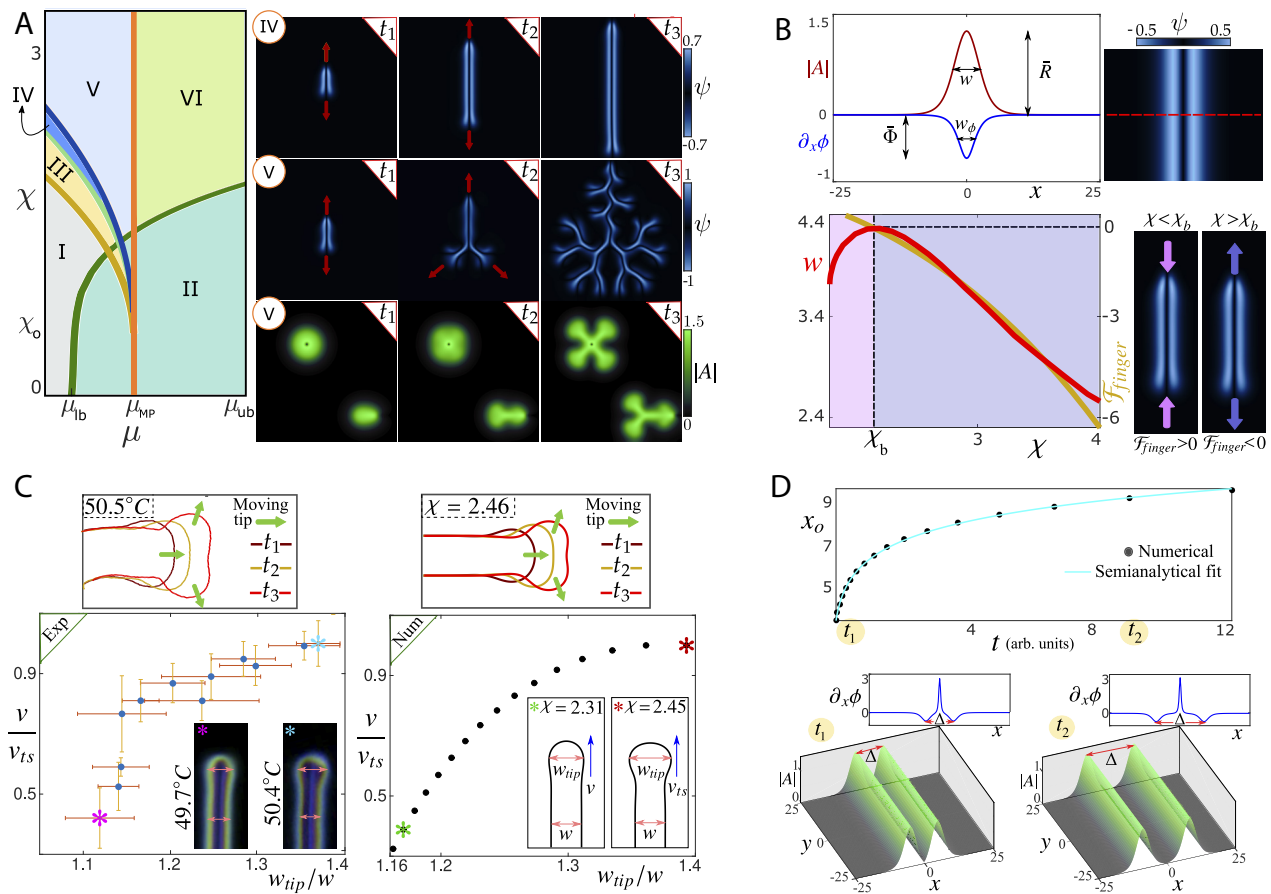
Fig. 3. Local ingredients for the appearance of cholesteric labyrinths. (A), Phase diagram of Eq. **1** with $\delta = 0.05$ and $\beta = 1$. $\mu_{lb} = -1/4$ and $\mu_{ub} = 0$ are the boundaries of the bistability region between A_o (I) and A_T (II). $\mu_{MP} = -3/16$ is the Maxwell point. χ_o is the critical chirality, where chiral bubbles appear. The dark yellow line marks the saddle-node transition of chiral bubbles. The light green curve delimits the emergence of chiral fingers. The blue line represents the tip-splitting instability. Region III is the stable zone of chiral bubbles. In region IV, fingers enlarge from their tips. Rounded tips of chiral fingers are unstable in region V. Regions V and VI exhibit modulated TIC. *Right* panels show temporal snapshots for three different initial conditions with $\mu = -0.4$, in the regions IV ($\chi = 2.31$) and V ($\chi = 2.70$). (B) shows (top) the profiles of the modulus $|A|$ and the gradient of the phase (ϕ) in the x-direction $\partial_x\phi$ of an infinite chiral finger, with $\chi = 2.4$ and $\mu = -0.4$, and (Bottom) shows the variation of the finger width w with respect to χ (red line) in the one-dimensional case, with $\chi_b = 2.3$ when $\mu = -0.4$; the yellow line shows the change in free energy $\mathcal{F}_{finger}$. The insets show the polarized field of chiral fingers with $\chi = 2.2 < \chi_b$ and $\chi = 2.4 > \chi_b$, exhibiting shrinking and elongation, respectively. (C), Different morphologies of chiral fingers were observed experimentally in cell #2 with $d/p \approx 0.68$ (*Left* panel) and numerically (*Right* panel) with $\mu = -0.4$. In the experimental case, the graph shows the speed of the rounded tip against the shape factor w_{tip}/w for different temperatures (the variations of the pitch with temperature in *SI Appendix*, Fig. S2). w_{tip} is the biggest diameter within the rounded tip of the chiral finger, and w is the width of the finger far from the rounded tip. The insets show the morphologies associated with 49.7 °C (pink asterisk) and 50.4 °C (light blue asterisk). Dots are the average of five fingers moving inside a cell of CNLC. The vertical and horizontal bars are the SD of the speed and the shape factor, respectively. In model Eq. **1**, the different morphologies are obtained by varying the χ parameter. The insets display the finger shapes in the case of $\chi = 2.31$ (green asterisk) and $\chi = 2.45$ (orange asterisk). The tip-splitting regime is shown for both cases (50.5 °C and $\chi = 2.46$). Three snapshots ($t_1 = 0.0$ s, $t_2 = 0.25$ s, and $t_3 = 0.4$ s) of the chiral fingers interface are shown, demonstrating the advance, flattening, and modulation of the rounded tips. All speeds are normalized to the average speed previous to tip-splitting v_{ts}. In the experiment, $v_{ts} = 27.4$ μm s^{-1}. (D), (*Top*) Evolution of the distance $x_o(t)$ in the repulsion between two infinite fingers for $\mu = -0.4$ and $\chi = 2.5$. Black dots were obtained from direct simulations, and the solid line corresponds to the integration of Eq. **5**. The *Bottom* panels display two instants, t_1 and t_2, of the repulsive dynamics.

a relationship between the optimal parameters of the finger solution; $w^3 \approx 3\pi^3 \chi w_\phi^3 \bar{R}^3 \bar{\Phi}/4F_o$ (*SI Appendix*). Therefore, the nontrivial phase structure plays a fundamental role in defining the width, and F_o must be positive to observe stable finger solutions, i.e., the most stable homogenous state needs to be A_o. Note that a similar energy dependence is obtained in bistable reaction–diffusion systems (6).

The bottom panel of Fig. 3B shows the variation of the one-dimensional finger width w as a function of the chirality χ (red curve), which has a maximum at $\chi = \chi_b$. When $\chi > \chi_b$, the free energy $\mathcal{F}_{finger}$ (Eq. **3**) becomes negative (yellow line in the *Bottom* panel of Fig. 3B) and the system favors the propagation of fingers by elongation of the two tips (*Bottom Right* panels of Fig. 3B). Conversely, when $\chi < \chi_b$, the chiral finger shrinks and eventually disappears due to the merging of both tips.

When chiral fingers emerge, they propagate and cover the whole system. In the experiment of CNLCs, the temperature specifies the pitch and finger width and fixes the propagation speed of CF1, v. We note that the chiral finger growth has a selection mechanism similar to that observed in dendritic growth (44, 45), where the propagation speed is controlled by the curvature of the tip. By increasing the temperature, fingers propagate faster, and the tip swells, as shown in Fig. 3C.

CF1 may be characterized morphologically by the shape factor w_{tip}/w, where w_{tip} is the diameter of the rounded tip and w is the finger width (cell #2 in the left panel of Fig. 3C). At the critical speed v_{ts} and corresponding critical shape factor, propagating tips become unstable, swelling and undergoing tip splitting. This branching process may be interpreted as a more efficient dissipation mechanism to develop chirality than simple tip

propagation. The tip-splitting dynamics is characterized by the inflation, flattening, and interfacial modulation of the rounded tip (see the snapshots $t_1 - t_3$ in the *Left* panel of Fig. 3C). The *Right* panel of Fig. 3C shows the change in morphology in numerical integrations of Eq. **1** for different values of the chiral parameter χ. Remarkably, the relation between speed and shape obtained through numerical simulations closely resembles the experimental observations. The critical value of the shape factor at which tip splitting takes place is close to its experimental value $w_{tip}/w \simeq 1.4$, and in both cases, tips suffer the same curvature and morphological changes during branching.

One way to understand the emergence of tip splitting is to analyze it from the perspective of local interface dynamics (5, 6). Recently, a local zero-dimensional interface equation was derived from Eq. **1** near the critical point $\{\mu_{MP}, \chi_o\}$ for chiral bubbles (29). There, it was shown that a balance between metastability, a linear curvature term due to chirality, and a squared curvature contribution defined the size of chiral bubbles. Here, to describe the tip-splitting instability, one needs to account for the spatial modulation along the interface and the proper stabilization mechanism at small wavelengths. We model the interface of the rounded tip as the interface of half of the chiral bubble in model Eq. **1**. The tip splitting is analogous then to a fourth mode instability of the interface of a full cholesteric bubble as shown in the *Bottom Right* panel of Fig. 3A. Therefore, to extract the curvature dynamics of the interface, we perform a nonlinear stability analysis around the interface of the chiral bubble solution, $A_{cb} = R_o e^{i\phi}$ in Eq. **1** and obtain the speed-curvature or Gibbs–Thomson (46) relation

$$v_N = -|\mu_1|A + B\chi_1\tilde{\kappa} + C\tilde{\kappa}^3 + D\partial_{SS}\tilde{\kappa}, \quad [4]$$

where A, B, C, and D are constants (*SI Appendix*). A similar version of Eq. **4** has been heuristically proposed to explore the local behavior of interface dynamics (5), derived in the study of growth laws of droplets (47) and bistable reaction–diffusion systems (6) and also used in the framework of bacterial growth (48). The constants A, B, and D are always positive above the dark yellow line in the phase diagram of Fig. 3A. For large wavelength perturbations, Eq. **4** has a modulational instability due to a Mullins–Sekerka type of term (linear in curvature $\tilde{\kappa}$), which is tuned by the chirality, i.e., growth is enhanced in curved regions of the interface. At short wavelengths, the instability is saturated by the last term in Eq. **4**, which plays the role of line tension. The cubic term in Eq. **4** is responsible for the tip splitting, where the constant C is defined by a nontrivial balance between chirality, diffusion, and energy differences between states, and it must be positive to ensure that the curvature dynamics is variational (*SI Appendix*). The relation between curvature and splitting explains why a tip must swell before branching, a dynamic that also explains the maturation (or refractory period) feature observed earlier in the segment length distribution (Fig. 2C).

Another key ingredient for the formation of the cholesteric branching patterns is the repulsion between the chiral fingers (25). To study the origin of the CF1 repulsion in our model, Eq. **1**, we consider two infinite cholesteric fingers. The *Bottom* panels of Fig. 3D show two different instants of the interaction between two cholesteric fingers, where a nontrivial structure in the gradient of the phase is observed between the two fingers. As it turns out, this structure is responsible for the repulsion between fingers. Following this idea and the symmetry of the modulus R and the phase gradient $\partial_x\phi$, we model the repulsion between fingers as the interaction between a single finger, at a position $x_o(t)$ from the origin, and half of the phase structure near $x = 0$,

that is, $R(t) = R(x - x_o(t))$ and $\partial_x\phi(t) = \partial_x\phi(x - x_o(t)) + \theta_b(x)$, where $A(t) = R(t)e^{i\phi(t)}$ and θ_b represents the phase structure near $x = 0$. Numerical observations show that the tail of θ_b decays like e^{-bx}/x for a positive constant b. Based on the variational form of model Eq. **1**, the dynamic of the position x_o is given by (*SI Appendix*)

$$\partial_t x_o = \mathcal{N}(\mu, \chi)\frac{e^{-bx_o}}{x_o}. \quad [5]$$

The prefactor $\mathcal{N}(\mu, \chi)$ is positive in the range of parameters where chiral fingers are observed (region IV and V of Fig. 3A). Thus, the interaction between fingers is repulsive in order to minimize the energy of the system. By integrating the repulsive relationship, we get the semianalytical curve $x_o(t)$ shown in the *Top* panel of Fig. 3D.

Organization of the Large-Scale Chiral Branching Pattern. In the previous section, we described how the local destabilization of the nematic phase leads to the propagation of a chiral (or cholesteric) phase, which organizes into a ramified pattern that expands through the propagation of chiral tips. The chirality drives the growth and splitting of tips as well as the repulsion between fingers. From the propagation of the branching pattern (experiment Fig. 2A and model Fig. 4A), we note that actively elongating and branching tips localize entirely at the periphery of the growing pattern, while tips submerged within the labyrinthine structure arrest their growth due to steric interactions with the surrounding pattern. The interactions that give rise to the branching cholesteric pattern can be reduced then to tip propagation and branching, repulsion (that results in alignment of neighboring segments), and tip inhibition. Moreover, the characteristic width of CF1 combined with the energy minimization dynamics leads to a spatial pattern structure with a well-defined wavelength, with a short-scale order but large-scale disorder (Fig. 2B).

To study how the large-scale disorder emerges from the local interaction rules, we first focused on the model (1), which allowed us to study the topological properties of large-scale patterns without the influence of additional structures (Fig. 4A). From these patterns, we were able to extract the branching trees (Fig. 4B), produced by reducing the pattern to a network of vertices and edges, where each edge corresponds to a chiral segment that connects vertices representing branching points. Here, we were concerned solely with the topology of the network, which is completely characterized by the levels (or generations) of branching. The subtrees of the network, defined as sets of branches with a last common ancestor node at level 2, showed a high heterogeneity of sizes (number of segments) and persistence (number of generations beyond level 2); see colored subtrees in Fig. 4 *A* and *B* indicating a rather random organization of the topology of the pattern as seen, for example, in biological tissues (7, 49, 50). A heterogeneous organization of the branching tree may arise from a stochastic process of branching and inhibition of propagating chiral tips, which was also supported by the exponential decay of segment lengths (Fig. 2C). To test this hypothesis, we computed the probability that tips at a given level arrest their growth (Fig. 4C). As time passes, tips that are not constrained may continue branching, lowering the termination probability. We then simulated a zero-dimensional birth–death process, where particles either branched or became inhibited with probabilities depending on their generations and given by Fig. 4C (*Methods* for details). To compare the results of the
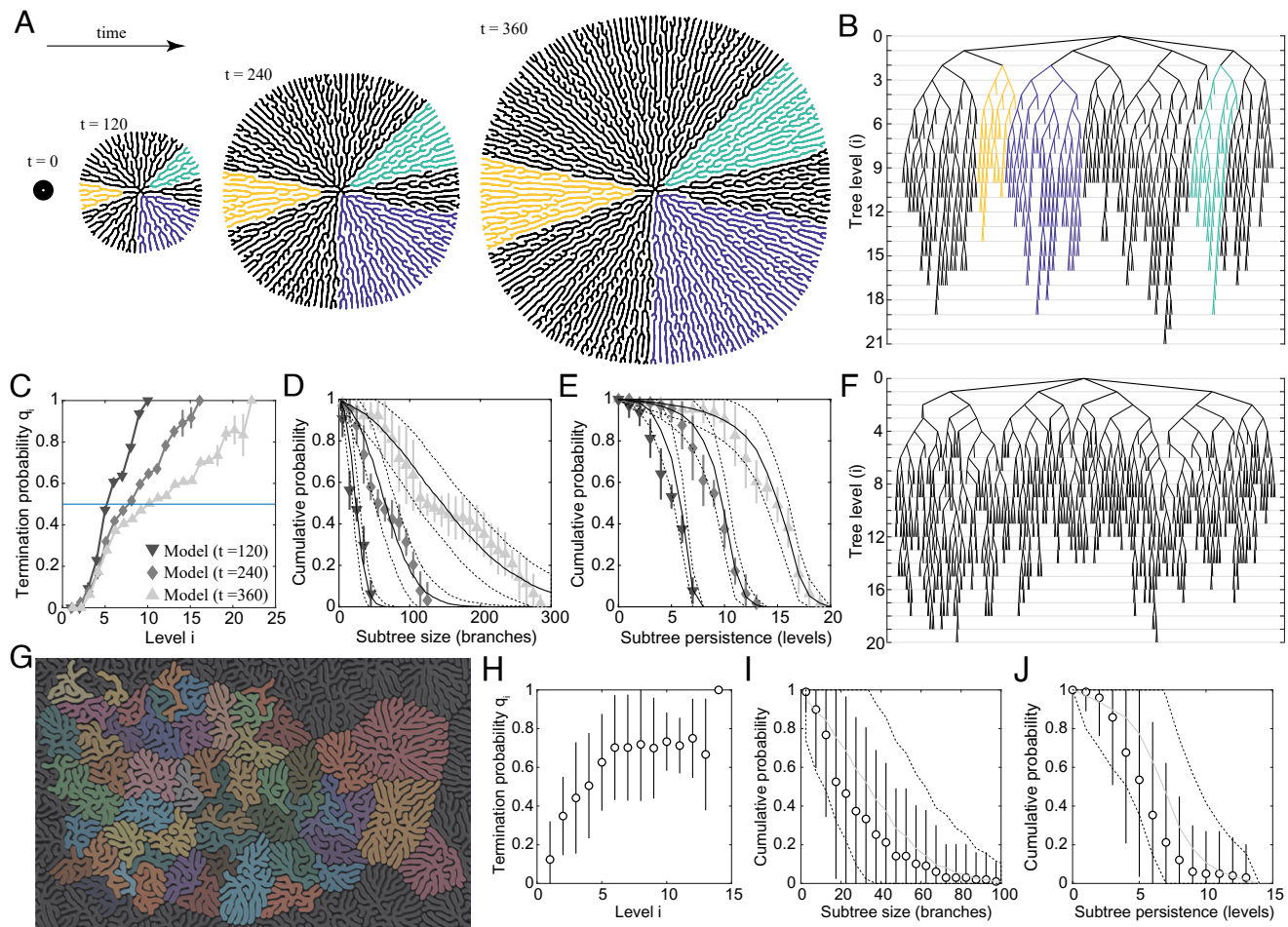
Fig. 4. The large-scale organization emerges from probabilistic tip branching and inhibition events. (*A*), Numerical integration of the Eq. **1** showing the destabilization of a chiral bubble-like initial condition ($t = 0$) into a branched pattern ($t = 240$ and $t = 360$, measured in arbitrary units). Subtrees of the branching structure, defined as those trees that have a last common ancestor at branching level 2, are colored at different times to emphasize the variability in the tree growth dynamics. (*B*), Branching tree representation of the pattern at time $t = 360$, shown in (*A*). (*C*) The probability that a tip terminates at a given level in the tree at different time point obtained from $n = 8$ large-scale simulations of the model (1). (*D* and *E*) show the cumulative probability of (*D*) subtree sizes and (*E*) subtree persistence obtained from large-scale simulations of the model (mean and SD from $n = 8$ realizations) and birth–death process when supplied with the termination probabilities at each time point in (*C*), with mean (line) and SD (shaded) from $n = 10^3$ realizations. (*F*), Branching tree resulting from the birth–death process using as input the termination probabilities at $t = 360$ shown in (*C*). (*G*), Representative stationary state from experiments; disconnected branching patterns are shown in different colors, and black-shaded patterns were not considered in the analysis as they cross the boundaries of the observation window. (*H*), Average termination probability obtained from 39 disconnected branching patterns from 7 experimental realizations. (*I* and *J*) show the cumulative probability of (*D*) tree sizes and (*E*) tree persistence (full trees were used due to their small size) obtained from experiments (mean and SD) and birth–death process when using the termination probabilities in (*G*) as input.

model (1) and the stochastic birth–death process, we looked at the distribution of subtree sizes and persistence, from which we found excellent agreement (Fig. 4 *C* and *D*). These results show that even though the system has well-defined interaction rules, their large-scale organization emerges from random events of branching and termination that are regulated locally, at the single tip level (see the typical branching tree from the birth–death process in Fig. 4*F*).

To verify that these observations also apply to the experimental branching patterns, we looked at 7 realizations of the experiments, where multiple distinct patterns nucleated from the glass beads in the sample (Figs. 1*E* and 4*G*). The final patterns had a range of sizes and interacted as they developed, in some cases inhibiting the growth of neighboring tips. By focusing on trees with more than one branching event, we reconstructed the termination probability (Fig. 4*H*) and used it as input in the stochastic birth–death process. These resulted, again, in good agreement between experiments and the stochastic process (Fig. 4 *I* and *J*, where full trees were analyzed due to their small size), strongly supported the

conclusion that the large-scale topology of the chiral branching patterns is regulated locally by statistical rules of branching and termination, resulting in the disordered patterns observed.

In summary, we have investigated experimentally and theoretically the spatial and temporal organization of thermally induced branching patterns in chiral nematic liquid crystal cells. By using the Ginzburg–Landau-type description of CNLCs, we established the role of chirality in the formation of disordered branching patterns. Here, the (de)stabilization of chiral fingers arises from an energy minimization process, which also leads to tip splitting and causes repulsive interactions between fingers. We extracted a minimal set of local rules that regulate the pattern growth—tip elongation, branching, repulsion, and inhibition—and showed that the large-scale organization of the branching pattern described a stochastic birth–death process, where branching and termination events are probabilistic in nature. The large-scale organization of the chiral phase emerges then from local interactions at the single tip level, which minimizes energy efficiently through branching.

Our analyzes show that even though the liquid crystal structure is inherently 3D, the dynamics of growth of the branching phase follows simple local rules that take place on the 2D midplane, resulting in branching and inhibition of tips. Therefore, neglecting the three-dimensional liquid crystal structure is a good approximation for studying the formation of disordered branching patterns resulting from CF1 destabilization. An interesting future direction of research is to explore other finger structures, such as CF2, CF3, and CF4 (21) and investigate their space-filling dynamics. Additionally, in the broader context, it will be interesting to explore possible branching processes of stripe phases in chiral magnets (51).

Materials and Methods

Materials and Experimental Setup. We consider a chiral liquid crystal composed of a mixture of a commercial multicomponent nematic liquid crystal E7 (pure components: 4-cyano-4'-n-pentyl-1,1'- biphenyl (5CB-51\%); 4-cyano-4'-n-heptyl-1,1'- biphenyl (7CB-25\%); 4-cyano-4'-n-octyloxy-1,1'- biphenyl (8OCB-16\%); 4-cyano-4"-n-pentyl- 1,1',1" -terphenyl (5CT-8\%)) from Merck with chiral molecules EOS-12 (4-(5-dodecylthio-1,3,4-oxadiazole-2-yl)phenyl 4'-(1"-methyl heptyl-oxy)benzoate) at 25 wt% and 7 wt%. The cholesteric pitch p associated with each chiral–nematic mixture is measured with the Grandjean–Cano technique at the temperatures of observation, by using a planoconvex cylindrical lens of radius 10.3 mm (Thorlabs) as thickness modulation. Two cell preparations were implemented. In the first one, a chiral liquid crystal droplet (with EOS-12 at 25 wt%) is deposited over a soda-lime glass sheet using a microcapillary tube and covered with another sheet of the same characteristics (2.5 cm×2.5 cm area and 4 mm thickness). This type of glass induces a homeotropic anchoring on the liquid crystal sample. The squeezed disk-shaped droplet reaches an equilibrium diameter of approximately 1 cm. The cell obtained with this method is cell #1 with $d = 200$ μm. The cell thickness was obtained with a Mitutoyo digital micrometer with an accuracy of 1 μm. We note that to increase the resolution of the images of chiral bubbles, we used a 50x objective with a small working distance (Leica, HC PL APO 50x/0,90). Then, in our experimental setup, it was unavoidable to squeeze cell #1 with the objective, thus pushing the cell thickness to an effective value $d < 200$ μm. For this reason, this cell was used exclusively for observational purposes (Fig. 1 F and H). The second method is by filling chiral nematic liquid crystals (with EOS-12 at 7 wt%), by capillary action at 70 °C, into a fabricated cell (SG025T090uT180 manufactured by Instec) of thickness $d = 9$ μm, which is chemically treated to give homeotropic boundary conditions, and its thickness is fixed by glass beads. This cell, #2, was used in the experimental measurements discussed in the text (Figs. 2, 3C, and 4 G–J) and in the observations shown in Fig. 1 G and I. The prepared cells are introduced into a LinkamT95-PE hot stage and placed between crossed polarizers in a Leica DM2700P microscope with 5x, 10x, and 50x objectives. A CMOS camera records the branching dynamics.

Numerical Integration of the Chiral–Anisotropic Ginzburg–Landau Equation. To solve model Eq. **1**, we write the equation in terms of its real part u and imaginary part v ($A = u + iv$). Then, we discretize the space by using a finite difference scheme with a spatial step of $\Delta x = 0.25$ and a three-point stencil using nonflux boundary conditions. The coupled equations for u and v are numerically integrated in time with the Runge–Kutta 4 time integrator with temporal step $\Delta t = 0.01$. The finger solutions shown in Fig. 3 were created by perturbing the zero solution with a rectangular perturbation of width $2w$ and amplitude $(u, v) = (1.5, 0)$ in region IV of the phase diagram in Fig. 3A. Depending on the proximity of the tips to the boundaries (with nonflux boundary conditions), we can annihilate tips and create fingers only with rounded tips (Fig. 3C) and without tips (Fig. 3 B and D). The chiral bubble solutions are created following the experiment. We start with a finger in region IV and sweep the

parameter χ or μ to access the branching region V of the phase diagram in Fig. 3A. The pointy tip of a finger can merge with a side branch and create a CF1 loop solution (29). Then we change the parameters into region III and the CF1 loop solution collapses into the chiral bubble solution. This localized solution is used as the initial condition in Figs. 3A and 4A (in the branching region V). All the numerical results related to Fig. 3 are obtained in square grids of size 200x200. In the case of Fig. 4A, we used a square grid of size 1000x1000.

Shape Factor w_{tip}/w and Speed of CF1. To characterize the morphology of the chiral fingers, we introduced in the text the dimensionless shape factor w_{tip}/w. The width w of the fingers is calculated as the finite width at half-maximum of the transversal profiles of the fingers from the binarized images in the experiment and from the numerical solutions of Eq. **1**. We determine the diameter of the tip w_{tip} as the diameter of the biggest circle that fits the rounded tips of CF1. Once the biggest circle is fitted in the rounded tip of a CF1, we track the position of the tip and measure its speed v. In the experimental case, mixture of E7 and EOS-12 at 7 wt% within cell #2 with $d/p \approx 0.68$, we averaged the width, tip diameter, and speed of five fingers, which are seen under crossed polarizers at different temperatures. Finally, the criteria to determine the tip-splitting speed v_{ts} is when the far-most point of the rounded tip interface has zero curvature (flat front).

Numerical Simulation of the Stochastic Birth–Death Process. The topology and statistics of a branching tree depend on the growth dynamic and how tips interact with the surrounding structures. In particular, the exponential decay of segment lengths in the chiral branching tree (Fig. 2C) suggests that the branching and termination events are uncorrelated, thus following a Poisson-like process, albeit with a short refractory period. With this in mind, we questioned whether the large-scale topology of the branching tree could be fully characterized by its branching (and terminating) probabilities. For this, we formulated a simple birth–death model: a zero-dimensional branching process, where tip branching and terminations follow a stochastic rule. In this birth–death model, which has also been used to describe ramified biological tissues (49), tips are allowed to branch and terminate with probabilities estimated from the data. These probabilities are obtained from the termination probabilities q_i (Fig. 4 C and H) and depend exclusively on the generation in the branching tree. We note that if the birth–death model was not able to recapitulate the branching topology of the tree, then it would indicate that correlations and spatial considerations would indeed be essential to the resulting large-scale chiral pattern. Numerically, the birth–death model was implemented as a discrete-time process, where, at every iteration, all active (tip) particles were allowed to either branch (with probability $p_{\text{branch}} = 1 - q_i$) or become inactive (inhibited) with probability $p_{\text{inhib}} = q_i$, depending on the generation i at which the particles are. For this, we initialized the system with a number $N \geq 1$ of particles to match the initial state observed either in the model (1) or the experiments. For each realization, we kept track of the history of all particles in order to reconstruct the branching trees (Fig. 4F).

1. V. Fleury, J. F. Gouyet, M. Leonetti, *Branching in Nature: Dynamics and Morphogenesis of Branching Structures, from Cell to River Networks* (Springer Science, Business Media, 2001), vol. 14.
2. P. G. Saffman, G. I. Taylor, The penetration of a fluid into a porous medium or Hele-Shaw cell containing a more viscous liquid. *Proc. R. Soc. London. Ser. A. Math. Phys. Sci.* **245**, 312–329 (1958).
3. A. Buka, J. Kertész, T. Vicsek, Transitions of viscous fingering patterns in nematic liquid crystals. *Nature* **323**, 424–425 (1986).
4. K. J. Lee, W. McCormick, Q. Ouyang, H. L. Swinney, Pattern formation by interacting chemical fronts. *Science* **261**, 192–194 (1993).
5. R. C. Brower, D. A. Kessler, J. Koplik, H. Levine, Geometrical approach to moving-interface dynamics. *Phys. Rev. Lett.* **51**, 1111 (1983).
6. R. E. Goldstein, D. J. Muraki, D. M. Petrich, Interface proliferation and the growth of labyrinths in a reaction-diffusion system. *Phys. Rev. E* **53**, 3933 (1996).
7. E. Hannezo et al., A unifying theory of branching morphogenesis. *Cell* **171**, 242–255 (2017).
8. A. Stieb, Structure of elongated and spherulitic domains in long pitch cholesterics with homeotropic boundary alignment. *J. de Phys.* **41**, 961–969 (1980).
9. P. Oswald, J. Bechhoefer, A. Libchaber, Instabilities of a moving nematic-isotropic interface. *Phys. Rev. Lett.* **58**, 2318 (1987).
10. P. Ribiere, S. Pirkl, P. Oswald, Electric-field-induced phase transitions in frustrated cholesteric liquid crystals of negative dielectric anisotropy. *Phys. Rev. A* **44**, 8198 (1991).
11. T. Nagaya, Y. Hikita, H. Orihara, Y. Ishibashi, Experimental study of the growth of the cholesteric finger pattern. *J. Phys. Soc. Japan* **65**, 2707–2712 (1996).
12. P. G. de Gennes, J. Prost, *The Physics of Liquid Crystals* (Clarendon Press, Oxford, UK, ed. 2, 1993).
13. P. Oswald, P. Pieranski, *Nematic and Cholesteric Liquid Crystals* (CRC Press, London, 2005).
14. I. Dierking, *Textures of Liquid Crystals* (John Wiley & Sons, 2003).
15. A. B. Harris, R. D. Kamien, T. C. Lubensky, Molecular chirality and chiral parameters. *Rev. Mod. Phys.* **71**, 1745 (1999).
16. S. Pieraccini, S. Masiero, A. Ferrarini, G. P. Spada, Chirality transfer across length-scales in nematic liquid crystals: Fundamentals and applications. *Chem. Soc. Rev.* **40**, 258–271 (2011).
17. H. De Vries, Rotatory power and other optical properties of certain liquid crystals. *Acta Crystallogr.* **4**, 219–226 (1951).
18. R. Cano, Interprétation des discontinuités de grandjean. *Bull. de Minéral.* **91**, 20–27 (1968).
19. W. E. Haas, J. E. Adams, Electrically variable diffraction in spherulitic liquid crystals. *Appl. Phys. Lett.* **25**, 263–264 (1974).
20. N. Nawa, K. Nakamura, Observation of forming process of bubble domain texture in liquid crystals. *Japan. J. Appl. Phys.* **17**, 219 (1978).
21. J. Baudry, S. Pirkl, P. Oswald, Topological properties of singular fingers in frustrated cholesteric liquid crystals. *Phys. Rev. E* **57**, 3038 (1998).
22. R. Takagi et al., Spin-wave spectroscopy of the Dzyaloshinskii-Moriya interaction in room-temperature chiral magnets hosting skyrmions. *Phys. Rev. B* **95**, 220406 (2017).
23. T. H. R. Skyrme, A unified field theory of mesons and baryons. *Nucl. Phys.* **31**, 556–569 (1962).
24. F. Lequeux, P. Oswald, J. Bechhoefer, Influence of anisotropic elasticity on pattern formation in a cholesteric liquid crystal contained between two plates. *Phys. Rev. A* **40**, 3974 (1989).
25. P. Ribiere, P. Oswald, Nucleation and growth of cholesteric fingers under electric field. *J. de Phys.* **51**, 1703–1720 (1990).
26. T. Frisch, L. Gil, J. M. Gilli, Two-dimensional Landau-de Gennes dynamical model for the unwinding transition of a cholesteric liquid crystal. *Phys. Rev. E* **48**, R4199 (1993).
27. L. Gil, Numerical resolution of the cholesteric unwinding transition problem. *J. de Phys.* II (5), 1819–1833 (1995).
28. S. Thiberge, Ph.D. thesis (Université de Nice–Sophia Antipolis) (1999).
29. M. G. Clerc, G. González-Cortés, S. Echeverría-Alar, Localized dissipative vortices in chiral nematic liquid crystal cells. *Phys. Rev. Res.* **4**, L022021 (2022).
30. P. Oswald, J. Baudry, S. Pirkl, Static and dynamic properties of cholesteric fingers in electric field. *Phys. Rep.* **337**, 67 (2000).
31. I. I. Smalyukh et al., Electric-field-induced nematic-cholesteric transition and three-dimensional director structures in homeotropic cells. *Phys. Rev. E* **72**, 061707 (2005).
32. P. Oswald, J. Baudry, T. Rondepierre, Growth below and above the spinodal limit: The cholesteric-nematic front. *Phys. Rev. E* **70**, 041702 (2004).
33. J. Baudry, S. Pirkl, P. Oswald, Looped finger transformation in frustrated cholesteric liquid crystals. *Phys. Rev. E* **59**, 5562 (1999).
34. J. S. B. Tai, P. J. Ackerman II, Smalyukh,, Topological transformations of Hopf solitons in chiral ferromagnets and liquid crystals. *Proc. Natl. Acad. Sci. U.S.A.* **115**, 921–926 (2018).
35. P. J. Ackerman II, Smalyukh,, Diversity of knot solitons in liquid crystals manifested by linking of preimages in Torons and Hopfions. *Phys. Rev. X* **7**, 011006 (2017).
36. I. I. Smalyukh, Y. Lansac, N. A. Clark, R. P. Trivedi, Three-dimensional structure and multistable optical switching of triple-twisted particle-like excitations in anisotropic fluids. *Nat. Mater.* **9**, 139–145 (2010).
37. S. Muhlbauer et al., Skyrmion lattice in a chiral magnet. *Science* **323**, 915–919 (2009).
38. I. I. Smalyukh, Knots and other new topological effects in liquid crystals and colloids. *Rep. Progr. Phys.* **83**, 106601 (2020).
39. M. L. Parra, P. I. Hidalgo, E. Y. Elgueta, Synthesis and mesomorphic properties of oxadiazole esters derived from (r)-2-octanol,(s)-2-n-octyloxypropanol and (2 s, 3 s)-2-chloro-3-methylpentanol. *Liq. Cryst.* **35**, 823–832 (2008).
40. S. Echeverría-Alar, M. Clerc, Labyrinthine patterns transitions. *Phys. Rev. Res.* **2**, 042036 (2020).
41. V. Zambra, M. G. Clerc, R. Barboza, U. Bortolozzo, S. Residori, Umbilical defect dynamics in an inhomogeneous nematic liquid crystal layer. *Phys. Rev. E* **101**, 062704 (2020).
42. T. Frisch, S. Rica, P. Coullet, J. M. Gilli, Spiral waves in liquid crystal. *Phys. Rev. Lett.* **72**, 1471 (1994).
43. R. E. Goldstein, G. H. Gunaratne, L. Gil, P. Coullet, Hydrodynamic and interfacial patterns with broken space-time symmetry. *Phys. Rev. A* **43**, 6700 (1991).
44. J. S. Langer, Instabilities and pattern formation in crystal growth. *Rev. Mod. Phys.* **52**, 1 (1980).
45. E. Ben-Jacob, P. Garik, The formation of patterns in non-equilibrium growth. *Nature* **343**, 523–530 (1990).
46. L. M. Pismen, *Patterns and Interfaces in Dissipative Dynamics* (Springer Science & Business Media, 2006).
47. D. Gomila, P. Colet, G. L. Oppo, M. San Miguel, Stable droplets and growth laws close to the modulational instability of a domain wall. *Phys. Rev. Lett.* **87**, 194101. (2001).
48. L. Xiong et al., Flower-like patterns in multi-species bacterial colonies. *Elife* **9**, e48885 (2020).
49. C. L. Scheele et al., Identity and dynamics of mammary stem cells during branching morphogenesis. *Nature* **542**, 313–317 (2017).
50. F. J. Roos et al., Human branching cholangiocyte organoids recapitulate functional bile duct formation. *Cell Stem Cell* **29**, 776–794 (2022).
51. X. Wang, X. Hu, H. Wu, Stripe skyrmions and skyrmion crystals. *Commun. Phys.* **4**, 142 (2021).

Supporting Information for

Emergence of disordered branching patterns in confined chiral nematic liquid crystals

Sebastián Echeverría-Alar, Marcel G. Clerc and Ignacio Bordeu

Sebastián Echeverría-Alar.
E-mail: sebastianecheverria@ug.uchile.cl

This PDF file includes:

Supporting text
Figs. S1 to S3
Legend for Movie S1
SI References

Other supporting materials for this manuscript include the following:

Movie S1

Supporting Information Text

Derivation of the chiral-anisotropic Ginzburg-Landau (CAGL) model. The CAGL model can be derived from first principles, based on the dissipative dynamics of the director field $\vec{n}(\vec{r}, t)$, where $\vec{r}$ and t indicate spatial and temporal dependence, respectively. This procedure gives a unique dependence of the parameters μ, β, δ, and χ with the elastic constants and the confinement ratio d/p of chiral nematic liquid crystal (CNLC) cells. We are interested in the experimental situation where a nematic phase $\vec{n} \equiv \vec{n}_o$, induced by the homeotropic anchoring of a cell with thickness d, is invaded by a cholesteric phase $\vec{n} \equiv \vec{n}(\vec{r})$ in the form of cholesteric fingers of type I (CF1) when energy is injected in the system. In our case, an increase in temperature is the injection of energy, but it could also be an electric field (1).

The starting point is a continuum theory for the chiral nematic liquid crystal. We follow a simple approach and suppose that in a weakly distorted regime, the local properties of the material are the ones of a uniaxial liquid crystal (2). This supposition allows us to write the Frank-Oseen free energy

$$F_{ed} = \int \left[\frac{K_1}{2} (\nabla \cdot \vec{n})^2 + \frac{K_2}{2} (\vec{n} \cdot \nabla \wedge \vec{n} + 2\pi/p)^2 + \frac{K_3}{2} (\vec{n} \wedge \nabla \wedge \vec{n})^2 \right] d\vec{r}, \qquad [1]$$

where K_1, K_2, and K_3 are the splay, twist, and bend elastic constants, respectively. The volumetric free energy F_{ed} is valid in the limit of strong anchoring where surface terms can be neglected. The cholesteric pitch p needs to be big, compared to a molecular scale, so the supposition of uniaxiality remains valid (3). When energy is injected into the system, the molecules will dissipate it following a minimization process that can be accounted by the evolution of the director $\vec{n}(\vec{r}, t)$, while maintaining its unitary norm (4)

$$\gamma \frac{d\vec{n}}{dt} = -\frac{\delta F_{ed}}{\delta \vec{n}} + \vec{n} \left(\vec{n} \cdot \frac{\delta F_{ed}}{\delta \vec{n}} \right), \qquad [2]$$

where γ is a rotational viscosity constant. Then, introducing the free energy Eq. (1) into Eq. (2), one obtains (5)

$$\gamma \frac{d\vec{n}}{dt} = K_3 [\nabla^2 \vec{n} - \vec{n}(\vec{n} \cdot \nabla^2 \vec{n})] + (K_3 - K_1)[\vec{n}(\vec{n} \cdot \nabla)(\nabla \cdot \vec{n}) - \nabla(\nabla \cdot \vec{n})]$$
$$+ (K_2 - K_3)[2(\vec{n} \cdot \nabla \wedge \vec{n})\{\vec{n}(\vec{n} \cdot \nabla \wedge \vec{n}) - \nabla \wedge \vec{n}\} + \vec{n} \wedge \nabla(\vec{n} \cdot \nabla \wedge \vec{n})] + \frac{4\pi K_2}{p}[-\nabla \wedge \vec{n} + \vec{n}(\vec{n} \cdot \nabla \wedge \vec{n})], \qquad [3]$$

with the homeotropic boundary conditions, $\vec{n}(x, y, z = 0) = \vec{n}(x, y, z = d) = \hat{z}$. Note that the last term accounts for the torque induced by chiral effects.

We perform a linear stability analysis of the homeotropic nematic phase $\vec{n}_o = (0, 0, 1)$ against small perturbations to find the critical confinement ratio d/p, at which the winding/unwinding transition is developed. Then, we replace the perturbative ansatz $\vec{n} = (n_1, n_2, \sqrt{1 - n_1^2 - n_2^2})$ into Eq. (3) and retain only linear terms in n_1 and n_2, which leads to the coupled equations

$$\gamma \frac{\partial n_1}{\partial t} = K_3 \partial_{zz} n_1 + \frac{4\pi K_2}{p} \partial_z n_2, \qquad [4]$$

$$\gamma \frac{\partial n_2}{\partial t} = K_3 \partial_{zz} n_2 - \frac{4\pi K_2}{p} \partial_z n_1. \qquad [5]$$

Note that the third component of the perturbation was restrained to higher order corrections in n_1 and n_2 due to the norm conservation $|\vec{n}| = 1$. The next step is to find the condition at which the first unstable winding mode grows, that is, we consider an ansatz of the form $n_1 = \alpha_o \cos(fz) \sin(\pi z/d)e^{\sigma t}$ and $n_2 = \alpha_o \sin(fz) \sin(\pi z/d)e^{\sigma t}$. These components satisfy the homeotropic boundary conditions at $z = 0$ and $z = d$ (see Fig. S1a) and correspond to a helicoidal rotation at rate f within the cell. The linear growth rate is σ and a_o is a constant. The rotation of the director components in the z-axis is motivated by the translationally invariant configuration (TIC) phase (see Fig. S1b). We incorporate the ansatz $n_1(z, t)$ and $n_2(z, t)$ in Eqs. (4) and (5), and set the marginal stability condition $\sigma = 0$ to obtain the critical rate $f_c = 2\pi/pK_{32}$ and the critical confinement $d_c/p = K_{32}/2$, where $K_{32} = K_3/K_2$. Indeed the helical structure of the chiral nematic liquid crystal will be recovered when a critical confinement ratio is surpassed (1, 6).

Close to the critical confinement ratio, winding/unwinding transition, we perform a weakly nonlinear analysis to find the slow spatiotemporal dynamics of the director $\vec{n}$ near this critical point and to saturate the instability revealed by the linear analysis. In the nonlinear regime, we need to take into account the spatial variations of n_1 and n_2 in the plane x-y. Only with this consideration, for example, we are able to observe CF1 (see Fig. S1c). A simple way to consider the spatial dependence near the winding/unwinding transition is by introducing the following director field (7, 8)

$$\begin{pmatrix} n_1 \\ n_2 \\ n_3 \end{pmatrix} \approx \begin{pmatrix} \cos(f_c z + \theta) \sin\left(\alpha \sin\left(\frac{\pi z}{d_c}\right)\right) \\ \sin(f_c z + \theta) \sin\left(\alpha \sin\left(\frac{\pi z}{d_c}\right)\right) \\ \cos\left(\alpha \sin\left(\frac{\pi z}{d_c}\right)\right) \end{pmatrix}, \qquad [6]$$

Sebastián Echeverría-Alar, Marcel G. Clerc and Ignacio Bordeu

where $\alpha = \alpha(x,y,t)$ and $\theta = \theta(x,y,t)$ correspond to the angle tilt of $\vec{n}$ from the z-axis, and the angle between the x-axis and the projection of $\vec{n}$ in the plane of the cell, respectively (Fig. S1). Both α and θ vary slowly in space and time. Note that Eq. (6) is the representation on the surface of the unit sphere S2 of the TIC texture plus a bidimensional modulation modeled by θ (1, 7, 9). In the limit $\alpha \ll 1$, we may introduce the complex small order parameter $A(x,y,t) \equiv \alpha e^{i\theta} \equiv Re(A) + iIm(A) \equiv u + iv$ to describe the behavior of CNLCs close to the winding/unwinding transition (7). Then, we write Eq. (6) in terms of u and v

$$\begin{pmatrix} n_1 \\ n_2 \\ n_3 \end{pmatrix} \approx \begin{pmatrix} u\cos\left(\dfrac{\pi z}{d_c}\right)\sin\left(\dfrac{\pi z}{d_c}\right) - v\sin^2\left(\dfrac{\pi z}{d_c}\right) + W_1^{[3]} + W_1^{[5]} + \cdots \\ v\cos\left(\dfrac{\pi z}{d_c}\right)\sin\left(\dfrac{\pi z}{d_c}\right) + u\sin^2\left(\dfrac{\pi z}{d_c}\right) + W_2^{[3]} + W_2^{[5]} + \cdots \\ 1 - \dfrac{n_1^2}{2} - \dfrac{n_2^2}{2} - \dfrac{n_1^4}{8} - \dfrac{n_2^4}{8} - \dfrac{n_1^2 n_2^2}{4} + \cdots \end{pmatrix}, \qquad [7]$$

where $W_1^{[3]}$, $W_1^{[5]}$, $W_2^{[3]}$, and $W_2^{[5]}$ are higher nonlinear corrections of order cubic and quintic in A, respectively. Now, we substitute the previous ansatz into Eq. (3) and at order $\vec{W}^{[3]} = (W_1^{[3]}, W_2^{[3]})$, we obtain

$$\gamma\partial_t ucs - \gamma\partial_t vs^2 = -2\frac{\pi^2}{d^2}K_3 us_2 - 2\frac{\pi^2}{d^2}K_3 vc_2 + K_3\partial_{zz}W_1^{[3]} + K_3\frac{\pi^2}{d^2}(usc - vs^2)(u^2+v^2) + K_3(\partial_{xx}+\partial_{yy})ucs - K_3(\partial_{xx}+\partial_{yy})vs^2 +$$
$$(K_3-K_1)\frac{\pi^2}{d^2}\left\{-(ucsc_2-vs^2c_2)(u^2+v^2) + \frac{d^2}{\pi^2}(-\partial_{xx}ucs+\partial_{xx}vs^2) + \frac{d}{\pi}[s_2u\partial_x u + s_2v\partial_x v + \frac{s_2^2}{2}u\partial_y u + \frac{c_2 s_2}{2}u\partial_y v - s^2 s_2 v\partial_y u - s^2 c_2 v\partial_y v + \right.$$
$$\frac{s_2 c_2}{2}u\partial_x u - \frac{s_2^2}{2}u\partial_x v - s^2 c_2 v\partial_x u + s^2 s_2 v\partial_x v]\bigg\} + (K_1-K_2)\bigg\{\partial_{xy}us^2 + \partial_{xy}vcs\bigg\} + (K_2-K_3)\bigg\{\partial_{yy}ucs - \partial_{yy}vs^2 - 2\frac{\pi^2}{d^2}\bigg[\frac{u^3}{2}s_2 s^2 c_2 -$$
$$\frac{u^2 v}{2}s_2^2 s^2 + \frac{u^2 v}{4}s_2^2 c_2 - \frac{uv^2}{4}s_2^3 - u^2 vs^4 c_2 + uv^2 s^4 s_2 - \frac{uv^2}{2}s^2 s_2 c_2 + \frac{v^3}{2}s^2 s_2^2 + u^3 s_2 s^4 + u^2 vs_2^2 s^2 + \frac{uv^2}{4}s_2^3 + u^2 vs^4 c_2 + uv^2 s^2 s_2 c_2 + \frac{v^3}{4}c_2 s_2^2 +$$
$$\frac{u^3}{2}s_2^3 + u^2 vs_2^2 c_2 + \frac{uv^2}{2}s_2 c_2^2 - u^2 vs^2 s_2^2 - 2uv^2 s^2 s_2 c_2 - v^3 s^2 c_2^2 - u^3 s^2 s_2 c_2 - u^2 vs^2 c_2^2 + u^2 vs^2 s_2^2 + uv^2 s^2 s_2 c_2 - \frac{u^2 v}{2}s_2^2 c_2 - \frac{uv^2}{2}s_2 c_2^2 +$$
$$\frac{uv^2}{2}s_2^3 + \frac{v^3}{2}s_2^2 c_2\bigg] - \frac{2\pi}{d}\bigg[-s_2 s^2 u\partial_x u - \frac{s_2^2}{2}u\partial_x v + \frac{s_2^2}{2}u\partial_y u - s_2 s^2 u\partial_y v - c_2 s^2 v\partial_x u - \frac{c_2 s_2}{2}v\partial_x v + \frac{c_2 s_2}{2}v\partial_y u - c_2 s^2 v\partial_y v\bigg] + \frac{\pi}{d}\bigg[\frac{s_2^2}{2}u\partial_y u$$
$$-s_2 s^2 u\partial_y v + \frac{c_2 s_2}{2}v\partial_y u - c_2 s^2 v\partial_y v + s^2 s_2 u\partial_x u + s^2 c_2 u\partial_x v + \frac{s_2^2}{2}v\partial_x u + \frac{s_2 c_2}{2}v\partial_x v - 2s^2 c_2 u\partial_y u + 2s^2 s_2 u\partial_y v - s_2 c_2 v\partial_y u + s_2^2 v\partial_y v$$
$$+ \frac{s_2^2}{2}u\partial_y u + \frac{c_2 s_2}{2}u\partial_y v - s^2 s_2 v\partial_y u - c_2 s^2 v\partial_y v - c_2 s^2 u\partial_y u - \frac{c_2 s_2}{2}u\partial_y v + s_2 s^2 v\partial_y u + \frac{s_2^2}{2}v\partial_y v\bigg]\bigg\}$$
$$+ \frac{4\pi^2 K_2}{dp}(us_2 + vc_2) + \frac{4\pi K_2}{p}\partial_z W_2^{[3]} + \frac{4\pi K_2}{p}\bigg\{[u\partial_x u - v\partial_x v + u\partial_y v + v\partial_y u]s^3 c + [v\partial_y v + u\partial_x v]c^2 s^2 + [u\partial_y u - v\partial_x u]s^4\bigg\}$$
$$+ \frac{4\pi^2 K_2}{dp}\bigg\{-\frac{s_2^3}{4}u^3 + \frac{s_2^2 s^2}{2}u^2 v + \frac{s_2 c_2 s^2}{2}uv^2 - c_2 s^4 v^3 + \frac{s_2 c_2 s^2}{2}u^3 - \frac{s_2^3}{4}uv^2 - c_2 s^4 u^2 v + \frac{s_2^2 s^2}{2}v^3\bigg\},$$

$$\gamma\partial_t us^2 + \gamma\partial_t vcs = 2\frac{\pi^2}{d^2}K_3 uc_2 - 2\frac{\pi^2}{d^2}K_3 vs_2 + K_3\partial_{zz}W_2^{[3]} + K_3\frac{\pi^2}{d^2}(us^2 + vcs)(u^2+v^2) + K_3(\partial_{xx}+\partial_{yy})us^2 + K_3(\partial_{xx}+\partial_{yy})vcs +$$
$$(K_3-K_1)\frac{\pi^2}{d^2}\bigg\{-(us^2 c_2 + vcsc_2)(u^2+v^2) - \frac{d^2}{\pi^2}(\partial_{yy}us^2 + \partial_{yy}vcs) + \frac{d}{\pi}[s_2 u\partial_y u + v\partial_y v + s^2 c_2 u\partial_x u - s^2 s_2 u\partial_x v + \frac{s_2 c_2}{2}v\partial_x u - \frac{s_2^2}{2}v\partial_x v +$$
$$s^2 s_2 u\partial_y u + s^2 c_2 u\partial_y v + \frac{s_2^2}{2}v\partial_y u + \frac{c_2 s_2}{2}v\partial_y v]\bigg\} + (K_1-K_2)\bigg\{\partial_{xy}ucs - \partial_{xy}vs^2\bigg\} + (K_2-K_3)\bigg\{\partial_{xx}us^2 + \partial_{xx}vcs + \frac{2\pi^2}{d^2}\bigg[\frac{u^3}{4}s_2^2 c_2 -$$
$$\frac{u^2 v}{4}s_2^3 - u^2 vs_2 c_2 s^2 + uv^2 s_2^2 s^2 + uv^2 c_2 s^4 - v^3 s^4 s_2 + \frac{u^3}{2}s_2^2 s^2 + \frac{u^2 v}{4}s_2^3 - u^2 vs_2 s^4 - \frac{uv^2}{2}s_2^2 s^2 + \frac{u^2 v}{2}s_2 c_2 s^2 + \frac{uv^2}{4}s_2^2 c_2 - uv^2 c_2 s^4 -$$
$$\frac{v^3}{2}c_2 s^2 s_2 - u^3 s^2 c_2^2 + 2u^2 vs^2 c_2 s_2 - uv^2 s^2 s_2^2 - \frac{u^2 v}{2}s_2 c_2^2 + uv^2 c_2 s_2^2 - \frac{v^3}{2}s_2^3 + \frac{u^3}{2}s_2^2 c_2 + \frac{u^2 v}{2}s_2 c_2^2 - \frac{u^2 v}{2}s_2^3 - \frac{uv^2}{2}s_2^2 c_2 - u^2 vs^2 s_2 c_2 -$$
$$uv^2 s^2 c_2^2 + uv^2 s^2 s_2^2 + v^3 s^2 s_2 c_2\bigg] - \frac{2\pi}{d}\bigg[c_2 s^2 u\partial_x u + \frac{c_2 s_2}{2}u\partial_x v - \frac{c_2 s_2}{2}u\partial_y u + c_2 s^2 u\partial_y v - s_2 s^2 v\partial_x u - \frac{s_2^2}{2}v\partial_x v + \frac{s_2^2}{2}v\partial_y u - s_2 s^2 v\partial_y v\bigg] +$$
$$\frac{\pi}{d}\bigg[-\frac{s_2^2}{2}u\partial_x u + s_2 s^2 u\partial_x v - \frac{c_2 s_2}{2}v\partial_x u + s^2 c_2 v\partial_x v - s_2^2 u\partial_x u - \frac{c_2 s_2}{2}u\partial_x v + 2s_2 s^2 v\partial_x u + 2c_2 s^2 v\partial_x v + \frac{s_2 c_2}{2}u\partial_y u - \frac{s_2^2}{2}u\partial_y v -$$
$$s^2 c_2 v\partial_y u + s^2 s_2 v\partial_y v + c_2 s^2 u\partial_x u + \frac{c_2 s_2}{2}u\partial_x v - s_2 s^2 v\partial_x u - \frac{s_2^2}{2}v\partial_x v + s^2 c_2 u\partial_x u - s^2 s_2 u\partial_x v + \frac{s_2 c_2}{2}v\partial_x u - \frac{s_2^2}{2}v\partial_x v\bigg]\bigg\}$$
$$+ \frac{4\pi^2 K_2}{dp}(-uc_2 + vs_2) - \frac{4\pi K_2}{p}\partial_z W_1^{[3]} - \frac{4\pi K_2}{p}\bigg\{[u\partial_y u - v\partial_y v - u\partial_x v - v\partial_x u]s^3 c + [v\partial_y u + u\partial_x u]c^2 s^2 + [v\partial_x v - u\partial_y v]s^4\bigg\}$$
$$+ \frac{4\pi^2 K_2}{dp}\bigg\{-\frac{s_2^2 s^2}{2}u^3 + c_2 s^4 uv^2 - \frac{s_2^2 s^2}{2}uv^2 + c_2 s^4 u^3 - \frac{s_2^3}{4}u^2 v + \frac{s_2 c_2 s^2}{2}v^3 + \frac{c_2 s_2 s^2}{2}u^2 v - \frac{s_2^3}{4}v^3\bigg\}.$$

We have used the simplified notation $d = d_c$, $c = \cos(\pi z/d)$, $s = \sin(\pi z/d)$, $c_2 = \cos(2\pi z/d)$, and $s_2 = \sin(2\pi z/d)$. The above equations are an inhomogeneous linear problem on $\vec{W}^{[3]}$ of the form $\mathcal{L}\vec{W}^{[3]} = \vec{b}$, where

$$
\mathcal{L} = \begin{pmatrix} K_3 \partial_{zz} & \dfrac{4\pi K_2}{p}\partial_z \\[2mm] -\dfrac{4\pi K_2}{p}\partial_z & K_3 \partial_{zz} \end{pmatrix},
$$

[8]

and $\vec{b} = (b_1, b_2)$ is the collection of all the other terms. To solve the inhomogeneous problem $\mathcal{L}\vec{W}^{[3]} = \vec{b}$, we must introduce an inner product to apply a solvability condition, i.e., the linear inhomogeneous equation will have a solution if and only if $\vec{b}$ is orthogonal to the $Ker\{\mathcal{L}^\dagger\}$. Let us consider the canonical inner product $\langle \vec{g}|\vec{h}\rangle = \int_0^d \vec{g} \cdot \vec{h}\, dz$, in order to be able to project the dynamics ($\vec{b}$) in the elements of $Ker\{\mathcal{L}^\dagger\}$. Note that $\mathcal{L} = \mathcal{L}^\dagger$ is self-adjoint. The elements of the kernel are $Ker\{\mathcal{L}^\dagger\} = \{\mathcal{H}_1, \mathcal{H}_2\} = \{(\cos(\pi z/d)\sin(\pi z/d), \sin^2(\pi z/d)), (\sin^2(\pi z/d), -\cos(\pi z/d)\sin(\pi z/d))\}$. The next step is to apply the solvability conditions, that is, $\langle \mathcal{H}_1|\vec{b}\rangle = 0$ and $\langle \mathcal{H}_2|\vec{b}\rangle = 0$. After straightforward calculations and combining the resulting two equations using $A = u + iv$, we get

$$
\frac{\gamma}{2K_2}\partial_t A = \frac{\pi^2}{d^2}(2\mathcal{C} - K_{32})A - \frac{\pi^2}{4d^2}(3 + K_{12} - 6K_{32} + 6\mathcal{C})|A|^2 A + \frac{K_{12}+1}{4}\nabla^2 A +
$$
$$
\frac{1-K_{12}}{8}\partial_\eta \partial_\eta \bar{A} + \frac{\pi}{8d}(3 - 4K_{32} + K_{12} + 3\mathcal{C})(A\partial_{\bar\eta} A - \bar{A}\partial_\eta A),
$$

(9)

where $\partial_\eta = \partial_x + i\partial_y$, $K_{12} = K_1/K_2$, and $\mathcal{C} = d/p$. The functional form of the solution of the inhomogeneous problem is $(W_1^{[3]}, W_2^{[3]}) = (\mathcal{G}_1(z)u|A|^2 + \mathcal{G}_2(z)v|A|^2, -\mathcal{G}_2(z)u|A|^2 + \mathcal{G}_1(z)v|A|^2)$. The functions $\mathcal{G}_1$ and $\mathcal{G}_2$ depend on the elastic constants and in the confinement ratio.

Near the recovery of the twisted structure, $\mathcal{C} \simeq K_{32}/2$, the type of the bifurcation is imposed by the sign of $b \simeq 3 + K_{12} - 3K_{32}$. This elastic dependence on the winding/unwinding transition in chiral nematic liquid crystals is well known (1, 6, 8). In particular, the system undergoes a supercritical bifurcation if $b > 0$; otherwise, the winding/unwinding bifurcation is subcritical. In our case of interest, the mixture of E7 and EOS12, we have measured a first-order transition (subcritical bifurcation) between the nematic phase and the TIC phase (10). Therefore, Eq. (9) is not enough to saturate the winding/unwinding instability in our experiment. We fix this problem by considering the next nonlinear correction $\vec{W}^{[5]}$ and $|b|\ll 1$. After applying the same solvability conditions as before, we obtain

$$
\frac{\gamma}{2K_2}\partial_t A = \frac{\pi^2}{d^2}(2\mathcal{C} - K_{32})A - \frac{\pi^2}{4d^2}(3 + K_{12} - 6K_{32} + 6\mathcal{C})|A|^2 A + \frac{K_{12}+1}{4}\nabla^2 A +
$$
$$
\frac{1-K_{12}}{8}\partial_\eta \partial_\eta \bar{A} + \frac{\pi}{8d}(3 - 4K_{32} + K_{12} + 3\mathcal{C})(A\partial_{\bar\eta} A - \bar{A}\partial_\eta A) - \frac{5\pi^2}{16d^2}(K_{32} - \frac{7K_{12}}{40} - 1 - \frac{16\mathcal{M}}{5})|A|^4 A,
$$

(10)

where $\mathcal{M}$ is the projection of the first nonlinear correction $\vec{W}^{[3]}$ into the dynamics at order $\vec{W}^{[5]}$ and is equal to

$$
\mathcal{M} = -K_{32}\int_0^1 [(-\mathcal{G}_1 s_2^2 + 2\mathcal{G}_1 s^2 c_2 - s_2 c_2 \partial_z \mathcal{G}_1 + s_2^2 \partial_z \mathcal{G}_2)cs + (s_2^2 \mathcal{G}_2 - 2c_2 s^2 \mathcal{G}_2 - 2c_2 s^2 \partial_z \mathcal{G}_1 + 2s_2 s^2 \partial_z \mathcal{G}_2)s^2]dz'
$$

$$
+ (K_{32} - K_{12})\int_0^1 [(-s_2 \partial_{zz}(cs\mathcal{G}_1) + s_2 \partial_{zz}(s^2 \mathcal{G}_2) - 2c_2 \mathcal{G}_1)\frac{cs}{2} + (-s^2 \partial_{zz}(cs\mathcal{G}_1) + s^2 \partial_{zz}(s^2 \mathcal{G}_2) + c_2 \mathcal{G}_2)s^2]dz'
$$

$$
+ 4\mathcal{C}\int_0^1 [(\frac{s_2^4}{4}\partial_z \mathcal{G}_2 - s_2^2 \mathcal{G}_1 + cs^3 \partial_z \mathcal{G}_1 - csc_2 \mathcal{G}_2 + c_2 s^2 \mathcal{G}_1)cs + (cs^3 \partial_z \mathcal{G}_2 - s^2 s_2 \mathcal{G}_1 + s^4 \partial_z \mathcal{G}_1 - 2c_2 s^2 \mathcal{G}_2 + 2cs \mathcal{G}_2)s^2]dz'
$$

$$
+ (1 - K_{32})\int_0^1 [(s^2 \partial_z(cs\partial_z \mathcal{G}_2) - s^2 \partial_z(s_2 \mathcal{G}_1) + s^2 \partial_z(s^2 \partial_z \mathcal{G}_1) - s^2 \partial_z(c_2 \mathcal{G}_2) + 2\mathcal{G}_2 s_2 c_2 - \mathcal{G}_2 \partial_z(s^2 c_2) + s_2^2 \partial_z \mathcal{G}_2]
$$

$$
- (1 - K_{32})\int_0^1 [2s_2^2 \mathcal{G}_1 + 2s^2 s_2 \mathcal{G}_1 - 2c_2 s_2 \mathcal{G}_2 + s_2^2 \partial_z \mathcal{G}_2 - 2c_2 s^2 \partial_z \mathcal{G}_2)cs + (-cs\partial_z(cs\partial_z \mathcal{G}_2) + cs\partial_z(s_2 \mathcal{G}_1) - cs\partial_z(s^2 \partial_z \mathcal{G}_1)]
$$

$$
+ (1 - K_{32})\int_0^1 cs\partial_z(c_2 \mathcal{G}_2) + 2s_2 c_2 \mathcal{G}_1 - \mathcal{G}_1 \partial_z(s^2 c_2) - s_2 c_2 \partial_z \mathcal{G}_2 + 2c_2 s_2 \mathcal{G}_1 - 2c_2 s^2 \partial_z \mathcal{G}_1 + 2c_2^2 \mathcal{G}_2)s^2]dz'.
$$

(11)

In the above equation, the change of variable $z' = z/d$ was employed. In the double limit $\mathcal{C} \simeq K_{32}/2$ and $b \simeq 3 + K_{12} - 3K_{32}$, the functions $\mathcal{G}_1$ and $\mathcal{G}_2$ are

$$
\mathcal{G}_1(z') = -\frac{dz'}{4} + \frac{\sin(2\pi z')}{8} + \frac{\sin(4\pi z')}{48} + \frac{1}{4K_{32}}(dz' - dz'\cos(2\pi z') - \sin(2\pi z')),
$$

(12)

Sebastián Echeverría-Alar, Marcel G. Clerc and Ignacio Bordeu

$$\mathcal{G}_2(z') = \frac{z'}{4K_{32}} \sin(2\pi z') + \frac{1}{96} \cos(4\pi z'). \tag{13}$$

Thus, we obtain $\mathcal{M} = 0.11K_{12} + 0.65/K_{32} - 0.07K_{12}/K_{32} - 0.68$. Then, the sign of the quintic term in Eq. (10) is governed by $Q = K_{32} - 0.53K_{12} - 2.1/K_{32} + 0.22K_{12}/K_{32} + 1.18$, which is always positive. Finally, after rescaling time, space, and the complex parameter A, we get the dimensionless equation

$$\partial_t A = \mu A + \beta|A|^2 A - |A|^4 A + \partial_\eta \partial_{\bar{\eta}} A - \delta \partial_\eta \partial_\eta \bar{A} + \chi \left(A \partial_{\bar{\eta}} A - \bar{A} \partial_\eta A \right), \tag{14}$$

where μ is the bifurcation parameter describing the winding/unwinding transition, $\beta = -\pi^2(3 + K_{12} - 6K_{32} + 6\mathcal{C})/d^2$ controls the type of the bifurcation, $\delta = (K_{12} - 1)/2(K_{12} + 1)$, and

$$\chi = \left(\frac{16}{5Q} \right)^{1/4} \frac{3 - 4K_{32} + K_{12} + 3\mathcal{C}}{2\sqrt{2}\sqrt{1 + K_{12}}}. \tag{15}$$

controls the two-dimensional chiral effects expressed by the term $\left(A\partial_{\bar{\eta}} A - \bar{A}\partial_\eta A \right)$. This chiral term has been predicted by symmetry arguments before (7, 10). Note that the rotational transformation $A \to Ae^{i\pi/2}$ in Eq. (14) gives

$$\partial_t A = \mu A + \beta|A|^2 A - |A|^4 A + \partial_\eta \partial_{\bar{\eta}} A + \delta \partial_\eta \partial_\eta \bar{A} + i\chi \left(A \partial_{\bar{\eta}} A + \bar{A} \partial_\eta A \right). \tag{16}$$

We have termed this model the chiral-anisotropic Ginzburg-Landau (CAGL) equation in the main text. Equation (16) is variational, i.e., $\partial_t A = -\delta \mathcal{F}[A, \bar{A}]/\delta \bar{A}$, where

$$\mathcal{F} = \int \int dx dy \left[-\mu |A|^2 - \beta \frac{|A|^4}{2} + \frac{|A|^6}{3} + |\nabla A|^2 + 2\delta Re \left\{ (\partial_\eta \bar{A})^2 \right\} - i\chi |A|^2 (\partial_{\bar{\eta}} A - \partial_\eta \bar{A}) \right]. \tag{17}$$

Free energy of a very long finger. To address the stabilization of a chiral finger as an energy minimization process, we consider a finger solution $A = Re^{i\phi}$ of model Eq. (16) with longitudinal length L. The transversal profiles of the finger solution, in amplitude and phase gradient, can be approximated by $R \approx \bar{R}sech(x/w)$ and $\partial_x \phi \approx -\bar{\Phi}sech(x/w_\phi)$, respectively. We study a very long finger on a square domain, i.e., $w/L \ll 1$ and $w_\phi/L \ll 1$. Replacing the ansatz for the finger into the free energy Eq. (17), we have $\mathcal{F}[R, \phi] = L\mathcal{F}_{finger}[R, \phi]$, where

$$\mathcal{F}_{finger}[R, \phi] = -\mu \bar{R}^2 \int_{-L}^{L} sech^2(x/w)dx - \frac{\beta \bar{R}^4}{2} \int_{-L}^{L} sech^4(x/w)dx$$

$$+ \frac{\bar{R}^6}{3} \int_{-L}^{L} sech^6(x/w)dx + \frac{(1+\delta)\bar{R}^2}{w^2} \int_{-L}^{L} sech^2(x/w) \tanh^2(x/w)dx + (1+\delta)\bar{\phi}^2 \bar{R}^2 \int_{-L}^{L} sech^2(x/w)sech^2(x/w_\phi)dx$$

$$+ \frac{2\chi \bar{R}^3}{w} \int_{-L}^{L} sech^3(x/w) \tanh(x/w) \sin(2w_\phi \bar{\phi} \tan^{-1}[\tanh(x/2w_\phi)])dx$$

$$- 2\chi \bar{R}^3 \bar{\phi} \int_{-L}^{L} sech^3(x/w)sech(x/w_\phi) \cos(2w_\phi \bar{\phi} \tan^{-1}[\tanh(x/2w_\phi)])dx$$

$$\equiv F_o w + \frac{2(1+\delta)}{3w} \bar{R}^2 + (1+\delta)\bar{R}^2 \bar{\Phi}^2 I_5(w, w_\phi) + 2\chi \bar{R}^3 I_6(w, w_\phi, \bar{\Phi}) - 2\chi \bar{R}^3 \bar{\Phi} I_7(w, w_\phi, \bar{\Phi}). \tag{18}$$

In the above equation, we have used the limit $L/w \gg 1$ to calculate the first four integrals, and we defined $F_o = -2\mu \bar{R}^2 - 2\beta \bar{R}^4/3 + 16\bar{R}^6/45$. A numerical exploration of the five energy terms in Eq. (18) show that $F_o w \approx (1+\delta)\bar{R}^2 \bar{\Phi}^2 I_5(w, w_\phi)$ when $\delta \to 0$, and that $2(1+\delta)\bar{R}^2/w$ is negligible. Therefore, the transversal energy of the finger can be simplified to $\mathcal{F}_{finger}[R, \phi] \approx 2F_o w + 2\chi \bar{R}^3 I_6(w, w_\phi, \bar{\Phi})/w - 2\chi \bar{R}^3 \bar{\Phi} I_7(w, w_\phi, \bar{\Phi})$. We minimize $\mathcal{F}_{finger}[R, \phi]$ with respect to w, considering the limit $w_\phi/w \ll 1$, and obtain at leading order $w^3 \approx 3\pi^3 \chi w_\phi^3 \bar{R}^3 \bar{\Phi}/4F_o$. Note that $\partial I_6/\partial w = 0$ due to the odd symmetry of the integrand.

Local speed-curvature equation. To shed light on the interface dynamics of the cholesteric phase, at the rounded tips of CF1 or at the interface of chiral bubbles, we perform a nonlinear analysis around the interface of the chiral bubble solution, that is $A_{cb} = R_o e^{i\phi}$ in Eq. (16). Note that here we do not take into account the phase jump in ϕ (10), as we are interested in the branching dynamics away from the center of the chiral bubble. Changing variables in Eq. (16), $A = Re^{i\phi}$, and supposing that the temporal evolution of the phase is negligible compared to the dynamics of the modulus, which is reasonable at the interface, and that the phase only has a local linear dependence at the interface, the dynamics of the modulus R may be written in curvilinear coordinates $\{n, s\}$ and in the limit $\delta \to 0$ as

$$-v_n \partial_n R = \mu R + \beta R^3 - R^5 + \partial_{nn} R + \kappa \partial n R - \kappa^2 R + \chi \kappa R^2 + \partial_{ss} R, \qquad [19]$$

where κ is the curvature, s is the arclength, and $v_n = \partial_t \mathbf{r} \cdot \hat{\mathbf{n}}$ is the speed normal to the interface (described by a position vector $\mathbf{r}$). Equation (19) is the evolution of the modulus $R = |A|$ in the sharp-interface limit $\kappa \ll \sqrt{3/4}$ (11). We have used the local approximation $\partial_s \phi \approx \kappa$ for the phase.

Near the Maxwell point μ_{MP}, the modulus of the interface of the chiral bubble can be approximated by the flat front solution $R_o = [3/4(1 + e^{\sqrt{3/4n}})]^{1/2}$ (10, 12). Now, we introduce curvature and chirality to the flat front by performing a weakly nonlinear analysis near the critical point $\{\mu_{MP}, \chi_o\}$. We introduce the ansatz $R(n, s, t) = R_o(n) + \epsilon^{1/2} R_1 + \epsilon R_2 + \epsilon^{3/2} R_3$, $\mu = \mu_{MP} + \epsilon^{3/2}\mu_1$, $\chi = \chi_o + \epsilon^{1/2}\chi_1$, $v_n = \epsilon^{3/2}v_N$, $\partial_s = \epsilon^{1/2}\partial_S$ and $\kappa = \epsilon^{1/2}\tilde{\kappa}$ with $\epsilon \ll 1$ into Eq. (19), and solve at every order in ϵ by applying solvability conditions (as we have elaborated already in this Supporting Information text). At order $\epsilon^{3/2}$, we obtain the speed-curvature (or Gibbs-Thomson (13)) relation

$$v_N = -|\mu_1|A + B\chi_1\tilde{\kappa} + C\tilde{\kappa}^3 + D\partial_{SS}\tilde{\kappa}, \qquad [20]$$

where

$$A = \frac{\langle|\partial_n R_o||R_o\rangle}{\langle\partial_n R_o|\partial_n R_o\rangle} > 0, \qquad [21]$$

$$B = \frac{\langle|\partial_n R_o||R_o^2\rangle}{\langle\partial_n R_o|\partial_n R_o\rangle} > 0, \qquad [22]$$

$$D = \frac{\langle|\partial_n R_o||f(n)\rangle}{\langle\partial_n R_o|\partial_n R_o\rangle} > 0, \qquad [23]$$

and

$$C = \frac{\langle\partial_n R_o|\{-6R_o f(n)g(n) - f(n)^3 + 20R_o^3 f(n)g(n) + 10R_o^2 f(n)^3 - \partial_n g(n) + f(n) - \chi_o(f(n)^2 + R_o g(n))\}\rangle}{\langle\partial_n R_o|\partial_n R_o\rangle} > 0. \qquad [24]$$

In the above equations, we have used the inner product $\langle q_1|q_2\rangle = \int_{-\infty}^{\infty} q_1 q_2 dn$. $f(n)$ and $g(n)$ are functions associated to the corrections of the modulus R. The functional form of $f(n)$ and $g(n)$ can be obtained numerically and with it approximate the coefficients C and D.

The interfacial equation (20) can be transformed into the reference-frame independent equations of motion (14)

$$\dot{\tilde{\kappa}} = -(\partial_{SS} + \tilde{\kappa}^2)U, \qquad [25]$$

$$\dot{g} = 2g\tilde{\kappa}U, \qquad [26]$$

where g is the curve metric, and $U = -|\mu_1|A + B\chi_1\tilde{\kappa} + C\tilde{\kappa}^3 + D\partial_{SS}\tilde{\kappa}$. Considering the arclength $S = \int_0^\sigma \sqrt{g(\sigma')}d\sigma'$, where σ is the variable parameterizing the interface, and introducing the full form of U in Eqs. (25) and (26), we get

$$\dot{\tilde{\kappa}} = |\mu_1|A\tilde{\kappa}^2 - B\chi_1\tilde{\kappa}^3 - C\tilde{\kappa}^5 - B\chi_1\partial_{SS}\tilde{\kappa} - D\partial_{SSSS}\tilde{\kappa} - C\tilde{\kappa}(\partial_S\tilde{\kappa})^2 - (3C + D)\tilde{\kappa}^2\partial_{SS}\tilde{\kappa}, \qquad [27]$$

$$\dot{S} = \int_0^{S'} (-|\mu_1|A\tilde{\kappa} + B\chi_1\tilde{\kappa}^2 + C\tilde{\kappa}^4 + D\tilde{\kappa}\partial_{SS}\tilde{\kappa})dS'. \qquad [28]$$

As the growth of the cholesteric interface must be variational, that is, introducing the good twist in the frustrated sample to minimize the energy in the system, the restriction D=3C is needed. Indeed, both constants have the same sign. From Eqs. (27) and (28), one can see that at a linear stage, a modulational instability with wavelength $2\pi\sqrt{D}/\sqrt{B\chi_1}$ can destabilize a flat front ($\tilde{\kappa} = 0$). The subsequent nonlinear dynamics at the cholesteric interface shape the morphologies of the rounded tips.

Sebastián Echeverría-Alar, Marcel G. Clerc and Ignacio Bordeu

Repulsion between two very long fingers. In numerical integrations of Eq. (16), we have seen that repulsion between two infinite fingers (at $x = \pm x_o(t)$) is mediated by a non-trivial phase structure between them. Then, we decided to approximate this interaction by taking into account only the effect at zeroth order of the phase structure near $x = 0$ in one finger (at $x = x_o(t)$). In terms of the complex field we have $A = R(t)e^{i\phi(t)}$, where $R(t) = R(x - x_o(t))$ and $\partial_x\phi(t) = \partial_x\phi(x - x_o(t)) + \theta_b(x)$. The variable $\theta_b(x)$ represents the phase gradient shape near $x = 0$. Numerical observations show that the tail of θ_b behaves as $C_o e^{-bx}/x$, where C_o and b are positive constants. We approximate the transversal profiles of the finger by bell-shaped soliton functions, $R \approx \bar{R}sech(x/w)$ and $\partial_x\phi \approx -\bar{\Phi}sech(x/w_\phi)$. We rely on the variational form of our model to extract the key features of the interaction (15). The chiral-anisotropic Ginzburg-Landau Equation is variational, $\partial_t A = -\delta\mathcal{F}/\delta A^*$, that is

$$\partial_t\mathcal{F} = -\int|\partial_t A|^2 dxdy. \tag{29}$$

Introducing the moving frame of reference $A(x - x_o)$, and considering the limit $x_o >> \{w, w_\phi\}$, into Eq. (17) we obtain the temporal variation of the energy

$$\partial_t\mathcal{F} = -L\dot{x}_o\int_0^\infty dx\left\{-2\mu R(\partial_z R) - 2R^3(\partial_z R) + 2R^5(\partial_z R) + 2(\partial_x R)(\partial_{zx}R) + 2R(\partial_z R)(\partial_x\phi)^2 + 2R^2(\partial_x\phi)(\partial_{xz}\phi)\right.$$
$$\left. + 2R(\partial_z R)\theta_b^2 + 4R(\partial_z R)(\partial_x\phi)\theta_b + 2R^2(\partial_{zx}\phi)\theta_b + 6\chi R^2(\partial_z R)(\partial_x\phi) + 2\chi R^3(\partial_{xz}\phi) + 6\chi R^2(\partial_z R)\theta_b\right\}, \tag{30}$$

where $z = x - x_o$ and L is the longitudinal length of the finger. Changing the integration variable from x to z, Eq. (30) reduces to

$$\partial_t\mathcal{F} = -L\dot{x}_o\int_{-x_o}^\infty dz\left\{2R(\partial_z R)\theta_b(z + x_o)^2 + 4R(\partial_z R)(\partial_z\phi)\theta_b(z + x_o) + 2R^2(\partial_{zz}\phi)\theta_b(z + x_o) + 6\chi R^2(\partial_z R)\theta_b(z + x_o)\right\}. \tag{31}$$

Now, we take the limit $x_o \to \infty$ and introduce the tail behavior of θ_b, that is $C_o\exp(-bx)/x$. The first term in the integral of Eq. (31) can be neglected, as we retain only to first order in $\exp(-bx_o)/x_o$. Then, we have to analyze three terms

$$T_1 = 4C_o\frac{\bar{R}^2\bar{\Phi}}{w}\frac{e^{-bx_o}}{x_o}\int_{-\infty}^\infty sech^2\left(\frac{z}{w}\right)tanh\left(\frac{z}{w}\right)sech\left(\frac{z}{w_\phi}\right)e^{-bz}dz, \tag{32}$$

$$T_2 = 2C_o\frac{\bar{R}^2\bar{\Phi}}{w_\phi}\frac{e^{-bx_o}}{x_o}\int_{-\infty}^\infty sech^2\left(\frac{z}{w}\right)tanh\left(\frac{z}{w_\phi}\right)sech\left(\frac{z}{w_\phi}\right)e^{-bz}dz, \tag{33}$$

$$T_3 = -6\chi C_o\frac{\bar{R}^3}{w}\frac{e^{-ax_o}}{x_o}\int_{-\infty}^\infty sech^3\left(\frac{z}{w}\right)tanh\left(\frac{z}{w}\right)e^{-bz}dz, \tag{34}$$

where we have introduced the functional form proposed for the transversal profiles of the cholesteric finger. All the integrals listed above are negative. This is because the exponential term makes smaller the positive side of the hyperbolic tangent function. Hereafter, we name the absolute value of the integrals I_1, I_2, and I_3. Replacing all into Equation (29) we obtain at dominant order

$$\dot{x}_o = \frac{\left(-4\frac{\bar{\Phi}}{w}I_1 - 2\frac{\bar{\Phi}}{w_\phi}I_2 + 6\chi\bar{R}\frac{I_3}{w}\right)}{\left(\frac{2}{3w} + 2\bar{\Phi}^2\int_{-\infty}^\infty sech^2\left(\frac{z}{w}\right)sech^2\left(\frac{z}{w_\phi}\right)dz\right)}C_o\frac{e^{-bx_o}}{x_o} = \mathcal{N}(\chi,\mu)\frac{e^{-bx_o}}{x_o}. \tag{35}$$

We find numerically that the constant $\mathcal{N}(\chi,\mu)$ is positive in a range of χ values at fixed $\mu = -0.4$ (Fig. S3). Therefore, the interaction between cholesteric fingers is repulsive at zeroth order. We can integrate Eq. (35) to obtain the temporal dependence of x_o

$$x_o = \frac{W((C_1 + \mathcal{N}(\chi,\mu)t)/e) + 1}{a}, \tag{36}$$

where C_1 is a constant, which depends on the initial conditions, e is the Euler number and W is the Lambert function.
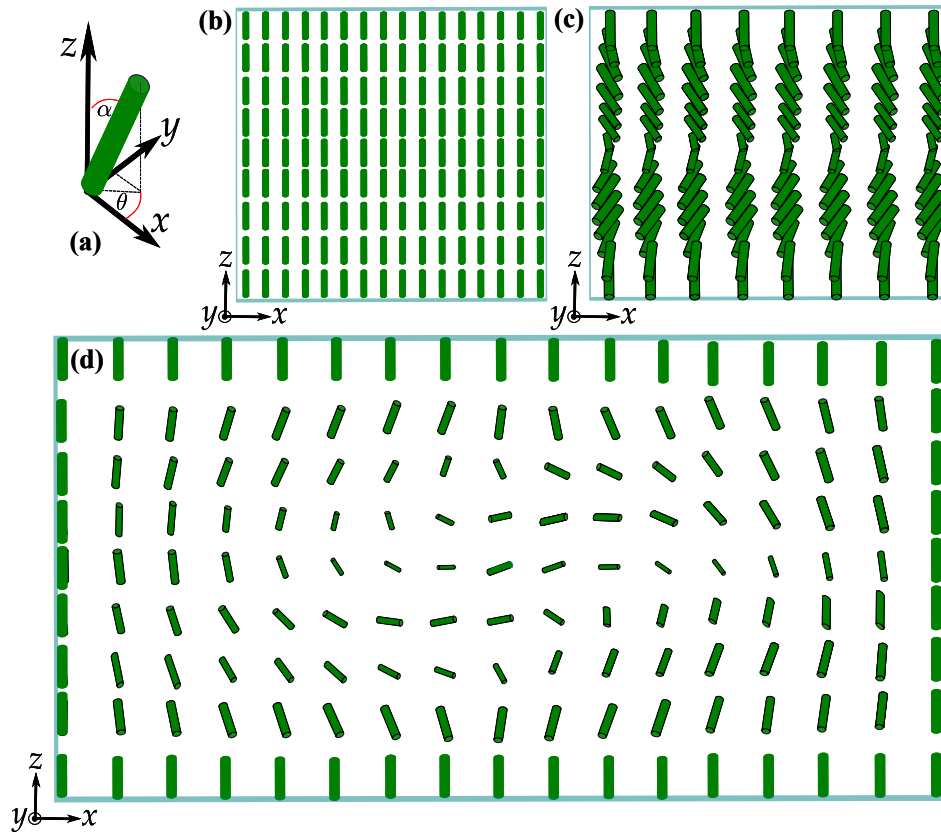
Fig. S1. Schematic representation of nematic director within a cell of thickness d with homeotropic boundary conditions. **a** Representation of the nematic director $\vec{n}$ as tubes in a spherical coordinate system. The angle α represents the tilt of $\vec{n}$ from the z-axis and θ corresponds to the angle between the x-axis and the projection of $\vec{n}$ in the plane $x - y$. **b** Nematic phase induced by homeotropic anchoring. **c** Translationally invariant configuration (TIC) is characterized by a uniform twist parallel to the cell thickness. **d** Director distribution of the cross-section of a cholesteric finger of type I far from its tips. In this case, spatial modulations of $\vec{n}$ are in z and in the plane $x - y$. This director representation is adapted from (16).

Sebastián Echeverría-Alar, Marcel G. Clerc and Ignacio Bordeu
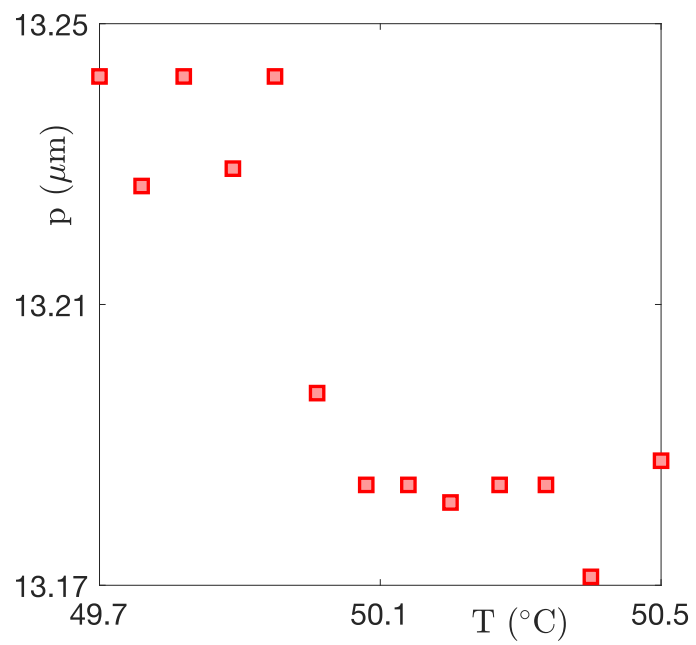
Fig. S2. Temperature dependence of the cholesteric pitch p of the mixture between E7 and EOS-12 at 7 wt% within the range 49.7°C-50.5°C.
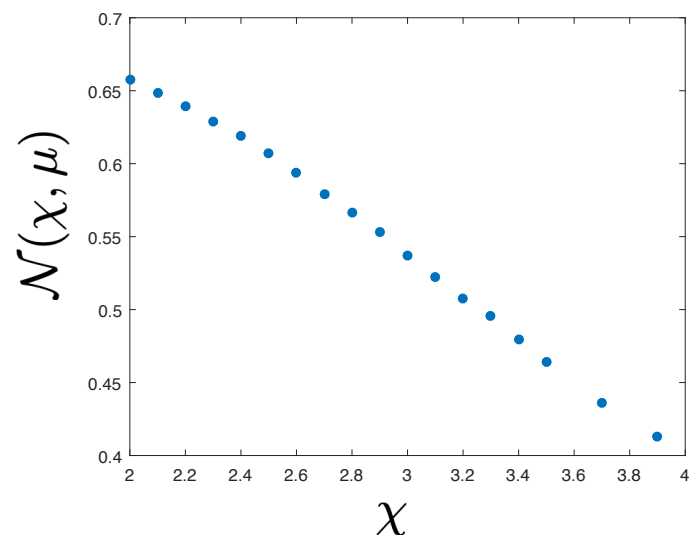
Fig. S3. Numerical values of the constant $\mathcal{N}(\chi, \mu)$ with μ=-0.4, b =0.31.

Movie S1. This movie shows an example of branching dynamics in chiral nematic liquid crystals under crossed polarizers. It corresponds to cell #1 (T =51.3°C, p=3.4 μm, d/p <58.8). The nucleation sites are chiral bubbles created by cooling closed loops of CF1.

References

1. P Oswald, P Pieranski, *Nematic and Cholesteric Liquid Crystals.* (CRC Press, London), (2005).
2. PG de Gennes, J Prost, *The Physics of Liquid Crystals.* (Clarendon Press, Oxford, UK), 2 edition, (1993).
3. AB Harris, RD Kamien, TC Lubensky, Molecular chirality and chiral parameters. *Rev. Mod. Phys.* **71**, 1745 (1999).
4. S Chandrasekhar, *Liquid Crystals.* (Cambridge University Press, Cambridge, UK), (1992).
5. T Frisch, S Rica, P Coullet, JM Gilli, Spiral waves in liquid crystal. *Phys. Rev. Lett.* **72**, 1471 (1994).
6. P Ribiere, S Pirkl, P Oswald, Electric-field-induced phase transitions in frustrated cholesteric liquid crystals of negative dielectric anisotropy. *Phys. Rev. A* **44**, 8198 (1991).
7. T Frisch, L Gil, JM Gilli, Two-dimensional landau-de gennes dynamical model for the unwinding transition of a cholesteric liquid crystal. *Phys. Rev. E* **48**, R4199 (1993).
8. P Oswald, J Baudry, S Pirkl, Static and dynamic properties of cholesteric fingers in electric field. *Phys. Reports* **337**, 67 (2000).
9. F Lequeux, P Oswald, J Bechhoefer, Influence of anisotropic elasticity on pattern formation in a cholesteric liquid crystal contained between two plates. *Phys. Rev. A* **40**, 3974 (1989).
10. MG Clerc, G González-Cortés, S Echeverría-Alar, Localized dissipative vortices in chiral nematic liquid crystal cells. *Phys. Rev. Res.* **4**, L022021 (2022).
11. A Karma, WJ Rappel, Phase-field method for computationally efficient modeling of solidification with arbitrary interface kinetics. *Phys. Rev. E* **53**, R3017 (1996).
12. MG Clerc, C Falcón, Localized patterns and holesolutions one-dimensional extended systems. *Phys. A* **356**, 48 (2005).
13. LM Pismen, *Patterns and interfaces in dissipative dynamics.* (Springer Science & Business Media), (2006).
14. RC Brower, DA Kessler, J Koplik, H Levine, Geometrical models of interface evolution. *Phys. Rev. A* **29**, 1335 (1984).
15. MC Cross, PC Hohenberg, Pattern formation outside of equilibrium. *Rev. Mod. Phys.* **65**, 851 (1993).
16. M Press, A Arrott, Static strain waves in cholesteric liquid crystals.-i. homeotropic boundary conditions. *J. de Physique* **37**, 387–395 (1976).

9.1. Perspectives

In this chapter, we have investigated experimentally and theoretically the spatial and temporal organization of branching patterns in frustrated chiral nematic liquid crystals. Our analyzes show that even though the liquid crystal structure is inherently 3D, the growth dynamic of the branching phase follows simple local rules that take place on the 2D transversal plane, resulting in branching and inhibition of tips. Therefore, neglecting the three-dimensional liquid crystal structure is a good approximation to studying the formation of disordered branching patterns resulting from CF1 destabilization. An interesting future direction of research is to explore other finger structures, such as CF2, CF3, and CF4 [138], and investigate their space-filling dynamics. Additionally, in the broader context, it will be interesting to investigate possible branching processes of stripe phases in chiral magnets [166], where Eq. (8.1) should be valid in some limit.

Chapter 10

Morphological transition of labyrinthine patterns in frustrated chiral nematic liquid crystals (Liquid Crystals XXVI 12207, 75-81)

In the context of chiral nematic liquid crystals, we have discussed the emergence of labyrinthine patterns only by a tip-splitting mechanism suffered by the rounded tips of CF1. Nevertheless, chiral fingers can exhibit another type of instability, giving rise to labyrinthine patterns. Figure 10.1 illustrates an invaginated dynamics of cholesteric fingers of type I, in which the finger elongates and modulates itself through a transversal instability with a well-defined wavelength [37, 143]. The interaction between different fingers undergoing this instability creates invaginated labyrinthine patterns. In this chapter, we characterize these patterns and reveal some differences between them and the branching labyrinths. Additionally, with the help of model (8.1), we show that a cholesteric finger invaginates to minimize energy.
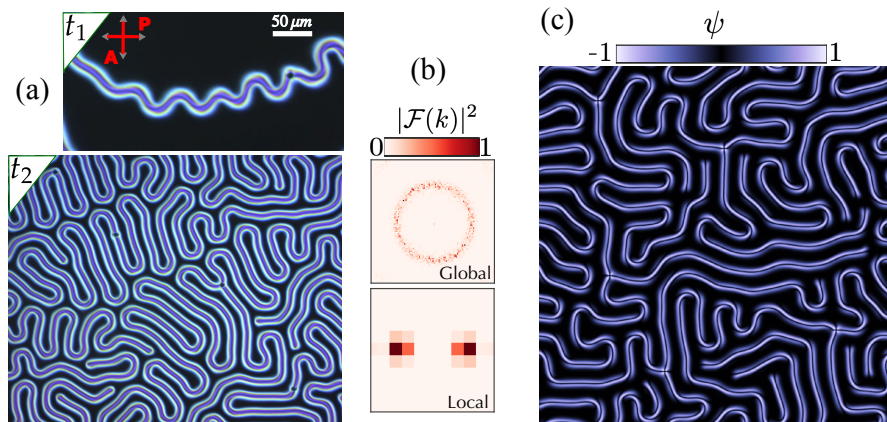
Figure 10.1: Invaginated labyrinthine pattern (a) temporal snapshots ($t_2 > t_1$) of the invagination dynamics in a chiral nematic liquid crystal sample at $T = 49.8°C$ and $d/p = 0.7$. (b) Global and local Fourier transforms of the invaginated texture (t_2 in (a)) display the spatial structure of a labyrinthine pattern (see Chapter 3). (c) Numerical invaginated pattern obtained from Eq. (8.1) with $\mu = -0.4$, $\chi = 2.22$, $\delta = 0.1$, and $\beta = 1$ in a squared box of size 600×600.

Morphological transition of labyrinthine patterns in frustrated chiral nematic liquid crystals

Sebastián Echeverría-Alar

Departamento de Física and Millennium Institute for Research in Optics, FCFM, Universidad de Chile, Casilla 487-3, Santiago, Chile

ABSTRACT

Several morphologies are observed in out-of-equilibrium systems. They can be highly symmetric as stripes, hexagons, or squares, and more complicated such as labyrinthine patterns. These shapes arise in different contexts, ranging from chemistry, biology, and physics. Here we study the emergence of chiral labyrinthine patterns near the winding/unwinding transition of a chiral liquid crystal under geometrical frustration. The patterns emerge due to morphological instabilities of cholesteric fingers of type 1. Experimentally, we show that when heating the cholesteric liquid crystal cell at different rates, the winding/unwinding transition is remarkably different. At low rates, chiral fingers appear and exhibit a serpentine instability along their longitudinal direction. At higher rates, after the chiral fingers nucleate, the splitting of their rounded tips and side-branching along their body is observed. Both mechanisms create labyrinthine patterns. Theoretically, based on an amplitude equation inferred by symmetry arguments, we study the morphological instabilities and characterize them by their interface curvature distribution. We discuss the possible velocity-curvature relationship of the finger rounded tips.

Keywords: chiral fingers, curvature, morphological instabilities, cholesteric liquid crystals, amplitude equation.

1. INTRODUCTION

Dissipative structures have been studied in many fields of nonlinear science, ranging from biology and chemistry to physics (see[1–4] and references therein). Patterns emerge in out-of-equilibrium systems, which are subjected to injection and dissipation of energy. These patterns can be extended or localized in space.[5,6] The main ingredient of pattern-forming systems is the stabilization of a characteristic length. This spatial scale can be related to intrinsic factors (diffusion of reactants in chemical reactions, facilitative and competitive processes in ecosystems, helical pitch, and so on) or extrinsic factors such as the spatial geometry (for example, convection of rolls in the Rayleigh-Bernard experiment).[7–10] In general, patterns are observed in macroscopic systems that exhibit a spontaneous spatial symmetry breaking instability of a homogeneous state.[2,3] Near this bifurcation, the equilibria displayed by the system are stripes, hexagons, squares, and superlattices. Nevertheless, the creation of patterns is also possible far from this spatial instability. For example, in bistable chemical reactions and ferrofluids, the interaction of fronts and the modulational instability of their interfaces produce complicated shapes with a characteristic wavelength.[11,12] Furthermore, far from a symmetry-breaking instability, localized dissipative structures may undergo an interfacial instability.[13–15] This instability creates fingers, which elongate and eventually develop an oscillatory instability or a splitting of their tips.[15,16] Both mechanisms can create labyrinthine patterns in a two-dimensional isotropic system by filling all the space with the finger phase. The labyrinths are characterized by a powdered-ring Fourier spectrum and a short-range order described by a local single wavenumber.[17,18]

Frustrated chiral liquid crystals (CLC) are a natural physical context where dissipative labyrinthine patterns can be observed.[19] The cholesteric phase is characterized by the inherent twist of the liquid crystal molecules, the so-called cholesteric pitch p.[20] This pitch length depends on the temperature and the concentration of chiral molecules in the CLC mixture.[19,21] When a CLC is confined into a cell with homeotropic boundary conditions

---

and thickness $d < p$, the helical structure is frustrated and unwinded into a nematic phase. The chirality of the CLC can be recovered by applying a voltage, a thermal gradient, or by increasing the cell thickness.[9,19,22] This transition is termed winding/unwinding. The recuperation of the chiral structure is often mediated by the nucleation of cholesteric fingers of type 1 (CF1).[9,23–25] These chiral fingers possess structurally different tips. One is rounded and associated with the good twist rotation of the liquid crystals, which is imposed by the chiral dopant. The other is pointed and related to the opposite twist of the molecules (see[19] and references therein). After the emergence of the chiral fingers, they elongate from both ends and start to suffer an oscillatory instability or a tip-splitting of their rounded tips.[19,24] Although these mechanisms have been observed experimentally in the last decades, the theoretical description of these morphological instabilities and their transition has not been completely elucidated.

This work investigates the appearance of cholesteric fingers of type 1 and their instabilities close to a winding/unwinding transition in a CLC cell under homeotropic anchoring. Experimentally, we show that by heating the cell at different rates, the CF1 experience two different morphological instabilities: serpentine and tip-splitting. Theoretically, based on an amplitude equation inferred by symmetry arguments and the first-order type of transition between the nematic and chiral phase, we reveal the transformations suffered by the chiral fingers. We characterize the morphological instabilities in terms of the curvature distribution along the interface of the CF1. Finally, we comment on the relation between the velocity of the propagation of the fingers and their tip curvature.

2. EXPERIMENTAL OBSERVATION OF MORPHOLOGICAL INSTABILITIES

Cholesteric fingers of type 1 and their instabilities have been observed in various experiments in the last decades (see textbook[19] and references therein). They appear when a CLC sample is geometrically frustrated due to homeotropic boundary conditions. Commonly, an electric field parallel to the thickness of the cell is applied to a CLC with negative dielectric anisotropy to recover the winding phase (in the form of CF1). The chiral fingers also emerge when a CLC cell is subjected to a thermal gradient parallel to the cell thickness.[26]

We consider a chiral liquid crystal composed of a mixture of a commercial nematic liquid crystal E7 (Merck) with a chiral molecule EOS-12[27] at 16 wt% (this is a new molecule, and its properties are soon to be published). The cholesteric pitch associated with the chiral-nematic mixture is $p = 3.1$ μm at 57°C. The pitch length is
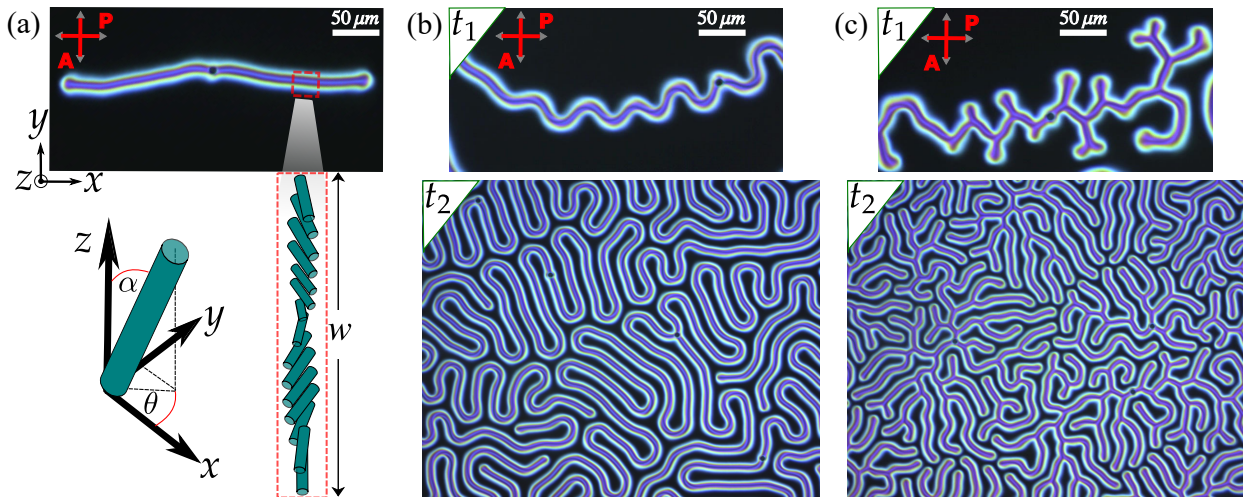
Figure 1. The emergence of labyrinthine patterns in frustrated cholesteric liquid crystal sample. (a) Two cholesteric fingers of type 1 nucleating from a glass bead at a heating rate of 0.5°C/min. The inset shows a schematic draw of the nematic director (green tubes) across the width w of the CF1 in the midplane of the cell. The α and θ angles are introduced in the main text. (b) Serpentine instability of a chiral finger at a time t_1, and the asymptotic labyrinth observed at $t_2 \gg t_1$. The heating rate is 1.2°C/min. (c) Tip-splitting and side-branching instability of a chiral finger at a time t_1, and the asymptotic labyrinth observed at $t_2 \gg t_1$. The heating rate, in this case, is 2.0°C/min.

determined with Grandjean-Cano technique.[19] A droplet of the mixture is deposited inside a cell (Instec) using a microcapillary tube. The cell is chemically treated to induce homeotropic anchoring on the cholesteric liquid crystal sample. The cell thickness is $d = 9$ μm, maintained by glass beads uniformly distributed in the sample. The prepared cell is introduced into a LinkamT95-PE hot stage and placed between crossed polarizers in an Olympus BX51 microscope. A white light illuminates the sample. Starting from room temperature (20°C), the frustrated cholesteric liquid crystal, which is in a homeotropic phase (unwinding state), is heated from below at different rates to induce the winding/unwinding transition. The cholesteric phase accounts for the winding state. For the mixture used in this study, the winding/unwinding transition is always first-order.[26] A CMOS camera monitors the emergence of the cholesteric phase. The winding/unwinding transition is characterized by the sudden nucleation of cholesteric fingers of type 1 in the homeotropic background state.[9] The nucleation is heterogeneous due to the presence of glass beads. Indeed, the chiral fingers nucleate from the interface of these imperfections. Note that for this reason, we do not observe pointed tips in our experiment. Figure 1a shows a snapshot of two CF1, which undergo elongation when the sample is being heated at 0.5°C/min. Besides, Fig. 1a depicts the organization of the nematic director (green tubes), which is the average orientation of the liquid crystal molecules in the CF1. Note that the width w of the finger is intimately related to the rotation of the molecules in the $x - y$ plane. When the sample is heated at 1.2°C/min, while the chiral fingers elongate, they also exhibit a serpentine instability with a finite wavelength (see the top panel in Fig. 1b). After the interaction with several fingers, the asymptotic labyrinthine pattern observed is shown in the bottom panel of Fig. 1b. The convoluted shape of this labyrinth is associated with the serpentine instability of the individual fingers. Increasing further the heating rate (2°C/min), the CF1 quickly grow and manifest a side-branching instability and a tip-splitting of their tips, as shown in the top panel of Fig. 1c. The asymptotic branching labyrinthine pattern is shown in the bottom panel of Fig. 1c. This labyrinth displays a weaker spatial coherence compared to the previous one.

3. AMPLITUDE EQUATION FOR THE UNWINDING/WINDING TRANSITION

Near the unwinding/winding transition and in the long-pitch limit ($p \gg l$), where l is a typical molecular length, the chiral-nematic liquid crystal, inside a homeotropic cell of thickness d, can be modelled locally as an uniaxial nematic, described by the director vector[28, 29]

$$
\vec{n}(x,y,z,t) = \begin{pmatrix} \cos\left(\dfrac{z}{p} + \theta(x,y,t)\right) \sin\left(\alpha(x,y,t)\sin\left(\dfrac{\pi z}{d}\right)\right) \\[12pt] \sin\left(\dfrac{z}{p} + \theta(x,y,t)\right) \sin\left(\alpha(x,y,t)\sin\left(\dfrac{\pi z}{d}\right)\right) \\[12pt] \cos\left(\alpha(x,y,t)\sin\left(\dfrac{\pi z}{d}\right)\right) \end{pmatrix},
\tag{1}
$$

where the director $\vec{n}(x,y,z,t)$ accounts for the average molecular orientation, $\alpha(x,y,t)$ is the amplitude of angle tilt of $\vec{n}$ from the z–axis, and $\theta(x,y,t)$ is the angle between the projection of $\vec{n}$ into the x–y plane and the x–axis (cf. Fig. 1a). The $\sin(\pi z/d)$ accounts for the vertical rotation of the molecular orientation and ensures homeotropic boundary conditions at $z = 0$ and $z = d$, being $\vec{n} = (0,0,1)$, that is $\alpha = 0$, the corresponding homeotropic nematic state.

The solutions $\theta = \theta_0$ and $\alpha = \alpha_o$, with θ_0 and α_0 are constants, correspond to the translational invariant cholesteric (TIC) state.[19] The TIC state describes a uniform twist along the z–axis, across all the sample. The spatial dependence of $\alpha(x,y,t)$ and $\theta(x,y,t)$ allows the twist of the vector director $\vec{n}$ along the x and y axes. It gives the possibility of non-trivial configurations, such as cholesteric fingers of type 1, and labyrinthine patterns built from the morphological instabilities of the fingers.

Using the components of the director $\vec{n}$, formula Eq. (1), the order parameter $Q \equiv n_z(n_x + in_y)$ can be introduced,[28] which is invariant under the transformation $\vec{n} \to -\vec{n}$. This condition is a prerequisite for any liquid crystal theory since the director accounts for the molecular orientation. In the limit $\alpha \ll 1$, the order parameter becomes $Q(x,y,z,t) \approx \alpha(x,y,t)e^{i\theta(x,y,t)}\sin(\pi z/d)$. Let us introduce the complex field $A(x,y,t) \equiv \alpha e^{i\theta}$ that

accounts for the amplitude of the parameter of order $Q = A \sin(\pi z/d)$. This complex field A can be used to study the unwinding/winding transition.[28]

To shed light on the unwinding/winding transition and the different morphological instabilities of CF1 from a theoretical perspective, we use the following phenomenological amplitude equation for A in the limit of small elastic anisotropy[26]

$$\partial_t A = \mu A + \beta |A|^2 A - |A|^4 A + \partial_\eta \partial_{\bar\eta} A + \chi \left(A \partial_{\bar\eta} A - \bar A \partial_{\bar\eta} A \right), \tag{2}$$

where $\partial_\eta \equiv \partial_x + i\partial_y$ is a complex differential operator. μ is the bifurcation parameter that is proportional to the departure from the critical temperature T_c of the unwinding/winding transition. The second and third terms on the right hand side (RHS) of Eq. (2) account for the nonlinear saturation characteristic of a subcritical transition ($\beta > 0$). The fourth term accounts for the isotropic elastic coupling. The last term proportional to χ is the lowest order term that accounts for the chirality, that is, χ measures the mirror symmetry breaking in the mid-plane of the cell.

The model Eq. (2) is of variational nature, that is, $\partial_t A = -\delta \mathcal{F}/\delta \bar A$, where $\mathcal{F}$ is a Lyapunov Functional

$$\mathcal{F} = \int \int dx dy \left\{ -\mu |A|^2 - \beta \frac{|A|^4}{2} + \frac{|A|^6}{3} + |\nabla A|^2 - \chi |A|^2 \left(\partial_{\eta^*} A + \partial_\eta A^* \right) \right\}. \tag{3}$$

Hence the dissipative dynamics of Eq. (2) is characterized by the minimization of the free energy $\mathcal{F}$.

Figure 2. Numerical simulations of an infinite finger from Eq. (2) with $\mu = -0.4$ and $\beta = 1$. (a) At $\chi = 2.5$, the chiral finger is unstable to a sinusoidal deformation along its axis. The morphology is described by the absolute value of the normalized absolute value of the interfacial curvature $w|\kappa|$. The distribution $f(w|\kappa|)$ displays a divergent power-law with $c = 0.3$ and $w|\kappa_c| = 0.17$. (b) At $\chi = 3.0$, the chiral finger exhibit side-branching in the regions of high curvature and then tip-splitting. The tail of the distribution $f(w|\kappa|)$ shows an exponential behavior with $b = 3.1$. $|A|$ is the modulus of the complex field A.

For $\mu < 0$, the homeotropic state $A = 0$ is stable, and when $\mu \geqslant 0$, this phase is unstable. The model equation (2) has a bistability region in the range $\mu = -1/4$ and $\mu = 0$, between the homeotropic $A = 0$ and TIC $A = (1/2 + \sqrt{1/4 + \mu})^{1/2} e^{i\theta_o}$ state, with θ_o an arbitrary phase. This θ_o phase is an arbitrary constant due to the freedom of definition of the representation vectors $\hat x$ and $\hat y$. Close to the bistability region, one expects to find chiral fingers of type 1.[9,16] To study the CF1, the serpentine, and tip-splitting instability, we perform numerical simulations of the model equation (2) with periodic boundary conditions. We consider a square grid of 400×400, with $\Delta x = 0.25$. An isotropic finite difference method is used for the spatial derivatives, and a Runge-Kutta order-4 algorithm for the temporal evolution with a time step $\Delta t = 0.01$. The initial condition is an infinite chiral

finger in a homogeneous nematic background $A = 0$ at $\mu = -0.4$, where the homeotropic state $A = 0$ is stable. We choose this initial condition to annihilate the pointed tip and neglect the elongation of the finger. Figure 2a shows the serpentine instability at $\chi = 2.5$. The color map of $|A|$ shows the modulus of the complex field A. To characterize the instability, we have measured the absolute value of the interfacial curvature $|\kappa|$, which is normalized by the width w of the finger. Note that the distribution of the normalized interfacial curvature $f(w|\kappa|)$ follows a divergent power-law until $w|k_c|$. The absolute values of sinusoidal functions follow this type of distribution. The last two bars of the histogram are associated with the big accumulation of curvatures in the tips of the folds. Let us focus on the power-law behavior of the distribution, where the serpentine shape of the chiral finger can be approximated by the sinusoidal $x = b\sin(qy)$. In the limit of small amplitude $bq \ll 1$ and small curvature $\kappa b \ll 1$, the energy associated with the spatial oscillations is

$$\mathcal{F}_{serpentine} = F_{sf} \int ds + H \int \kappa^2 ds, \tag{4}$$

where F_{sf} is the energy per length of a straight finger, which is always negative because the finger is supported by the nematic phase $\mathcal{F}[A = 0] = 0$. H is a positive constant. The arclength is $s \approx L_y + b^2 q \pi/2$. L_y is the length of the initial straight finger. Note that Eq. (4) represents the competition between the minimization of energy by increasing the size of the finger and the cost of generating curvature.[24] The free energy $\mathcal{F}_{serpentine}$ can be minimized with respect to q to obtain the optimal wavelength of the oscillation $q_c = \sqrt{|F_{sf}|/6H}$. Replacing q_c into Eq. (4), one gets that $\mathcal{F}_{serpentine}[q_c] < 0$. Therefore, the chiral finger will suffer a serpentine instability with a sinusoidal shape of wavelength q_c to minimize the energy of the system.

In Figure 2b, the distribution of interfacial curvature of a finger undergoing side-branching and tip-splitting is shown at $\chi = 3$. The distribution $f(w|\kappa|)$ exhibits an exponential tail bounded by the triads (produced by side-branching and tip-splitting) and the inflated rounded tips of the CF1. Therefore, a transition between the different morphologies exists and is mediated by the curvature of the chiral fingers, which is controlled by the chirality in the system.

Finally, we investigate the propagation of a single finger into the nematic phase $A = 0$. In the case of serpentine instability, the tip of the fingers advances straightly with a constant velocity v as shown in Fig. 3a. However, in the tip-splitting regime $\chi = 3$, the fingers suffer a deceleration process, while the curvature near the tip starts to decrease (cf. Fig. 3b). When the curvature is zero on the tip of the finger, the tip-splitting takes place (vertical black line in Fig. 3b).
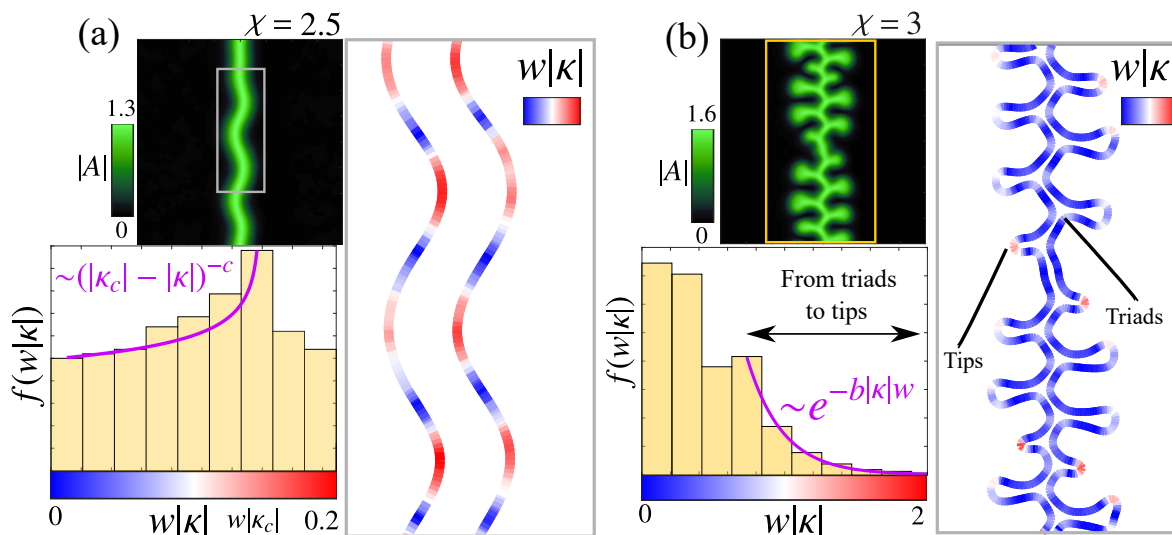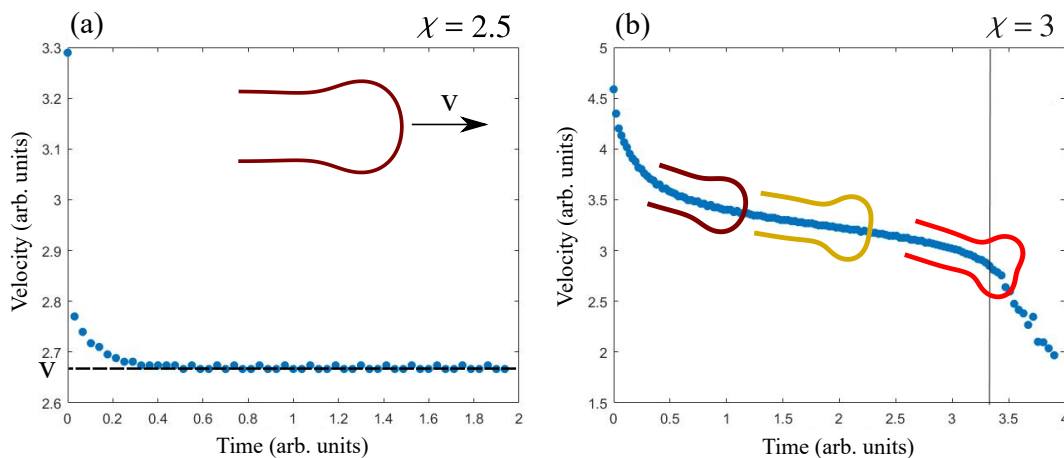

Figure 3. Numerical simulations of a propagative finger from Eq. (2) with $\mu = -0.4$ and $\beta = 1$. (a) At $\chi = 2.5$, the rounded tip of the chiral finger advance in a straight manner with a constant velocity v. (b) At $\chi = 3.0$, the rounded tip undergoes a flattening deformation, decelerating the propagation of the finger and eventually dividing the tip into two new fingers. The colored insets are the interface of the rounded tip.

4. CONCLUSIONS

The comprehension of how the transition between morphologies in a non-living system (CLC) occurs can open the avenue to understanding and controlling morphologies observed in living systems. For example, one can think of shaping forms during biological growing processes by artificially controlling the chemical signal rate.

In this study, we have shown that the heating rate of the sample can control the transition between different morphological instabilities in frustrated CLC. Moreover, in terms of a phenomenological amplitude equation, we reveal that the transition is mediated by curvature. Apparently, in these chiral systems, a selection mechanism between curvature and velocity is mediated by chirality. Work is in progress in this direction.

ACKNOWLEDGMENTS

REFERENCES

[1] Nicolis, G. and Prigogine, I., [*Self-Organization in Non-Equilibrium Systems*], John Wiley & Sons, New York (1977).

[2] Pismen, L. M., [*Patterns and interfaces in dissipative dynamics*], Springer Science & Business Media (2006).

[3] Cross, M. and Greenside, H., [*Pattern Formation and Dynamics in Non-Equilibrium Systems*], Cambridge University Press, New York (2009).

[4] Buka, A. and Kramer, L., [*Pattern formation in liquid crystals*], Springer Science & Business Media (2012).

[5] Coullet, P., "Localized patterns and fronts in nonequilibrium systems," *International Journal of Bifurcation and Chaos* **12**(11), 2445–2457 (2002).

[6] Tlidi, M., Staliunas, K., Panajotov, K., Vladimirov, A., and Clerc, M., "Localized structures in dissipative media: from optics to plant ecology," (2014).

[7] Turing, A. M., "The chemical basis of morphogenesis," *Philosophical Transactions of the Royal Society of London. Series B, Biological Sciences* **237**(641), 37–72 (1952).

[8] Swift, J. B. and Hohenberg, P. C., "Hydrodynamic fluctuations at the convective instability," *Physical Review A* **15**(1), 319 (1977).

[9] Ribière, P., Pirkl, S., and Oswald, P., "Electric-field-induced phase transitions in frustrated cholesteric liquid crystals of negative dielectric anisotropy," *Phys. Rev. A* **44**, 8198 (1991).

[10] Lefever, R. and Lejeune, O., "On the origin of tiger bush," *Bulletin of Mathematical biology* **59**(2), 263–294 (1997).

[11] Rosensweig, R. E., Zahn, M., and Shumovich, R., "Labyrinthine instability in magnetic and dielectric fluids," *Journal of Magnetism and Magnetic Materials* **39**(1-2), 127–132 (1983).

[12] Lee, K. J., McCormick, W., Ouyang, Q., and Swinney, H. L., "Pattern formation by interacting chemical fronts," *Science* **261**(5118), 192–194 (1993).

[13] Dickstein, A. J., Erramilli, S., Goldstein, R. E., Jackson, D. P., and Langer, S. A., "Labyrinthine pattern formation in magnetic fluids," *Science* **261**(5124), 1012–1015 (1993).

[14] Tlidi, M., Vladimirov, A., and Mandel, P., "Curvature instability in passive diffractive resonators," *Physical review letters* **89**(23), 233901 (2002).

[15] Bordeu, I., Clerc, M. G., Lefever, R., and Tlidi, M., "From localized spots to the formation of invaginated labyrinthine structures in a swift–hohenberg model," *Communications in Nonlinear Science and Numerical Simulation* **29**(1-3), 482–487 (2015).

[16] Goldstein, R. E., Muraki, D. J., and Petrich, D. M., "Interface proliferation and the growth of labyrinths in a reaction-diffusion system," *Physical Review E* **53**(4), 3933 (1996).

[17] Le Berre, M., Ressayre, E., Tallet, A., Pomeau, Y., and Di Menza, L., "Example of a chaotic crystal: The labyrinth," *Physical Review E* **66**(2), 026203 (2002).

[18] Echeverría-Alar, S. and Clerc, M., "Labyrinthine patterns transitions," *Physical Review Research* **2**(4), 042036 (2020).

[19] Oswald, P. and Pieranski, P., [*Nematic and Cholesteric Liquid Crystals*], CRC Press (2005).

[20] De Gennes, P.-G. and Prost, J., [*The physics of liquid crystals*], vol. 83, Oxford university press (1993).

[21] Dierking, I., [*Textures of liquid crystals*], John Wiley & Sons (2003).

[22] Oswald, P., Baudry, J., and Rondepierre, T., "Growth below and above the spinodal limit: The cholesteric-nematic front," *Physical Review E* **70**(4), 041702 (2004).

[23] Stieb, A., "Structure of elongated and spherulitic domains in long pitch cholesterics with homeotropic boundary alignment," *Journal de Physique* **41**(9), 961–969 (1980).

[24] Ribiere, P. and Oswald, P., "Nucleation and growth of cholesteric fingers under electric field," *Journal de Physique* **51**(16), 1703–1720 (1990).

[25] Nagaya, T., Hikita, Y., Orihara, H., and Ishibashi, Y., "Experimental study of the growth of the cholesteric finger pattern," *Journal of the Physical Society of Japan* **65**(8), 2707–2712 (1996).

[26] Clerc, M., González-Cortés, G., and Echeverría-Alar, S., "Localized dissipative vortices in chiral nematic liquid crystal cells," *Physical Review Research* **4**(2), L022021 (2022).

[27] Parra, M., Hidalgo, P., and Elgueta, E., "Synthesis and mesomorphic properties of oxadiazole esters derived from (r)-2-octanol,(s)-2-n-octyloxypropanol and (2 s, 3 s)-2-chloro-3-methylpentanol," *Liquid Crystals* **35**(7), 823–832 (2008).

[28] Frisch, T., Gil, L., and Gilli, J. M., "Two-dimensional landau-de gennes dynamical model for the unwinding transition of a cholesteric liquid crystal," *Phys. Rev. E* **48**, R4199 (1993).

[29] Oswald, P., Baudry, J., and Pirkl, S., "Static and dynamic properties of cholesteric fingers in electric field," *Physics Reports* **337**, 67 (2000).

10.1.   Perspectives

In this chapter, we briefly described the invaginated labyrinthine patterns and made qualitative distinctions between them and the cholesteric branching labyrinthine patterns. An interesting research direction is to address quantitatively the transition between the cholesteric labyrinthine patterns, that is, identify the nature of the transition and propose the good order parameters to describe it (defects, correlation length, energy, and others).

Chapter 11

Conclusions

This dissertation was dedicated to the understanding of the emergence, stabilization, destabilization, and transitions of labyrinthine patterns in dissipative systems. The main scientific driving of this work was the lack of analytical and computational tools to approach the disordered patterns, which were introduced in this work in the best possible way. In particular, the focus was on labyrinthine patterns exhibited by common pattern-forming equations, labyrinthine-like patterns observed in irregular landscapes of arid and semi-arid regions, and cholesteric disordered patterns manifested in confined CNLCs.

To explore the robustness of labyrinthine patterns, we spent our first steps performing numerical integrations of the prototype SH equation, which allowed us to propose a definition of labyrinths: *spatial state with a minimum number of defects displaying a short-range order characterized by a single wave number and a powdered spectrum.* This was possible by introducing the averaged windowed Fourier transform numerical algorithm. In the framework of the SH equation, we have demonstrated that different types of labyrinthine patterns can be distinguished by implementing algorithms of defect counting, computation of orientational fields, and measurement of correlation lengths.

We have proved the existence of localized labyrinthine patterns when scurfy labyrinths coexist with stable homogeneous solutions in the SH equation. We have revealed the behavior of some stable branches of these non-trivial symmetry localized patterns, elucidating that the stable equilibria are given by a complicated balance of bulk defects, curvature, and a complex-shaped interface. To our knowledge, this was the first time that the problem of localization of complex patterns had been addressed. Additionally, we showed the existence of localized labyrinths in other pattern-forming models. In particular, we have explored the observations of localized labyrinthine patterns in ecology where disordered vegetation bands, intercalated with bare soil bands, are supported by a uniform vegetated background, and studied its stabilization in three relevant ecological models of vegetation in arid environments.

To unveil the key ingredients responsible for the stabilization of the irregular vegetation structures observed in arid climates, we have incorporated the effects of topographic variations, as a spatially modulated aridity parameter, in population dynamics models. We have shown the role of heterogeneities in the transitions between homogenous states and in the stabilization of labyrinthinelike vegetation patterns. This new modeling framework allowed us to introduce the concept of imperfect labyrinths, which result from combining perfect labyrinths with a minimum degree of heterogeneity. We revealed the transition between these labyrinths with the help of a numerical protocol implemented in this work.

Disordered patterns in CNLCs (labyrinths under our definition) have intrigued *liquid crys-*

talers for almost three decades. We have investigated their emergence and stabilization from the perspective of an amplitude equation of the Ginzburg-Landau type (CAGL). This model was derived close to the winding/unwinding transition from the dissipative dynamics related to the minimization of the Frank-Oseen energy of CNLCs, in the limit of strong homeotropic anchoring and large cholesteric pitch. The CAGL equation includes the minimal representation of the breaking of mirror symmetry projected into the plane.

The chiral-anisotropic Ginzburg-Landau equation allowed us to explore numerically and theoretically localized vortices, chiral fingers, and labyrinthine patterns. We think that the qualitative agreement with the textures seen in experiments of confined CNLCs controlled by temperature (also with voltage) is remarkably good. The theoretical approach to investigate the solutions mentioned was to derive interface equations considering curvature effects. On the one hand, by establishing an equation for the interface of chiral bubbles, we proved that a critical chiral parameter, which depends on the confinement ratio and the elastic constants of the material, is needed for their stabilization. Additionally, we revealed that the appearance/disappearance mechanism of the localized vortices is governed by a saddle-node bifurcation. On the other hand, a curvature-velocity relationship was derived for the rounded tips of CF1, revealing the tip-splitting mechanism underlying the emergence of branching labyrinthine patterns. Tip detection algorithms for the comparison between experiments and numerical integrations of the CAGL equation were implemented. Also, we have performed analytical calculations regarding the minimization of the free energy of the CAGL model, which helped us to find criteria for the stabilization, repulsion, and invagination instability of chiral fingers.

Bibliography

[1] I. Prigogine and G. Nicolis, "On symmetry-breaking instabilities in dissipative systems," *The Journal of Chemical Physics*, vol. 46, no. 9, pp. 3542–3550, 1967.

[2] I. Prigogine and R. Lefever, "Symmetry breaking instabilities in dissipative systems. ii," *The Journal of Chemical Physics*, vol. 48, no. 4, pp. 1695–1700, 1968.

[3] G. Nicolis and I. Prigogine, *Self-Organization in Non-Equilibrium Systems.* John Wiley & Sons, New York, 1977.

[4] P. Manneville, "Dissipative structures and weak turbulence," in *Chaos—The Interplay Between Stochastic and Deterministic Behaviour: Proceedings of the XXXIst Winter School of Theoretical Physics Held in Karpacz, Poland 13–24 February 1995*, pp. 257–272, Springer, 2005.

[5] M. C. Cross and P. C. Hohenberg, "Pattern formation outside of equilibrium," *Reviews of modern physics*, vol. 65, no. 3, p. 851, 1993.

[6] M. I. Rabinovich, A. B. Ezersky, and P. D. Weidman, *The dynamics of patterns.* World Scientific, Singapore, 2000.

[7] P. W. Anderson, "More is different: broken symmetry and the nature of the hierarchical structure of science.," *Science*, vol. 177, no. 4047, pp. 393–396, 1972.

[8] W. Macfadyen, "Soil and vegetation in british somaliland," *Nature*, vol. 165, no. 4186, pp. 121–121, 1950.

[9] P. Ball, "The self-made tapestry: pattern formation in nature," 1999.

[10] V. Fleury, J.-F. Gouyet, and M. Leonetti, *Branching in nature: dynamics and morphogenesis of branching structures, from cell to river networks*, vol. 14. Springer Science & Business Media, 2001.

[11] J. D. Murray, *Mathematical biology: I. An introduction.* Springer, 2002.

[12] M. Kücken and A. C. Newell, "Fingerprint formation," *Journal of theoretical biology*, vol. 235, no. 1, pp. 71–83, 2005.

[13] P. Ball, *Branches: Nature's patterns: a tapestry in three parts.* OUP Oxford, 2009.

[14] H. Bénard, "Les tourbillons cellulaires dans une nappe liquide," *Revue Gen. Sci. Pure Appl.*, vol. 11, pp. 1261–1271, 1900.

[15] L. Rayleigh, "On convection currents in a horizontal layer of fluid, when the higher temperature is on the under side," *The London, Edinburgh, and Dublin Philosophical Magazine and Journal of Science*, vol. 32, no. 192, pp. 529–546, 1916.

[16] J. Swift and P. Hohenberg, "Hydrodynamic fluctuations at the convective instability," *Phys. Rev. A*, vol. 15, p. 319, 1977.

[17] A. M. Turing, "The chemical basis of morphogenesis," *Phylosophical Transactions of the Royal Society of London. Series B, Biological Sciences*, vol. 237, no. 641, pp. 37–72, 1952.

[18] R. Hoyle and R. B. Hoyle, *Pattern formation: an introduction to methods.* Cambridge University Press, 2006.

[19] L. M. Pismen, *Patterns and interfaces in dissipative dynamics.* Springer Science & Business Media, 2006.

[20] A. C. Newell, T. Passot, and J. Lega, "Order parameter equations for patterns," *Annual review of fluid mechanics*, vol. 25, no. 1, pp. 399–453, 1993.

[21] A. O. León, M. G. Clerc, and S. Coulibaly, "Dissipative structures induced by spin-transfer torques in nanopillars," *Physical Review E*, vol. 89, no. 2, p. 022908, 2014.

[22] M. C. Walters, P. Subramanian, A. Archer, and R. Evans, "Structural crossover in a model fluid exhibiting two length scales: repercussions for quasicrystal formation," *Physical Review E*, vol. 98, no. 1, p. 012606, 2018.

[23] R. E. Goldstein, D. J. Muraki, and D. M. Petrich, "Interface proliferation and the growth of labyrinths in a reaction-diffusion system," *Physical Review E*, vol. 53, no. 4, p. 3933, 1996.

[24] M. Le Berre, E. Ressayre, A. Tallet, Y. Pomeau, and L. Di Menza, "Example of a chaotic crystal: The labyrinth," *Phys. Rev. E*, vol. 66, p. 026203, 2002.

[25] C. Bowman and A. Newell, "Natural patterns and wavelets," *Reviews of Modern Physics*, vol. 70, no. 1, p. 289, 1998.

[26] M. C. Cross, D. Meiron, and Y. Tu, "Chaotic domains: A numerical investigation," *Chaos*, vol. 4, p. 4, 1994.

[27] M. C. Cross and D. I. Meiron, "Domain Coarsening in Systems Far from Equilibrium," *Phys. Rev. Lett.*, vol. 75, p. 11, 1995.

[28] R. E. Rosensweig, M. Zahn, and R. Shumovich, "Labyrinthine instability in magnetic and dielectric fluids," *Journal of Magnetism and Magnetic Materials*, vol. 39, no. 1, pp. 127–132, 1983.

[29] A. J. Dickstein, S. Erramilli, R. E. Goldstein, D. P. Jackson, and S. A. Langer, "Labyrinthine pattern formation in magnetic fluids," *Science*, vol. 261, no. 5124, pp. 1012–1015, 1993.

[30] K. J. Lee, W. McCormick, Q. Ouyang, and H. L. Swinney, "Pattern formation by interacting chemical fronts," *Science*, vol. 261, no. 5118, pp. 192–194, 1993.

[31] G. H. Gunaratne, R. E. Jones, Q. Ouyang, and H. L. Swinney, "An invariant measure of disorder in patterns," *Physical review letters*, vol. 75, no. 18, p. 3281, 1995.

[32] J. von Hardenberg, E. Meron, M. Shachak, and Y. Zarmi, "Diversity of vegetation patterns and desertification," *Phys. Rev. Lett.*, vol. 87, p. 19, 2001.

[33] V. Deblauwe, P. Couteron, O. Lejeune, J. Bogaert, and N. Barbier, "Environmental modulation of self-organized periodic vegetation patterns in sudan," *Ecography*, vol. 34, pp. 990–1001, jul 2011.

[34] A. Marasco, A. Iuorio, F. Cartení, G. Bonanomi, D. M. Tartakovsky, S. Mazzoleni, and

F. Giannino, "Vegetation pattern formation due to interactions between water availability and toxicity in plant–soil feedback," *Bulletin of mathematical biology*, vol. 76, pp. 2866–2883, 2014.

[35] C. Yuan, L. Guo, D. F. Levia, M. Rietkerk, B. Fu, and G. Gao, "Quantity or efficiency: Strategies of self-organized xerophytic shrubs to harvest rain," *Water Resources Research*, vol. 58, no. 10, p. e2022WR032008, 2022.

[36] P. Ribiere, S. Pirkl, and P. Oswald, "Electric-field-induced phase transitions in frustrated cholesteric liquid crystals of negative dielectric anisotropy," *Phys. Rev. A*, vol. 44, p. 8198, 1991.

[37] P. Oswald, J. Baudry, and S. Pirkl, "Static and dynamic properties of cholesteric fingers in electric field," *Phys. Rep.*, vol. 337, 2000.

[38] D. Pociecha, E. Gorecka, N. Vaupotič, M. Čepic, and J. Mieczkowski, "Spontaneous breaking of minimal surface condition: Labyrinths in free standing smectic films," *Physical review letters*, vol. 95, no. 20, p. 207801, 2005.

[39] Q. X. Liu, P. M. Herman, W. M. Mooij, J. Huisman, M. Scheffer, H. Olff, and J. Van De Koppel, "Pattern formation at multiple spatial scales drives the resilience of mussel bed ecosystems," *Nat. Commun.*, vol. 5, p. 5234, 2014.

[40] S. Park, "Manipulating the sequences of block copolymer patterns on corrugated substrates," *Polymer*, vol. 180, p. 121726, 2019.

[41] A. Nakhoul, C. Maurice, M. Agoyan, A. Rudenko, F. Garrelie, F. Pigeon, and J.-P. Colombier, "Self-organization regimes induced by ultrafast laser on surfaces in the tens of nanometer scales," *Nanomaterials*, vol. 11, p. 1020, apr 2021.

[42] P. Kavle, J. A. Zorn, A. Dasgupta, B. Wang, M. Ramesh, L.-Q. Chen, and L. W. Martin, "Strain-driven mixed-phase domain architectures and topological transitions in pb1- xsrxtio3 thin films," *Advanced Materials*, vol. 34, no. 37, p. 2203469, 2022.

[43] J. Dawes, "After 1952: The later development of Alan Turing's ideas on the mathematics of pattern formation," *Historia mathematica*, vol. 43, p. 49, 2016.

[44] R. Lefever and O. Lejeune, "On the origin of tiger bush," *Bulletin of Mathematical biology*, vol. 59, no. 2, pp. 263–294, 1997.

[45] O. Lejeune and M. Tlidi, "A model for the explanation of tiger bush vegetation stripes," *J Veg Sci*, vol. 10, pp. 201–208, 1999.

[46] J. von Hardenberg, E. Meron, M. Shachak, and Y. Zarmi, "Diversity of vegetation patterns and desertification," *Physical review letters*, vol. 87, no. 19, p. 198101, 2001.

[47] M. Rietkerk, M. C. Boerlijst, F. van Langevelde, R. HilleRisLambers, J. v. de Koppel, L. Kumar, H. H. Prins, and A. M. de Roos, "Self-organization of vegetation in arid ecosystems," *The American Naturalist*, vol. 160, no. 4, pp. 524–530, 2002.

[48] V. Deblauwe, N. Barbier, P. Couteron, O. Lejeune, and J. Bogaert, "The global biogeography of semi-arid periodic vegetation patterns," *Global Ecology and Biogeography*, vol. 17, no. 6, pp. 715–723, 2008.

[49] F. Borgogno, P. D'Odorico, F. Laio, and L. Ridolfi, "Mathematical models of vegetation pattern formation in ecohydrology," *Reviews of geophysics*, vol. 47, no. 1, 2009.

[50] O. Lejeune, M. Tlidi, and P. Couteron, "Localized vegetation patches: a self-organized

response to resource scarcity," *Physical Review E*, vol. 66, no. 1, p. 010901, 2002.

[51] M. Rietkerk, S. C. Dekker, P. C. De Ruiter, and J. van de Koppel, "Self-organized patchiness and catastrophic shifts in ecosystems," *Science*, vol. 305, no. 5692, pp. 1926–1929, 2004.

[52] E. Meron, H. Yizhaq, and E. Gilad, "Localized structures in dryland vegetation: forms and functions," *Chaos: An Interdisciplinary Journal of Nonlinear Science*, vol. 17, no. 3, p. 037109, 2007.

[53] P. Couteron, F. Anthelme, M. Clerc, D. Escaff, C. Fernandez-Oto, and M. Tlidi, "Plant clonal morphologies and spatial patterns as self-organized responses to resource-limited environments," *Philosophical Transactions of the Royal Society A: Mathematical, Physical and Engineering Sciences*, vol. 372, no. 2027, p. 20140102, 2014.

[54] M. Tlidi, E. Berríos-Caro, D. Pinto-Ramo, A. Vladimirov, and M. G. Clerc, "Interaction between vegetation patches and gaps: A self-organized response to water scarcity," *Physica D: Nonlinear Phenomena*, vol. 414, p. 132708, 2020.

[55] M. Van Rooyen, G. Theron, N. Van Rooyen, W. Jankowitz, and W. Matthews, "Mysterious circles in the namib desert: review of hypotheses on their origin," *Journal of Arid Environments*, vol. 57, no. 4, pp. 467–485, 2004.

[56] M. Tlidi, R. Lefever, and A. Vladimirov, "On vegetation clustering, localized bare soil spots and fairy circles," *Lect. Notes. Phys.*, vol. 751, no. 5, pp. 381–982, 2008.

[57] N. Juergens, "The biological underpinnings of namib desert fairy circles," *Science*, vol. 339, no. 6127, pp. 1618–1621, 2013.

[58] M. D. Cramer and N. N. Barger, "Are namibian "fairy circles" the consequence of self-organizing spatial vegetation patterning?," *PloS one*, vol. 8, no. 8, p. e70876, 2013.

[59] C. Fernandez-Oto, M. Tlidi, D. Escaff, and M. Clerc, "Strong interaction between plants induces circular barren patches: fairy circles," *Philosophical Transactions of the Royal Society A: Mathematical, Physical and Engineering Sciences*, vol. 372, no. 2027, p. 20140009, 2014.

[60] D. Escaff, C. Fernandez-Oto, M. Clerc, and M. Tlidi, "Localized vegetation patterns, fairy circles, and localized patches in arid landscapes," *Physical Review E*, vol. 91, no. 2, p. 022924, 2015.

[61] S. Getzin, K. Wiegand, T. Wiegand, H. Yizhaq, J. von Hardenberg, and E. Meron, "Adopting a spatially explicit perspective to study the mysterious fairy circles of namibia," *Ecography*, vol. 38, no. 1, pp. 1–11, 2015.

[62] C. E. Tarnita, J. A. Bonachela, E. Sheffer, J. A. Guyton, T. C. Coverdale, R. A. Long, and R. M. Pringle, "A theoretical foundation for multi-scale regular vegetation patterns," *Nature*, vol. 541, no. 7637, pp. 398–401, 2017.

[63] P. G. de Gennes and J. Prost, *The Physics of Liquid Crystals.* Oxford, UK: Clarendon Press, 2 ed., 1993.

[64] P. Oswald and P. Pieranski, *Nematic and Cholesteric Liquid Crystals.* London: CRC Press, 2005.

[65] I. Dierking, *Textures of liquid crystals.* John Wiley & Sons, 2003.

[66] M. L. Parra, P. I. Hidalgo, and E. Y. Elgueta, "Synthesis and mesomorphic properties

of oxadiazole esters derived from (r)-2-octanol,(s)-2-n-octyloxypropanol and (2 s, 3 s)-2-chloro-3-methylpentanol," *Liquid Crystals*, vol. 35, no. 7, pp. 823–832, 2008.

[67] A. B. Harris, R. D. Kamien, and T. C. Lubensky, "Molecular chirality and chiral parameters," *Reviews of Modern Physics*, vol. 71, no. 5, p. 1745, 1999.

[68] W. E. Haas and J. E. Adams, "Electrically variable diffraction in spherulitic liquid crystals," *Applied Physics Letters*, vol. 25, no. 5, pp. 263–264, 1974.

[69] N. Nawa and K. Nakamura, "Observation of forming process of bubble domain texture in liquid crystals," *Japanese Journal of Applied Physics*, vol. 17, no. 1, p. 219, 1978.

[70] A. Stieb, "Structure of elongated and spherulitic domains in long pitch cholesterics with homeotropic boundary alignment," *Journal de Physique*, vol. 41, no. 9, pp. 961–969, 1980.

[71] P. Oswald, J. Bechhoefer, and A. Libchaber, "Instabilities of a moving nematic-isotropic interface," *Physical Review Letters*, vol. 58, no. 22, p. 2318, 1987.

[72] T. Nagaya, Y. Hikita, H. Orihara, and Y. Ishibashi, "Experimental study of the growth of the cholesteric finger pattern," *Journal of the Physical Society of Japan*, vol. 65, no. 8, pp. 2707–2712, 1996.

[73] P. J. Ackerman and I. I. Smalyukh, "Diversity of knot solitons in liquid crystals manifested by linking of preimages in torons and hopfions," *Phys. Rev. X*, vol. 7, no. 1, p. 011006, 2017.

[74] I. I. Smalyukh, Y. Lansac, N. A. Clark, and R. P. Trivedi, "Three-dimensional structure and multistable optical switching of triple-twisted particle-like excitations in anisotropic fluids," *Nature materials*, vol. 9, no. 2, pp. 139–145, 2010.

[75] I. Prigogine, "Time, structure, and fluctuations," *Science*, vol. 201, no. 4358, pp. 777–785, 1978.

[76] E. Tirapegui, "Irreversibilidad y flecha del tiempo en la física," 1998.

[77] H. D. Abarbanel, M. I. Rabinovich, and M. M. Sushchik, *Introduction to nonlinear dynamics for physicists*, vol. 53. World Scientific, 1993.

[78] *Nonlinear Dynamics and Chaos: With Applications to Physics, Biology, Chemistry and Engineering.* Westview Press, 2000.

[79] H. Poincaré, "Sur l'équilibre d'une masse fluide animée d'un mouvement de rotation," *Bulletin astronomique, Observatoire de Paris*, vol. 2, no. 1, pp. 109–118, 1885.

[80] V. Gertsberg and G. Sivashinsky, "Large cells in nonlinear rayleigh-benard convection," *Progress of Theoretical Physics*, vol. 66, no. 4, pp. 1219–1229, 1981.

[81] M. Cross and D. Meiron, "Domain coarsening in systems far from equilibrium," *Physical review letters*, vol. 75, no. 11, p. 2152, 1995.

[82] H. Greenside and M. Cross, "Stability analysis of two-dimensional models of three-dimensional convection," *Physical Review A*, vol. 31, no. 4, p. 2492, 1985.

[83] S. Residori, A. Petrossian, T. Nagaya, C. Riera, and M. Clerc, "Fronts and localized structures in a liquid-crystal-light-valve with optical feedback," *Physica D: Nonlinear Phenomena*, vol. 199, no. 1-2, pp. 149–165, 2004.

[84] G. Kozyreff and M. Tlidi, "Nonvariational real swift-hohenberg equation for biologi-

cal, chemical, and optical systems," *Chaos: An Interdisciplinary Journal of Nonlinear Science*, vol. 17, no. 3, p. 037103, 2007.

[85] F. Alvarez-Garrido, M. Clerc, and G. Gonzalez-Cortes, "Transition to spatiotemporal intermittency and defect turbulence in systems under translational coupling," *Physical review letters*, vol. 124, no. 16, p. 164101, 2020.

[86] M. Clerc, D. Escaff, and V. Kenkre, "Patterns and localized structures in population dynamics," *Physical Review E*, vol. 72, no. 5, p. 056217, 2005.

[87] P. G. de Gennes, *Soft interfaces: the 1994 Dirac memorial lecture.* Cambridge University Press, 1997.

[88] G. Dee and J. Langer, "Propagating pattern selection," *Physical Review Letters*, vol. 50, no. 6, p. 383, 1983.

[89] D. Boyer and J. Viñals, "Grain boundary pinning and glassy dynamics in stripe phases," *Phys. Rev. E*, vol. 65, p. 046119, 2002.

[90] E. Meron, *Nonlinear physics of ecosystems.* CRC Press, 2015.

[91] P. Coullet, L. Gil, and D. Repaux, "Defects and subcritical bifurcations," *Physical review letters*, vol. 62, no. 25, p. 2957, 1989.

[92] R. E. Goldstein, G. H. Gunaratne, L. Gil, and P. Coullet, "Hydrodynamic and interfacial patterns with broken space-time symmetry," *Phys. Rev. A*, vol. 43, no. 12, p. 6700, 1991.

[93] R. C. Brower, D. A. Kessler, J. Koplik, and H. Levine, "Geometrical approach to moving-interface dynamics," *Physical Review Letters*, vol. 51, no. 13, p. 1111, 1983.

[94] M. G. Clerc and C. Falcón, "Localized patterns and holesolutions one-dimensional extended systems," *Physica A*, vol. 356, p. 48, 2005.

[95] J. S. Langer, "Instabilities and pattern formation in crystal growth," *Reviews of Modern Physics*, vol. 52, no. 1, p. 1, 1980.

[96] Y. Kuramoto, "Instability and turbulence of wavefronts in reaction-diffusion systems," *Progress of Theoretical Physics*, vol. 63, no. 6, pp. 1885–1903, 1980.

[97] D. A. Kessler, J. Koplik, and H. Levine, "Pattern selection in fingered growth phenomena," *Advances in physics*, vol. 37, no. 3, pp. 255–339, 1988.

[98] P. Pelcé and A. Libchaber, *Dynamics of curved fronts.* Elsevier, 2012.

[99] D. Gomila, P. Colet, G.-L. Oppo, and M. San Miguel, "Stable droplets and growth laws close to the modulational instability of a domain wall," *Physical review letters*, vol. 87, no. 19, p. 194101, 2001.

[100] A. C. Newell and J. A. Whitehead, "Finite bandwidth, finite amplitude convection," *Journal of Fluid Mechanics*, vol. 38, no. 2, pp. 279–303, 1969.

[101] L. A. Segel, "Distant side-walls cause slow amplitude modulation of cellular convection," *Journal of Fluid Mechanics*, vol. 38, no. 1, pp. 203–224, 1969.

[102] S. Ciliberto, E. Pampaloni, and C. Perez-Garcia, "Competition between different symmetries in convective patterns," *Physical review letters*, vol. 61, no. 10, p. 1198, 1988.

[103] S. Ciliberto, P. Coullet, J. Lega, E. Pampaloni, and C. Perez-Garcia, "Defects in roll-hexagon competition," *Physical review letters*, vol. 65, no. 19, p. 2370, 1990.

[104] N. Verschueren, U. Bortolozzo, M. Clerc, and S. Residori, "Spatiotemporal chaotic localized state in liquid crystal light valve experiments with optical feedback," *Physical review letters*, vol. 110, no. 10, p. 104101, 2013.

[105] A. Alvarez-Socorro, M. Clerc, G. González-Cortés, and M. Wilson, "Nonvariational mechanism of front propagation: Theory and experiments," *Physical Review E*, vol. 95, no. 1, p. 010202, 2017.

[106] A. Alvarez-Socorro, M. Clerc, and M. Tlidi, "Spontaneous motion of localized structures induced by parity symmetry breaking transition," *Chaos: An Interdisciplinary Journal of Nonlinear Science*, vol. 28, no. 5, p. 053119, 2018.

[107] C. Christov and J. Pontes, "Numerical scheme for swift-hohenberg equation with strict implementation of lyapunov functional," *Mathematical and Computer Modelling*, vol. 35, no. 1-2, pp. 87–99, 2002.

[108] M. Tlidi, P. Mandel, and R. Lefever, "Localized structures and localized patterns in optical bistability," *Physical review letters*, vol. 73, no. 5, p. 640, 1994.

[109] P. Coullet, C. Riera, and C. Tresser, "Qualitative Theory of Stable Stationary Localized Structures in One Dimension," *Progress of Theoretical Physics Supplement*, vol. 139, pp. 46–58, 2000.

[110] P. Coullet, "Localized patterns and fronts in nonequilibrium systems," *International Journal of Bifurcation and Chaos*, vol. 12, no. 11, pp. 2445–2457, 2002.

[111] M. Tlidi, K. Staliunas, K. Panajotov, A. Vladimirov, and M. Clerc, "Localized structures in dissipative media: from optics to plant ecology," 2014.

[112] K. Ouchi and H. Fujisaka, "Phase ordering kinetics in the Swift-Hohenberg Equation," *Phys. Rev. E*, vol. 54, p. 4, 1996.

[113] A. Hagberg, A. Yochelis, H. Yizhaq, C. Elphick, L. Pismen, and E. Meron, "Linear and nonlinear front instabilities in bistable systems," *Physica D: Nonlinear Phenomena*, vol. 217, no. 2, pp. 186–192, 2006.

[114] M. G. Clerc, S. Echeverría-Alar, and M. Tlidi, "Localized states with nontrivial symmetries: Localized labyrinthine patterns," *Physical Review E*, vol. 105, no. 1, p. L012202, 2022.

[115] https://earth.google.com/web/.

[116] P. S. White, "Pattern, process, and natural disturbance in vegetation," *The botanical review*, vol. 45, pp. 229–299, 1979.

[117] O. Lejeune, M. Tlidi, and R. Lefever, "Vegetation spots and stripes: dissipative structures in arid landscapes," *International journal of quantum chemistry*, vol. 98, no. 2, pp. 261–271, 2004.

[118] M. Rietkerk, S. C. Dekker, P. C. De Ruiter, and J. van de Koppel, "Self-organized patchiness and catastrophic shifts in ecosystems," *Science*, vol. 305, no. 5692, pp. 1926–1929, 2004.

[119] P. D'Odorico, F. Laio, and L. Ridolfi, "Vegetation patterns induced by random climate fluctuations," *Geophysical Research Letters*, vol. 33, no. 19, 2006.

[120] S. Kéfi, M. Rietkerk, C. L. Alados, Y. Pueyo, V. P. Papanastasis, A. ElAich, and P. C. De Ruiter, "Spatial vegetation patterns and imminent desertification in mediterranean

arid ecosystems," *Nature*, vol. 449, no. 7159, pp. 213–217, 2007.

[121] F. Meloni, G. M. Nakamura, C. R. Granzotti, and A. S. Martinez, "Vegetation cover reveals the phase diagram of patch patterns in drylands," *Physica A: Statistical Mechanics and its Applications*, vol. 534, p. 122048, 2019.

[122] M. G. Clerc, S. Echeverría-Alar, and M. Tlidi, "Localised labyrinthine patterns in ecosystems," *Scientific reports*, vol. 11, no. 1, pp. 1–12, 2021.

[123] F. Reinitizer, "Beiträge zur kenntniss des cholesterins," *Monatshefte für Chemie*, vol. 9, pp. 421–441, 1888.

[124] O. Lehmann, "Über fliessende krystalle," *Zeitschrift für Physikalische Chemie*, vol. 4, no. 1, pp. 462–472, 1889.

[125] G. Friedel, "Les états mésomorphes de la matière," *Ann. Phys.*, vol. 9, no. 18, pp. 273–474, 1922.

[126] M. Mitov, "Liquid-crystal science from 1888 to 1922: Building a revolution," *ChemPhysChem*, vol. 15, no. 7, pp. 1245–1250, 2014.

[127] P. De Gennes, "Short range order effects in the isotropic phase of nematics and cholesterics," *Molecular Crystals and Liquid Crystals*, vol. 12, no. 3, pp. 193–214, 1971.

[128] D.-K. Yang and S.-T. Wu, *Fundamentals of liquid crystal devices.* John Wiley & Sons, 2014.

[129] C. Oseen, "The theory of liquid crystals," *Transactions of the Faraday Society*, vol. 29, no. 140, pp. 883–899, 1933.

[130] F. C. Frank, "I. liquid crystals. on the theory of liquid crystals," *Discussions of the Faraday Society*, vol. 25, pp. 19–28, 1958.

[131] J. V. Selinger, "Director deformations, geometric frustration, and modulated phases in liquid crystals," *Annual Review of Condensed Matter Physics*, vol. 13, pp. 49–71, 2022.

[132] V. H. Schmidt, "Normal-distortion-mode approach to liquid crystal elastic energy," *Physical review letters*, vol. 64, no. 5, p. 535, 1990.

[133] H. Hakemi, E. Jagodzinski, and D. Dupré, "Temperature dependence of the anisotropy of turbidity and elastic constants of nematic liquid crystal mixture e7," *Molecular Crystals and Liquid Crystals*, vol. 91, no. 1-2, pp. 129–136, 1983.

[134] W. T. B. Kelvin, *The molecular tactics of a crystal.* Clarendon Press, 1894.

[135] H. De Vries, "Rotatory power and other optical properties of certain liquid crystals," *Acta Crystallographica*, vol. 4, no. 3, pp. 219–226, 1951.

[136] R. Cano, "Interprétation des discontinuités de grandjean," *Bulletin de Minéralogie*, vol. 91, no. 1, pp. 20–27, 1968.

[137] S. Pieraccini, S. Masiero, A. Ferrarini, and G. P. Spada, "Chirality transfer across length-scales in nematic liquid crystals: fundamentals and applications," *Chemical Society Reviews*, vol. 40, no. 1, pp. 258–271, 2011.

[138] J. Baudry, S. Pirkl, and P. Oswald, "Topological properties of singular fingers in frustrated cholesteric liquid crystals," *Physical Review E*, vol. 57, no. 3, p. 3038, 1998.

[139] S. Chandrasekhar, *Liquid Crystals.* Cambridge, UK: Cambridge University Press, 1992.

[140] M. Press and A. Arrott, "Static strain waves in cholesteric liquid crystals.-i. homeotropic boundary conditions," *Journal de Physique*, vol. 37, no. 4, pp. 387–395, 1976.

[141] M. Cross and H. Greenside, *Pattern Formation and Dynamics in Non-Equilibrium Systems.* Cambridge University Press, New York, 2009.

[142] D. A. Egolf, I. V. Melnikov, and E. Bodenschatz, "Importance of local pattern properties in spiral defect chaos," *Phys. Rev. Lett.*, vol. 80, p. 15, 1998.

[143] I. Bordeu, M. Clerc, and M. Tlidi, "From localized spots to the formation of invaginated labyrinthine structures in a Swift-Hohenberg model," *Commun. Nonlinear. Sci. Numer. Simulat.*, vol. 29, 2015.

[144] E. Knobloch, "Spatial localization in dissipative systems," *conmatphys*, vol. 6, no. 1, pp. 325–359, 2015.

[145] M. Beck, J. Knobloch, D. J. Lloyd, B. Sandstede, and T. Wagenknecht, "Snakes, ladders, and isolas of localized patterns," *SIAM Journal on Mathematical Analysis*, vol. 41, no. 3, pp. 936–972, 2009.

[146] D. J. Lloyd and A. Scheel, "Continuation and bifurcation of grain boundaries in the swift–hohenberg equation," *SIAM Journal on Applied Dynamical Systems*, vol. 16, no. 1, pp. 252–293, 2017.

[147] D. J. Hill, D. J. Lloyd, and M. R. Turner, "Localised radial patterns on the free surface of a ferrofluid," *Journal of nonlinear science*, vol. 31, no. 5, p. 79, 2021.

[148] B. Kostet, Y. Soupart, K. Panajotov, and M. Tlidi, "Coexistence of dark vector soliton kerr combs in normal dispersion resonators," *Physical Review A*, vol. 104, no. 5, p. 053530, 2021.

[149] P. Couteron, "Conservative or dissipative? two distinct processes for spatial pattern emergence," *Proceedings of the National Academy of Sciences*, vol. 120, no. 5, p. e2221117120, 2023.

[150] I. Bordeu, M. G. Clerc, P. Couteron, R. Lefever, and M. Tlidi, "Self-replication of localized vegetation patches in scarce environments," *Scientific reports*, vol. 6, no. 1, pp. 1–11, 2016.

[151] J. Greenwood, "The development of vegetation patterns in somaliland protectorate," *Geographical Journal*, pp. 465–473, 1957.

[152] C. Montana, "The colonization of bare areas in two-phase mosaics of an arid ecosystem," *Journal of Ecology*, pp. 315–327, 1992.

[153] B. Bookhagen and D. W. Burbank, "Topography, relief, and trmm-derived rainfall variations along the himalaya," *Geophysical Research Letters*, vol. 33, no. 8, 2006.

[154] P. Adler, D. Raff, and W. Lauenroth, "The effect of grazing on the spatial heterogeneity of vegetation," *Oecologia*, vol. 128, no. 4, pp. 465–479, 2001.

[155] P. D'Odorico, F. Laio, A. Porporato, L. Ridolfi, and N. Barbier, "Noise-induced vegetation patterns in fire-prone savannas," *Journal of Geophysical Research: Biogeosciences*, vol. 112, no. G2, 2007.

[156] T. E. Franz, E. G. King, K. K. Caylor, and D. A. Robinson, "Coupling vegetation organization patterns to soil resource heterogeneity in a central kenyan dryland using geophysical imagery," *Water resources research*, vol. 47, no. 7, 2011.

[157] I. Rodriguez-Iturbe, Z. Chen, A. C. Staver, and S. A. Levin, "Tree clusters in savannas result from islands of soil moisture," *Proceedings of the National Academy of Sciences*, vol. 116, no. 14, pp. 6679–6683, 2019.

[158] P. Ribiere and P. Oswald, "Nucleation and growth of cholesteric fingers under electric field," *Journal de Physique*, vol. 51, no. 16, pp. 1703–1720, 1990.

[159] S. Pirkl, P. Ribiere, and P. Oswald, "Forming process and stability of bubble domains in dielectrically positive cholesteric liquid crystals," *Liquid Crystals*, vol. 13, p. 413, 1993.

[160] J.-S. B. Tai, P. J. Ackerman, and I. I. Smalyukh, "Topological transformations of hopf solitons in chiral ferromagnets and liquid crystals," *Proceedings of the national Academy of Sciences*, vol. 115, no. 5, pp. 921–926, 2018.

[161] L. Kaup and B. Kaup, *Holomorphic functions of several variables: an introduction to the fundamental theory*, vol. 3. Walter de Gruyter, 2011.

[162] T. Frisch, S. Rica, P. Coullet, and J. M. Gilli, "Spiral waves in liquid crystal," *Phys. Rev. Lett.*, vol. 72, p. 1471, 1994.

[163] T. Frisch, L. Gil, and J. M. Gilli, "Two-dimensional landau-de gennes dynamical model for the unwinding transition of a cholesteric liquid crystal," *Phys. Rev. E*, vol. 48, p. R4199, 1993.

[164] L. M. Pismen, *Vortices in nonlinear fields: from liquid crystals to superfluids, from non-equilibrium patterns to cosmic strings*, vol. 100. Oxford University Press, 1999.

[165] M. G. Clerc, E. Vidal-Henriquez, J. D. Davila, and M. Kowalczyk, "Symmetry breaking of nematic umbilical defects through an amplitude equation," *Physical Review E*, vol. 90, no. 1, p. 012507, 2014.

[166] X. Wang, X. Hu, and H. Wu, "Stripe skyrmions and skyrmion crystals," *Communications Physics*, vol. 4, no. 1, p. 142, 2021.